UAV-Enabled Surface and Subsurface Characterization for Post-Earthquake Geotechnical Reconnaissance

by

William W. Greenwood

A dissertation submitted in partial fulfillment
of the requirements for the degree of
Doctor of Philosophy
(Civil Engineering)
in The University of Michigan
2018

Doctoral Committee:

Associate Professor Dimitrios Zekkos, Co-Chair
Professor Jerome P. Lynch, Co-Chair
Associate Professor Marin K. Clark
Professor Vineet R. Kamat
Professor Emeritus Richard D. Woods

William W. Greenwood

wwgreen@umich.edu

ORCID iD: 0000-0002-7908-5793

DEDICATION

To Lisa,
I would not be here without your love and support.

ACKNOWLEDGEMENTS

I extend my deepest gratitude to my advisor, Prof. Dimitrios Zekkos, who has guided my growth as a student and provided motivation throughout my doctoral research. I would also like to thank my co-advisor, Prof. Jerome Lynch, who has pushed me to expand my horizons and has strongly influenced the direction of my career. I sincerely thank Prof. Marin Clark, who presented incredibly unique opportunities that have shaped my motivations as a researcher. I would like to thank committee members Prof. Richard Woods and Prof. Vineet Kamat for their advice and sharing their unique perspectives. I am also grateful for advice and support provided by other faculty and staff in CEE and to John Manousakis for additional data. I would additionally like to acknowledge the tremendous assistance provided by other students in CEE and EARTH. And to my family, thank you for patience and unending support.

TABLE OF CONTENTS

DEDICATION……ii

ACKNOWLEDGMENTS……iii

LIST OF FIGURES……..ix

LIST OF TABLES……xxvi

LIST OF APPENDICES……..xxviii

LIST OF ACRONYMS……..xxix

ABSTRACT……...xxxi

CHAPTER

1. Introduction……..1

1.1. Background……1

1.2. Organization of the Dissertation……..…5

1.3. References……...8

2. UAVs in Civil Infrastructure Applications……..11

2.1. Introduction……...11

2.1.1. Structure……13

2.2. Unmanned Aerial Vehicles……...14

2.2.1. Platform Types……...14

2.2.2. Performance Characteristics……...19

2.3. UAV Deployed Sensors……23

2.3.1. Sensing Payloads……24

2.3.2. Comparison between Lidar and Camera Surveying……25

2.4. System Integration and Data Processing Challenges……27

2.4.1. Wireless Sensor Networks……..27

2.4.2. UAV-Specific Data Reduction……...29

2.5. Applications in Civil Engineering……32

2.5.1. Monitoring of Infrastructure System Components……34

2.5.2. Construction Safety and Progress Monitoring……38

2.5.3. Geological and Geotechnical Engineering……41

2.5.4. Post-Disaster Reconnaissance……43

2.6. Summary and Conclusions……48

2.7. References……56

3. UAV-Enabled 3D Imaging of Geotechnical Sites…….....66

3.1. UAV-Based Structure-from-Motion Photogrammetry……67

3.1.1. Fundamentals of SfM……67

3.1.2. Workflow and Outputs……...69

3.1.3. Generalized Field Procedure and Data Collection Considerations……70

3.1.4. Error Assessment of SfM Models……..73

3.2. Geotechnical Applications of UAV-Based SfM……74

3.2.1. Mapping of Geotechnical Sites……...75

3.2.2. Delineation of Landslide Geometry……...80

3.2.3. 3D Rock Mass Characterization……83

3.3. Summary of Lessons Learned from Aerial Surveying of Geotechnical Sites……..…….88

3.4. References……...111

4. Processing of UAV-Derived 2D and 3D Imagery Outputs for Rock Mass Characterization…….. 114

4.1. Development of a Fracture Detection Algorithm……....115

4.1.1. Image Gradient……..……118

4.1.2. Estimation of Gradient Threshold……119

4.1.3. Morphologic Filtering……..122

4.1.4. Additional Fracture Detection Components……123

4.1.5. Performance of Fracture Detection……...126

4.1.6. Limitations and Practical Considerations……130

4.1.7. Example Applications in Rock Mechanics……...134

4.2. Generation and Processing with Multimodal Images……..138

4.2.1. Generating RGBD Images……138

4.2.2. Framework for Depth-Enabled Superpixels……140

4.2.3. Estimation of Surface Roughness……143

4.2.4. Isolation of Discontinuities……..145

4.2.5. Mapping Detected Fractures to 3D Points……146

4.3. Conclusions and Recommendations for 3D-Enabled Image Processing Framework…..148

4.4. References……...185

5. UAV-Enabled Subsurface Imaging using Multichannel Analysis of Surface Waves…..187

5.1. Surface Wave Methods Background……...188

5.1.1. Rayleigh Wave Dispersion……...189

5.1.2. Dispersion Curve Inversion…….....190

5.1.3. Generalized Field Procedure in this Study……191

5.2. Open-Source Computer Dispersion Code……...193

5.2.1. Dispersion of Multichannel Data……..193

5.2.2. Estimation of Spatial Variability……..194

5.2.3. Modeling of Profiles…….……....195

5.2.4. Rayleigh Wave Attenuation……196

5.3. Surface Wave Methods Using UAV-Delivered Impulse Sources……..198

5.3.1. Limitations of Surface Wave Methods……198

5.3.2. UAV Platforms……199

5.3.3. Site Layout and Equipment……..200

5.3.4. Initial Testing Program – Low Energy Input……201

5.3.5. MASW with M600P – High Energy Input……203

5.3.6. Accuracy of Dropped Weights……205

5.3.7. Source Characterization……...207

5.3.8. Dispersion Analysis……212

5.3.9. Depth of Investigation……..214

5.3.10. Attenuation of Peak Vibrations……217

5.3.11. Drop Weight Recommendations…..……219

5.3.12. Conclusions and Future Work……..221

5.4. References……...256

6. Conclusions and Recommendations for Future Research…….……...260

6.1. Summary of Conclusions……260

6.1.1. UAV-Based 3D Imaging of Geotechnical Sites……260

6.1.2. 3D-Enabled Multimodal Image Processing……..262

6.1.3. UAV-Enabled Surface Wave Testing……...264

6.2. Recommendations for Future Research……...266

APPENDICES……269

LIST OF FIGURES

Figure 1-1: (Top row) current practice consists of manual reconnaissance requiring site access, deformation measurements, and manual site characterization processes; (bottom row) the UAV envisioned paradigm consists of UAVs gaining access to sites, collecting deformation data using SfM or LiDAR, and UAV-based site characterization through actuation and automation……..7

Figure 1-2: Potential automated UAV reconnaissance workflow…….....8

Figure 2-1: Examples of some commercial UAVs: (a) fixed-wing senseFly eBee (SenseFly, 2015); (b) multirotor DJI Inspire 1 (DJI, 2016); (c) VTOL FireFly 6 (BirdsEyeView Aerobotics, 2016)……51

Figure 2-2: Hierarchical taxonomy of UAV platform types……..52

Figure 2-3: Figure 5-3: Common trirotor (Y3), quadrotor (X4), hexarotor (HX6; Y6), and octorotor (OX8; X8) multirotor layouts……..53

Figure 2-4: Empirical relationship between total weight, flight time, and battery capacity derived from 26 commercially-available UAV configurations; labels correspond to index values in Table 2-1……..54

Figure 2-5: UAV application to surveying tasks (adapted from Siebert and Teizer, 2014)……..54

Figure 2-6: LiDAR scan of bridge deck before and after altitude estimate and scan-matching alignment (adapted from Brooks et al., 2014)……..55

Figure 2-7: Number of civil engineering-related applications cited in FAA UAS exemption applications; data from AUVSI (2016)……55
Figure 3-1: 3D imaging with SfM workflow……..95
Figure 3-2: Procedure for performing geotechnical aerial survey……...95
Figure 3-3: Maximum flight height to achieve GSD values for different cameras……96
Figure 3-4: Grass-covered wavefield (crests are approximately 2 m apart) 3D point cloud produced with (a) oblique images and (b) without oblique images……96
Figure 3-5: Example of GCP visible in a UAV-collected image……...97
Figure 3-6: (a) SfM 3D point cloud (in meters) and (b) cloud-to-cloud distance comparison between UAV-SfM and terrestrial LiDAR……...97
Figure 3-7: Satellite image of Kauhola Point with red line indicating survey area……98
Figure 3-8: Disjointed 3D model of eroding Kauhola Point cliff……98
Figure 3-9: (a) Stratigraphy interpretation from 3D model and (b) 2D Vs profile……99
Figure 3-10: Channel followed by UAV to investigate source of debris flow……...100
Figure 3-11: Debris flow sources identified by UAV reconnaissance……..100
Figure 3-12: Survey area normalized by GSD as a function of flight time for aerial surveys of 26 different sites……..101
Figure 3-13: Point cloud overview of landslide with debris cone delineated……101
Figure 3-14: GCPs placed at the landslide toe……102
Figure 3-15: Cross-section through centerline of the landslide and annotated with point cloud measurements……102
Figure 3-16: Satellite images of Small Awini Landslide (a) about 1 month after the 2006 Kiholo Bay earthquake and (b) in January 2014……103

Figure 3-17: UAV-collected image at top of landslide scarp showing alternating stratigraphy…104

Figure 3-18: Location of shear wave velocity profile on landslide deposit……..104

Figure 3-19: Shear wave velocity profile on landslide deposit……..105

Figure 3-20: Example of visual rock mass classification using the ISRM (1978) approach applied to a 4 m vertical cut…….105

Figure 3-21: Chart used to assign GSI values for a rock mass (from Marinos et al., 2005)…....106

Figure 3-22: Photo of landslide back-scarp revealing weathering profile……....107

Figure 3-23: Spatial GSI allocation on landslide scarp……....107

Figure 3-24: Hoek-Brown failure criterion using information derived from SfM data and point cloud……...108

Figure 3-25: Point cloud overview of structurally-controlled landslide……..109

Figure 3-26: Figure 3-25: Distribution of GCP and laser points used for SfM scaling……109

Figure 3-27: Illustration of foliation controlling failure and measurement location in 3D point cloud……...110

Figure 3-28: Structurally-controlled, wedge failure observed about 50 m upslope…….110

Figure 4-1: Developed computation sequence fracture detection method……154

Figure 4-2: 3D-enabled image processing framework…….154

Figure 4-3: (a) Sample Image; (b) Grayscale Image; (c) Vertical Image Gradient; and (d) Horizontal Image Gradient…….155

Figure 4-4: Effect of increasing gradient threshold……..155

Figure 4-5: (a) Photo of brick wall; (b) binary image of brick wall generated with threshold T; and (c) convergence of threshold value…….156

Figure 4-6: Example multi-threshold potential fracture map……157

Figure 4-7: Effect of kb on sample images: (a) kb = 0.2; (b) kb = 0.3; (c) kb = 0.4; (d) kb = 0.5..158

Figure 4-8: (a) 4-way and (b) 8-wayconnectivity neighborhoods……158

Figure 4-9 Example marble image (M1) subjected to (a) first morphologic filtering step; (b) binary object thinning; and (c) second morphologic filtering step……159

Figure 4-10: Sample image (a) before applying Gaussian filter and (b) after…….....160

Figure 4-11: Effect of blurring on fractures: (a) unfiltered fracture; (b) filtered fracture; (c) intensity across fracture; and (d) vertical gradient across fracture……160

Figure 4-12: Examples of staining of weathered basalt……160

Figure 4-13: (a) Unaltered grayscale image; (b) image altered using modified Otsu's threshold (Os = 0.5); (c) final fracture detection of unaltered image; (d) final fracture detection of altered image…….....161

Figure 4-14: Orthophoto of marble quarry wall with human-made objects highlighted…….161

Figure 4-15: (a) Example of automatic fracture detection performed on a marble image (M1) with examples of a positive detection and incomplete detection of fractures; and (b) simplified labeling of manually-detected fractures…….162

Figure 4-16: True positive rate as function of total false positives for marble orthophoto images……163

Figure 4-17: Precision-Recall Relationship for marble orthophoto images…….163

Figure 4-18: Example output from fracture detection on four marble images with kb=0.5……164

Figure 4-19: Example photos of a roughly 4 m high basalt outcrop in Hawaii……165

Figure 4-20: Detection rate as a function of false positives for basalt images…….166

Figure 4-21: Example of single basalt image subjected to different control parameters…….166

Figure 4-22: Example output from fracture detection on four basalt images…….....167

Figure 4-23: Detection rate as a function of false positives for the third image set…….168

Figure 4-24: Precision-recall relationship for third image set…….....168

Figure 4-25: Output from fracture detection performed on three examples from the third image set with kb = 0.4……..169

Figure 4-26: (a) SLIC (N_c=10) applied to a sample image and (b) median function applied to the superpixels……169

Figure 4-27: Sample transects for manual fracture counting, approximate height is 2 m……...170

Figure 4-28: Automatic fracture detection versus manual fracture counting for transects in Figure 4-27……....170

Figure 4-29: Transects used to assess fracture detection of interlocked angular blocky rock with k_b=0.4…….171

Figure 4-30: Results of fracture detection compared to manual fracture counting for transects in Figure 4-29…….171

Figure 4-31: Fracture detection with kb = 0.35 applied to the quarry orthophoto……172

Figure 4-32: Comparison of fracture detection results to manual counting for the quarry orthophoto……..173

Figure 4-33: Example of fracture detection; narrowest fractures are not detected, or are partially detected……..173

Figure 4-34: (a) Profile subjected to fracture detection (green pixels), and (b) automatic RQD computation on 10 cm wide vertical transects…….....174

Figure 4-35: Comparison between automatic RQD and manual RQD calculations for vertical transects labeled in Figure 4-26; automatic values are the average of three closest cells…..174

Figure 4-36: (a) Profile subjected to fracture detection; (b) contours indicating fracture density (fractures per meter) overlain on photo of profile; and (c) manual classification of profile using the ISRM (1978) system……175

Figure 4-37: Heat map of fractures per meter and profile; examples of good performance are highlighted…….176

Figure 4-38: Heat map of fractures per m and profile; examples of erroneous results are highlighted…….177

Figure 4-39: 2D Vs contours generated by MASW testing above outcrop……178

Figure 4-40: Correlation between approximate minimum and maximum fracture frequency and Vs generated by 2D MASW test……178

Figure 4-41: Example of camera and global coordinate systems…….179

Figure 4-42: Pixel coordinate system……...179

Figure 4-43: Slope profile derived from RGBD image……180

Figure 4-44: SLIC Procedure (from Achanta et al., 2012)……180

Figure 4-45: Impact of changing N_c in the original SLIC algorithm for an image; (a) N_c=40 and (b) N_c=10……..181

Figure 4-46: Comparison between depth values within a single cluster for RGB (left) versus RGBD (right) SLIC for two equivalent clusters with K=10 and N_c=10 (top) and N_c=40 (bottom)…181

Figure 4-47: Impact of K on clustering; (a) K=5, and (b) K=10……..182

Figure 4-48: (a) Manually-segmented region of RGBD image; (b) planar fit to points, and (c) estimation of surface roughness…….182

Figure 4-49: (a) Image of detected fracture (internal pixels have also been classified); (b) visualization of RGBD data for the image; (c) classified fracture pixels mapped to the depth

points; and (d) highlight of depth points identified as fracture in 3D but missed in 2D detection……183

Figure 4-50: (a) Photo of fractured rock; (b) fracture detection results transformed to 3D point cloud……...184

Figure 4-51: (a) Photo of a blocky rock mass; (b) 3D points projected to image plane……184

Figure 4-52: (a) Fractures identified in 2D and (b) transformed back to 3D (points are exaggerated)…….....185

Figure 5-1: Generalized workflow for surface wave inversion algorithms……...227

Figure 5-2: Sample output from dispersion code including sensor recordings for (a) the first, (b) eighth, and (c) sixteenth geophones in the array; (d) velocity-frequency spectrum; and (e) automatically selected spectral peaks…….228

Figure 5-3: Variability assessment of four V_s profiles at a soil site…….228

Figure 5-4: Median profile from Figure 5-3 with model fit…….229

Figure 5-5: (a) Coherence function; (b) frequency domain comparison; and (c) fitting of curve described by Equation 5-6……..229

Figure 5-6: Examples of attenuating active-source signals at (a) 14 Hz and (b) 60 Hz as a function of distance from the source…….230

Figure 5-7: Rayleigh wave coefficient of attenuation as a function of frequency derived from MASW data collected at the UAV test site…….230

Figure 5-8: Fundamental comparison of seismic surface wave sources……231

Figure 5-9: (a) Phantom 3 Professional with payload release attached; (b) payload-release system components; and (c) Matrice 600 Pro UAV……....232

Figure 5-10: Drop Weights used in this study; labels correspond to Table 5-6…….232

Figure 5-11: UAV-MASW test site location……233

Figure 5-12: Aerial photo showing layout of sensors at the test site……233

Figure 5-13: Aerial photo of equipment and target weight drop area……234

Figure 5-14: 2D Shear wave velocity cross-section produced using CMPCC MASW method…235

Figure 5-15: Time histories at first geophone of stacked signals for P3P UAV (8 stacks) and hammer sources (5 stacks)……..235

Figure 5-16: Frequency content of mean signals generated by P3P UAV (a) compared to the mean hammer signal and (b) compared to background noise……..236

Figure 5-17: (a) Frequency content of stacked signals generated by P3P UAV (8 stacks) and hammer (5 stacks) and (b) at low frequencies……236

Figure 5-18: Weight landing locations for P3P and M600 UAVs; northing and easting measured from the center of the drop target……..237

Figure 5-19: Interpreted dispersion curves from single drops using the S1 (large sphere) from 60 m……....238

Figure 5-20: Hammer-generated dispersion curves indicating seasonal effects on subsurface properties at the test site…….....238

Figure 5-21: Individual and mean signals for (a) 5.4 kg hammer; (b) low frequency 5.4 kg Hammer; (c) 4.7 kg weight dropped from 15 m; (d) and low frequency 4.7 kg weight dropped from 15 m……...239

Figure 5-22: Frequency content (5 - 20 Hz) of sledgehammer signals (5 stacks) at the first geophone compared to the M600P UAV (5 stacks)……..240

Figure 5-23: Phase velocity-frequency spectra for (a) 4.7 kg mass dropped from 15 m (stacked 5 times); and (b) 5.4 kg sledgehammer (stacked 5 times); (c) frequency domain of stacked sledgehammer and UAV-generated signals; and (d) dispersion curves…….....240

Figure 5-24: Individual and mean signals for (a) 4.7 kg plate from 30 m; (b) 7 kg plate from 30 m; (c) 7 kg plate from 60 m; and (d) 7 kg large sphere from 60 m…….....241

Figure 5-25: Comparison of stacked time domain signals for (a) 4.7 kg plates and (b) 7 kg plates versus hammer……...242

Figure 5-26: Comparison of mean frequency domain signals for (a) 4.7 kg plates and hammer; and (b) at low frequencies…….242

Figure 5-27: Comparison of mean frequency domain signals for (a) 7 kg plates and hammer; and (b) at low frequencies…….243

Figure 5-28: Comparison of stacked signals in the frequency domain for (a) 4.7 kg plates with hammer; and (b) 7 kg plates with hammer…….243

Figure 5-29: Frequency content of signals generated by (a) 7 kg spherical weights; (b) and at low frequencies…….244

Figure 5-30: Impact craters of small spherical 7 kg weight (S1) dropped from (a) 15 m and (b) 30 m…….....244

Figure 5-31: Individual and mean signals generated by (a) 7 kg weights and hammer; and (b) at low frequencies……..245

Figure 5-32: Stacked signals generated by 7 kg weights and hammer……245

Figure 5-33: Phase velocity-frequency spectra for 5 stacked 7 kg sphere at 60 m signals (a) and single 7 kg sphere at 60 m signal……..…….246

Figure 5-34: Dispersion curves for single weight drops using (a) 7 kg plate 60 m (4 trials); (b) 7 kg sphere 60 m (5 trials); (c) 7 kg plate 30 m (8 trials); (d) 4.7 kg plate 30 m (5 trials); and (e) 4.7 kg plate 15 m (8 trials)……..247

Figure 5-35: Mean dispersion curves for independent 7 kg weights dropped from 60 m and stacked 5.4 kg hammer dispersion curves……248

Figure 5-36: Stacked (5x) time domain signals for large sphere dropped from 60 m and hammer (a) at the first geophone; and (b) at the last geophone (90 m from first geophone)……248

Figure 5-37: (a) Mean frequency domain signal for large sphere dropped from 60 m and hammer; and (b) at low frequencies……..249

Figure 5-38: (a) Stacked (5x) frequency domain signal for large sphere dropped from 60 m and hammer; and (b) at low frequencies……249

Figure 5-39: Phase velocity-frequency spectra for stacked signals (5x) for (a) 7 kg large sphere dropped from 60 m and (b) hammer……...250

Figure 5-40: Dispersion curves interpreted from spectra in Figure 5-39; estimated depth of investigation is approximated as one half of the longest wavelength……250

Figure 5-41: Vs profiles for dispersion curves in Figure 5-40……....251

Figure 5-42: Comparison of SNR for stacked and unstacked hammer and UAV signals……251

Figure 5-43: Estimated PPV induced by hammer and UAV-dropped weight impact sources…252

Figure 5-44: Estimated PPV induced by hammer and UAV-dropped weight impact sources compared to pseudo-attenuation curves produced from drop weight results reported by Woods and Jedele (1985)……253

Figure 5-45: Estimated PPV induced by hammer and UAV-dropped weight impact sources as a function of scaled distance……254

Figure 5-46: (a) Experimental dispersion curve for UAV-deployed source and 90 m geophone array and (b) range of theoretical depth of investigation based on wavelength approximations……255
Figure B-1: Image M1……...283
Figure B-2: Image M1 kb=0.4……...283
Figure B-3: Image M2……...284
Figure B-4: Image M2 kb=0.4……...284
Figure B-5: Image M3……...285
Figure B-6: Image M3 kb=0.4……...285
Figure B-7: Image M4……...286
Figure B-8: Image M4 kb=0.4……...286
Figure B-9: Image M5……...287
Figure B-10: Image M5 kb=0.4…….287
Figure B-11: Image M6…….288
Figure B-12: Image M6 kb=0.4…….288
Figure B-13: Image M7…….289
Figure B-14: Image M7 kb=0.4…….289
Figure B-15: Image M8…….290
Figure B-16: Image M8 kb=0.4…….290
Figure B-17: Image M9…….291
Figure B-18: Image M9 kb=0.4…….291
Figure B-19: Image M10……...292
Figure B-20: Image M10 kb=0.4……...292

Figure B-21: Image M11……...293

Figure B-22: Image M11 kb=0.4……...293

Figure B-23: Image M12……...294

Figure B-24: Image M12 kb=0.4……...294

Figure B-25: Image M13……...295

Figure B-26: Image M13 kb=0.4……...295

Figure B-27: Image M14……...296

Figure B-28: Image M14 kb=0.4……...296

Figure B-29: Image M15……...297

Figure B-30: Image M15 kb=0.4……...297

Figure B-31: Image M16……...298

Figure B-32: Image M16 kb=0.4……...298

Figure B-33: Image M17……...299

Figure B-34: Image M17 kb=0.4……...299

Figure B-35: Image M18……...300

Figure B-36: Image M18 kb=0.4……...300

Figure B-37: Image BA1……301

Figure B-38: Image BA1 kb=0.3 Os=0.5……...301

Figure B-39: Image BA2……301

Figure B-40: Image BA2 kb=0.3 Os=0.5……...301

Figure B-41: Image BA3……302

Figure B-42: Image BA3 kb=0.3 Os=0.5……...302

Figure B-43: Image BA4……302

Figure B-44: Image BA4 kb=0.3 Os=0.5……....302

Figure B-45: Image BA5……303

Figure B-46: Image BA5 kb=0.3 Os=0.5……....303

Figure B-47: Image BA6……303

Figure B-48: Image BA6 kb=0.3 Os=0.5……....303

Figure B-49: Image BA7……304

Figure B-50: Image BA7 kb=0.3 Os=0.5……....304

Figure B-51: Image BA8……304

Figure B-52: Image BA8 kb=0.3 Os=0.5……....304

Figure B-53: Image BA9……305

Figure B-54: Image BA9 kb=0.3 Os=0.5……....305

Figure B-55: Image BA10……...305

Figure B-56: Image BA10 kb=0.3 Os=0.5……..306

Figure B-57: Image BA11……...306

Figure B-58: Image BA11 kb=0.3 Os=0.5……..306

Figure B-59: Image BA12……...307

Figure B-60: Image BA12 kb=0.3 Os=0.5……..307

Figure B-61: Image BA13……...307

Figure B-62: Image BA13 kb=0.3 Os=0.5……..307

Figure B-63: Image BA14……...308

Figure B-64: Image BA14 kb=0.3 Os=0.5……..308

Figure B-65: Image BA15……...308

Figure B-66: Image BA15 kb=0.3 Os=0.5……..308

Figure B-67: Image BA16……...309

Figure B-68: Image BA16 kb=0.3 Os=0.5……..309

Figure B-69: Image BA17……...309

Figure B-70: Image BA17 kb=0.3 Os=0.5……..309

Figure B-71: Image BA18……...310

Figure B-72: Image BA18 kb=0.3 Os=0.5……..310

Figure B-73: Image BA19……...310

Figure B-74: Image BA19 kb=0.3 Os=0.5……..310

Figure B-75: Image BA20……...311

Figure B-76: Image BA20 kb=0.3 Os=0.5……..311

Figure B-77: Image BA21……...311

Figure B-78: Image BA21 kb=0.3 Os=0.5……..311

Figure B-79: Image BA22……...312

Figure B-80: Image BA22 kb=0.3 Os=0.5……..312

Figure B-81: Image BA23……...313

Figure B-82: Image BA23 kb=0.3 Os=0.5……..313

Figure B-83: Image BA24……...314

Figure B-84: Image BA24 kb=0.3 Os=0.5……..314

Figure B-85: Image BA25……...314

Figure B-86: Image BA25 kb=0.3 Os=0.5……..314

Figure B-87: Image BA26……...315

Figure B-88: Image BA26 kb=0.3 Os=0.5……..315

Figure B-89: Image BA27……...315

Figure B-90: Image BA27 kb=0.3 Os=0.5……315

Figure B-91: Image BA28……316

Figure B-92: Image BA28 kb=0.3 Os=0.5……316

Figure B-93: Image H2……317

Figure B-94: Image H2 kb=0.4……317

Figure B-95: Image H3……318

Figure B-96: Image H3 kb=0.4……318

Figure B-97: Image H4……319

Figure B-98: Image H4 kb=0.4……319

Figure B-99: Image IDL……320

Figure B-100: Image IDL kb=0.4……320

Figure B-101: Image K1……320

Figure B-102: Image K1 kb=0.4……320

Figure B-103: Image K2……321

Figure B-104: Image K2 kb=0.4……321

Figure B-105: Image L1……321

Figure B-106: Image L1 kb=0.4……321

Figure B-107: Image L2……322

Figure B-108: Image L2 kb=0.4……322

Figure B-109: Image NP1……322

Figure B-110: Image NP1 kb=0.4……322

Figure B-111: Image NP4……323

Figure B-112: Image NP4 kb=0.4……323

Figure B-113: Image NP5……...323

Figure B-114: Image NP5 kb=0.4……...323

Figure B-115: Image NZ1……...324

Figure B-116: Image NZ1 kb=0.4……...324

Figure B-117: Image NZ2……...325

Figure B-118: Image NZ2 kb=0.4……...325

Figure B-119: Image NZ3……...326

Figure B-120: Image NZ3 kb=0.4……...326

Figure B-121: Image NZ4……...327

Figure B-122: Image NZ4 kb=0.4……...327

Figure B-123: Image NZ5……...328

Figure B-124: Image NZ5 kb=0.4……...328

Figure B-125: Image NZ10…….328

Figure B-126: Image NZ10 kb=0.4…….328

Figure B-127: Image NZ11…….329

Figure B-128: Image NZ11 kb=0.4…….329

Figure B-129: Image NZ12…….329

Figure B-130: Image NZ12 kb=0.4…….329

Figure B-131: Image NZ13…….330

Figure B-132: Image NZ13 kb=0.4…….330

Figure B-133: Image NZ17…….330

Figure B-134: Image NZ17 kb=0.4…….331

Figure B-135: Image NZ18…….331

Figure B-136: Image NZ18 kb=0.4…….332

Figure B-137: Image NZ21…….332

Figure B-138: Image NZ21 kb=0.4…….332

Figure B-139: Image S1……..333

Figure B-140: Image S1 kb=0.4……..333

Figure B-141: Image S2……..334

Figure B-142: Image S2 kb=0.4……..334

Figure B-143: Image S3……..335

Figure B-144: Image S3 kb=0.4……..335

Figure B-145: Image S4……..336

Figure B-146: Image S4 kb=0.4……..336

Figure B-147: Image S5……..336

Figure B-148: Image S5 kb=0.4……..336

LIST OF TABLES

Table 2-1: Specifications of popular commercial UAV platforms……..50

Table 2-2: UAV-based sensors and corresponding applications…….51

Table 3-1: Sites in Hawaii surveyed by UAV…….....92

Table 3-2: Sites in Nepal surveyed by UAV……...…93

Table 3-3: Selected sites mapped using UAV-enabled SfM……...94

Table 4-1: Recent crack and discontinuity mapping approaches……..151

Table 4-2: Performance of fracture detection on marble images……..151

Table 4-3: F-measure for five values of k_b in marble images……151

Table 4-4: Performance evaluation of basalt images……152

Table 4-5: Fracture detection rates in basalt images for six different combinations of control parameters……153

Table 4-6: Performance of third image set……..…153

Table 4-7: F-measure for third image set…….....154

Table 5-1: Various available surface wave dispersion techniques……...224

Table 5-2: Examples of surface wave inversion algorithms……..225

Table 5-3: Empirical model for various waste materials in containment facilities……225

Table 5-4: Primary Matlab functions to perform operations described in this section……226

Table 5-5: Characteristics of UAVs used for releasing weights……..…226

Table 5-6: Physical characteristics of drop weights used for Rayleigh wave generation……..…226

Table 5-7: Summary of Drop-Weight Trials used for MASW using M600P UAV……...227

Table 5-8: Details of drop weight vibration sites (modified from Woods and Jedele, 1985)…....227

LIST OF APPENDICES

APPENDIX

A **Matlab Functions for Multichannel Analysis of Surface Waves**……270

B **Fracture Detection Test Images**……282

B.1 **Marble Image Set**……...283

B.2 **Basalt Image Set**…….....301

B.3 **Third Image Set**……..317

LIST OF ACRONYMS

UAV:	Unmanned Aerial Vehicle	2
LiDAR:	Light Detection and Ranging	2
SfM:	Structure-from-Motion	5
WSN:	Wireless Sensor Network	5
FAA:	Federal Aviation Administration	12
UAS:	Unmanned Aircraft System	14
VTOL:	Vertical Take-off and Landing	15
RTK:	Real-Time Kinematic	18
GPS:	Global Positioning System	18
GCP:	Ground Control Point	26
DTM:	Digital Terrain Model	26
SAR:	Synthetic Aperture Radar	29
IMU:	Inertial Measurement Unit	30
SIFT:	Scale-Invariant Feature Transform	31
MVS:	Multi-View Stereo	31
DOT:	Department of Transportation	38
BIM:	Building Information Modeling	39
DSM:	Digital Surface Model	41
IR:	Infrared	42
MASW:	Multichannel Analysis of Surface Waves	43
NOAA:	National Oceanic and Atmospheric Administration	44
GSD:	Ground Sampling Distance	44
VMS:	Vision Measurement System	45
P2V:	Phantom 2 Vision+	75
P3P:	Phantom 3 Professional	77
GSI:	Geologic Strength Index	83
ISRM:	International Society of Rock Mechanics	83
SLIC:	Simple Linear Iterative Clustering	115
RANSAC:	Random Sample Consensus	116
ROC:	Receiver Operating Characteristic	127
RQD:	Rock Quality Designation	134
CMPCC:	Common Midpoint Cross Correlation	136
SWM:	Surface Wave Methods	188
MAM:	Microtremor Analysis Method	188
COV:	Coefficient of Variation	194

MSW: Municipal Solid Waste……....195
M600P: Matrice 600 Pro……200
SNR: Signal to Noise Ratio……203
PPV: Peak Particle Velocity……..217

ABSTRACT

Major earthquakes continue to cause significant damage to infrastructure systems and the loss of life (e.g. 2016 Kaikoura, New Zealand; 2016 Muisne, Ecuador; 2015 Gorkha, Nepal). Following an earthquake, costly human-led reconnaissance studies are conducted to document structural or geotechnical damage and to collect perishable field data. Such efforts are faced with many daunting challenges including safety, resource limitations, and inaccessibility of sites. Unmanned Aerial Vehicles (UAV) represent a transformative tool for mitigating the effects of these challenges and generating spatially distributed and overall higher quality data compared to current manual approaches. UAVs enable multi-sensor data collection and offer a computational decision-making platform that could significantly influence post-earthquake reconnaissance approaches. As demonstrated in this research, UAVs can be used to document earthquake-affected geosystems by creating 3D geometric models of target sites, generate 2D and 3D imagery outputs to perform geomechanical assessments of exposed rock masses, and characterize subsurface field conditions using techniques such as in situ seismic surface wave testing. UAV-camera systems were used to collect images of geotechnical sites to model their 3D geometry using Structure-from-Motion (SfM). Key examples of lessons learned from applying UAV-based SfM to reconnaissance of earthquake-affected sites are presented. The results of 3D modeling and the input imagery were used to assess the mechanical properties of landslides and rock masses. An automatic and semi-automatic 2D fracture detection method was developed and integrated with a 3D, SfM, imaging framework. A UAV was then integrated with seismic surface wave testing to estimate the shear

wave velocity of the subsurface materials, which is a critical input parameter in seismic response of geosystems. The UAV was outfitted with a payload release system to autonomously deliver an impulsive seismic source to the ground surface for multichannel analysis of surface waves (MASW) tests. The UAV was found to offer a mobile but higher-energy source than conventional seismic surface wave techniques and is the foundational component for developing the framework for fully-autonomous in situ shear wave velocity profiling.

CHAPTER 1

Introduction

1.1 Background

In recent years, the engineering community has witnessed many natural disasters (e.g., earthquakes, landslides, tsunamis, tropical storms) causing significant damage to infrastructure systems and loss of human life. When appropriate, teams of civil engineers perform costly reconnaissance studies to document structural or geotechnical damage and collect perishable field performance data of system behavior during extreme natural hazard events. Some examples of intensely-studied earthquakes from just the previous three years include 2016 Kaikoura, New Zealand (Bastin et al., 2017; Bradley et al., 2017; Dellow et al., 2017; Woods et al., 2017), 2016 Muisne, Ecuador (Alvarado et al., 2016; Lanning et al., 2016), 2015 Gorkha, Nepal (Clark et al., 2015; Collins and Jibson et al., 2015; Hashash et al., 2015; Kargel et al., 2015; Zekkos et al., 2017). Findings from reconnaissance studies are then used to refine the scientific understanding of geotechnical behavior so that design methods can be improved and achieve greater system resiliency. Findings are also a critical input to real-time decision making centered on recovery efforts (Murphy et al. 2015). Data collection in these harsh operational environments presents many challenges including: ensuring safety of personnel, perishable nature of field data, inaccessibility of many sites, and the challenges associated with acquiring physical measurements. These challenges prevent reconnaissance teams from identifying sites of interest, particularly if they are not accessible by roadways. The narrow scope of site identification reduces the breadth

of site types and causes site selection bias. A broader array of sites can be identified over time as more information is gathered and data from secondary sources (*e.g.*, satellite imagery) is acquired, but the sites may be affected by data perishability. Pressure to collect data as rapidly as possible caused by perishability and the general inaccessibility of sites both reduce the scope of individual site investigations. The combination of these factors reduces both the breadth of sites that can be documented and the detail to which they are characterized. Unmanned aerial Vehicles (UAV) are potentially highly effective in mitigating these obstacles by improving the rate of data collection, improving data quality when necessary, accessing dangerous sites, and potentially being the catalyst for developing new site reconnaissance strategies.

Figure 1-1 shows the current post-disaster reconnaissance paradigm (top row) of initial reconnaissance, deformation documentation, and *in situ* testing. For example, following an earthquake, sites of interest must be identified often from traveling on available roadways and initial reconnaissance is therefore hindered by a lack of information. Ground based travel is often obstructed, helicopters are costly or unavailable, and satellite imagery may be too coarse, unavailable, or obstructed. The deformation of geostructures is ideally documented by terrestrial LiDAR (Light Detection and Ranging) scans from limited perspectives, however, this is not always true. Even now, hand measurements are commonplace as the primary method of documenting displacements. Site characterization is typically limited by site accessibility and available resources. Equipment is difficult to mobilize in earthquake-affected regions. And as mentioned previously, the perishability of data dramatically limits both the number of sites that can be investigated and the scope of individual site characterization plans. The ability of UAVs to geometrically document sites has already started to influence post-disaster schemes on a limited basis.

During the duration of this doctoral research, UAVs have started to be used in a post-disaster reconnaissance context primarily to leverage their mobility to acquire imagery. The imagery can then be used for generating 3D surface geometry models and general site documentation, however, this has not become the standard practice. UAV integration with all three stages of reconnaissance has obvious potential to transform the paradigm other than boosting the collection rate of imaging data. The potential scope of using UAVs in post-disaster reconnaissance is much broader. The capabilities of a UAV can extend well-beyond mobilization of a single optical sensor. They are robotic platforms with computational resources and communication architectures that can be outfitted with multiple sensors to acquire geometry and material properties at the surface and in the subsurface. Expanding computational power means that UAVs can be used to perform real-time data processing and, if the framework exists, conduct real-time decision making. Additionally, a robust communication architecture could allow a UAV to transmit data to stakeholders and decision makers as it is collected and interpreted, whether that data be collected by on-board sensors or interrogated from off-board sensors (*e.g.* wireless sensor network).

Figure 1-1 also shows an envisioned paradigm (bottom row) where the suite of UAV capabilities (computational power, communication, sensing, and mobility) has transformed the initial reconnaissance, deformation documentation, and site characterization phases of reconnaissance. In addition to augmenting the strategies employed during each of the three phases, an automation step has been envisioned that would introduce information acquired in other stages of reconnaissance as more conclusions are made at specific sites to expand on data collection and site selection. Figure 1-2 shows a proposed workflow for future automated UAV reconnaissance. The workflow in Figure 1-2 contains several stages including regional mapping to identify

potential sites of interest, localized mapping of individual sites, geometric documentation, and *in situ* testing. Steps in the workflow where the work presented herein has made contributions are highlighted in Figure 1-2. The workflow emphasizes the concept of automation, where previous steps can be returned to as new information is gathered and higher-resolution data needs to be collected. The major barriers to achieving such a transformative result are not only the development of data processing techniques, but the interpretation of the data, synthesis of all available data, and subsequent decision making. This will help reduce site selection bias by improving the depth and breadth of documented sites, which has a direct impact on the conclusions derived for the purpose of improving the resilience of critical infrastructure systems.

The goal of this dissertation is to make contributions toward documenting geometry and material properties both at the surface and in the subsurface by leveraging UAV technology for the purpose of characterizing geotechnical reconnaissance sites. The number of potential directions for research is vast. The topics herein address the valuable areas of rapid documentation of 3D geometry, extending data used for geometric documentation to estimate material properties and characterize (visible) materials, and acquire subsurface properties using remote *in situ* tests. These areas are useful for achieving more effective data collection and interpretation for geotechnical site reconnaissance. More specifically, this research makes contributions toward the envisioned paradigm shift by constructing some of the foundational components in the following research thrusts for combined documentation of geometry and material properties:

1. 3D imaging of geotechnical sites to document post-failure conditions.
2. Synthesis of 3D modeling with 2D images for geomechanical assessments of rock masses.
3. UAV-enabled subsurface imaging through *in situ* seismic surface wave testing.

1.2 Organization of the Dissertation

The dissertation contains five chapters. Chapter 1 introduces the topic of post-disaster reconnaissance, the current limitations faced by engineers in conducting this work, and outlines the dissertation. In Chapter 2, recent impactful, novel research related to civil infrastructure systems is reviewed. First, basic guidance on UAV selection for civil engineering applications and the fundamental principles of UAVs are discussed. Second, the broad array of sensor payloads being used for research studies are presented. UAV-based surveying with cameras and LiDAR are compared (camera-based surveying is performed in the third chapter). Third, UAV interaction with wireless sensor networks (WSN) and high-level system operations is discussed. Examples of the challenges for processing UAV-collected data are then provided. Fourth, recent examples of UAVs applied to cutting-edge research in monitoring of infrastructure systems, construction progress monitoring, geotechnical engineering, and post-disaster reconnaissance. Observations on open-ended research topics revealed by a review of the current literature are presented.

In Chapter 3, the fundamental processes for UAV-based mapping of geotechnical sites using optical sensors are described. The approach used is Structure-from Motion (SfM) photogrammetry. SfM-associated data outputs, along with a generalized field procedure developed from performing surveys at geotechnical sites are described. Examples of sites surveyed in Hawaii and Nepal are detailed. The two landslides discussed in detail were documented with SfM and the point cloud was used to perform a geomechanical analysis of the rock structure in 3D. The chapter ends with a discussion of lessons-learned from performing aerial mapping of geotechnical sites.

In Chapter 4, a targeted effort to characterize rock masses using 2D and 3D imagery collected by UAV, is presented. Specifically, a fracture detection algorithm is developed for use at rock sites. The algorithm is assessed on three different data sets: images extracted from an

orthophoto derived from a SfM-developed 3D model of a marble quarry using the principles learned in Chapter 3; higher-resolution images collected of a weathered, vesicular basalt rock mass; and a mixed set of images including broken-up or disintegrated rocks, sparse fractures, and poor resolution images collected by UAVs during the landslide documentation discussed in Chapter 3. UAV-enabled SfM results are further utilized by transforming the 3D point cloud to a camera coordinate system and projecting to an image plane to generate RGB-Depth images. A well-established unsupervised pixel clustering algorithm is then updated for use with RGBD images. The fracture detection and clustering algorithms are then integrated in a proposed workflow where the detected fractures are mapped back to 3D points produced by Chapter 3 and can assist with 3D geomechanical characterization.

In Chapter 5, the foundation for a computational framework to interpret data from *in situ* seismic surface wave testing is developed. The analytical components, including dispersion analysis, attenuation analysis, statistical analysis, and profile modeling, are described and presented with examples. Finally, a UAV is modified to lift and drop a weight for generating seismic surface waves. The feasibility of using UAV-dropped weights relative to the commonly-used sledgehammer is assessed and the two source types are compared. The effects of drop height, payload mass, and shape are investigated. Chapter 6 concludes the dissertation by summarizing the contributions made and their limitations, lessons learned, and directions for continuing and future research.

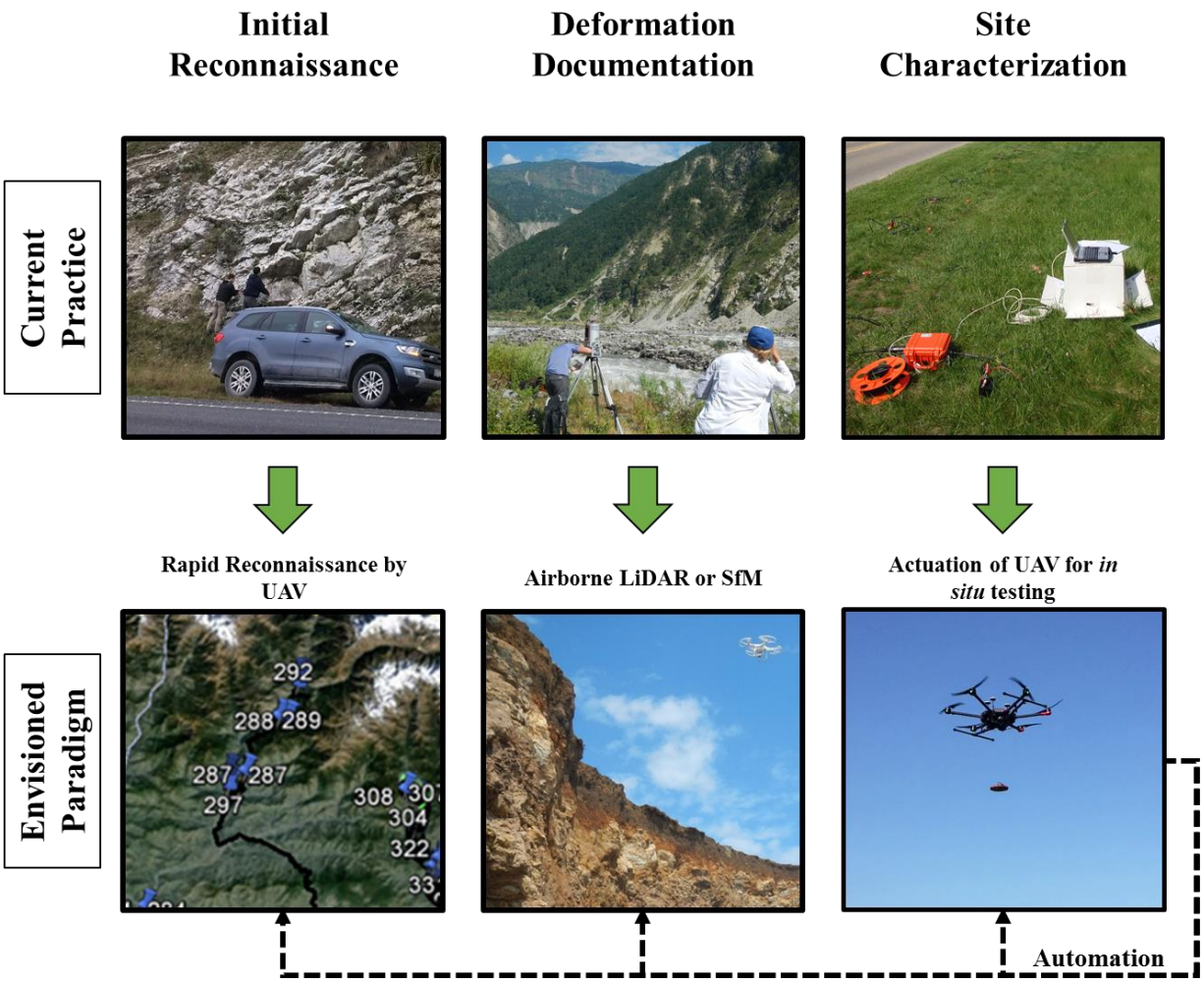

Figure 1-1: (Top row) current practice consists of manual reconnaissance requiring site access, deformation measurements, and manual site characterization processes; (bottom row) the UAV envisioned paradigm consists of UAVs gaining access to sites, collecting deformation data using SfM or LiDAR, and UAV-based site characterization through actuation and automation

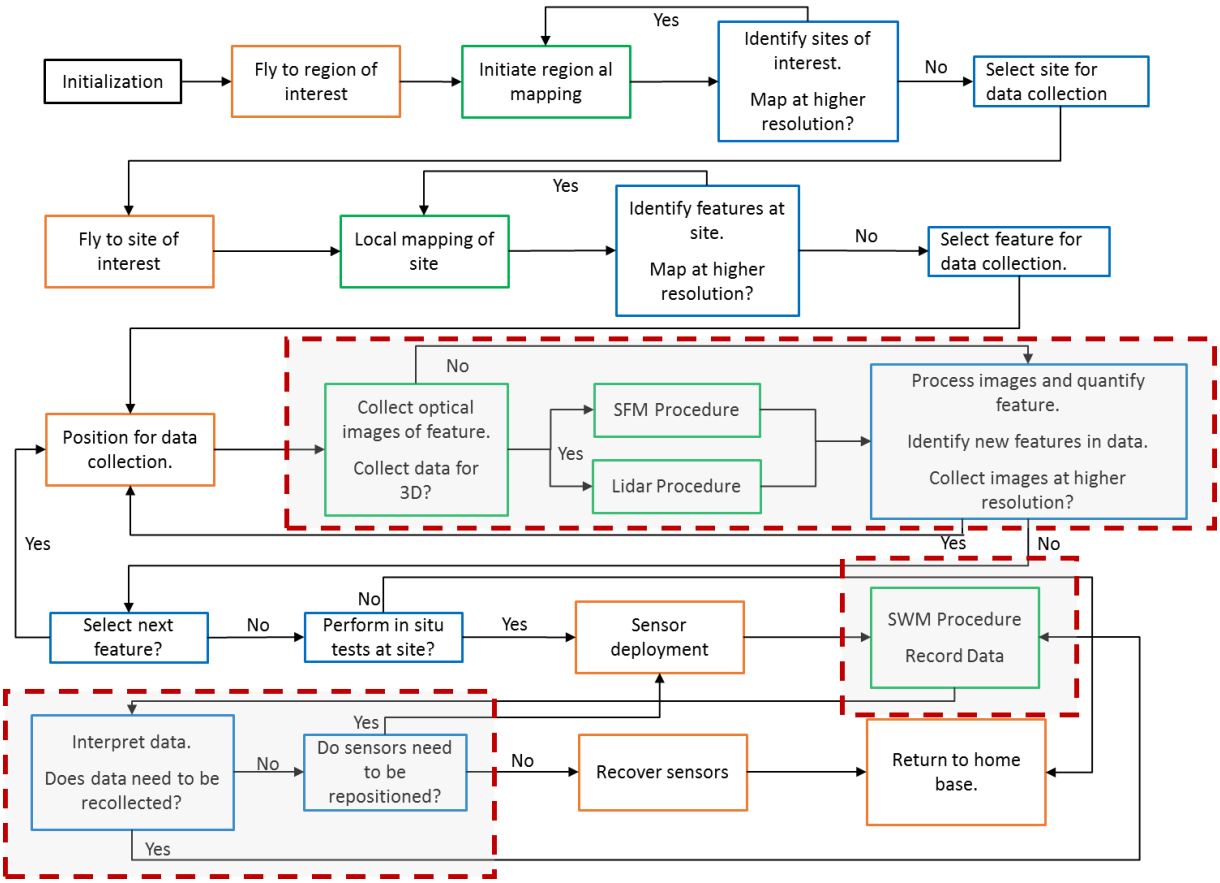

Figure 1-2: Potential automated UAV reconnaissance workflow

1.3 References

Alvarado, A., Alzamora, D., Antonaki, N., Arteta, C., Athanasopoulos-Zekkos, A., Bassal, P., Caicedo, A., Casares, B., Davila, D., Diaz, V., Diaz-Fanas, G., Gilsanz, R., González, O., Hernandez, L., Kishida, T., Kokkali, P., López, P., Luque, R., Lyvers, G.M., Maalouf, S., Mezher, J., Miranda, E., Morales Moncayo, E., Nikolaou, S., O'Rourke, T., Ochoa, I., O'Connor, J.S., Ripalda, F., Rodríguez, L.F., Rollins, K., Stavridis, A., Toulkeridis, T., Vaxevanis, E., Vera-Grunauer, X., Villagrán León, N., Wood, C., Yepes, H., Yepez, Y. (2016). "GEER-ATC Earthquake reconnaissance, April 16, 2016 Muisne, Ecuador." *GEER report GEER-049*, Nikolaou, Grunauer and Gilsanz eds.

Bastin, S., Bradley, B., Bray, J., Capellaro, C., Cubrinovski, M., del la Torre, C., Green, R., McGann, C., Olsen, M., Palermo, A., M., Stringer, Wotherspoon, L., Aricheta, J., Athanasopoulos-Zekkos, A., et al. (2017). "Geotechnical reconnaissance of the 2016 Mw 7.8 Kaikoura, New Zealand earthquake." *GEER report GEER-053*, Cubrinovski and Bray eds,

Bradley B. A., Comerio M., Cubrinovski M., Dellow S., Dizhur D., Elwood K., Giaretton M., Horspool N., Hughes M. W., and Ingham J. (2017). "M7.8 Kaikōura, New Zealand Earthquake on November 14, 2016." *QuakeCORE, GEER, and EERI Preliminary Earthquake Reconnaissance Report.*

Clark, M. K., S. Gallen, A. J. West, D. Chamlagain, K. Roback, K. Lowe, N. Niemi, W.

Greenwood, J. Bateman, D. Zekkos. (2015). "Coseismic landslides associated with the 2015 Gorkha earthquake sequence in Nepal." (Invited) *Eos Trans., Fall Meet. Suppl.*, Abstract Session S42C-02.

Collins, B. D., and R. W. Jibson. (2015). "Assessment of existing and potential landslide hazards resulting from the April 25, 2015 Gorkha, Nepal earthquake sequence." U.S. Dept. of the Interior, U.S. Geological Survey, Open-File Report 2015-1142, August 2015.

Dellow, S., Massey, C., Cox, S., Archibald, G., Begg, J., Bruce, Z., Carey, J., Davidson, J., Della Pasqua, F., Glassey, P., Hill, M., Jones, K., Lyndsell, B., Lukovic, B., McColl, S., Rattenbury, M., Read, S., Rosser, B., Singeisen, C., Townsend, D., Villamor, P., Villeneuve, M., Godt, J., Jibson, R., Allstadt, K., Rengers, F., Wartman, J., Rathje, E., Sitar, N., Athanasopoulos-Zekkos, A., Manousakis, J. and Little, M. (2017). "Landslides caused by the Mw7.8 Kaikōura earthquake and the immediate response*." Bulletin of the New Zealand Society for Earthquake Engineering*, 50(2), 106-116.

Hashash, Y. M. A., Tiwari, B., Moss, R. E. S., Asimaki, D., Clahan, K. B., Kieffer, D. S., Dreger, D. S., Macdonald, A., Madugo, C. M., Mason, H. B., Pehlivan, M., Rayamajhi, D., Acharya, I., and Adhikari, B. (2015b). "Geotechnical Field Reconnaissance: Gorkha (Nepal) Earthquake of April 25 2015 and Related Shaking Sequence." *GEER Association Report No. GEER-040*, 7 August 2015.

Hayes, G. P., R. W. Briggs, W. D. Barnhart, W. L. Yeck, D. E. McNamara, D. J. Weld, J. L. Nealy, H. M. Benz, R. D. Gold, K. S. Jaiswal, and K. Marano. (2015). "Rapid characterization of the 2015 Mw 7.8 Gorkha, Nepal earthquake sequence and its seismotectonic context." *Seismological Research Letters*, 86(6), 1557-1567.

Kargel, J. S., G. J. Leonard, D. H. Shugur, U. K. Haritashya, A. Beyington, E. J. Fielding, K. Fujita, M. Geertsema, E. S. Miles, J. Steiner, E. Anderson, S. Bajracharya, G. W. Bawden, D. F. Breashears, A. Byers, B. Collins, M. R. Dhital, A. Donnellan, T. L. Evans, M. L. Geai, M. T. Glasscoe, D. Green, D. R. Gurung, R. Heijenk, A. Hilborn, K. Hudnut, C. Huyck, W. W. Immerzeel, J. Liming, R. Jibson, A. Kääb, N.R. Khanal, D. Kirschbaum, P. D. A. Kraaijenbrink, D. Lamsal, L. Shiyin, L. Mingyang, D. McKinney, N. K. Nahirnick, N. Zhoutong, S. Ojha, J. Olsenholler, T. H. Painter, M. Pleasants, K. C. Pratima, Q. I. Yuan, B. H. Raup, D. Regmi, D. R. Rounce, A. Sakai, S. Donghui, J. M. Shea, A. B. Shrestha, A. Shukla, D. Stumm, M. van der Kooij, K. Voss, W. Xin, B. Weihs, D. Wolfe, W. Lizong, Y. Xiaojun, M. R. Yoder, and N. Young. (2016). "Geomorphic and geologic controls of geohazards induced by Nepal's 2015 Gorkha earthquake." *Science*. 351, DOI: 10.1126/science.aac8353.

Lanning, F. et al. (2016). "EERI Earthquake Reconnaissance Team Report: M7.8 Muisne, Ecuador Earthquake on April 16, 2016." *EERI.*

Roback, K., Clark, M. K., West, A. J., Zekkos, D., Li, G., Gallen, S. F., Chamlagain, D., and Godt, J. W. (2018). "The Size, Distribution, and Mobility of Landslides Caused by the 2015 M_W7.8 Gorkha Earthquake, Nepal." *Geomorphology*, 301, 121-138.

Woods, R.J., McBride, S.K., Wotherspoon, L.M., Beavan, S., Potter, S.H., Johnston, D.M., Wilson, T.M., Brunsdon, D., Grace, E.S., Brackley, H. and Becker, J.S. (2017). "Science to emergency management response: Kaikōura earthquakes 2016." *Bulletin of the New Zealand Society for Earthquake Engineering*, 50(2), 329-337.

Zekkos, D., Clark, M., Whitworth, M., Greenwood, W., West, J., Roback, K., Li, G., Chamlagain,

D., Manousakis, J., Quackenbush, P., Medwedeff, W., and Lynch, J. (2017). “Observations of landslides caused by the April 2015 Gorkha earthquake in Nepal based on land, UAV and satellite reconnaissance.” *Earthquake Spectra,* 33(S4) S1-S20.

CHAPTER 2

UAVs in Civil Infrastructure Applications

2.1 Introduction

Unmanned aerial vehicles (UAVs), also commonly termed drones, are defined as aeronautical platforms that operate without the use of on-board human operators. Recently, UAVs have been the focus of both significant praise and criticism. Media coverage has primarily driven the dialogue on UAVs in the public sphere. From this perspective, the focus has largely been related to their use in military operations (BBC, 2012; Mazzetti, 2012; Syed, 2012; Savage, 2016). UAV technology is much more advanced in this sector and has seen about a century of development. For example, the Kettering Bug, a self-flying torpedo, was developed in the United States (US) but never used in combat (Stamp, 2013). Radio-controlled aircraft were used by the British military for target practice before World War II. During World War II, US and German militaries used radio-controlled aircrafts to fly into heavily-fortified targets (Connor, 2014). Additionally, pulse-jet UAVs based on German Vergeltungswaffe Eins (V-1) cruise missiles were developed in the US and France following the war for target practice (Winter, 2000). Outside of the military realm, UAVs have also been used for decades by public entities such as police and fire departments in North American cities and this use is currently expanding (Nguyen, 2014; Mangione, 2015; FAA, 2016; Rojas, 2016). More recently, the commercial sector has explored UAVs for use in their businesses (Syed, 2012; Nguyen, 2014; Boucher, 2015). In fact, many of the UAVs originally

developed for military purposes are now being used for civilian applications (Syed, 2012; Boucher, 2015).

In the early 2000s, the public began to show greater interest in UAV technologies due to reductions in UAV costs and the availability of more functional platforms. In response to the broad proliferation of interest in UAVs in the US, the Federal Aviation Administration (FAA) initiated a small unmanned aerial vehicle registration program in December 2015. During the first 30 days of this program, nearly 300,000 individual owners registered their personal UAVs (FAA, 2016). Regulations in the US imposed by the FAA have been met with some criticism and have created a debate over how extensively UAVs should be used in the national airspace system. Outside of the US, UAV regulations vary widely from country to country, or may not even exist. Despite scientific and regulatory hurdles, many scientific and engineering communities have also delved into UAV technology development or incorporated UAVs into their respective fields. Some industries (*e.g.,* precision agriculture) have fully incorporated UAVs into their field, making them an integral part of their state of practice. Other fields (*e.g.,* geotechnical and structural engineering) have only begun to explore the potential of UAVs but their impact is already evident, as will be discussed.

Given the rapid growth in interest in UAV technology, this chapter aims to present a broad overview of UAV technology and how it is being adopted in the field of civil engineering. Emphasis is placed on the most recent technological advancements and on the breadth of applications UAVs have in the field of civil engineering while highlighting the research challenges that remain.

2.1.1 Structure

The first section provides a fundamental overview of UAVs and discusses the pros and cons of different platform types. In this section, basic guidance is provided to readers interested in implementing UAVs for their own applications. To frame this guidance, the details of several popular commercial platforms are provided. This section is primarily geared toward researchers looking to begin UAV integration with their work. It should be noted that the UAV platforms reported on are likely to rapidly change over the coming years, however, the fundamental principles presented will remain. The second section presents examples of the ever-growing set of sensor payloads that can be carried by UAVs. Due to their popularity, the greatest emphasis is placed on UAV-based light detection and ranging (LiDAR) systems. The comparable nature of LiDAR- and image-derived point clouds is also covered. The third section provides an overview of UAV integration with high-level systems such as wireless sensor networks. The challenges associated with interpreting data collected by UAVs and combining it with other data sources is discussed. The fourth section summarizes recent examples of UAVs applied to broad research domains of civil infrastructure including post-disaster reconnaissance, monitoring of critical infrastructure components, construction progress monitoring, and geotechnical engineering. These broad domains contain the most cutting-edge advancements in topics relevant to civil infrastructure systems.

It should be noted that the literature discussed herein is not intended to serve as an exhaustive compilation of all applications of UAVs in civil infrastructure systems; rather, the aim is to present representative research efforts that highlight the transformative impact UAVs can have when applied in the field. The paper concludes with a discussion of the focus areas for future work to continue advancing UAV technologies as a valuable tool in civil infrastructure. Naturally,

areas of overlap exist within the topics covered herein. For example, many of the post-disaster reconnaissance examples presented are of geotechnical interest, however, they are not discussed in the subsection on geotechnical applications.

2.2 Unmanned Aerial Vehicles

When introducing UAV-related engineering literature, it is important to define some key terms. Unmanned aircraft systems (UAS) is a closely related term which encompasses the UAV itself, communication, piloting, sensing, flight planning and other critical components for UAV operation. Readers of engineering literature may find the terms UAS and UAV used interchangeably, however the distinction should be made. Thorough discussion of a UAV-related topic cannot be made without reference to the relevant UAS components. Remotely-operated UAVs are actively controlled by a pilot. Autonomous UAVs perform functions without active human involvement. However, varying degrees of automation will appear in most modern UAS. For example, a UAV may be remotely operated by a pilot but may use automation to maintain its position in the absence of commands from the pilot. The relative autonomy of a specific platform will also depend on the software used. Both manufacturer-included and third party software packages offer a variety of options for automating functions (*e.g.* image capture, stabilization, flight path routing, and landing).

2.2.1 Platform Types

For the purposes of this paper, the FAA definition of small UAVs as those weighing less than 25 kg (55 lbs.) is adopted (DOT, 2016). In fact, the vast majority of the applications identified in this paper use small UAVs with most weighing less than 4.5 kg (10 lbs.). UAVs can generally

be divided into three types: fixed-wing, rotorcraft, and vertical take-off and landing (VTOL) vehicles. Fixed-wing UAVs fly similarly to a traditional aircraft. Fixed-wing airframes can vary as much as traditional aircraft. Rotorcraft can be further divided into two sub categories: helicopters and multirotors. Helicopters use one rotating propeller attached to the main body while multirotor UAVs are propelled by multiple rotating propellers attached to arms extending from the UAV body. VTOL UAVs can be considered as a combination of multirotor and fixed-wing UAV designs (Byun et al., 2016). These platforms lift off the ground vertically, as a multirotor platform does, but then fly horizontally with fixed wings after takeoff. There are few VTOL UAVs commercially available with the platform type still under development. Examples of the different aircraft types are shown in Figure 2-1. Blimps and balloons have also been used as airborne sensing systems; however, they have a limited scope and have not been at the forefront of current research. Balloon platforms are most useful when sensors need to remain airborne and stationary for long durations. Take et al. (2007) used a helium-filled airship to monitor thermal expansion and wrinkling of exposed geomembrane landfill liners. More discussion of blimps and balloons in transportation engineering can be found in Brooks et al. (2014).

Each type of UAV has advantages and disadvantages that may be more or less critical depending on the application. In general, fixed-wing flight is much more efficient in covering large areas. Hence, fixed-wing UAVs are generally used to cover large distances rapidly and are ideal for mapping applications or kilometer-scale measurements. Multirotor UAVs have flexible mobility and the ability to hold their position and rotate in 3D space. They are ideal for applications requiring precise vehicle placement and mapping of complex three-dimensional features. UAV platform types can be broken down further based on wing or rotor geometries. Figure 2-2 shows a more detailed breakdown of UAV platform types. Fixed-wing UAVs can be constructed with as

many wing geometries as traditional aircraft can (*e.g.,* bi-planes or tri-planes). However, for the purposes of this discussion, fixed-wing UAVs will be divided into three generalized wing orientations (and not by the number of wings). Straight-wing UAVs appear as prototypical model airplanes. The wings protrude perpendicularly from the sides of the aircraft body. The wings can have a variety of shapes in plan-view, such as elliptical, but are typically rectangular. Straight-wing alignments allow for good flight control at lower speeds. Swept-wing UAVs appear similar to straight-wing UAVs but the wings are angled (*i.e.,* swept) towards the tail of the aircraft. The senseFly eBee shown in Figure 2-1a is an example of the swept wing alignment. Swept-wings allow for greater flight efficiency relative to straight-wing UAVs but these UAVs must maintain higher velocities making them less maneuverable than their straight-wing counterparts. Delta-wing UAVs are an exaggerated version of the swept-wing alignment. In plan view, the aircraft is shaped similarly to an isosceles triangle. The pros and cons of this wing alignment are the same as the swept-wing, but more exaggerated.

The types of UAV rotorcraft platforms are defined by the number and alignment of the rotors. There are two distinct types of rotorcraft: helicopters and multirotors. Helicopters have a single overhead rotor and long tail containing a small rotor in an orthogonal plane for stabilizing and adjusting heading. Helicopters are popular with model aircraft hobbyists and offer less flexibility for use in civil engineering applications. Due to being more difficult to fly manually, they tend to have a steeper learning curve than multirotor platforms for novice users. In general, multirotor platforms consist of several arms bearing rotors extending from the central body of the aircraft. Multirotors offer shallow learning curves and are easier to control in space. However, they are comparatively more complex in terms of their development. In Figure 2-3, multirotor platforms with three, four, six, and eight rotors are identified; these platforms are singled out because they

are the most popular. Obviously, a multirotor platform with any number of rotors could be developed. A general rule of thumb is the more rotors the UAV has, the more lift capacity it has. In addition, more motors offer increased flight stability making them easier to control and offer some redundancy in the case of motor failure. A UAV with six or more rotors may have the ability to remain airborne or make an emergency landing if motor failure occurs. Tri- and quadrotors do not offer redundancy and will crash upon failure of a single motor. The cost of the UAV platform also roughly scales with the number of rotors due to the need to buy more motors and larger batteries.

Trirotor platforms typically have three rotors attached to arms either 120° apart (Y-configuration) or 90°-180° apart (T-configuration). While inexpensive, these platforms are less stable and have low lift capacities due to the small number of rotors. Quadrotor platforms are by far the most popular multirotor platforms and have been shown to be flexible platforms with fewer moving parts than hexarotors and octorotors. The quadrotor mounts the rotors to four arms each 90° apart; to balance the frame in flight, two opposite rotors (180° apart) rotate in a clockwise direction while the other two rotors rotate counter-clockwise (X4 configuration). With only four arms, quadrotors can be constructed to a small diameter making them ideal for casual hobbyists. The reliability and subsequent popularity of commercial quadrotor platforms has also resulted in them being viewed as the iconic multirotor design.

Hexarotors come in two frame types: either in a Y-rotor frame with arms 120° apart or in a HX-6 configuration which consists of six arms 60° apart. The Y-configuration includes two rotors on each arm and is referred to as a Y-6 configuration. As with all configurations using stacked motors, the top and bottom rotors rotate in opposite directions (clockwise and counterclockwise). In the HX-6, the rotors alternate between clockwise and counter clockwise.

Octorotor platforms have two configuration types: OX-8 configuration or a classical X-8 configuration. The OX-8 configuration consists of eight arms each 45° apart with rotors alternating between clockwise and counterclockwise motion. The classical X-8 consists of four arms 90° apart with each arm supporting two rotors rotating in opposite directions. In general, the X-8 and Y-6 configurations are resilient in the face of rotor failure. Stacking two rotors on each arm in the X-8 and Y-6 configurations reduces their flight efficiency due to each rotor disturbing the air surrounding the other rotor. Stacked rotors can be beneficial because they reduce the number of arms on the aircraft, greatly reducing the total weight. Reducing the base weight of the UAV has a significant effect on flight time and allows larger payloads to be carried. In general, hexarotors or octorotors are used to lift heavy payloads such as multi-camera systems and other expensive sensors. Figure 2-3 illustrates some of the most popular multirotor layouts.

Year-to-year technology improvements have made UAVs more functionally rich while their costs have continued to decrease. Specifics on the cost of individual platforms is not provided as this changes rapidly and is typically tied to integration of the latest technological innovations. The cost of new commercial small UAVs varies widely from less than 50 USD for a low-definition camera quadrotor to 50,000 USD or more for a highly-specialized multirotor platform. Additional technology advancements increase the cost of multirotor UAVs such as multi-sensor obstacle avoidance, and real-time kinematic (RTK) Global Positioning System (GPS) add-ons which may cost several thousand USD. Other capabilities can significantly influence the cost of a UAV package including GPS-denied navigation, photo/video resolution and framerate, image processing software, and flight planning software. Platforms originally developed for military operations, such as the General Atomics Predator line are available for long-range surveillance applications at great cost. However, these military-based UAV platforms have not found many

uses in civil engineering because of their costs and due to the social complexities of integrating previously militarized UAV platforms into civilian applications (Boucher, 2015).

2.2.2 Performance Characteristics

The high demand for civilian UAVs has driven the market to provide a wide range of options available at many price levels. The range of UAV costs is dictated by how specialized the UAV platform is including the following performance attributes: vehicle type (multirotor versus fixed-wing), position accuracy, permissible payload, maximum flight time, sensor compatibility, flight controller, on-board data processing capabilities, and closed versus open-source software framework. The relative importance of these performance characteristics will depend on the specific application. Accurate and stable positioning is critical when movement leads to increased sensor measurement error or when the UAV must be close to the object of interest. For example, for inspecting bridges and rock structures, the UAV must be able to resist abrupt changes in wind speed while conducting close-range inspections. In general, maximizing flight time is important for any application and is primarily controlled by the UAV payload and battery configuration. The flight time required for surveying applications is a function of camera resolution and desired survey quality. For a given required image resolution of the target, a higher-resolution camera can collect the images from a greater altitude and therefore fly along a shorter flight path. Table 1 summarizes some basic performance attributes reported by manufacturers for a range of currently available low-cost commercial UAV solutions from popular manufacturers. Many of the platforms identified in Table 1 have integrated cameras. The resolution of the photos and videos recorded by the cameras varies widely and can increase significantly between model generations. For example, between the DJI Phantom 3 Professional and the DJI Phantom 4, the camera resolution increased

from 12 MP to 20 MP. For platforms without integrated cameras, the user can select a camera with their desired resolution. State of the art digital cameras can be carried as long as payload limitations are met.

In Table 1, the weight for each UAV is the out-of-the-box base weight or a typical flying weight for the platform. Each UAV can also carry a maximum takeoff weight which represents the base weight plus the weight of payloads (if so desired). Hence, the maximum payload weight is the difference between the maximum takeoff weight and the base weight. In general, UAVs can carry a greater payload than identified by the manufacturer, which can be estimated by considering the maximum thrust of a multirotor's motors. When the maximum payload capacity of a platform is reached, it has a significant negative impact on flight performance including shorter flight time and potential instability. The eBee is a fixed-wing platform made of a light-weight foam material, both contributing to a long flight time of 50 min. The hardware associated with octorotors and hexarotors make these UAVs the heaviest on the list. The provided flight times correspond to the reported platform weight. If the payload is reduced when possible for some of the above platforms (e.g. Matrice 600) the flight time increases. Similarly, as payload is added to any of the platforms, the flight time decreases as more energy is required by the motors. Aside from the fixed wing eBee, the estimated flight times of these platforms range from 15 to 30 min. The flight times are reported from manufacturer-conducted flight endurance testing. The exact parameters, other than time and weight, of the flight testing are not necessarily reported. The unknown parameters will result in some variance with respect to flight times. These parameters may include battery level at flight termination, ambient or battery temperature, flight pathing, and wind. For this reason, users can expect variation from manufacturer-reported values when using a platform. As users gain

experience, they become competent at estimating flight times depending on environmental conditions and flight aggressiveness.

Figure 2-4 contains a compilation of the multirotor platforms summarized in Table 1. The Matrice 600 and Matrice 100 UAVs have multiple points in Figure 2-4 because they have more extensive flight endurance testing including different battery and payload combinations. Flight time is normalized by total battery capacity (in terms of mAh) and shown to be a function of the UAV total mass. As is evident from the plot, the normalized flight time (NFT) is inversely proportional to the total UAV mass (M_{UAV}). A regression analysis is performed and it is found that:

$$NFT = 1.75{M_{UAV}}^{-0.8} \quad (R^2 = 0.87) \tag{1}$$

This relationship is important because it captures the physics of UAV flight and the energy needed to fly UAVs for a period of time. More importantly, it provides UAV operators a means of accurately predicting how long a UAV would operate if the payload is altered. As seen in subsequent sections, researchers often modify UAVs to carry sensing payloads of varying size and weight. The *NFT-*M_{UAV} curve provides such researchers a means of estimating their flight times independent of their UAV platform. Additionally, the curve can be used to estimate the impact of changing battery and payload configurations on a given platform. Researchers that change their UAV's payload often or have an application where the UAV's total mass varies during flight may find developing a platform-specific curve similar to Figure 2-4 useful. Based on experience using the DJI Matrice 600 Pro hexarotor UAV, in Chapter 5, with a battery capacity of 27000 mAh, a takeoff weight of 9.5 kg results in an approximate flight time while hovering in 0-5 mph wind of 35 minutes and a takeoff weight of 16.8 kg results in an approximate flight time of 16 minutes

while hovering in 0-5 mph wind. Equation 1 predicts 31 minutes and 19 minutes for these payload conditions respectively.

As can be noted from Table 1, the most popular UAV platforms have integrated cameras or are intended to carry a camera as the primary sensing payload. This is a reflection of the fact that most UAV-based applications have been based on collecting imagery as discussed subsequently in this paper. When selecting a UAV platform, it is important to understand what the UAV will need to do and to select a UAV that meets those needs. This would be more efficient than pre-selecting a platform and then attempting to make significant alterations that allow the UAV to meet the needs of the application. Table 1 may provide guidance for novice UAV users looking to select an appropriate platform for their application. After exploring off-the-shelf products, researchers may be interested in constructing their own specialized platforms. In general, it is recommended that novice UAV users gain experience using lower-cost quadrotor platforms before expanding into larger, heavy-lift multirotors and open-source frameworks. Open-source software frameworks allow for the integration of external sensors into the UAS, the implementation of user-defined control algorithms, and operational parameters for specific applications. The knowledgebase for camera-equipped multirotors is vast and should allow new users to advance quickly assuming sufficient experience is gained and safety procedures are implemented. Newer users should be aware of and ensure safety components are contained in the UAS. This includes flight termination, return-to-home, virtual tethers, and geo-fencing. These components are critical in cases of lost/poor communication during flight. Communication range is typically not a critical consideration as most ranges for UAV to remote control extend far beyond what is needed for line-of-sight flying (reported to be several thousand meters). Communications disruption caused by physical obstruction or signal interference are much greater concerns. It is

recommended that novice users also avoid GPS-denied environments (*e.g.* tunnels, mountainous regions, etc.) until experience is gained and greater understanding of other navigation methods, such as vision-based localization is developed. Other factors, such as noise generation, may not be reported by the manufacturer and are not typically a major consideration for most researchers outside of ecological and human-interactive applications. Weather conditions must be monitored including precipitations, temperature, and wind. Few commercial platforms capable of handling precipitation, or even high-moisture, environments exist. Most multirotor platforms are highly-susceptible to precipitation, particularly due to overexposure of motors which is necessary for heat dissipation. Low temperatures have a significant impact on battery performance.

2.3 UAV Deployed Sensors

The use of UAV-mounted RGB cameras is the dominant configuration in the current literature. This is evident in earlier reviews which focus on UAV-based imaging applications in civil engineering (Ezequiel et al., 2014; Chan et al., 2015; Ham et al., 2016; Jordan et al., 2017). However, many other types of sensors on UAVs can play a role in civil engineering for multiscale data collection, remote sensing, and even sample collection. It should also be noted that non-RGB and multimodal imaging is becoming more common on UAVs including hyperspectral (Crocker et al., 2012; Lin et al., 2013) and thermal (Berni et al., 2009; Nishar et al., 2016) imaging. This section provides examples of non-imaging sensors used in applications relevant to infrastructure systems. The most popular of these sensors is LiDAR (Ngai et al., 2009; Lin et al., 2011b). LiDAR is mentioned several times in the applications section as both an airborne sensor and as a terrestrial sensor used in UAV data synthesis. The differences between LiDAR and Structure-from-Motion (SfM) (Snavely et al., 2008; Westoby et al., 2012) have been debated often. In this section, a

discussion of some of the numerous comparisons between LiDAR and image-derived point clouds is provided.

2.3.2 Sensing Payloads

Despite the prevalence of RGB cameras and, to a lesser extent LiDAR, other sensors have been implemented in a variety of fields. Many of the non-imaging sensors and their associated applications are summarized in Table 2. The list in Table 2 is not exhaustive and includes study areas outside of civil engineering to demonstrate the breadth of sensors being used on UAVs. Some of the sensor types, such as hyperspectral and thermal imaging, and synthetic aperture radar (SAR) are fundamentally similar to the RGB imaging and LiDAR techniques discussed earlier. Brooks et al. (2014) and Nishar et al. (2016) provide examples of thermal imaging using IR sensors from a UAV for bridge deck inspection and geothermal field mapping respectively. The secondary imaging techniques can be coupled with traditional RGB camera outputs such as orthophotos and 3D point clouds. Combining nontraditional imaging with RGB images produces multimodal images which are valuable for data synthesis when analyzing infrastructure system components.

Biological sensors are used in civil and environmental engineering fields to identify specific airborne contaminants or pathogens. They are categorically similar to gas and radiation detection because they require contact between the sensor and target. Unsurprisingly, all of the listed sensor types in Table 2 include a spatial data collection component. This is expected due to spatial mobility being a strength of UAV platforms. Magnetometers are the only sensor listed in Table 2 capable of probing beneath the ground surface. This is a frontier area for UAVs that has not been investigated extensively yet. In Chapter 5, another way to integrate UAVs with subsurface

sensing is introduced. In this case, the UAV is not used to carry a sensor, but is used to actively generate a stress wavefield at the ground surface.

All sensors mentioned in Table 2, as well as cameras and LiDAR, require some degree of confidence in the UAV's positioning. The absolute accuracy needed for the UAV positioning will depend heavily on sensor type and the specific application. The positioning provided by standard GPS units is generally suitable for collecting relatively coarse geospatial data. RTK positioning systems have started to be developed for small UAVs in recent years and can provide positioning accuracy as low as 1 cm. However, achieving such accuracy is only attainable if position is held for some time (minutes). For example, Turner et al. (2016) found that manually-surveyed control points were no longer necessary for coastal surveys of beaches when using UAV-mounted RTK-GPS systems. Tziavou et al. (2018) recommended using a minimum of one point surveyed on the ground surface for control of the vertical GPS component. The innovation of UAV-based RTK-GPS has dramatically improved the already robust aerial surveying methods used with UAVs. Removing the need for broadly distributed ground survey points for image-based surveying makes the methods even more competitive with LiDAR surveying. Advanced RTK positioning methods, such as those using network-based architectures, have great potential to benefit data collection for all integrated sensors and should be pursued in research.

2.3.3 Comparison of LiDAR and Camera-Based Surveying

The dominant photogrammetry technique adopted to derive 3D point clouds from UAV imagery is SfM, which utilizes sequences of two-dimensional pictures to extract features and derive 3D information. Camera positions and orientations are indirectly derived from the imagery using a bundle adjustment algorithm. Models are then scaled and georeferenced using physical

ground control points (GCP) with known locations. The density and location of GCPs used to scale a model have a significant impact on the mean error, and distribution of error within the model (Manousakis et al., 2016; Agüera-Vega et al., 2017). Adaptations of traditional SfM have also been introduced, such as methods specifically tuned for infrastructure assessment. Both LiDAR and optical cameras can be used to generate 3D point clouds. Many instances of aerial surveying for SfM are outlined in the applications section. LiDAR point clouds have the advantage that they are not as significantly affected as optical cameras by semi-penetrable obstacles such as vegetation or water. However, LiDAR scanning relies upon knowing the position and orientation of the scanner. This can be difficult to manage when mounted on a UAV. Comparatively, camera positions can be determined from consecutive images in photogrammetric techniques. LiDAR scanners are also much heavier than typical cameras. However, recent interest in UAV-mounted LiDAR has resulted in concerted efforts to make LiDAR scanners smaller and lighter. For example, the Velodyne LiDAR Puck has a mass less than 1 kg and is about 100 mm in diameter with a laser pulse range of 100 m.

Hugenholtz et al. (2013) used a small, fixed-wing UAV to map and identify surface geomorphologic features. UAV imagery was used to develop a digital terrain model (DTM). The authors found that the error of the image-based DTM, relative to a GPS survey, was comparable to a LiDAR DTM of the same site. Siebert and Teizer (2014) used a UAV with mounted RGB camera as a surveying tool for construction projects and compared UAV-based photogrammetry to conventional surveying methods as ground truth. The possible sources of error in UAV surveying are also discussed in depth. Figure 2-5 illustrates the authors' comparison of UAV-based photogrammetry to other surveying methods in terms of total coverage area and survey error; arrows have been added by the writers to illustrate existing and, potentially, future expansion of

the UAV Photogrammetry region (established by Siebert and Teizer, 2014) initiated by advancements in camera hardware, imaging methodologies, and UAV control. Hugenholtz et al. (2014) showed that cm-scale DTMs developed from UAV-based photogrammetry are a competitive alternative to LiDAR scans. Additional discussion on the post-processing implications of UAV-collected LiDAR scans is presented in the following section.

2.4 System Integration and Data Processing Challenges:

UAS contain processing power which has the potential to transform them into advanced computational platforms for real-time decision making for management of complex infrastructure systems. For example, UAVs have been integrated in many wildfire monitoring and firefighting schemes to protect towns and communities (Yuan et al., 2015). Barrado et al. (2010) described the integration of UAS in a multi-layered network including firefighter, tethered communication relays, and surveillance UAVs. Murphy et al. (2015) explored the integration of UAVs with immediate post-disaster reconnaissance and search-and-rescue efforts. Similar efforts have yet to be made fully incorporating UAVs into civil infrastructure systems, however, the greatest strides in this direction have been made in the construction management community (Ham et al., 2016).

2.4.1 Wireless Sensor Networks

It has been theorized and demonstrated that the spatial and temporal flexibility of wireless sensors coupled with their computational capabilities are ideal attributes for utilizing networks of wireless sensors with UAVs (Mascareñas et al., 2009; Maza et al., 2011; Jawhar et al., 2014; Zekkos et al., 2014; Malaver et al., 2015; Greenwood et al., 2016b; Zhou et al., 2016). Wireless sensors are a critical component of state-of-the-art structural health and infrastructure monitoring.

Mascareñas et al. (2009) proposed a mobile host wireless sensor network paradigm. The proposed paradigm utilizes wireless sensor nodes powered and interrogated by a mobile host, such as a UAV. This methodology would improve data collection efficiency and make for a more cost-effective wireless sensor network integration for infrastructure monitoring. Data collection and sensor node interrogation by UAV makes using widely distributed sensor networks more attractive. Networks distributed over large spatial areas can be very expensive and time-consuming to maintain. Specifically, deploying WSN over large areas necessitates significant infrastructure such as power sources and long-range communication networks.

Recently, there have been significant efforts made to improve incorporating UAVs with wireless sensor networks to both provide power and also to collect data (Fadlullah et al., 2016). Cobano et al. (2010) developed a path-planning method for optimal data collection from stationary wireless sensor nodes. Flight path waypoints were selected based on a heterogeneous distribution of sensor nodes while considering safety and required proximity for communication with the sensor nodes. Dong et al. (2014) discussed some challenges of collecting sensor data with UAVs such as coordinating platform velocity with sensor network density. The authors proposed an algorithm for mobile agents to aggregate sensor data over specific regions before transmitting packaged data to the UAV. Ho et al. (2015) discussed the selection of wireless sensor network communication topology to optimize the efficiency of communicating data. When recovering data from distributed networks, efficiency is critical due to the presently limited endurance of most small UAVs. The efficiency of wireless networks can also be improved with UAVs. Villas et al. (2015) proposed using the GPS receiver on-board to solve localization and time synchronization among sensor nodes. This would eliminate the need for individual nodes to contain their own GPS receiver. Kim and Choi (2015) developed an *ad hoc* 3D localization scheme for UAVs in GPS-

denied environments by leveraging ground-based and airborne sensor nodes. Acquiring UAV position from ground-based sensor nodes presents some difficulties when expanded to 3D localization. Airborne sensor nodes, namely other UAVs, can be used to determine the position and relative distances with other communicating UAVs.

The deployment of wireless sensors by UAVs has also been explored on a limited basis. Zhou et al. (2016) used a UAV to physically distribute and mount accelerometers on a simple beam structure using a robotic arm mounted to the UAV. The UAV placed wireless sensors on the structure and communicated with them to record data while introducing an impulse for modal analyses. Maza et al. (2011) used multiple autonomous helicopter UAVs to deploy wireless sensor nodes and IR cameras for a firefighting proof-of-concept test. Wireless nodes contained sensors for temperature, humidity, carbon monoxide, and smoke. Sensor nodes were attached to firefighters at the site and additional nodes were distributed by UAV to monitor the movement of fire to sensitive locations in a building. UAV was also used to deploy optical and IR cameras on the top of a building providing real-time information on fire propagation, firefighters, and victims. The major limitation to sensor deployment by UAVs is the limited payload capacity of small UAVs and the reduced flight endurance caused by sensor payloads (*e.g.* see Figure 2-4).

2.4.2 UAV-Specific Data Reduction

Remote sensing methods that have been incorporated on UAVs often require additional (and extensive) data processing (Frey et al., 2009; Harwin and Lucieer, 2012; Hirose et al., 2015). Examples of this include the data associated with UAV-based Synthetic Aperture Radar (SAR) (Frey et al., 2009), LiDAR (Brooks et al., 2014; Hirose et al 2015), magnetic surveys (Wood et al., 2016), and high-resolution imaging (Harwin and Lucieer, 2012). The uncertainty of UAV

position and pose propagates as uncertainty in the collected data, but can often be eliminated with correcting algorithms. The reliability of UAV-based LiDAR data is highly dependent on confidence in UAV pose and position estimations. In response to this, recent attempts have been made to improve the reliability of LiDAR data collected on a UAV through signal processing or synthesizing with other data sources (*e.g.* Lin et al., 2013). Droeschel et al. (2016) combined stereo cameras, ultrasonic sensors, and LiDAR to map obstacles for UAV navigation. Kaul et al. (2016) developed a 3D mapping system using a rotating 2D LiDAR scanner capable of 3D mapping in a GPS-denied environment. Hirose et al. (2015) demonstrated UAV-based LiDAR monitoring of structures in a GPS-denied environment. Understanding the pose and motion of the UAV is imperative for LiDAR measurements and becomes most difficult in GPS-denied environments. Hirose et al. (2015) implemented an iterative closest point algorithm to correct resulting distortions in the LiDAR point cloud. UAV localization was improved by feeding inertial measurement unit (IMU) and camera data into a Kalman filter. Brooks et al. (2014) used UAV-mounted LiDAR to develop 3D models of a highway bridge. A 3D SLAM algorithm was used to improve the quality of the LiDAR point cloud. Figure 2-6 shows the 3D LiDAR results before and after scan-matching alignment. Sensor payload orientation and positioning can be measured using onboard IMU sensors but may contain debilitating errors and must be addressed through post-processing of IMU data (Brooks et al., 2014; Hirose et al., 2015; Gautum et al., 2017; Klingbeil et al., 2017).

As previously mentioned, the uncertainty of UAV position has become a less-critical concern in GPS-enabled environments and when utilizing some imaging methods such as SfM. Processing methods specifically for data collected in GPS-denied environments, such as in buildings or in remote valleys, must still be pursued. Vision-based methods for localization are being investigated extensively, partly to address this issue.

UAV-based photogrammetric techniques such as SfM and multi-view stereo (MVS) quickly became popular because they have become well-established and validated methods; they are also resistant to some of the problems associated with remote sensing by UAV such as pose estimation. This is because of the robustness of camera pose extraction from a series of images in photogrammetric methods and the reliability of feature detection algorithms developed for computer vision and image processing such as scale-invariant feature transform (SIFT) (Lowe, 1999; Lowe, 2004). New image processing methods have been developed or expanded based on the collection of UAV-based images. Jahanshahi et al. (2017) approached the issue of positional inaccuracies and outliers in SfM, developing an algorithm to improve 3D reconstruction when misassociated features exist in the SfM data. The algorithm was used following standard outlier rejection methods within the bundle adjustment process.

Adaptations of traditional SfM have also been introduced, such as methods specifically for infrastructure assessment based on the same algorithm structure. For example, Khaloo and Lattanzi (2017) present a dense SfM approach used to resolve small-scale details needed for infrastructure inspection. However, other photogrammetry and computer vision techniques can be used including those dependent on directly measuring camera position and orientation. Direct measurement of camera position and orientation can be made using onboard inertial sensors and GPS (Klingbeil et al., 2017). Irrespective of the method used to derive them, 3D topological models provide engineers with a quantitative measurement of the topologies corresponding to ground and structural surfaces. Carpin et al. (2013) developed a variable-resolution object detection method. This object search method utilizes the ability of UAVs to rapidly adjust imaging resolution by changing vehicle altitude. Vetrivel et al. (2015b) developed an image segmentation methodology

for UAVs. Images are collected by a UAV and used to produce a 3D point cloud. The point cloud is segmented and used to similarly segment the original UAV-collected images.

Novel methodologies in infrastructure system monitoring and inspection can be expected to be extended to UAV platforms in the near future, such as the crack detection and quantification method developed by Jahanshahi et al. (2013), 3D crack detection developed by Torok et al. (2014), crack change detection method by Adhikari et al. (2016), 3D city modeling by Cornelis et al. (2008), and digital image correlation (Take et al., 2015). The current and future extension of these imaging techniques is enabled by increasing on-board computational capacity and potential for real-time processing as well as the addition of serial camera perspectives.

2.5 UAV Applications in Civil Engineering

Over the past decade, UAVs and other robotic systems have shown tremendous promise for use in a wide variety of applications in the realm of civil infrastructure systems (Lattanzi and Miller, 2017). Fundamentally, UAVs are revolutionizing the field by providing never-before-seen dynamic data collection capabilities that surpass existing methods in terms of ease, accuracy and cost. Using FAA UAS exemption applications as a metric, Figure 2-7 shows the broad number of applications submitted through January 2016 that identify an infrastructure-related use (AUVSI, 2016). The attraction of integrating UAVs in many civil infrastructure applications is primarily based on accelerating accessibility to remote and dangerous sites, sensor mobility, and overall speed of data collection. Any application that could utilize a highly-mobile data collection or communication platform could conceivably incorporate UAVs as a primary data collection component. In particular, UAVs have begun to emerge as an essential data collection tool for applications involving natural hazards (*e.g.*, earthquakes, hurricanes) where site accessibility can

be challenging post-event and the need to collect highly perishable data is urgent. In such applications, UAV-based photogrammetry provides advantages over other remote sensing platforms such as satellites and people on the ground (Colomina and Molina 2014). Satellites are limited by return time, cloud coverage, image resolution, and collect imagery in plan-view. UAVs can be deployed on demand and flight parameters can be adjusted to acquire the desired image resolution and perspective. Human teams on the ground (walking or using ground-based vehicles) can be challenged by treacherous terrain, physical obstacles, or dangerous site conditions. As a result of these challenges, UAVs also offer an economic advantage including reduction of costs associated with personnel, travel and site logistics. The role of UAVs can also go well beyond photogrammetry by offering the possibility to carry other sensor types for data collection, a role in processing data, and interacting with users on the ground. The top application areas in civil infrastructure where UAVs have had transformative impact on the state of practice are infrastructure system component monitoring, construction safety and progress monitoring, geotechnical engineering, and post-disaster reconnaissance. These application areas are described in this section to provide the reader with insight to how UAVs may be used on-site with clear benefit to the application. It is important to identify literature reviews related to the use of UAVs as they may pertain to civil infrastructure. Ezequiel et al. (2014) reviewed applications in post-disaster assessment, environmental management, and infrastructure development where UAV-based remote sensing is used within data-sharing networks. A broad overview of application areas in civil engineering was reviewed by Liu et al. (2014) with a strong focus on control. Colomina and Molina (2014) provided an in-depth review of UAV-based photogrammetry with RGB cameras. The review also provides insight into remote sensing where UAVs have been utilized and includes details of other camera types for UAV-based remote sensing (*e.g.* multispectral). A

targeted review of UAVs as bridge inspection was presented by Chan et al. (2015). Vision-based efforts for monitoring infrastructure were reviewed by Ham et al. (2016) from a construction perspective. This review provides a useful synthesis of contributions from the robotics and computer vision communities. Lattanzi and Miller (2017) presented a thorough overview of robotic platforms used to inspect infrastructure components. This review details inspection robots of several different mobility types including aerial, underwater, ground-based, and climbing robots. Jordan et al. (2017) provided a contextual review of UAV-based inspection of power facilities and structures. The review discusses the critical technologies addressing current implementation challenges.

2.5.1 Monitoring of Infrastructure System Components

In this section, key cases of UAVs being used for infrastructure monitoring are discussed. The discussion begins with monitoring linear structures such as pipelines, then bridge inspection and monitoring, and finish with UAVs applied to monitoring traffic conditions in transportation systems. For each of these topics the discussion is presented chronologically. Clearly, there is a large number of infrastructure system components that can be, and have been, monitored by a UAV. The subtopics in this section have been selected due to their prominence in transformative UAV research. The use of UAVs to monitor other infrastructure components and features such as road surfaces, power lines, concrete dams and communication towers among many others should not be discounted.

As previously mentioned, UAVs can be useful, low-cost tools for visual inspection and monitoring of infrastructure systems at many scales (Lattanzi and Miller, 2017). In the United States, “infrastructure” was listed as an application for about 40% of FAA exemptions as of 20

January 2016 (AUVSI, 2016). Rathinam et al. (2008) used a UAV with a pre-determined flight path to inspect linear structures, such as pipelines. The authors proposed a real-time, vision-based detection algorithm for linear structures. However, frame-by-frame operations on the video feed were found to be too computationally intensive. UAVs have computational potential which has greatly improved in recent years, but the computationally-intensive nature of real-time image processing is a consistent point of emphasis in the literature, especially as camera technology (resolution, multimodal imaging) improves. Pipelines represent an infrastructure component with significant consequences of failure. Monitoring of pipelines over a significant spatial range is therefore critical to their performance. Due to the significant distances covered by similar types of infrastructure, such as railroads, levees, powerlines, and pipelines, rapid data collection over large distances is desirable. For example, Gao et al. (2011) investigated the use of UAVs for data collection of geologic hazards threatening pipelines. Jawhar et al. (2014) proposed a strategy for collecting data via UAV from sensor arrays distributed on pipelines. The characteristic nature of monitoring a linear structure such as a pipeline can be applied across the other examples mentioned above. Monitoring over large, rural areas allows infrastructure in these places to receive newfound attention and improves the response rate to performance changes. The risk associated with UAV failure is also lower relative to urban environments. However, depending on consequences, monitoring over such expanses can be too costly (Jawhar et al., 2014). The relative cost of using a UAV over large distances is much lower for fixed-wing platforms. If functions that require multirotor platforms must be performed, the monitoring effort could quickly become unsustainable. The ability of VTOL platforms to combine the benefits of fixed-wing and multirotor platforms will have a profound impact as their usage expands.

UAV-based remote sensing for critical infrastructure is a possible method to aid visual inspection, or in some cases completely replace inspectors in the field. In fact, bridge inspection is the most widely approached topic for UAV integration in infrastructure monitoring. Ellenberg et al. (2014a) used a UAV for visual inspection of bridges for deformations and cracking. The algorithms proposed by the authors suggest placement of markers tracked in 3D by photogrammetry or 3D visual simultaneous localization and mapping (SLAM). Similarly, Ellenberg et al. (2014b) used a UAV to collect imagery of cracked masonry. Several crack detection algorithms were used on the imagery including edge detection, percolation approach, fractal method, and tensor voting. Lattanzi and Miller (2014) used a UAV to collect images of bridge structural elements and generate 3D models. The UAV-based imaging is demonstrated as a low cost, computationally efficient way to repeatedly model structures and compare to previous models. Brooks et al. (2014) used UAVs for bridge inspections and greatly expanded the role of UAVs beyond using traditional imaging by including thermal imaging as a component of bridge inspection. Gillins et al. (2016) also demonstrated bridge inspection with a low-cost UAV. Significant emphasis was placed in leveraging the mobility of the UAV to acquire images at many viewing angles of critical details such as fasteners, joints, and evidence of material deterioration. Implementations of bridge inspection are numerous but have some general limitations. There are few recommendations made for practical implementations which combine visual inspection with sensor-based health monitoring. Additionally, it is still challenging to acquire necessarily high-resolution images of the most obscure or difficult to reach fasteners. Future work into obstacle avoidance and localization within the spatial challenges of bridges will help alleviate the limitations. Zhou et al. (2016) demonstrated the deployment of mobile wireless sensors onto a structure by a UAV. The demonstration was performed in a controlled environment where wireless

sensor nodes were distributed on a simply-supported beam structure and an impulsive source was introduced for modal analyses. The implementation of UAVs for the deployment and redistribution of wireless sensor nodes has the potential to dramatically enhance the distributed data collection required for infrastructure monitoring as well as improve the safety and efficiency of distributing sensor nodes. Eschmann and Wundsam (2017) developed a multisensor UAV bridge inspection platform to carry three sensors: long-wavelength IR, optical camera, and LiDAR. Each sensor performed different tasks which were then fused into a complete 3D visualization. Surfaces and deformation were recorded using the LiDAR, images from the optical camera were used to overlay model textures and monitor cracks, and the IR camera was used to detect moisture around cracks. Hackl et al. (2018) used UAV-based photogrammetry to develop 3D meshes of a 24-m span, reinforced concrete bridge and surrounding terrain in Switzerland. The meshes were integrated with hydrodynamic models to simulate complex flow scenarios and perform risk assessments. Khaloo et al. (2018) used a UAV to develop a 3D model of a timber truss footbridge for detecting defects and inspecting connections. The model was developed from over 2000 photos acquired from 22 different flight paths around the 85 m span bridge. The primary efforts identified in the literature include visual inspections of bridge components. 3D imaging is extremely popular in structure monitoring as well as many other fields. However, most studies utilizing robust 3D imaging do not demonstrate implementation of 3D outputs in further analysis. Hackl et al. (2018) demonstrates how detailed imagery of a bridge can be transferred to hydrodynamic models, thus promoting collaboration and cross-field use of data.

Traffic surveillance and monitoring was explored as one of the first applications for UAVs in civil engineering (Srinivasan et al., 2004; Coifman et al., 2006). Traffic modeling based on UAV-collected data was demonstrated by Coifman et al. (2006). Recent efforts have been made

to use UAVs for streamlining roadway condition assessments. Several state departments of transportation (DOT) have already begun to implement UAVs in recent years (Barfuss et al., 2012; Brooks et al., 2014; Irizarry and Johnson, 2014). Zhang et al. (2012) used UAV-collected imagery to produce 3D models of distressed unpaved roads. A 3D model with absolute resolution less than 1 cm was used to detect potholes and ruts within the roads. Dobson et al. (2013) developed a system for detecting damage on unpaved roads. A helicopter UAV was used to collect imagery of unpaved roads and produce 3D point clouds. Potholes are detected in the point clouds using Canny edge detection and Hough circle transform algorithms. Brooks et al. (2014) explored possible applications for UAVs in transportation engineering. The authors found UAVs to be cost-effective tools for monitoring traffic and inspecting road assets. Additional applications such as crash scene reconstruction, roadside slope stability assessments, and optimizing platforms for sharing UAV datasets are offered as needed research concentrations by the authors. Data collection on the performance of transportation systems within civil infrastructure is often sparse and can ignore specific details. For example, basic traffic counting may ignore vehicle type and speed, vision-based data collected by UAV can provide greater detail when monitoring traffic patterns. This level of detail can also be acquired using fixed cameras, but a UAV can be mobilized to many locations without requiring equipment installation at locations where constant surveillance is unnecessary. The desire of state governments to develop new methodologies based on data collection with UAVs may help facilitate the development of positive regulatory environments.

2.5.2 Construction Safety and Progress Monitoring

Using UAVs in construction management is developing into a staple of the construction industry. Construction was the fifth most cited application among FAA UAS exemptions as of 20

January 2016, appearing in nearly half of the exemptions (AUVSI, 2016). In this section key examples of UAVs being used for construction management are discussed. The discussion begins with excavations, then considers progress monitoring for construction projects, and finishes with UAV-based safety concerns and interaction with construction personnel. For each of these topics the presentation is chronological.

Development of 3D models at construction sites over time to document progress has been the most common application of UAVs in construction management. Lin et al. (2015) proposed a model-driven, automated methodology for construction progress monitoring. The monitoring method was intended to replace manual image collection with efficient, more complete documentation collected via automated UAV. The proposed methodology utilizes building information modelling (BIM) to drive the autonomous data collection. Recent research efforts have also included more than updating images, with a focus on resource tracking at construction sites (Teizer, 2015). Lin and Golparvar-Fard (2016) developed a web-based system to track construction work flows utilizing BIM. Irizarry and Costa (2016) also demonstrated additional uses for UAVs on construction sites beyond documenting progress; images collected by the UAV at construction sites in the United States and Brazil were used to identify and track specific management tasks and became part of an asset database. The work demonstrated by the construction management community has pioneered the augmentation of established workflows with UAS. Efforts have been made to use UAV platforms to go beyond data collection and approach systemic integration.

Documenting construction progress in urban excavations is critical due to the damage construction-induced deformations can cause to nearby infrastructure (Hashash et al., 2015a). The development of underground space in cities places greater emphasis on monitoring techniques for

subsurface excavations (Fleming et al., 2016). Fleming et al. (2016) used a low-cost UAV to monitor excavation bracing in an urban excavation site. UAV imagery was used to generate 3D models over time. One of the top challenges for using UAVs for excavation inspection and monitoring is that they often need to perform in GPS-denied environments.

UAVs have also been explored as safety inspection tools on construction sites. Innovative technologies such as UAVs, wireless sensor networks, and information technology are expected to be staples of construction and safety management (Irizarry et al., 2012). Irizarry et al. (2012) explored the use of low-cost UAVs as tools for safety managers on construction sites. The UAV provided the safety manager with rapid access to images anywhere on the site. The authors found that a camera-equipped UAV with a large visual interface was just as effective for the safety manager as making observations in plain view. Irizarry et al. (2012) also recommended specific features that should be required of construction safety UAVs such as autonomous flight, voice recognition, and a user-interface useful for collaboration. It should be noted that incorporating UAVs in active construction sites introduces additional safety concerns such as personnel distraction and increased collision risk with equipment or personnel (Irizarry et al., 2012). Training of construction site personnel is necessary for safe UAV integration (Irizarry and Costa, 2016). These factors are all critical considerations for integrating UAVs into infrastructure construction practices. This notion is highlighted by the envisioned next generation construction site presented by Ham et al. (2016). In this vision, UAV-based cameras are used to collect informative images which document progress, productivity, construction quality, and safety requirements.

2.5.3 Geological and Geotechnical Engineering

The benefits presented by UAVs makes them potentially invaluable tools for geotechnical site reconnaissance and have been employed following recent events. These examples have been covered within the Post-Disaster Reconnaissance subsection. Terrestrial photogrammetric techniques have been established methods for imaging rock masses in 3D in structural geology (Bemis et al., 2014). Similarly, UAV-collected imagery has been used to characterize rock masses in 3D (Stumpf et al., 2013; Bemis et al., 2014; Salvini et al., 2015; Greenwood et al., 2016a; Vollgger and Cruden, 2016). Emphasis has been placed on identifying and measuring discontinuities to quantify spatial variations and acquire geomechanical parameters (Greenwood et al., 2016a; Vollgger and Cruden, 2016). Stumpf et al. (2013) mapped surface fissures at the Super-Sauze landslide. The mapping efforts were used to better understand the mechanics of rock mass and the deformation of the slope over time. Lucieer et al. (2014) collect imagery of active landslide sites using a UAV. The imagery was collected over time and used to develop cm-scale 3D point clouds to measure landslide deformations. The accuracy of the image-based models was verified by differential GPS control points. Turner et al. (2015) used UAV-collected imagery and SfM photogrammetry to generate a time series of digital surface models (DSM) to measure landslide mass displacement over time. Salvini et al. (2015) used a UAV to collect images of rock masses in a marble quarry. The images were used to identify discontinuities and map them to identify the location and types of potential failures as part of a broad stability monitoring scheme. UAV-mounted cameras are powerful tools for mapping large areas rapidly and acquiring data in very difficult to reach locations. It is worth mentioning that the ability of UAVs to reach difficult locations and cover large distances has started to make them popular tools for collected imagery of geomorphologic features (d'Oleire-Oltmanns et al., 2012; Hugenholtz et al., 2013; Neugirg et

al., 2016; James et al., 2017). d'Oleire-Oltmanns et al. (2012) used SfM to monitor erosion processes in Morocco. Images were collected with a fixed-wing UAV and georeferenced using two different methods. Neugirg et al. (2016) produced 3D models over time to monitor erosion processes and estimate volume changes. Manousakis et al. (2016) and Saraglou et al. (2017) used SfM to document a rockfall caused by the 2015 Lefkada earthquake. Evidence in the UAV-generated DSM was used to identify the rockfall kinematic behavior (rolling, bouncing, etc.) and input into a rockfall analysis. These approaches of synthesizing UAV-based data with data generated from other sources is beneficial to better understanding how UAVs can be integrated with current analytical practices.

Clearly, the use of UAVs in geological and geotechnical engineering has been dominated by RGB imaging and relative displacement sensing. Other camera types, such as infrared (IR), multispectral, or hyperspectral, can be mounted on robotic platforms but have had limited use in geotechnical engineering. Nishar et al. (2016) used a UAV mounted with RGB and thermal imaging cameras to explore a geothermal field in New Zealand. Similarly, Harvey et al. (2016) used thermal imaging generated with a low-cost UAV to generate thermal orthophotos of the Waikite geothermal region in New Zealand.

There have also been data collection methods explored beyond imaging. While imaging is critical for many geotechnical projects, other methods of data collection are still necessary. For example, Fernandes Jr. et al. (2015) used UAV-collected images to complement ground penetrating radar (GPR) surveys of outcropping carbonate rocks to better understand karst features in GPR images. Utilizing a UAV platform for additional data collection or test execution is of great interest and has only been explored on a very limited basis. Zekkos et al. (2014) demonstrated a proof-of-concept test of UAV-enabled seismic surface wave methods. The UAV dropped a

weight used as the impulsive source for multichannel analysis of surface waves (MASW). The small-scale test was performed in an indoor sand pit and an outdoor site. The authors also demonstrated the applicability of integrating wireless geophone vibrations sensors with the UAV as a data collection platform. Greenwood et al. (2016b) used a UAV to introduce an impulsive source to a 2D geophone array placed on a concrete surface at an indoor flight facility. Geophone time histories were used to back-calculate an estimate of the source position relative to the array. Wood et al. (2016) conducted preliminary testing of an airborne magnetic survey with a UAV. Magnetometers were mounted to the wingtips of a fixed-wing UAV and flown in a grid pattern. Aeromagnetic surveys performed with UAVs have some particular challenges, such as magnetic anomalies generated by aircraft components (Forrester et al., 2014).

2.5.4 Post-Disaster Reconnaissance

There is high demand for improved methods in post-disaster reconnaissance (Murphy et al., 2015). The discussion to follow begins with damage to structures and infrastructure components, then considers landslide mapping, and finishes with UAV cooperation with search-and-rescue personnel. For each of these topic areas, the presentation of past work with UAVs is presented in a chronological manner.

UAVs have recently been incorporated into teams of immediate post-disaster reconnaissance experts (PEER, 2014; Rollins et al., 2014; Hashash et al., 2015b; El Mohtar et al., 2016; Sun et al., 2016; Zekkos et al., 2016). In all these cases, small UAVs were flown equipped with conventional optical cameras. Images were used to develop 3D point clouds of a variety of targets ranging in size. Having been used for a number of years as part of post-event reconnaissance, operational frameworks for reconnaissance planning and execution using UAVs

are emerging. For example, Murphy et al. (2015) provide a review of planning and execution methods for UAV-based reconnaissance, and also highlight some of the complications involved in performing immediate post-disaster reconnaissance with UAVs such as coordination with search-and-rescue teams. The authors emphasized the importance of accurate geotagging of images and maintaining high-resolution real-time video feeds during flight. Data archiving was also identified as a major issue in UAV-based data collection.

UAVs have been vital to collecting perishable data immediately after high-wind, flood, and seismic events. For example, Adams et al. (2013) conducted UAV-based image collection of tornado-induced damage in Alabama. The authors demonstrated that the UAV could collect aerial images with a sub-centimeter ground sampling distance (GSD) which was an improvement over what could be done with NOAA (National Oceanic and Atmospheric Administration) satellite images. While photographs were taken using UAVs, they were only used to qualitatively assess damage and to make distance measurements. As part of reconnaissance after the 2014 Iquique, Chile earthquake, Rollins et al. (2014) collected photos of a damaged pier. Using Agisoft PhotoScan (Agisoft, 2017), a commercial SfM package, point clouds of the pier with a reported absolute resolution of about 5.5 cm were used to demonstrate the potential of UAV-collected imagery in a post-earthquake setting. The reconnaissance team in Iquique, Chile also used a UAV-mounted camera to collect images and produce 3D models of the Tana Bridge and liquefaction-induced lateral spreading adjacent to the Tana River. The resulting models had absolute resolutions of about 1 cm and were used to accompany field observations of lateral spreading. The Pacific Earthquake Engineering Research Center (PEER) also used a UAV as part of reconnaissance after the 2014 South Napa, California earthquake (PEER 2014). The team executed both manual and semi-automated UAV surveys to collect imagery of a variety of sites including damaged buildings

in urban and rural settings, suburban residential areas, bridges, and a water tower. Collected imagery was used to develop 3D point clouds using SfM photogrammetry. The 3D models were, in several cases, coupled with terrestrial LiDAR surveys. Terrestrial LiDAR surveys are the standard practice for the acquisition of relative displacement measurements in post-disaster scenarios. UAV-collected images were used to survey areas inaccessible to the terrestrial LiDAR scan such as building roofs. LiDAR scans were also used to provide scale for the photogrammetric models obtained from the UAV imagery. Torok et al. (2014) used a UAV to deploy a ground-based robot used in a post-disaster structural crack detection scheme in concrete structures. SfM was used to reconstruct three-dimensional models of concrete structural elements with major cracks imaged and their width and depth profiles captured. Zekkos et al. (2016) documented the geometric characteristics of four damaged infrastructure projects by deploying a low-cost UAV within 48 hours following three different natural disasters in Greece. A point cloud model using SfM software package Pix4D (2017) was derived for a damaged port pier in which millimeter to centimeter sized crack openings could be measured. A bridge failure due to scour was also mapped, showing the settlement, rotation, and dip of a bridge pier.

UAVs are especially valuable tools for difficult-to-reach sites following disasters due to terrain or simply due to sheer size. For example, Niethammer et al. (2012) collected imagery of the Super-Sauze landslide near Grenoble, France. The landslide deposit was thoroughly mapped to identify key features. Digital terrain models (DTM) were developed using a close-range photogrammetry tool chain consisting of Vision Measurement System (VMS) (VMS, 2010) and the dense stereo matcher GOTCHA (Gruen-Otto-Chau) (Otto and Chau, 1989). The UAV-developed orthophotos were compared to older orthophotos of the landslide and were used to estimate daily average displacement rates. Murphy et al. (2015) employed multiple small UAVs

in response to the 2014 Oso, Washington landslide. UAV imagery was collected to address four priorities: low-altitude imagery of the riverbed, imagery of lower scarp section, imagery of upper scarp section, and mapping of potential access points. These imaging priorities allowed the UAV to critically assist with search-and-rescue operations. Mapping with the images allowed engineers and geologists to identify the possibility of additional ground movement and how to approach removing the debris. El Mohtar et al. (2016) collected close-range UAV-based imagery of the Kfarnabrakh landslide in Lebanon. A digital surface model (DSM) of the site was generated using the collected imagery; the model had an absolute resolution of 10 cm. The model was then compared to the pre-failure geometry synthesized from satellite images. Geometries were co-registered based on notable fixtures such as buildings. The comparison yielded estimates of the ground surface retreat and volume of the failure mass. Hashash et al. (2015b) used a low-cost, commercial UAV in Nepal after the 2015 Gorkha earthquake. The UAV was used to collect an extensive amount of imagery of earthquake-affected sites most especially landslides and hydropower facilities. Imagery was a critical aspect of qualitative assessment of geotechnical system performance during the Gorkha earthquake. Greenwood et al. (2016a) also collected UAV-based imagery of seismic-induced and typhoon-enhanced landslides caused by the 2015 Gorkha earthquake. 3D point clouds of the landslides were created using the commercial SfM software package Pix4D; point clouds were used to define landslide surface geometries and identify rock mass failure modes. The exposed landslide rock mass imagery was segmented and geomechanically characterized based on fracture spacing in the 3D point cloud.

As previously mentioned, sites affected by extreme events can pose serious risks to search-and-rescue personnel and scientific investigators. Risks may even include radiation, such as with the 2011 Fukushima nuclear disaster (Duncan and Murphy, 2014). Use on dangerous sites is one

area where UAVs can play a major role. For example, Duncan and Murphy (2014) demonstrated the use of autonomous radiation-detecting UAVs at a simulated building collapse. It was found that UAVs could perform a radiological survey more efficiently than a ground-based reconnaissance team, while reducing the radiation exposure to the team, and reducing the number of team members required to perform the survey. The UAV was also used as part of decision-making processes in the field by rapidly transmitting data to all human parties.

Post-disaster scenarios are multi-faceted problems as demonstrated by the many applications of UAVs discussed above. Kochersberger et al. (2014) developed an autonomous helicopter UAV capable of performing several post-disaster reconnaissance tasks such as ground-based robot deployment and retrieval, radiation measurement and source localization, and terrain mapping. Michael et al. (2012) coordinated ground-based robots and UAVs to map the interior of earthquake damaged structures and to identify access paths for first responders. The authors emphasized the need to not only define conditions for autonomous vehicles to interact with each other, but for the vehicles to interact with humans (such as search-and-rescue personnel) during operation. The development of unmanned vehicle platforms for post-disaster reconnaissance has taken different approaches: development of platforms to perform many, if not all, tasks (Kochersberger et al., 2014) or development of multiple platforms collaborating to performs tasks (Michael et al., 2012). It may be unclear which approach will become most prevalent in the future. UAV collaboration certainly indicates greater data collection speed, as a single, flexible platform consolidates the risk of UAV interactions with other vehicles and humans. It is expected that teams of UAVs will become the preferred approach including swarms and platforms performing complimentary functions that may only interact virtually.

2.6 Summary and Conclusions

Novel research focused on the application of UAVs for civil infrastructure systems was reviewed with emphasis placed on recent, transformative advances in civil engineering. In general, the main thrust of UAV efforts in data collection and processing has been with imaging. Imaging methods such as structure-from-motion and stereo-vision have been established for an extended period of time. The robustness of established imaging methods, and the popularity of UAVs with onboard cameras has led to imaging being the early focus of research efforts. This has also led to new imaging methods being developed largely for vehicle automation, such as vision-based localization. Recent discussions in the US about integrating UAVs in the national airspace at night raises some interest in investigating non-vision sensors for autonomous navigation and obstacle avoidance such as sonar and LiDAR. In recent years, research efforts in data collection and processing have extended beyond imaging methods to include other sensors such as gases, biological pathogens, and SAR (Leuschen et al., 2014; Lu et al., 2015; Rossi and Brunelli, 2016 among others). However, these transformative efforts are often occurring outside of civil engineering, but are certainly of interest for these particular sensors (*e.g.* modeling air quality, detecting methane emissions, and ground displacements).

In civil engineering, UAVs are already used for post-disaster response, structural damage assessment, infrastructure inspection, rock characterization, mining, magnetic surveys, seismic geophysical methods, and construction monitoring. The most interesting UAV research developments have involved incorporating UAVs into high-functioning complex systems capable of interacting with humans and interfacing with data streams (*e.g.* Murphy et al 2015). UAVs will become powerful autonomous systems having the ability to develop an action plan, collect data, process data, perform computations, analyze results, and make next-step decisions. These

components of autonomous UAV systems are being explored individually. However, more efforts into incorporating all of these components into fully autonomous systems are needed (*e.g.* Song and Jo, 2017). Developments in UAV autonomy offer an opportunity to develop platforms to approach some of the multifaceted problems of infrastructure systems. Challenges exist from social and political perspectives as well for the integration of UAVs with science and engineering fields including civil infrastructure projects (Straub, 2014; Boucher, 2015; Bakx and Nyce, 2016).

Table 2-1: Specifications of popular commercial UAV platforms

ID	Platform	Type	Takeoff Weight	Max Speed	Flight Time	Diameter/ Wingspan	Integrated Camera?	Open Source?	Customizable Payload?
1	DJI Inspire 2	X4	3440 g	18 m/s	15 min	559 mm	Yes	No	No
2	DJI Inspire 1	X4	3060 g	22 m/s	18 min	559 mm	Yes	No	No
3	DJI Mavic Pro	X4	743 g	18 m/s	27 min	335 mm	Yes	No	No
4	DJI Phantom 4 Pro	X4	1388 g	20 m/s	30 min	350 mm	Yes	No	No
5	DJI Phantom 4	X4	1380 g	20 m/s	28 min	350 mm	Yes	No	No
6	DJI Phantom 3 Pro	X4	1280 g	16 m/s	25 min	350 mm	Yes	No	No
7	DJI Phantom 2 Vision+	X4	1242 g	15 m/s	25 min	350 mm	Yes	No	No
8	DJI Phantom 2	X4	1242 g	15 m/s	25 min	350 mm	No	No	No
9	Spreading Wings S1000	OX8	9500 g	16 m/s	15 min	1045 mm	No	No	Yes
10	Spreading Wings S900	HX6	6800 g	16 m/s	18 min	900 mm	No	No	Yes
11	DJI Matrice 100	X4	2855 g	22 m/s	17 min	650 mm	No	Yes	Yes
12	DJI Matrice 600	HX6	15100 g	18 m/s	16 min	1833 mm	No	No	Yes
13	3DR Solo	X4	1990 g	25 m/s	25 min	460 mm	No	Yes	No
14	3DR Iris	X4	1282 g	23 m/s	20 min	550 mm	No	Yes	No
15	Yuneec Typhoon 4K	X4	1700 g	8 m/s	25 min	420 mm	Yes	No	No
16	Yuneec Typhoon H	HX6	1950 g	19 m/s	25 min	520 mm	Yes	No	No
17	SenseFly Albris	X4	1800 g	12 m/s	22 min	800 mm	Yes	No	No
-	SenseFly eBee	Fixed-Wing	690 g	25 m/s	50 min	960 mm	Yes	No	No

Table 2-2: UAV-based sensors and corresponding applications

Sensor Type	Applications	References
Gas Detection	Volcanology, Environmental Monitoring, Climatology	Rossi and Brunelli 2016; Malaver et al., 2015; Rosser et al., 2015; McGonigle et al., 2007
Lidar	Civil Engineering, Glaciology, Forestry, Precision Agriculture, Mapping	Eschmann and Wundsam, 2017; Hirose et al., 2015; Yang and Chen 2015; Zarco-Tejada et al., 2014; Lin et al., 2013; Crocker et al., 2012; Wallace et al., 2012; Lin et al., 2011b; Nagai et al., 2009
Biosensor	Agriculture, Environmental Monitoring	Lu et al., 2015; Techy et al., 2010
Magnetometer	Geophysics/Geology/Geotechnical Engineering	Wood et al., 2016; Forrester et al., 2014
SAR	Glaciology, Mapping	Leuschen et al., 2014; Frey et al., 2009; Xing et al., 2009
Temperature	Glaciology	Crocker et al., 2012
Thermal Imaging	Precision Agriculture, Geology/Geotechnical Engineering	Eschmann and Wundsam, 2017; Nishar et al., 2016; Calderon et al., 2013; Berni et al., 2009a; Berni et al., 2009b
Multispectral Imaging	Precision Agriculture,	Candiago et al., 2015; Berni et al., 2009b;
Hyperspectral Imaging	Precision Agriculture,	Aasen et al., 2015; Calderon et al., 2013; Crocker et al., 2012

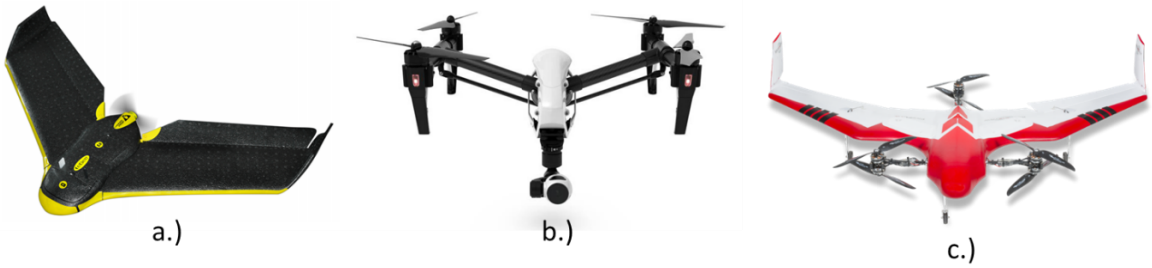

Figure 2-1: Examples of some commercial UAVs: (a) fixed-wing senseFly eBee (SenseFly, 2015); (b) multirotor DJI Inspire 1 (DJI, 2016); (c) VTOL FireFly 6 (BirdsEyeView Aerobotics, 2016)

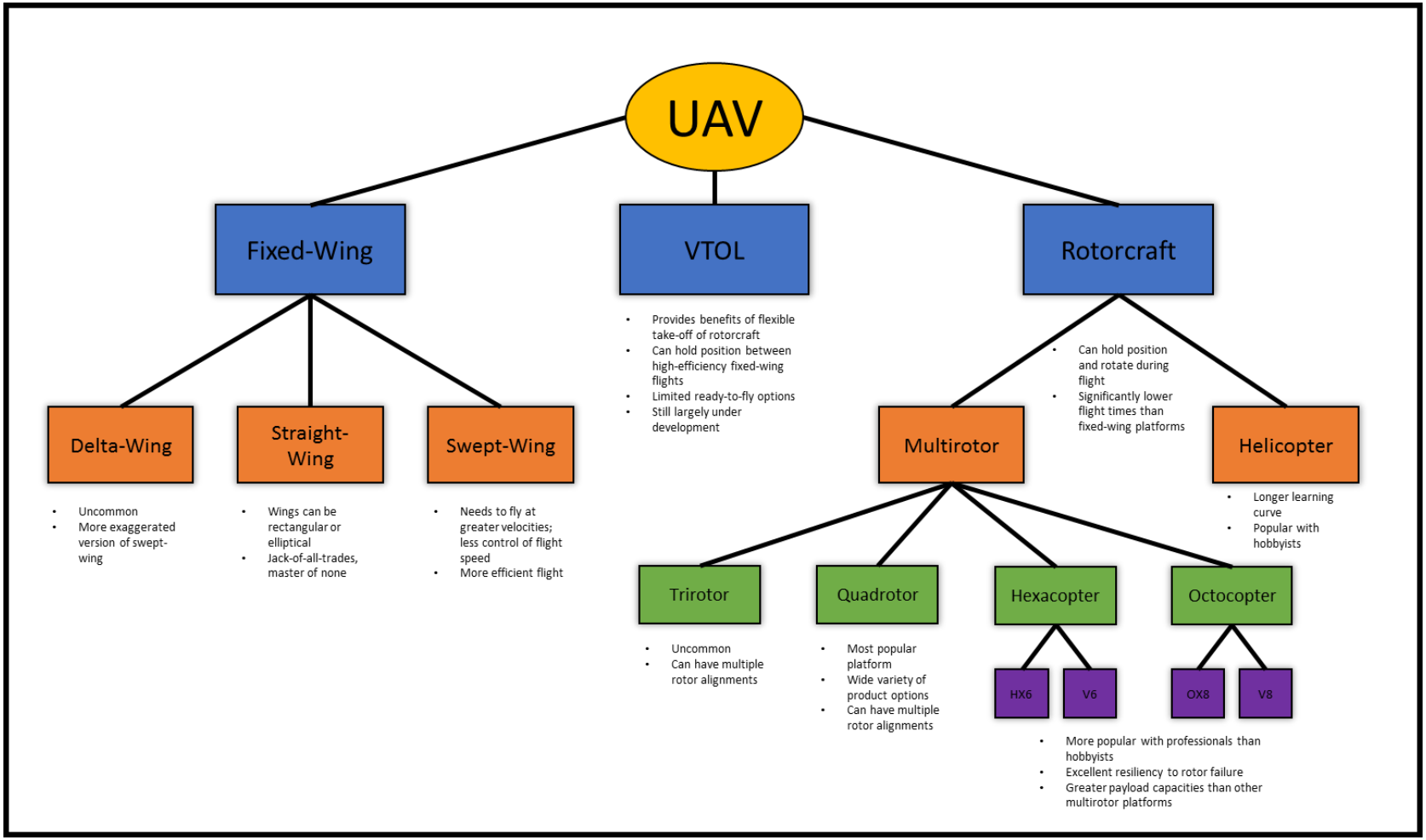

Figure 2-2: Hierarchical taxonomy of UAV platform types

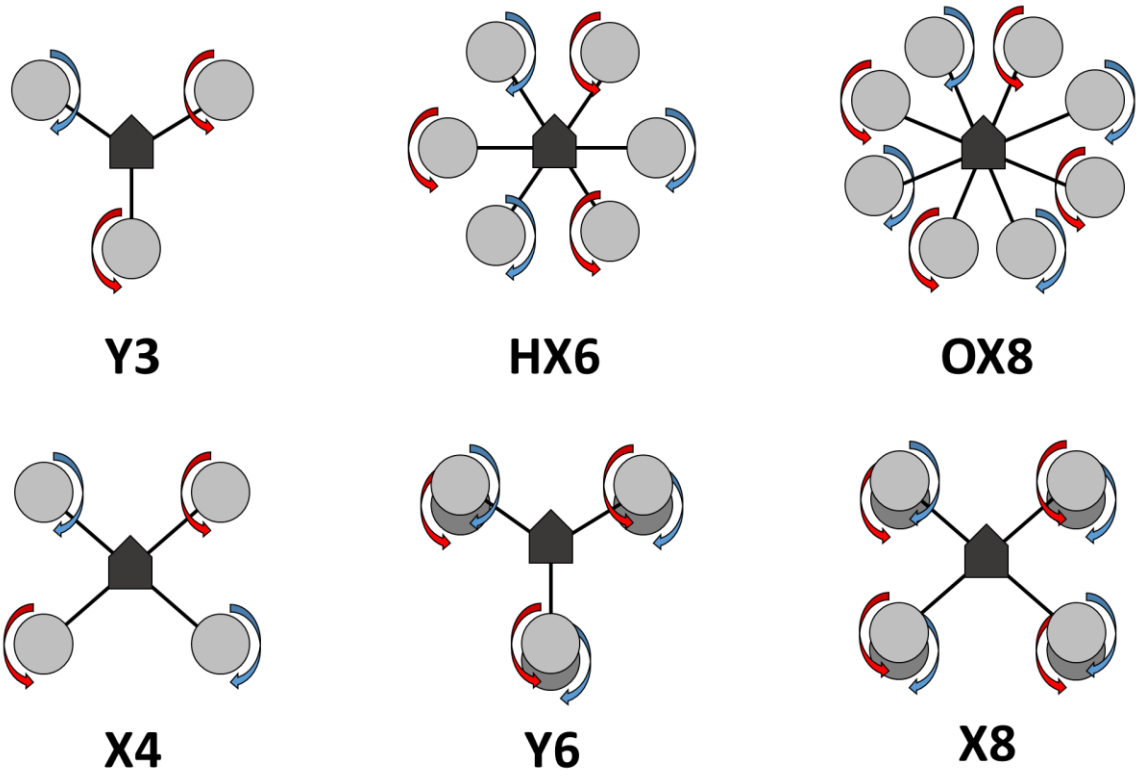

Figure 2-3: Common trirotor (Y3), quadrotor (X4), hexarotor (HX6; Y6), and octorotor (OX8; X8) multirotor layouts

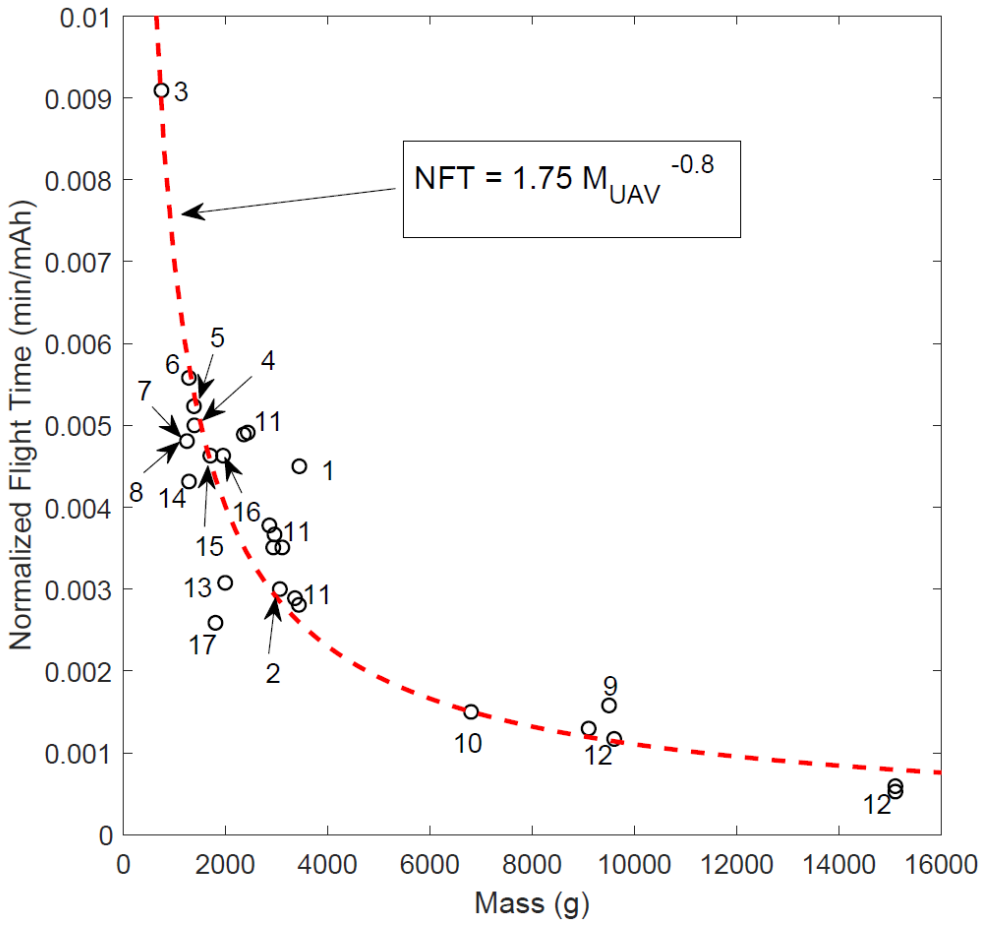

Figure 2-4: Empirical relationship between total weight, flight time, and battery capacity derived from 26 commercially-available UAV configurations; labels correspond to index values in Table 2-1

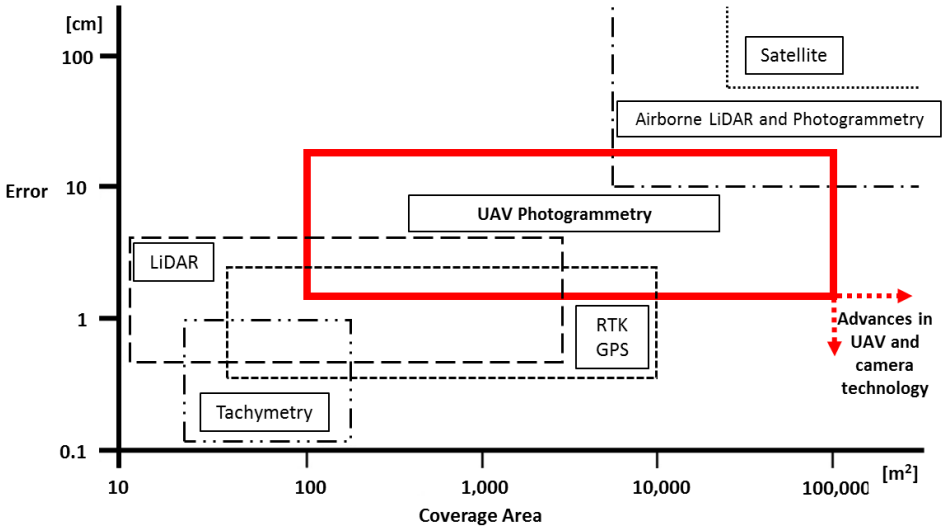

Figure 2-5: UAV application to surveying tasks (adapted from Siebert and Teizer, 2014)

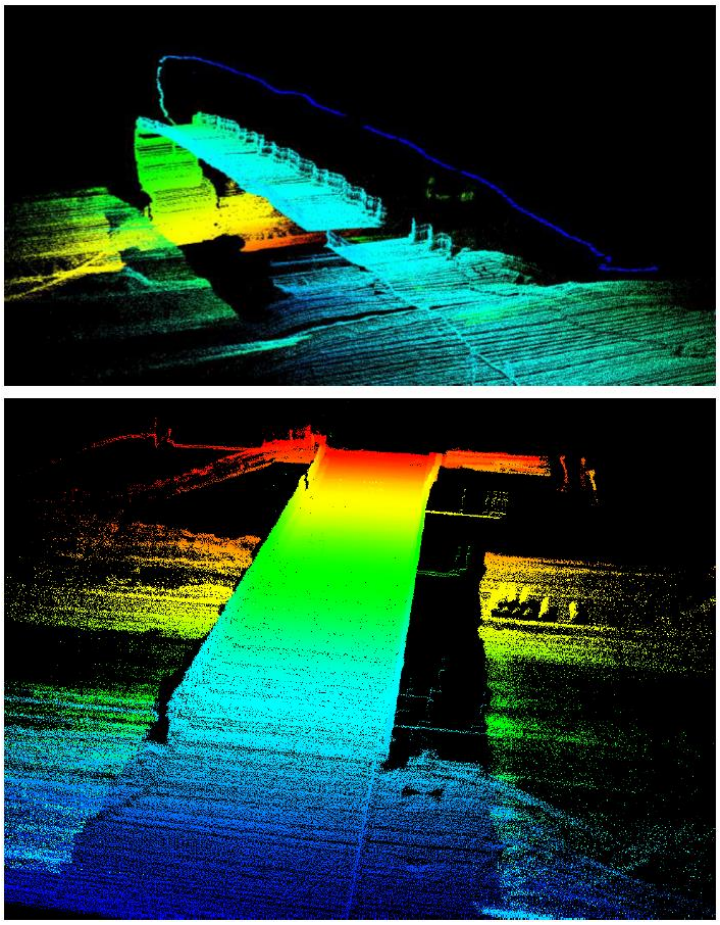

Figure 2-6: LiDAR scan of bridge deck before and after altitude estimate and scan-matching alignment (adapted from Brooks et al., 2014)

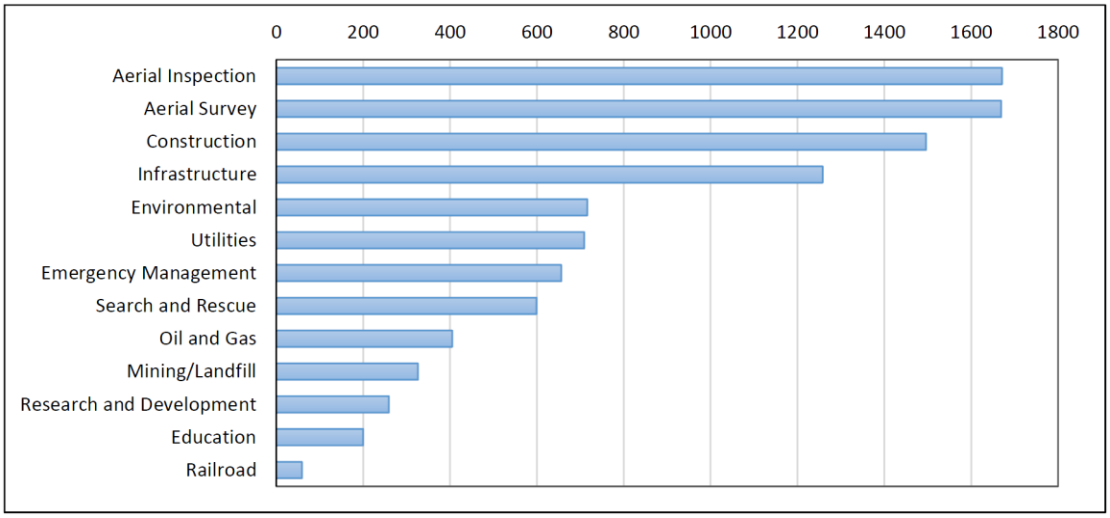

Figure 2-7: Number of civil engineering-related applications cited in FAA UAS exemption applications; data from AUVSI (2016)

2.7 References

Adams, S. M., Levitan, M. L., and Friedland, C. J. (2012). "High Resolution Imagery Collection Utilizing Unmanned Aerial Vehicles (UAVs) for Post-Disaster Studies." *Advances in Hurricane Engineering*, Miami, FL, 777-793.

Adhikari, R. S., Moselhi, O., Bagchi, A., and Rahmatian, A. (2016). "Tracking of Defects in Reinforced Concrete Bridges Using Digital Images." *Journal of Computing in Civil Engineering*, DOI 10.1061/(ASCE)CP.1943-5487.0000566, 04016004.

Agisoft. (2016). "Agisoft PhotoScan User Manual: Professional Edition." *Version 1.2*, Agisoft LLC.

Agüera-Vega, F., Carvajal-Ramírez, F., and Martínez-Carricondo, P. (2017). "Accuracy of Digital Surface Models and Orthophotos Derived from Unmanned Aerial Vehicle Photogrammetry." *Journal of Surveying Engineering*, 143(2), DOI: 10.1061/(ASCE)SU.1943-5428.0000206.

AUVSI. (2016). "Commercial UAS Exemptions by the Numbers." *Association for Unmanned Aerial Systems International*, <http://www.auvsi.org/auvsiresources/exemptions>.

Bakx, G. C. H., and Nyce, J. M. (2016). "The Safe Integration of Military UAS in the (Inter)national Airspace: Some Underlying Processes." *Cogn. Tech, Work*, 18, 465-477.

Barfuss, S. L., Jensen, A., and Clemens, S. (2012). "Evaluation and Development of Unmanned Aircraft (UAV) for UDOT Needs." Utah Dept. of Transportation, Salt Lake City.

Barrado, C., Meseguer, R., López, J., Pastor, E., Santamarina, E., and Royo, P. (2010). "Wildfire Monitoring Using a Mixed Air-Ground Mobile Network." *Pervasive Computing*, 10, 24-32.

BBC (2012). "Drones: What are they and how do they work?" British Broadcast Company (BBC), London, England <http://www.bbc.com/news/world -south-asia-10713898> (20 September 2016).

Bemis, S. P., Micklethwaite, S., Turner, D., James, M. R., Akciz, S., Thiele, S. T., and Bangash, H. A. (2014). "Ground-Based and UAV-Based Photogrammetry: A Multi-scale, High-Resolution Mapping Tool for Structural Geology and Paleoseismology." *Journal of Structural Geology*, 69, 163-178.

Berni, J. A. J., Zarco-Tejada, P. J., Sepulcre-Cantó, Fereres, E., and Villalobos, F. (2009). "Mapping Canopy Conductance and CWSI in Olive Orchards Using High Resolution Thermal Remote Sensing Imagery." *Remote Sensing of Environment*, 113, 2380-2388.

Boucher, P. (2015). "Domesticating the Drone: The Demilitarisation of Unmanned Aircraft for Civil Markets." *Sci. Eng. Ethics*, 21, 1393-1412.

Brachman, R. W. I., Rentz, A., Rowe, R. K., and Take, W. A. (2015). "Classification and Quantification of Downslope Erosion from a Geosynthetic Clay Liner (GCL) when Covered only by a Black Geomembrane." *Canadian Geotechnical Journal*, 52(4), 395-412.

Brooks, C., Dobson, R. J., Banach, D. M., Dean, D., Oommen, T., Wolf, R. E., Havens, T. C., Ahlborn, T. M., and Hart, B. "Evaluating the Use of Unmanned Aerial Vehicles for Transportation Purposes." Michigan Tech Research Institute Final Report, No RC-1616.

Byun, Y., Song, J., Song, W., and Kang, B. (2016). "Conceptual Study of a Smart Docking System for VTOL-UAV." *Journal of Aerospace Engineering*, 29(2), DOI: 10.1061/(ASCE)AS.1943-5525.0000508.

Carpin, S., Burch, D., Basilico, N., Chung, T. H., and Kölsch, M. (2013). "Variable Resolution

Search with Quadrotors: Theory and Practice." *Journal of Field Robotics*, 30(5), 685-701.
Chan, B., Guan, H., Jo, J., and Blumenstein, M. (2015). "Towards UAV-Based Bridge Inspection Systems: A Review and an Application Perspective." *Structural Monitoring and Maintenance,* 2(3), 283-300.
Cobano, J. A., Martinez-de Dios, J. R., Conde, R., Sánchez-Matamoros, J. M., and Ollero, A. (2010). "Data Retrieving From Heterogeneous Wireless Sensor Network Nodes Using UAVs." *Journal of Intelligent Robotic Systems*, 60, 133-151.
Coifman, B., McCord, M., Mishalani, R., Iswalt, M., and Ji, Y. (2006). "Roadway Traffic Monitoring from an Unmanned Aerial Vehicle." *Proc. Intell. Transp. Syst.*, 153(1), 11–20.
Colomina, I., and Molina, P. (2014). "Unmanned Aerial Systems for Photogrammetry and Remote Sensing: A Review." *ISPRS Journal of Photogrammetry and Remote Sensing*, 92, 79-97.
Connor, R. (2014). "Remembering the Death of Lt. Joe Kennedy Jr. and America's First Combat Drones." *Smithsonian National Air and Space Museum* <https://airandspace.si.edu/stories/editorial/remembering-death-lt-joe-kennedy-jr-and-america%E2%80%99s-first-combat-drones> (20 September 2016).
Cornelis, N., Leibe, B., Cornelis, K., and Van Gool, L. (2008). "3D Urban Scene Modeling Integrating Recognition and Reconstruction." *Int. J. Comput. Vis.*, 78, 121-141.
Crocker, R. I., Maslanik, J. A., Adler, J. J., Palo, S. E., Herzfeld, U. C., and Emery, W. J. (2012). "A Sensor Package for Ice Surface Observations Using Small Unmanned Aircraft Systems." *IEEE Transactions on Geoscience and Remote Sensing*, 50(4), 1033-1047.
Department of Transportation. (2016). "Operation and Certification of Small Unmanned Aircraft Systems." *Federal Register Vol. 81 No. 124, 28 Jun. 2016, 42064-42214.*
Díaz-Varela, R. A., de la Rosa, R., León, L., and Zarco-Tejada, P. J. (2015). "High-Resolution Airborne UAV Imagery to Assess Olive Tree Crown Parameters Using 3D Photo Reconstruction: Application in Breeding Trials." *Remote Sensing*, 7, 4213-4232.
DJI. (2016). "Inspire 1 V.2.0." *DJI*, <http://www.dji.com/product/inspire-1>.
Dobson, R. J., Brooks, C., Roussi, C., and Colling, C. (2013). "Developing an Unpaved Road Assessment System for Practical Deployment with High-Resolution Optical Data Collection using a Helicopter UAV." *2013 International Conference on Unmanned Aircraft Systems (ICUAS),* 28-31 May 2013, Atlanta, GA, 235-243.
d'Oleire-Oltmanns, S., Marzolff, I., Peter, K. D., and Ries, J. B. (2012). "Unmanned Aerial Vehicle (UAV) for Monitoring Soil Erosion in Morocco." *Remote Sensing*, 4, 3390-3416.
Dong, M., Ota, K., Lin, M., Tang, Z., Du, S., and Zhu, H. (2014). "UAV-Assisted Data Gathering in Wireless Sensor Networks." *Journal of Supercomputing*, 70, 1142-1155.
Droeschel, D., Nieuwenhuisen, M., Beul, M., Holz, D., Stückler, J., and Behnke, S. (2016). "Multilayered Mapping and Navigation for Autonomous Micro Aerial Vehicles." *Journal of Field Robotics,* 33(4), 451-475.
Duncan, B. A., and Murphy, R. R. (2014). "Autonomous Capabilities for Small Unmanned Aerial Systems Conducting Radiological Response: Findings from a High-fidelity Discovery Experiment." *Journal of Field Robotics*, 31(4), 522-536.
Eckerstorfer, M., Bühler, Y., Frauenfelder, R., and Malnes, E. (2016). "Remote Sensing of Snow Avalanches: Recent Advances, Potential." *Cold Regions Science and Technology*, 121, 126-140.
Ellenberg, A., Branco, L., Krick, A., Bartoli, I., and Kontsos, A. (2014a). "Use of Unmanned Aerial Vehicle for Quantitative Infrastructure Evaluation." *Journal of Infrastructure*

Systems, 21(3), 04014054.
Ellenberg, A., Kontsos, A., Bartoli, I., and Pradhan, A. (2014b). "Masonry Crack Detection Application of an Unmanned Aerial Vehicle." *Computing in Civil and Building Engineering*, 1788-1795.
El Mohtar, C. S., Abou-Jaoude, G., Abdullah, C., and Harb, J. (2016). "The Kfarnabrakh Landslide of November 30th, 2015: A Geological and Geotechnical Evaluation of the Landslide and Risk of Future Failures." *GEER Association Report No. GEER-047*, 16 March 2016.
Eschmann, C., Kuo, C. M., Kuo, C. H., and Boller, C. (2012). "Unmanned Aircraft Systems for Remote Building Inspection and Monitoring." *Proc., 6th European Workshop on Structural Health Monitoring*, Vol. 2, Dresden, Germany.
Eschmann, C., and Wundsam, T. (2017). "Web-Based Georeferenced 3D Inspection and Monitoring of Bridges with Unmanned Aircraft Systems." *Journal of Surveying Engineering*, 143(3), DOI: 10.1061/(ASCE)SU.1943-5428.0000221.
Ezequiel, C. A. F., Cua, M., Libatique, N. C., Tangonam, G. L., Alampay, R., Labuguen, R. T., Favila, C. M., Honrado, J. L. E., Caños, V., Devaney, C., Loreto, A. B., Bacsumo, J., and Palma, B. (2014) "UAV Aerial Imaging Applications for Post-Disaster Assessment, Environmental Management and Infrastructure Development." *2014 International Conference on Unmanned Aircraft Systems (ICUAS)*. IEEE, 2014.
FAA. (2016). "FAA Registered Nearly 300,000 Unmanned Aircraft Owners." 22 January 2016, <http://www.faa.gov/news/press_releases/news_story.cfm?newsId=19914>.
Fadlullah, Z. M., Takaishi, D., Nishiyama, H., Kato, N., and Miura, R. (2016). "A Dynamic Control Algorithm for Improving the Communication Throughput and Delay in UAV-Aided Networks." *IEEE Network*, 100-105.
Fernandes Jr., A. L., Medeiros, W. E., Bezerra, F. H. R., Oliveira Jr., J. G., and Cazarin, C. L. (2015). "GPR Investigation of Karst Guided by Comparison with Outcrop and Unmanned Aerial Vehicle Imagery." *Journal of Applied Geophysics*, 112, 268-278.
Fleming, K. L., Hashash, Y. M. A., McLandrich, S., O'Riordan, N., and Riemer, M. (2016). "Novel Technologies for Deep-Excavation Digital Construction Records." *Practice Periodical on Structural Design and Construction*, 05016002.
Forrester, R., Huq, M. S., Ahmadi, M., and Straznicky, P. (2014). "Magnetic Signature Attenuation of an Unmanned Aircraft System for Aeromagnetic Survey." *IEEE/ASME Transactions on Mechatronics*, 19(4), 1436-1446.
Franke, K. W., Rollins, K. M., Ledezma, C., Hedengren, J. D., Wolfe, D., Ruggles, S., Bender, C., and Reimschiissel, B. (2016). "Reconnaissance of Two Liquefaction Sites Using Small Unmanned Aerial Vehicles and Structure from Motion Computer Vision Following the April 1, 2014 Chile Earthquake." *Journal of Geotechnical and Geoenvironmental Engineering*, 143(5), DOI: 10.1061/(ASCE)GT.1943-5606.0001647.
Frey, O., Magnard, C., Rüegg, M., and Erich, M. (2009). "Focusing of Airborne Synthetic Aperture Radar Data from Highly Nonlinear Flight Tracks." *IEEE Transactions on Geoscience and Remote Sensing*, 47(6), 1844-1858.
Gao, J., Yan, Y., and Wang, C. (2011). "Research on the Application of UAV Remote Sensing in Geologic Hazards Investigation for Oil and Gas Pipelines." *ICPTT*, 381-390.
Gautman, D., Lucieer, A., Malenovsky, Z., and Watson, C. (2017). "Comparison of MEMs-Based and FOG-Based IMUs to Determine Sensor Pose on an Unmanned Aircraft System." *Journal of Surveying Engineering*, 143(4), DOI: 10.1061/(ASCE)SU.1943-

5428.0000225.
Gillins, M. N., Gillins, D. T., and Parrish, C. "Cost-Effective Bridge Safety Inspections Using Unmanned Aircraft Systems (UAS)." *Geotechnical and Structural Engineering Congress 2016*, 1931-1940.
Gonzalez, F., Castro, M. P. G., Narayan, P., Walker, R., and Zeller, L. (2011). "Development of an Autonomous Unmanned Aerial System to Collect Time-Stamped Samples from the Atmosphere and Localize Potential Pathogen Sources." *Journal of Field Robotics*, 28(6), 961-976.
González-Jorge, H., Puente, I., Roca, D., Martínez-Sánchez, J., Conde, B., and Arias, P. (2014). "UAV Photogrammetry Application to the Monitoring of Rubble Mount Breakwaters." *Journal of Performance of Constructed Facilities*, 30(1), 04014194-8.
Greenwood, W., Zekkos, D., Clark, M. K., Lynch, J. P., Bateman, J., and Chamlagain, D. (2016a). "UAV-Based 3-D Characterization of Rock Masses and Rock Slides in Nepal." *50th US Rock Mechanics/Geomechanics Symposium*, Houston, TX.
Greenwood, W., Zhou, H., Lynch, J. P., and Zekkos, D. (2016b). "UAV-Deployed Impulsive Source Localization with Sensor Network." *CIMTEC 2016, 5th International Conference Smart and Multifunctional Materials, Structures and Systems*, Perugia, Italy, 5-9 June, 2016.
Hackl, J., Adey, B. T., Woźniak, M., and Schümperlin, O. (2018). "Use of Unmanned Aerial Vehicle Photogrammetry to Obtain Topographical Information to Improve Bridge Risk Assessment." *Journal of Infrastructure Systems*, 24(1), DOI: 10.1061/(ASCE)IS.1943-555X.0000393.
Ham, Y., Han, K. K., Lin, J. J., and Golparvar-Fard, M. (2016). "Visual Monitoring of Civil Infrastructure Systems via Camera-Equipped Unmanned Aerial Vehicles (UAVs): A Review of Related Works." *Visualization in Engineering*, 4(1), DOI: 10.1186/s40327-015-0029-z.
Harvey, M. C., Rowland, J. V., and Luketina, K. M. (2016). "Drone with Thermal Infrared Camera Provides High Resolution Georeferenced Imagery of the Waikite Geothermal Area, New Zealand." *J. of Volcon. and Geotherm. Research*, 325, 61-69.
Harwin, S., and Lucieer, A. (2012). "Assessing the Accuracy of Georeferenced Point Clouds Produced via Multi-Views Stereopsis from Unmanned Aerial Vehicle (UAV) Imagery." *Remote Sensing*, 4, 1573-1599.
Hashash, Y. M. A., Jammoul, M., Fleming, K. L., McLandrich, S., Yeskoo, A., O'Riordan, N., Gouvin, P., and Riemer, M. (2015a). "Construction Monitoring for the Transbay Transit Center Excavation in San Francisco, California." *IFCEE 2015*, 2502-2511.
Hashash, Y. M. A., Tiwari, B., Moss, R. E. S., Asimaki, D., Clahan, K. B., Kieffer, D. S., Dreger, D. S., Macdonald, A., Madugo, C. M., Mason, H. B., Pehlivan, M., Rayamajhi, D., Acharya, I., and Adhikari, B. (2015b). "Geotechnical Field Reconnaissance: Gorkha (Nepal) Earthquake of April 25 2015 and Related Shaking Sequence." *GEER Association Report No. GEER-040*, 7 August 2015.
Hirose, M., Xiao, Y., Zuo, Z., Kamat, V. R., Zekkos, D., and Lynch, J. (2015). "Implementation of UAV Localization Methods for a Mobile Post-Earthquake Monitoring System."
Ho, D. –T., Grøtli, E. I., Sujit, P. B., Johansen, A. T., and Sousa, J. B. (2015). "Optimization of Wireless Sensor Network and UAV Data Acquisition." *Journal of Intelligent Robotic Systems*, 78, 159-179.
Hugenholtz, C. H., Whitehead, K., Brown, O. W., Barchyn, T. E., Moorman, B. J., LeClair, A.,

Riddell, K., and Hamilton, T. (2013). "Geomorphological Mapping with a Small Unmanned Aircraft System (sUAS): Feature Detection and Accuracy Assessment of a Photogrammetrically-driven Digital Terrain Model." *Geomorphology*, 194, 16-24.
Hugenholtz, C. H., Walker, J., Brown, O., and Myshak, S. (2014). "Earthwork Volumetrics with an Unmanned Aerial Vehicle and Softcopy Photogrammetry." *Journal of Surveying Engineering*, 141(1), 06014003.
Irizarry, J., Gheisari, M., and Walker, B. N. (2012). "Usability Assessment of Drone Technology as a Safety Inspection Tools." *Journal of Information Technology in Construction*, 17, 194-212.
Irizarry, J., and Johnson, E. N. (2014). "Feasibility Study to determine the Economic and Operational Benefits of Utilizing Unmanned Aerial Vehicles (UAVs)." *Georgia DOT Research Project 12-38*, Georgia Institute of Technology.
Irizarry, J., and Costa, D. B. (2016). "Exploratory Study of Potential Applications of Unmanned Aerial Systems for Construction Management Tasks." *Journal of Management in Engineering*, 32(3), 05016001.
Jahanshahi, M. R., Masri, S. F., Padgett, C. W., and Sukhatme, G., S. (2013). "An Innovative Methodology for Detection and Quantification of Cracks through Incorporation of Depth Perception." *Machine Vision and Applications*, 24, 227-241.
Jahanshahi, M. R., Chen, F. –C., Ansar, A., Padgett, C. W., Clouse, D., and Bayard, D. S. (2017). "Accurate and Robust Scene Reconstruction in the Presence of Misassociated Features for Aerial Sensing." *Journal of Computing in Civil Engineering*, 31(6), DOI: 10.1061/(ASCE)CP.1943-5487.0000702.
Javadnejad, F., Simpson, C. H., Gillins, D. T., Claxton, T., and Olsen, M. J. (2017). "An Assessment of UAS-Based Photogrammetry for Civil Integrated Management (CIM) Modeling of Pipes." *Pipelines 2017*, ASCE. 6-9 August 2017, Phoenix, AZ.
Jawhar, I., Mohamed, N., Al-Jaroodi, J., and Zhang, S. (2014). "A Framework for Using Unmanned Aerial Vehicles for Data Collection in Linear Wireless Sensor Networks." *J. of Intell. Robot. Sys.*, 74, 437-453.
Jordan, S., Moore, J., Hovet, S., Box, J., Perry, J., Kirsche, K., Lewis, D., and Tse, Z. T. H. (2018). "State-of-the-Art Technologies for UAV Inspections." *IET Radar, Sonar & Navigation*, 12(2), 151-164.
Kaul, L., Zlot, R., and Bosse, M. (2016). "Continuous-Time Three-Dimensional Mapping for Micro Aerial Vehicles with a Passively Actuated Rotating Laser Scanner." *Journal of Field Robotics*, 33(1), 103-132.
Khaloo, A., and Lattanzi, D. (2017). "Hierarchical Dense Structure-from-Motion Reconstructions for Infrastructure Condition Assessment." *Journal of Computing in Civil Engineering*, 31(1), DOI: 10.1061/(ASCE)CP.1943-5487.0000616.
Khaloo, A., Lattanzi, D., Cunningham, K., Dell'Andrea, R., and Riley, M. (2018). "Unmanned Aerial Vehicle Inspection of the Placer River Trail Bridge through Image-Based 3D Modeling." *Structure and Infrastructure Engineering*, 14(1), 124-136.
Kim, E., and Choi, D. (2015). "A 3D Ad Hoc Localization System Using Aerial Sensor Nodes." *IEEE Sensors Journal*, 15(7), 3716-3723.
Klingbeil, L., Eling, C., Heinz, E., Wieland, M., and Kuhlmann, H. (2017). "Direct Georeferencing for Portable Mapping Systems: In the Air and on the Ground." *Journal of Surveying Engineering*, 143(4), DOI: 10.1061/(ASCE)SU.1943-5428.0000229.
Kochersberger, K., Kroeger, K., Krawiec, B., Brewer, E., and Weber, T. (2014). "Post-disaster

Remote Sensing and Sampling via an Autonomous Helicopter." *Journal of Field Robotics*, 31(4), 510-521.
Lattanzi, D., and Miller, G. R. (2015). "3D Scene Reconstruction for Robotic Bridge Inspection." *Journal of Infrastructure Systems*, 21(2), DOI: 10.1061/(ASCE)IS.1943-555X.0000229.
Lattanzi, D., and Miller, G. R. (2017). "Review of Robotic Infrastructure Inspection Systems." *Journal of Infrastructure Systems*, 23(3), DOI: 10.1061/(ASCE)IS.1943-555X.0000353.
Leuschen, C., Hale, R., Keshmiri, S., Yan, J. B., Rodriguez-Maroales, F., Mahmood, A., and Gogineni, S. (2014). "UAS-Based Radar Sounding of the Polar Ice Sheets." *IEEE Geoscience and Remote Sensing Magazine*, March 2014, 8-17.
Lin, Y., Hyyppä, J., and Jaakkola, A. (2011). "Mini-UAV-Borne Lidar for Fine-Scale Mapping." *IEEE Geoscience and Remote Sensing Letters*, 8(3), 426-430.
Lin, Y., Hyyppä, J., Rosnell, T., Jaakkola, A., and Honkavaara, E. (2013). "Development of a UAV-MMS-Collaborative Aerial-to-Ground Remote Sensing System – A Preparatory Field Evaluation." *IEEE Journal of Selected Topics in Applied Earth Observations and Remote Sensing*, 6(4), 1893-1898.
Lin, J. J., Han, K. K., and Golparvar-Fard, M. (2015). "A Framework for Model-Driven Acquisition and Analytics of Visual Data Using UAVs for Automated Construction Progress Monitoring." *Computing in Civil Engineering 2015*, 156-164.
Lin, J. J., and Golparvar-Fard, M. (2016). "Web-Based 4D Visual Production Models for Decentralized Work Tracking and information Communication on Construction Sites." *Construction Research Congress 2016*, 1731-1741.
Liu, J., Jennesse Jr., M., and Holley, P. (2016). "Utilizing Light Unmanned Aerial Vehicles for the Inspection of Curtain Walls: A Case Study." *Construction Research Congress 2016*, 2651-2659.
Liu, P., Chen, A. Y., Huang, Y. –N., Han, J. –Y., Lai, J. –S., Kang, S. –C., Wu, T. –W., Wen, M. –C., and Tsai, M. –H. (2014). "A Review of Rotorcraft Unmanned Aerial Vehicle (UAV) Developments and Applications in Civil Engineering." *Smart Structures and Systems*, 13(6), 1065-1094.
Lowe, G. D. (1999). "Object Recognition from Local Scale-Invariant Features." *International Conference on Computer Vision*, Corfu, Greece, pp. 1150-1157.
Lowe, G. D. (2004). "Distinctive Image Features from Scale-Invariant Keypoints." *International Journal of Computer Vision*, 60(2), pp. 91-110.
Lu, Y., Macias, D., Dean, Z. S., Kreger, N. R., and Wong, P. K. (2015). "A UAV-Mounted Whole Cell Biosensor System for Environmental Monitoring Applications." *IEEE Transactions on Nanobioscience*, 14(8), 811-817.
Lucieer, A., de Jong, A. M., and Turner, D. (2014). "Mapping Landslide Displacements using Structure from Motion (SfM) and Image Correlation of Multi-temporal UAV Photography." *Progress in Physical Geography*, 38(1), 97-116.
Malaver, A., Motta, N., Corke, P., and Gonzalez, F. (2015). "Development and Integration of a Solar Powered Unmanned Aerial Vehicle and a Wireless Sensor Network to Monitor Greenhouse Gases." *Sensors*, 15, 4072-4096.
Mangione, K. (2015). "Drones to Help Police Clear Crash Scenes Quickly." *CTV News Toronto* <http://toronto.ctvnews.ca/drone-to-help-police-clear-crash-scenes-quickly-1.2463692> (20 September 2016).
Manousakis, J., Zekkos, D., Saroglou, F., and Clark, M. (2016). "Comparison of UAV-Enabled

Photogrammetry-Based 3D Point Clouds and Interpolated DSMs of Sloping Terrain for Rockfall Hazard Analysis." *Int. Arch. Photogramm. Remote Sens. Spatial Inf. Sci.*, XLII-2/W2, 71-77, DOI: 10.5194/isprs-archives-XLII-2-W2-71-2016.

Mascareñas, D., Flynn, E., Farrar, C., Park, G., and Todd, M. (2009). "A Mobile Host Approach for Wireless Powering and Interrogation of Structural Health Monitoring Sensor Networks." *IEEE Sensors Journal*, 9(12), 1719-1726.

Maza, I., Caballero, F., Capitan, J., Martinez-de-Dios, J. R., and Ollero, A. (2011). "A Distributed Architecture for a Robotic Platform with Aerial Sensor Transportation and Self-Deployment Capabilities." *Journal of Field Robotics*, 28(3), 303-328.

Mazzetti, M. (2012). "The Drone Zone." *The New York Times Magazine* <http://www.nytimes.com/2012/07/08/magazine/the-drone-zone.html> (20 September 2016).

Meng, X., Currit, N., and Zhao, K. (2010). "Ground Filtering Algorithms for Airborne LiDAR Data: A Review of Critical Issues." *Remote Sensing*, 2, 833-860.

Michael, N., Shen, S., Mohta, K., Mulgaonkar, Y., Kumar, V., Nagatani, K., Okada, Y., Kiribayashi, S., Otake, K., Yoshida, K., Ohno, K., Takeuchi, E., and Tadokoro, S. (2012). "Collaborative Mapping of an Earthquake-Damaged Building via Ground and Aerial Robots." *Journal of Field Robotics*, 29(5), 832-841.

Murphy, R. R., Duncan, B. A., Collins, T., Kendrick, J., Lohman, P., Palmer, T., and Sanborn, F. (2015). "Use of a Small Unmanned Aerial System for the SR-530 Mudslide Incident near Oso, Washington." *Journal of Field Robotics*, DOI: 10.1002/rob.21586.

Nagai, M., Chen, T., Shibasaki, R., Kumagai, H., and Ahmed, A. (2009). "UAV-Borne 3-D Mapping System by Multisensor Integration." *IEEE Transactions on Geoscience and Remote Sensing*, 47(3), 701-708.

Neugirg, F., Stark, M., Kaiser, A., Vlacilova, M., Seta, M. D., Vergari, F., Schmidt, J., Becht, M., and Haas, F. (2016). "Erosion Processes in Calanchi in the Upper Orcia Valley, Southern Tuscany, Italy based on Multitemporal High-Resolution Terrestrial Lidar and UAV Surveys." *Geomorphology*, 269, 8-22.

Nguyen, L. (2014). "From Police Work to Inspecting Farms, Drones can be Big Business in Canada." *CTV News Winnipeg* <http://winnipeg.ctvnews.ca/from-police-work-to-inspecting-farms-drones-can-be-big-business-in-canada-1.1804588> (20 September 2016).

Niethammer, U., James, M. R., Rothmund, S., Travelletti, J., and Joswig, M. (2012). "UAV-Based Remote Sensing of the Super-Sauze Landslide: Evaluation and Results." *Engineering Geology*, 128, 2-11.

Nishar, A., Richards, S., Breen, D., Robertson, J., and Breen, B. (2016). "Thermal and Infrared Imaging of Geothermal Environments and by an Unmanned Aerial Vehicle (UAV): A Case Study of the Wairakei – Tauhara Geothermal Field, Taupo, New Zealand." *Renewable Energy*, 86, 1256-1264.

Olsen, M. J., Kuester, F., Chang, B. J., and Hutchinson, T. C. (2010). "Terrestrial Laser Scanning-Based Structural Damage Assessment." *Journal of Computing in Civil Engineering*, 24(3), 264-272.

Otto, G. P., and Chau, T. K. W. (1989). "Region-Growing Algorithm for Matching of Terrain Images." *Image Vision Comput.*, 7(2), 83-94.

PEER. (2014). "PEER Preliminary Notes and Observations on the August 24, 2014, South Napa Earthquake." *Pacific Earthquake Engineering Research Center Report No. 2014/13*, Kang, G. S., and Mahin, S. A., Eds. 17 September 2014.

Pirotti, F., Guarnieri, A., and Vettore, A. (2013). "Ground Filtering and Vegetation Mapping using Multi-Return Terrestrial Laser Scanning." *ISPRS Journal of Photogrammetry and Remote Sensing*, 76, 56-63.

Rathinam, S., Kim, Z. W., and Sengupta, R. (2008). "Vision-Based Monitoring of Locally Linear Structures Using an Unmanned Aerial Vehicle." *Journal of Infrastructure Systems*, 14(1), 52-63.

Pix4D. (2017), "Pix4Dmapper 3.2 User Manual." *Version 3.2*, Pix4D SA.

Rojas, R. (2016). "New York City's Firefighting Arsenal Will Soon Include Drones." *The New York Times* <http://www.nytimes.com/2016/09/09/nyregion/new-york-city-fire-department-drones.html> (20 September 2016).

Rollins, K., Ledezma, C., and Montalva, G. (2014). "Geotechnical Aspects of April 1, 2014, M8.2 Iquique, Chile Earthquake." *GEER Association Report No. GEER-038*, 22 October 2014.

Rosser, K., Pavey, K., FitzGerald, N., Fatiaki, A., Neumann, D., Carr, D., Hanlon, B., and Chahl, J. (2015). "Autonomous Chemical Vapour Detection by Micro UAV." *Remote Sensing*, 7, 16865-16882.

Rossi, M., and Brunelli, D. (2016). "Autonomous Gas Detection and Mapping with Unmanned Aerial Vehicles." *IEEE Transactions on Instrumentation and Measurement*, 65(4), 765-775.

Salvini, R., Vanneschi, C., Riccucci, S., Francioni, M., and Gullì, D. (2015). "Application of an Integrated Geotechnical and Topographic Monitoring System in the Lorano Marble Quarry (Apuan Alps, Italy)." *Geomorphology*, 241, 209-223.

Saroglou, C., Asterious, P., Tsiambaos, G., Zekkos, D., Clark, M., and Manousakis, J. (2017). "Investigation of Two Co-Seismic Rockfalls During the 2015 Lefkada and 2014 Cephalonia Earthquakes in Greece." *3rd North American Symposium on Landslides*, Roanoke, VA.

Savage, C. (2016). "U.S. Releases Rules for Airstrike Killings of Terror Suspects." *The New York Times* <http://www.nytimes.com/2016/08/07/us/politics/us-releases-rules-for-airstrike-killings-of-terror-suspects.html> (20 September 2016).

Schmale, D. G. III, Dingus, B. R., and Reinholtz, C. (2008). "Development and Application of an Autonomous Unmanned Aerial Vehicle for precise Aerobiological Sampling above Agricultural Fields." *Journal of Field Robotics*, 25(3), 133-147.

SenseFly. (2015). "Extended User Manual eBee and eBee Ag." *senseFly Ltd.*, April 2015. <https://www.sensefly.com/fileadmin/user_upload/sensefly/documents/manuals/Extended_User_Manual_eBee_and_eBee_Ag_v16.pdf>.

Siebert, S., and Teizer, J. (2014). "Mobile 3D Mapping for Surveying Earthwork Projects Using an Unmanned Aerial Vehicle (UAV) System." *Automation in Construction*, 41, 1-14.

Snavely, N., Seitz, S. M., and Szeliski, R. (2008). "Modeling the World from Internet Photo Collections." *International Journal of Computer Vision*, 80(2), 189-210.

Song, S., and Jo, S. (2017). "Online Inspection Path Planning for Autonomous 3D Modeling using a Micro-Aerial Vehicle." *2017 International Conference on Robotics and Automation (ICRA)*, IEEE, 6217-6224.

Srinivasan, S., Latchman, H., Shea, J., Wong, T., and McNair, J. (2004). "Airborne Traffic Surveillance Systems: Video Surveillance of Highway Traffic." *ACM 2nd Int. Workshop on Video Surveillance and Sensor Networks*, Association for Computing Machinery, New York.

Stamp, J. (2013). "Unmanned Drones Have Been Around Since World War I." *Smithsonian Magazine* <http://www.smithsonianmag.com/arts-culture/unmanned-drones-have-been-around-since-world-war-i-16055939/> (5 March 2018).
Straub, J. (2014). "Unmanned Aerial Systems: Consideration of the Use of Force for Law Enforcement Applications." *Technology in Society*, 39, 100-109.
Stumpf, A., Malet, J.-P., Kerle, N., Niethammer, U., and Rothmund, S. (2013). "Image-based Mapping of Surface Fissures for the Investigation of Landslide Dynamics." *Geomorphology*, 186, 12-27.
Syed, S. (2012). "Drone-Makers Target Asia for Growth." *BBC* <http://www.bbc.com/news/business-17028684> (20 September 2016).
Take, W. A., Chappel, M. J., Brachman, R. W. I., and Rowe, R. K. (2007). "Quantifying Geomembrane Wrinkles using Aerial Photography and Digital Image Processing." *Geosynthetics International*, 14(4), 219-227.
Take, W. A. (2015). "Thirty-Sixth Canadian Geotechnical Colloquium: Advances in Visualization of Geotechnical Processes through Digital Image Correlation." *Canadian Geotechnical Journal*, 52, 1199-1220.
Techy, L., Schmale III, D. G., and Woolsey, C. A. (2010). "Coordinated Aerobiological Sampling of a Plant Pathogen in the Lower Atmosphere Using Two Autonomous Unmanned Aerial Vehicles." *Journal of Field Robotics*, 27(3), 335-343.
Teizer, J. (2015). "Status Quo and Open Challenges in Vision-based Sensing and Tracking of Temporary Resources on Infrastructure Construction Sites." *Advanced Engineering Informatics*, 29, 225-238.
Tong, X., Liu, X., Chen, P., Liu, S., Luan, K., Li, L., Liu, S., Liu, X., Xie, H., Jin, Y., and Hong, Z. (2015). "Integration of UAV-Based Photogrammetry and Terrestrial laser Scanning for the Three-Dimensional Mapping and Monitoring of Open-Pit Mine Areas." *Remote Sensing*, 7, 6635-6662.
Torok, M. M., Golparvar-Fard, M., and Kochersberger, K. B. (2014). "Image-Based Automated 3D Crack Detection for Post-Disaster Building Assessment." *Journal of Computing in Civil Engineering*, 28(5), A4014004.
Turner, D., Lucieer, A., and de Jong, S. M. (2015). "Time Series Analysis of Landslide Dynamics Using an Unmanned Aerial Vehicle (UAV)." *Remote Sensing*, 7, 1736-1757.
Turner, I. L., Harley, M. D., and Drummond, C. D. (2016). "UAVs for Coastal Surveying." *Coastal Engineering*, 114, 19-24.
Tziavou, O., Pytharouli, S., and Souter, J. (2018). "Unmanned Aerial Vehicle (UAV) based Mapping in Engineering Geological Surveys: Considerations for Optimum Results." *Engineering Geology*, 232, 12-21.
Vetrivel, A., Gerke, M., Kerle, N., and Vosselman, G. (2015a). "Identification of Damage in Buildings Based on Gaps in 3D Point Clouds from Very High Resolution Oblique Airborne Images." *ISPRS Journal of Photogrammetry and Remote Sensing*, 105, 61-78.
Vetrivel, A., Gerke, M., Kerle, N., and Vosselman, G. (2015b). "Segmentation of UAV-based Images Incorporating 3D Point Cloud Information." *PIA15+HRIGI15 Joint ISPRS Conference 2015*, 25-27 Mar. 2015, Munich, Germany, 261-268.
Villas, L. A., Guidoni, D. L., Maia, G., Pazzi, R. W., Ueyama, J., and Loureiro, A. A. F. (2015). "An Energy Efficient Joint Localization and Synchronization Solution for Wireless Sensor Networks Using Unmanned Aerial Vehicle." *Wireless Networks*, 21, 485-498.
VMS. (2010). "Geometric Software Videometric and Survey Network Solutions."

<http://www.geomsoft.com> (29 June 2016).
Vollgger, S. A., and Cruden, A. R. (2016). "Mapping Folds and Fractures in Basement and Cover Rocks using UAV Photogrammetry." Cape Liptrap and Cape Paterson, Victoria, Australia." *Journal of Structural Geology*, 85, 168-187.
Wallace, L., Lucieer, A., Watson, C., and Turner, D. (2012). "Development of a UAV-Lidar System with Application to Forest Inventory." *Remote Sensing*, 4, 1519-1543.
Westoby, M. J., Brasington, J., Glasser, N. F., Hambrey, M. J., and Reynolds, J. M. (2012). "'Structure-from-Motion' Photogrammetry: A Low-Cost, Effective Tool for Geoscience Applications." *Geomorphology*, 179, 300-314.
Winter, F. (2000). "V-1 Cruise Missile." *Smithsonian National Air and Space Museum* <https://airandspace.si.edu/collection-objects/missile-cruise-v-1-fi-103-fzg-76> (20 September 2016).
Wood, A., Cook, I., Doyle, B., Cunningham, M., and Samson, C. (2016). "Experimental Aeromagnetic Survey Using an Unmanned Air System." *The Leading Edge*, March 2016, 270-273.
Xing, M., Jiang, X., Wu, R., Zhou, F., and Bai, Z. (2009). "Motion Compensation for UAV SAR Based on Raw Radar Data." *IEEE Transactions on Geoscience and Remote Sensing*, 47(8), 2870-2883.
Yang, B., and Chen, C. (2015). "Automatic Registration of UAV-Borne Sequent Images and Lidar Data." *ISPRS Journal of Photogrammetry and Remote Sensing*, 101, 262-274.
Yuan, C., Zhang, Y., and Liu, Z. (2015). "A Survey on Technologies for Automatic Forest Fire Monitoring, Detection, and Fighting using Unmanned Aerial Vehicles and Remote Sensing Techniques." *Canadian Journal of Forestry Research*, 45, 783-792.
Zarco-Tejada, P. J., Diaz-Varela, R., Angileri, V., and Loudjani, P. (2014). "Tree Height Quantification Using Very High Resolution Imagery Acquired from an Unmanned Aerial Vehicle (UAV) and Automatic 3D Photo-Reconstruction Methods." *European Journals of Agronomy*, 55, 89-99.
Zekkos, D., Lynch, J., Sahadewa, A., Hirose, M., and Ellis, D. (2014a). "Proof-of-Concept Shear Wave Velocity Measurements Using an Unmanned Autonomous Aerial Vehicle." *Geo-Congress 2014 Technical Papers*, 953-962.
Zekkos, D., Manousakis, J., Greenwood, W., and Lynch, J. (2016). "Immediate UAV-enabled Infrastructure Reconnaissance following Recent Natural Disasters: Case Histories from Greece."*1st International Conference on Natural Hazards & Infrastructure*, Chania, Greece, 28-30 June 2016.
Zhang, C., and Elaksher, A. (2012). "An Unmanned Aerial Vehicle-Based Imaging System for 3D Measurement of Unpaved Road Surface Distresses." *Computer-Aided Civil and Infrastructure Engineering*, 27(2), 118-129.
Zhang, S., Teizer, J., Pradhananga, N., and Eastman, C. M. (2015). "Workforce Location Tracking to Model, Visualize and Analyze Workspace Requirements in Building Information Models for Construction Safety Planning." *Automation in Construction*, 60, 74-86.
Zhou, H., Hirose, M., Greenwood, W., Xiao, Y., Lynch, J., Zekkos, D., and Kamat, V. (2016). "Demonstration of UAV Deployment and Control of Mobile Wireless Sensing Networks for Modal Analysis of Structures." *Sensors and Smart Structures Technologies for Civil, Mechanical, and Aerospace Systems 2016, Proc. of SPIE* Vol. 9803, 98031X.

CHAPTER 3

UAV-Enabled 3D Imaging of Geotechnical Sites

When a natural disaster occurs, geotechnical systems supporting critical infrastructure are often damaged. When a geotechnical system fails, engineers need to understand how and why the failure occurred. Engineers attempt to characterize failures, or damage, and document the failure mechanism. However, the ability to document cases of damage is limited by several factors:

- Limited initial data
- Mobility of the reconnaissance team
- Accessibility of sites
- Perishability of data

The limiting factors mentioned above are caused by the nature of disasters; they produce significant safety concerns and hamper infrastructure. As discussed previously, the geometric documentation of sites in post-disaster scenarios is often sparse and laborious. The perishability of data imposes time constraints and often prevents multiple passes. The quality of data must be optimized to balance with time constraints and as much information as possible must be extracted from data of limited quality. UAV-based surveying can rapidly provide nearly continuous geometric documentation at sites of interest. Outside of post-disaster scenarios, UAV-based surveying also has tremendous value for rapid site documentation and coverage, as well as a robust framework for repeated measurements to observe changes to sites over time. In this chapter, SfM

photogrammetry is used to survey and develop 3D models of geotechnical sites with a focus on earthquake-induced landslides. The fundamentals and general workflow of SfM are outlined and a generalized field procedure is presented. The site mapping performed in association with this work is documented and the lessons learned from performing the UAV-based mapping are discussed. Four sites which made the greatest contribution to lessons learned are documented in greater detail including two sites affected by the 2006 Kiholo Bay Earthquake on the Big Island of Hawaii, and two landslides caused by the 2015 Gorkha earthquake in Nepal.

3.1 UAV-Based Structure-from-Motion Photogrammetry

SFM photogrammetry is a 3D imaging method which has gained recent attention for mapping rock masses and geomorphologic features (Westoby et al 2012; Stumpf et al., 2013; Bemis et al., 2014). It has also been shown to produce 3D point clouds comparable to terrestrial LiDAR scanning (Hugenholtz et al., 2014; Siebert and Teizer, 2014; Tong et al., 2015). When performed using a UAV-mounted camera, the position of the camera and distance from the target can be easily controlled, and the images can be collected rapidly from many perspectives. In the previous chapter, studies using UAVs to perform photogrammetric techniques for a wide range of applications in civil infrastructure engineering and geosciences were discussed. The recent prevalence of UAV-based SfM has driven novel adaptations and improvements to the method and its underlying algorithms (*e.g.* Jahanshahi et al., 2017).

3.1.1 Fundamentals of SfM:

The fundamental basis of SfM allows models to be constructed at many different scales (*e.g.* landslides or small machine parts) which makes it a robust technique for various applications

in and outside of civil engineering. SfM uses sequences of overlapping images to extract 3D information of the imaged region. The extraction of 3D information is analogous to stereoscopy. In general, the quality of the reconstruction is a function of camera (*i.e.* sensor) properties and image overlap. A minimum of 60% overlap between sequential images is recommended (Westoby et al., 2012). Where SfM differs from other photogrammetric techniques is that camera location and orientation do not need to be known *a priori*. Camera locations and orientations are solved iteratively based on feature pattern in sequential images through a bundle adjustment algorithm and chooses the optimal camera solution (Snavely et al., 2008). The image matching is performed using feature-detection algorithms such as scale-invariant feature transform (SIFT) (Lowe, 1999; Lowe 2004). The bundle adjustment process also contains algorithms for locating and matching points in 3D as well as filtering of moving objects.

In general, SfM is only capable of imaging features than are visible in several images collected with different camera orientations. As a result, it is difficult to produce models in areas with visual obstructions such as dense vegetation. In fact, SfM has gained popularity in forestry and precision agriculture where one goal of mapping is to measure tree or plant height. In places where vegetation is sparse, surface models can be developed and automatic or semi-automatic techniques exist to remove vegetation (Meng et al., 2010; Pirotti et al., 2013; Gruszczynski et al., 2017). While modern feature-detection algorithms are capable of identifying illumination-invariant features, dark shadows and other light-denied areas (*e.g.* fracture opening in a rock mass), or very bright area (*e.g.* flat surface under direct sunlight) can be difficult image to because repeated feature patterns cannot be identified. Similarly, images collected of patterned or textured surfaces without additional information are difficult to accurately resolve, because no unique feature patterns are available for grouping images within the bundle adjustment process.

3.1.2 Workflow and Outputs:

The workflow for the 3D imaging method implemented here is outlined in Figure 3-1. The workflow can be segmented in to three main components: acquisition of field data, data processing, and output generation. The acquisition of field data includes placement and measurement of ground control points, flight path planning, and collection of imaging. More details on field component are found in the Generalized Field Procedure subsection. In data processing, the core SfM algorithms are applied to produce a dense 3D point cloud. A coarse 3D point cloud is first produced from the feature identification and bundle adjustment stage. The coarse set of 3D points is then densified (*i.e.* the spaces between points are filled in) using another 3D imaging approach, multi-view stereovision (MVS) (*e.g.* Furukawa and Ponce, 2007; Furukawa et al., 2010). MVS is fundamentally similar to basic stereovision where 3D points can be extracted from two images of the same object collected from known relative positions. After the point cloud densification is complete, the point cloud can be scaled and transformed to meet the imposed scaling constraints and geo-referenced, if GPS tags are available. The scaling can be performed using image geotags generated by the UAV on-board positioning system, but will not be as accurate as scaling based on surveyed points on the ground surface. Without introducing the scaling stage, quantitative measurements cannot be performed and only general qualitative observations can be made. The final, densified point cloud is primary output from SfM but can be used to generate additional outputs including digital models of terrain or surfaces, triangular mesh surfaces, and orthophotos. The 3D point cloud produced by SfM is highly similar to those produced by laser scanning. Robust comparisons between the two have been made in the literature (as described in Chapter 2).

Orthophotos are generated from an orthorectified image, or series of images connected through image registration. Orthophotos are generally used for site maps and layout

documentation. The resolution (*i.e.* GSD) is uniform across the image which allows for distance measurements to be made. Most commonly, orthophotos are generated in plan-view, similar to satellite imagery. However, the orthogonal plane of the image can be arbitrary, meaning that an orthophoto can be produced on any plane in the SfM model. Some examples of analysis types orthophotos can be used for include change detection, monitoring of lateral displacements, and descriptions of site layout. Depending on the objective of the study, the model results can be presented as interpolated digital surface models (DSM) or digital terrain models (DTM). A DTM is a raster map with elevation assigned along a grid through interpolation of model points. In the DTM, objects such as buildings and trees have been removed so that the model is representative of the terrain (*i.e.* bare earth only). A DSM is a related model with complete model information including buildings and other objects. Repeated DSMs are useful for making temporal observations with change-detection methodologies. Repeated DTMs are useful for comparing pre- and post-failure geometry, defining topography, or measuring ground displacements. Similarly, a 3D mesh is created by generating triangular elements connecting the 3D points together. The triangular mesh is useful for integrating the SfM output with other workflows and data archetypes. The imagery used as input to the SfM process can then be overlain on the mesh to provide color and texture features to the mesh elements. SfM computations were performed and outputs generated by the software package Pix4D (2017). SfM outputs and the input imagery were both used for analyses performed in this chapter.

3.1.3 Generalized Field Procedure and Data Collection Considerations:

The acquisition of field data includes placement and measurement of ground control points, flight path planning, and finally collection of imaging. An additional component to verify the

collected data is sufficient for the desired analyses, such as rapid coarse model generation, is suggested, especially when deployment is costly or high risk. Based on lessons learned from performing aerial surveys of geotechnical features (detailed examples are documented in the following sections), a generalized field procedure was generated with recommendations for good practice in field image collection for geotechnical applications. The procedure is outlined in Figure 3-2.

The specific flight path, velocity, and image collection rate of the survey will be dependent on the required image (and model) resolution for the specific application (*e.g.* 3 pixels per feature, 10 pixels per feature, 5 cm per pixel, etc.). The resolution of collected imagery is defined by its ground sampling distance (GSD), or the nominal distance between pixel centers along the ground surface. For example, a GSD of 5 cm/pixel means that the pixel to pixel distance represents 5 cm along the imaged surface. The theoretical GSD for an image collected by a camera perpendicular to a flat surface is defined by:

$$GSD = \frac{H \cdot s_w}{f \cdot p_w} \tag{3-1}$$

Where H is distance of the camera from the surface, s_w is the width of the camera sensor, f is the focal length of the camera lens, and p_w is the width of image in pixels. Camera distortion models may need to be accounted for when projecting onto the ground surface. Equation 3-1 is useful for estimating the maximum flight height or distance from the survey target when the minimum required resolution of the imagery is known. Selecting flight height/distance for an aerial survey is important for optimizing flight parameters to minimize resource consumption (time, energy). If resolution requirements vary across an inspection target (*e.g.* fasteners versus bridge deck), the flight parameters can be adjusted to optimize energy conservation. Clearly the GSD of images collected from the same height by different cameras may vary significantly. Figure 3-3 shows four

design envelopes for estimating the maximum flight height as a function of the required GSD for different cameras mounted on UAVs. One implication of Figure 3-3 is that for a given GSD, camera quality can have a dramatic impact on the maximum allowable flight height and therefore on the flight distance and total number of images collected.

An approach of flight planning by estimating flight height based on the camera's intrinsic parameters and including more than 60% image overlap may be appropriate for relatively flat sites but additional image collection must be performed for sites with multiple surfaces, topographic relief, and complex 3D geometric features is required. For example, when collecting data for a landslide, images must be collected facing the ground surface, facing the landslide scarp and debris, and obliquely. Oblique, or nadir, images are important for collecting information on protruding elements and 3D geometric features. Figure 3-4 shows 3D point clouds of a constructed, grass-covered "wavefield" on the University of Michigan North Campus. In Figure 3-4a, the model has been produced using images collected on two flight passes, one perpendicular and one oblique view. In Figure 3-4b, the images have been collected on a single pass with the UAV camera directed vertically. Clearly, there is information missing to describe the 3D geometric features of the wavefield. It is important to capture the additional information provided by oblique views from all directions. For imaging a structure with significant 3D features, such as a bridge, many passes will be necessary.

GCP acquisition is performed to pin the SfM model at known positions within a coordinate system. GCPs are ideally engineered objects, or targets, placed on the survey target and designed to be easily visible within imagery. Figure 3-5 shows an example of a GCP visible in an image collected by a UAV. The GCP in Figure 3-5 is approximately 500 cm^2. GCPs can also be natural objects or features that will also be easily identifiable within the collected imagery. Using natural

features is typically necessary at landslide sites because targets cannot be easily, or safely, placed in an even distribution vertically on the slope. The distances between GCPs or the distances from a known point should be measured. Enough GCPs should be used to evenly distribute them across the target area, including near the edges. Additional GCPs can be added near areas where error needs to be minimized. In an ideal situation, the GCPs (or as many as possible) are measured with survey-grade RTK-GPS equipment. Having robust GPS positioning of the SfM model is beneficial because it places the model in a global coordinate system compatible with many other forms of geospatial data. The results of model development can then be integrated with geospatial databases and quickly accessed at later dates (*e.g.* following a future seismic event). When using natural GCPs, it is recommended that more than necessary be collected. Natural GCPs have a significantly higher chance of not being discernable in the point cloud than engineered targets. For example, if a landslide survey team determines that 10 natural GCPs upslope of a landslide will be necessary then 15-20 should be collected. Natural GCPs should not be selected near potential obstructions (*e.g.* vegetation).

3.1.4 Error Assessment of SfM Models

As previously mentioned, GCPs should be distributed throughout the entire area of interest. Model errors will accumulate away from GCPs if they are concentrated in one area (Manousakis et al., 2016). In addition to GCPs, check points must also be collected. Check points are only differentiated from GCPs in that they are not included in the SfM model generation and georeferencing. They are collected along with GCPs during field surveys and are used after final model generation to provide an estimate of error in the point cloud. If check points are not evenly distributed through model, similarly to GCPs, the spatial distribution of error in the model will be

difficult to describe. This is particularly true for models that are complex in 3D. Additionally, error will increase as image overlap decreases or at the edges of models.

Figure 3-6 shows an example comparison between SfM and terrestrial Lidar scanning for mapping a set of landslides. The site (Landslide 3 in Table 3-2) had a series of tightly-spaced co-seismic landslides along the Trishuli River in Nepal. The landslides were rapidly mapped (9 minutes of flight time) at a coarse resolution of about 11 cm/pixel (see Site 6 in Table 3-3). The landslides were mapped simultaneously with a Riegl VZ-6000 LiDAR unit that has an accuracy of 15 mm and precision of 10 mm at 150 m range. The SfM point cloud is shown in Figure 3-6a. Figure 3-6b shows a cloud-to-cloud comparison. The mean difference between the two clouds is 0.02 m with the standard deviation of 0.77 m. The largest differences are observed in areas of vegetation and at the corners of the model which are not considered reliable. Specific areas that were obscured to one of the platforms also generated significant differences. The findings from this study indicate that the SfM has a comparable accuracy. Additionally, SfM has advantages of being able to collect higher-resolution images by flying closer to the target and robust RGB attributes for the point clouds. RGB attributes can be attached to terrestrial Lidar scans but is not standard practice. These findings are consistent with previous studies that indicate that UAV-based photogrammetry can be a low cost alternative to LiDAR surveying for developing DTMs (Hugenholtz et al., 2013; Hugenholtz et al., 2014; Siebert and Teizer, 2014; Tong et al. 2015; Cook 2017; Zekkos et al., 2018).

3.2 Geotechnical Applications of UAV-Based SfM

The underlying principles of SfM were learned through application of the technique at numerous geotechnical sites. As a result of performing the UAV-based mapping, lessons learned

for practical applications during early expeditions helped refine the strategies employed in future mapping projects. In this section the sites where UAV-based SfM was applied are documented. Two practical application areas, landslide delineation and rock mass characterization are described. A subset of sites are detailed to demonstrate some of the key lessons learned.

3.2.1 Mapping of Geotechnical Sites

UAV-based image collection was utilized during several field expeditions, including two more significant mapping efforts in Hawaii and Nepal. The first effort, on the Big Island of Hawaii, was part of a broader investigation of weathering processes in layered basalts and included the mapping of sites affected by the 2006 Kiholo Bay earthquake. Some outcomes of the study can be found in Von Voigtlander et al. (2018). Sites where a UAV was used to collect images are summarized in Table 3-1. Images were collected at four of the five sites using a DJI Phantom 2 Vision+ (P2V) UAV. Images at the Cobble Beach site were collected using a GoPro Hero3 camera mounted on a 3DR X8 octorotor UAV. The P2V uses an integrated 14 MP camera and has a maximum reported flight time of 25 minutes. The P2V and GoPro cameras both have a fisheye lens which has a wide field of view but induces significant radial distortion within the image. The distortion is corrected in post processing but some pixels are discarded from the image and residual distortion (*i.e.* stretching) can be observed at the edges and corners of the image. For this reason it is recommended that more than 60% overlap be ensured for consecutive images for the fisheye lens. Most commercial UAV platforms now use rectilinear lenses, which is preferred for imaging applications. The change was partially in response to a shift in focus from hobbyists to aerial photography, cinematography, surveying, visual inspection/monitoring, and other industrial

applications. The Kauhola Point Lighthouse and Small Awini Landslide sites, which are bolded in Table 3-1, are discussed in further detail in this section.

Kauhola Point Lighthouse was the first site where the UAV-based imaging techniques were implemented. The sites were previously affected by the M_w 6.7 2006 Kiholo Bay earthquake. The site is located at a 7 m high eroding sea cliff located at Kauhola Point in the northwestern side of the island. The site originally held a lighthouse that was moved multiple times due to erosion of the cliff. The foundations of old lighthouse structures still exist at the site. During the 2006 Kiholo Bay earthquake, a significant portion of the cliff retreated, reportedly about 2 m measured relative to the lighthouse. A P2V UAV was used to collect images of the sea cliffs along the perimeter of Kauhola Point. The survey of cliff was performed with two personnel, a pilot and a camera operator. The UAV was flown manually to collect 320 images of the cliff in approximately 60 minutes of flight time. A satellite image of Kauhola Point indicating the surveyed cliff is shown in Figure 3-7. The flight time was much higher than expected due to significant wind (15-20 mph) and poor lighting conditions requiring image recollection for some portions of the cliff. The collected images were used in SfM to generate a 3D point cloud. The final model is shown in Figure 3-8. Due to poor image overlap around the center of the profile, the cliff model is discontinuous. The two segments of the profile could be aligned relative to observations in the UAV imagery and recent satellite imagery. The modeled cliff was used to provide supplemental information for a 2D seismic survey performed parallel to the cliff face. The identification of three distinct layers in the model and the 2D shear wave velocity profile are shown in Figure 3-9. The results of collecting imagery at the Kauhola Point Lighthouse were beneficial for preparing future UAV-based imaging strategies. The 3D model has limited detail for an in-depth material

characterization effort but has value for comparing with future measurements of the cliff as erosion continues or when another seismic event occurs.

The second major mapping effort was a reconnaissance expedition to investigate coseismic landslides caused by the 2015 Gorkha earthquake in Nepal. The M_w 7.8 event caused widespread damage across Nepal. The earthquake epicenter was located about 80 km northwest of Kathmandu and caused a 140 km rupture along the Main Himalayan Thrust (Galetzka et al., 2015). Previous regional seismic events are discussed in Hayes et al. (2015). This event resulted in nearly 9000 fatalities and over 500,000 destroyed homes which displaced millions of displaced people (NSET, 2015). There were several post-earthquake reconnaissance investigations into the event (Chiaro et al., 2015; Collins and Jibson et al., 2015; Hashash et al., 2015). The earthquake caused tens of thousands of landslides throughout the affected region (Clark et al., 2015; Collins and Jibson et al., 2015; Kargel et al., 2015; Roback et al., 2018). Landsliding was magnified by the steep terrain and varied in size. The landslides resulted in destruction of infrastructure, loss of life and, in some cases, destruction of entire villages. A wide variety of landslide types has been attributed to the Himalaya in other studies (Timilsina et al., 2014). For this event, most of the landslides occurred within the Greater Himalayan and Lesser Himalayan tectonostratigraphic units. The Greater Himalayan units are characterized by medium to high-grade schist and gneisses with granitic plutons, and the Lesser Himalayan units are characterized by low-grade metasedimentary rocks (e.g. Schelling, 1992; Le Fort, 1986; Gansser, 1964).

Some results generated from landslide mapping in Nepal can be found in Greenwood et al. (2016a) and Zekkos et al. (2017). A Phantom 3 Professional (P3P) quadrotor UAV was used to collect images or video of more than 20 landslides and other geohazards. Both video and photos were used to collect images of the investigated sites depending on the complexity of features and

possible flight limitations. Video allows for a dense set of images to be collected while eliminating the concern for acquiring the necessary overlap between images. However, processing of video frames recorded at high framerates is computationally intensive. In addition to the landslides, two other sites affected by earthquake-related hazards were investigated. The sites mapped in Nepal are summarized in Table 3-2. The two bolded sites in Table 3-2 are discussed in further detail in a following subsection. Aerial video was collected at a construction site where structures and equipment was destroyed by rockfall. The site was not as thoroughly mapped as desired due to poor GPS localization for the UAV within the valley. Most UAV platforms rely on GPS signals for positioning and basic autonomous navigation. In Chapter 2, research into UAV navigation in GPS-denied environments was mentioned. The rockfall site in Nepal is an important example demonstrating that GPS-denied environments are not exclusive to enclosed or indoor facilities (*e.g.* buildings, tunnels). The other site was a debris flow that traveled through a stream channel and blocked a river, causing severe flooding. The debris flow occurred during the monsoon season in Nepal during a heavy rainfall event. While the debris flow was not directly caused the earthquake, investigation via UAV at the site and surrounding area found that the material in the flow was partially sourced from coseismic landslide debris. Following UAV-based image collection of the debris flow fan, the UAV was used to follow the channel and potentially identify the source of the material. Figure 3-10 shows the path taken by the debris flow and followed by the UAV. Figure 3-11 shows the identification of landslides contributing material to the flow. The debris flow is an example of a seismic geohazard not directly tied to the shaking event, but certainly a consequence of the event. Further investigation of the landslides was ended due to lost connection with the UAV. The lost connection engaged the UAV return-to-home function until wireless connection was regained. In this example, the UAV was used for an on-demand reconnaissance decision

which yielded valuable results for analysis and understanding of the debris flow event. The reconnaissance was performed without requiring personnel at significant distance upstream. In fact, the interaction of the landslides with the debris flow would not have been obvious to ground-based reconnaissance due to the steeply inclined slopes and thick vegetation. Engagement of the UAV's return-to-home failsafe limited the depth of the investigation (*e.g.* landslides could not be modeled) and highlights the importance of robust communication architectures and potential value of autonomous navigation. The footage collected by the UAV provided a perspective unavailable by conventional reconnaissance efforts, unless a costly helicopter flight was made. As mentioned previously, ground-based reconnaissance cannot see beyond steep slopes and thick vegetation. Satellite imagery is too coarse and is often obstructed by cloud cover or distorted along steep slopes.

Additional sites mapped using UAVs are documented in Table 3-3. Some of the sites from the expeditions in Hawaii and Nepal are listed Table 3-3 as well. The table is intended to show the breadth of sites investigated by the research group's combined efforts. Table 3-3 also details the total flight time, approximate camera distance from target, area covered, and average GSD for each site. The flight parameter data has been synthesized in Figure 3-12 where total area normalized by average resolution is shown as a function of flight time. An affine best fit described by Equation 3-2 is shown on the figure with 95% confidence bounds.

$$A/_{GSD} = 2761.7 \cdot t + 3215.3 \tag{3-2}$$

Where A is the total 3D surface area in m^2, GSD is the ground sampling distance in cm/pixel, and t is the flight time in minutes. Clearly, the points in Figure 3-12 are clustered below t = 20 minutes. This is primarily caused by the types of sites investigated and that larger sites are generally mapped at coarser resolutions. The figure shows that to maintain a low flight time, resolution must be

sacrificed when covering a greater area. Similarly, to maintain a high resolution model when covering a greater area, significantly more flight time must be committed. The points in the figure are primarily from surveys conducted using the P3P UAV. Equation 3-2 provides a method for estimating flight time to map a given area at a desired resolution using a UAV-camera system similar to the P3P. It can also be used to estimate the lowest resolution a given area can be mapped at with a limited flight time. For example, Sites 19 and 20 required the longest flight times due to mapping large areas at a resolution of 2 cm/pixel. It should be noted that Site 1 is the Kauhola Point Lighthouse site in Hawaii that used P2V platform. The P2V was much less resistant to wind than the P3P which was used to map most of the sites. As mentioned earlier, Site 1 was also the first site where the team implemented image collection with a UAV. Thus, this point is an outlier of the data shown, but also highlights the effect of technology, pilot experience, and environmental conditions on the time required to survey a site. Similarly, Site 18 required more time to map relative to its area and GSD. This was because the site included a bridge that failed due to scour. Bridges are much more dimensionally complex than the other mapped sites and requires a greater flight time to effectively document with images.

3.2.2 Delineation of Landslide Geometry:

Satellite imagery can be used to map landslide events and coarsely relate volume, stratigraphic unit, and slope angle. For example, Roback et al. (2018) used satellite images to map approximately 25,000 landslides caused by the 2015 Gorkha earthquake. UAV-based surveys were conducted of individual landslides, listed in Table 3-2, to better understand the mechanical properties of the material, post-failure geometry, and failure mechanisms. In general, it is unlikely

that pre-failure geometry is known in detail. Geometry may be coarsely estimated from pre-failure satellite imagery, airborne LiDAR survey, or recent regional UAV survey if the data is available.

For the landslide sites in Table 3-2, the UAV was manually flown and the camera was operated by the pilot. GCPs, generally about 3-8 in total, were placed at accessible locations. The distances between these GCP targets were measured manually and tagged using a handheld GPS unit. The GCP targets are easily detected in imagery and, usually, in 3D point clouds. A tripod-mounted laser was also used to measure the distance between points-of-interest on the landslides as described earlier in this chapter. The rate of frame extraction from videos varied to maintain at least 60% overlap depending on the velocity of the UAV and the distance to the object of interest. The SfM software Pix4D was then used with the final image sets to generate 3D point clouds of each site. Figure 3-13 through Figure 3-15 show an example of landslide geometry acquisition at a landslide in Nepal (Site 4 in Table 3-3). Figure 3-13 shows an overview of the landslide where the debris cone has been identified and highlighted with boundaries. Four GCPs were distributed at the toe of the landslide and on the debris cone and are shown in Figure 3-14. Additional points were acquired by tripod-mounted laser. Following the collection of images and generation of the 3D point cloud, the model was used to delineate stratigraphy of the landslide in 3D. The landslide scarp exposes the rock mass structure over an area that was approximately 40 m high and 45 m wide. An example cross-section through the center of the landslide scarp is shown in Figure 3-15. The cross-section is annotated with stratigraphy interpreted from the UAV-collected imagery and the 3D point cloud. From the point cloud, the thickness of each layer is measured spatially and can be combined with rock mass characterization as discussed in the following subsection. The slope is angled at about 70° from the horizontal. However, the top 5 m of the slope was angled at about 50°. The debris cone was sloping at about 35°. It can be noted from Figure 3-15 that no information

below the debris cone is available. This means that there is significant uncertainty about the slope geometry behind the cone.

Information about the obstructed landslide geometry can be garnered from pre-failure documentation. But, as previously mentioned, pre-failure geometry may not be available or of sufficient resolution. In that case, *in situ* testing is needed to estimate geometry, such as landslide deposit thickness. Performing *in situ* tests on a landslide is dangerous and costly due to the limited resources, topography, and risk of subsequent failure. These conditions are a motivating factor for the UAV-based seismic surface wave testing performed in Chapter 5. Figure 3-16 shows satellite images of a landslide caused by the 2006 Kiholo Bay earthquake in Hawaii. This site is the Small Awini Landslide listed in Table 3-1. Images were collected using a P2V UAV. The survey was performed in two stages: first, large scale images were collected of the landslide scarp and deposit, then images were collected at higher resolution of the landslide scarp to observe the stratigraphy and weathering condition of the rock. The images collected of the landslide scarp were used to assess the structure of the rock mass. It was observed, and can be seen in Figure 3-17, that there is distinct layering in the rock. Closer inspection of the rock reveals that the layering alternates in terms of structure and weathering condition. The layers alternate between blocky, less-weathered rock, to highly-weathered, disintegrated rock. More discussion of rock mass characterization is provided in the following subsection. A seismic survey was also performed on the landslide deposit near the UAV launch point. The landslide runout was significant, but the shear wave velocity profile acquired from the seismic survey can provide some indication of the deposit thickness at that location. Figure 3-18 shows the 3D point cloud of the landslide and the location of the seismic survey performed on the deposit. The shear wave velocity profile is shown in Figure 3-19. The shear wave velocity profile has a significant velocity jump (about 100%) at 6 m depth. This depth

can be interpreted as a potential rough estimate of the deposit thickness at this location. It is desirable to perform many *in situ* tests distributed across the landslide deposit to thoroughly map its subsurface geometry and reduce uncertainty when estimating the deposit thickness. However, in this case, the positioning of the lone seismic survey was precarious and further testing could not be conducted due to the steep, dangerous terrain. This is a limitation often faced when documenting landslides and other earthquake-affected sites and is, again, a motivating factor behind developing UAV-based *in situ* testing methods.

3.2.3 3D Rock Mass Characterization:

Multiple frameworks exist for performing visual interpretations of rock masses. For example, the International Society of Rock Mechanics (ISRM) has developed and maintained a visual classification system (*e.g.* ISRM, 1978). Figure 3-20 shows an example rock mass segmented and classified based on the ISRM rock mass description grades. The grades focus on descriptions of the weathering condition and structural state of the rock mass. Unfortunately the grades are difficult to relate to strength parameters for use in stability analyses. Hoek and Brown (1980) developed a failure criterion for broken-up rock masses. The failure criterion was developed to model the strength of rock masses in the absence of discontinuity-controlled failure modes. One component of the Hoek and Brown failure criterion is the Geological Strength Index (GSI). The GSI is a critical parameter for the geomechanical characterization of the rock mass structure. It is only a function of the rock structure and the weathering condition of discontinuities as interpreted from visual observations. The guidance chart for assigning GSI values from Marinos et al. (2005) is shown in Figure 3-21.

The Marinos et al. (2005) procedure for assigning GSI values to a rock mass was applied to the Nepal landslide site (Site 4 in Table 3-3) discussed in the previous subsection and shown in Figure 3-13 through Figure 3-15. The slide is indicative of a broken-up rock mass failure that should be mechanically characterized as Hoek and Brown strength material. The 3D point cloud was generated from 257 images of the site. The point cloud has a mean resolution of 6 cm/pixel. The UAV was flown at two distances, roughly 30 m and 70 m, away from the landslide to collect images perpendicular to the scarp. The UAV was flown as close as 15 m above the debris cone. After the stratigraphy was investigated in the 3D point cloud, each layer was characterized to denote discontinuities in the rock mass and overall rock structure. Figure 3-22 shows a photo of the landslide scarp. It can be observed that the surface layer at the top of the slope was approximately 5 m thick and was primarily a combination of soil and extremely weathered rock. The remainder of the exposed rock can be separated into two categories. A shallow layer, between about 5 m and 15 m from the top of slope comprised of more weathered rock with dominant horizontal foliation. This layer classifies as disintegrated rock per Figure 3-21. According to visual observations, the GSI for this layer is estimated to be 25 - 45. Horizontal fractures are spaced at 0.4 – 0.8 m throughout the layer. The next layer is approximately 15 m from the top of the slope to the base. However, it should be noted that the rock mass and its geometry is partially obstructed by the debris cone. This second layer is less broken-up rock with perpendicular vertical and horizontal fracturing aligned with the slope face. This section of the rock mass classifies as blocky per Figure 3-21. The GSI for this layer is estimated to be 45 - 65. The spacing of vertical fractures is 0.3 – 0.9 m and the spacing of horizontal fractures is 2 – 3 m. Figure 3-23 shows a spatial delineation of the described GSI allocations overlain on the point cloud. Beyond about 40 m from the top of slope the rock structure is hidden by the slide debris, as mentioned above. A portion of

rock was exposed near the top of the debris cone and indicated dominant horizontal foliation. The exposed rock was located adjacent to the upslope GCP shown in Figure 3-14. The persistence of this foliation cannot be confirmed without excavation and further investigation of the slope.

Using only the data and results for a SfM reconstruction of the site, critical components for a stability analysis can be acquired including the surface geometry and compositional strength parameters along the 3D surface. Some basic information is missing and would need to be acquired from *in situ* testing. For Site 4 in Table 3-3, the surface geometry and GSI of the rock were estimated based on UAV-collected images. To continue with a stability analysis, it would be necessary to have information on how the visible stratigraphy changes as it is projected back into the rock behind the landslide, or an indication of how rock integrity improves behind the exposed outcrop. This is information that could be garnered from UAV-based seismic imaging which is investigated in Chapter 5. With the additional information to construct a complete strength model and identify subsurface structure, a back-analysis of the slope failure (given pre-failure geometry) can be performed. Additionally, stability calculations could be performed to predict future failure of the new slope geometry. Marinos et al. (2005) provides guidance on projecting GSI estimates below outcropping rocks and the effects of moisture. It can typically be expected that degree of fracturing and discontinuity weathering will decrease behind the exposed rock surface. However, in a reconnaissance effort, the exposed rock structure is unlikely to have experienced accelerated weathering. Moisture negatively affects discontinuities and thus reduces GSI. The Hoek et al. (2002) failure criterion is defined in equation 3-3:

$$\sigma'_1 = \sigma'_3 + \sigma_{ci}\left(m_b \frac{\sigma'_3}{\sigma_{ci}} + s\right)^a \tag{3-3}$$

Where σ_1 and σ_3 are the major and minor principal stresses respectively at failure, σ_{ci} is the intact compressive strength of the rock, a is a rock mass constant that is a function of GSI, s is a rock

mass constant that is a function of GSI and disturbance factor D, and m_b is a rock mass constant that is a function GSI, D, and m_i (m_i is a constant describing the material and structure, typically 7-25). The disturbance factor penalizes the material strength based on blasting and excavation conditions. The disturbance factor has not yet been extended to account for the effects of major seismic events. Hoek-Brown failure criterion using the Hoek et al. (2002) recommendations are shown in Figure 3-24 where the principal stresses are normalized by the intact compressive strength. Curves are shown for the two rock structures identified in Figure 3-23 using their mean GSI allocation and approximate upper and lower bounds for m_i. The mean GSI values are used as an example. In practice, the GSI is imprecise and a range of values should be considered (*i.e.* Figure 3-23). Estimated values for m_i and σ_{ci} could be acquired through additional testing of the material, such as physical interaction by a UAV in the redefined reconnaissance paradigm in Chapter 1 and potentially, in the future, predictive methods derived from high-resolution imaging.

The final point cloud model of the rock-slope had a mean resolution of 6 cm/pixel. In general, features in the rock structure smaller than 6 cm could not be observed. It is possible that additional discontinuity sets exist but are not visible in the imagery. Areas of higher and lower resolution exist within the model and are dependent on the flight parameters and path taken to collect the images. Because of the limited point cloud density, some features that can be resolved in 2D images cannot be detected in the 3D point cloud. These include foliation and fractures with small spacing relative to the point cloud resolution. This highlights the need for high-resolution imagery of landslide rock masses while balancing the risk involved in executing such flights. It should be noted that for measuring many of these discontinuities, color, in addition to 3D point position is utilized. This means that in many cases discontinuities were detected based on observed changes in color. This implies some reliance on the accompanying 2D images for delineating

discontinuities and rock features in the point cloud. In order to detect discontinuities based on the position of 3D points, a higher density, higher resolution point cloud would be required.

A SfM 3D model can also be used to describe landslides with structurally-controlled failures. Site 5 in Table 3-3 was a structurally-controlled failure caused by the 2015 Gorkha earthquake. The failure occurred on an approximately 150 m high slope angled at roughly 65° from horizontal. A point cloud overview of the rockslide is shown in Figure 3-25. Based on visual observations made from the ground and from the UAV, the landslide appeared to have exhibited a multimode failure. The slide is defined by a shallow failure of a broken-up rock mass overlain by soil up-slope from a wedge type failure. The distribution of GCPs and laser points collected at this site are shown in Figure 3-26. The collection of up-slope laser points was difficult at this site due to the spatial constraints at the base of the slope. The UAV collected images from 40-80 m away from the landslide scarp near the top of the slope. The UAV's camera was positioned 10-15 m away when imagery was collected of the wedge-type failure. This allowed for improved detail in the images of the rock structure at this critical location.

The spacing and orientation of discontinuities were observed in 2D images and subsequently measured in the point cloud. The layer located in the top 12 m of the slope was comprised of soil and extremely weathered rock. A weathering profile is apparent with a decreasing degree of weathering down the slope. At the site if the failed wedge, the visible rock structure is dominated by foliation with a strike of 255°, dipping at 20° to the northwest, shown in Figure 3-27. The wedge failure occurred at approximately one third of the slope height, about 50 m. The source of the wedge failure is shown in Figure 3-28. A large block of the material was observed within the debris which most likely originated from the failed wedge. The rock in the area of the wedge failure had few vertical fractures and appeared to be strictly governed by

foliation. The foliation was also visible in some sections of the 3D model due to the imagery collected 10-15 m away from the wedge. By referring back to Figure 3-3 earlier in the chapter, it can be observed that imagery collected with the P3P from 40-80 m has a GSD of approximately 2 - 3.5 cm/pixel and imagery collected from 10 – 15 m away has a GSD of approximately 5 mm/pixel. The mean resolution of this model was 1.2 cm/pixel. In the sections of the model where the greatest resolution imagery was used, small features and discontinuities are visible. At the initiation of making field observations at this site, the existence of the wedge failure 50 m upslope was not yet confirmed until UAV imagery was collected. Additionally, the failure of cover soil and broken-up, extremely weathered rock near the top of the slope was not visible until investigated via UAV.

3.3 Summary of Lessons Learned from Aerial Surveying of Geotechnical Sites

Based on the UAV surveying performed as part of this study, recommendations are provided as guidance on using UAV-enabled SfM for geotechnical site reconnaissance.

Flight Planning: Flight parameters should be clearly outlined prior to executing a flight. The flight plan should consider the required image resolution, battery capacity, visibility of targets, and any potential change to operational conditions (*e.g.* other aircraft, wildlife). GCPs should be placed to cover all areas which will be surveyed. The GCPs and checkpoints should be placed, or selected, in areas that will be reliably visible in the point cloud. More GCPs and check points than necessary should be measured to account for potential inaccessibility in the point cloud. Several considerations must be made when estimating the flight time required at a site. Automated flights can be accurately estimated based on specific path that will be followed. Pilot experience, environmental conditions, and UAV technology will all affect flight time, especially for manual

flights. Frameworks for basic automated flights to conduct surveys are available on most commercial platforms. However, current frameworks are not adequate for surveying areas with relatively significant elevation change, complex 3D geometry, or high-resolution image collection for analyzing small features. Advances in flight planning and obstacle avoidance technologies are expected to improve automated survey capabilities. This is of particular interest when collecting very high-resolution imagery for assessing small objects such as structural fasteners, rock discontinuities, and soil particle sizes. The required image resolution, and therefore flight parameters, is highly-dependent on the specific application. In general, at least 2 - 3 pixels per feature (*e.g.* fracture) are necessary to view in imagery. To assess grain sizes in soil or narrow fracturing in a rock, image resolution of 1 – 5 mm/pixel will likely be necessary. If only the major discontinuities in a rock mass are of interest, lower resolution imagery, 2 – 10 cm/pixel will typically be appropriate. Continuing novel research and development of UAVs integrating range detection and collision avoidance (*e.g.* Lidar, infrared, sonar, and stereo-vision) are making UAVs more accessible to these applications.

Weather: Monitoring of weather conditions must be monitored including precipitations, temperature, and wind. Few commercial platforms capable of handling precipitation, or even high-moisture, environments exist. Most multirotor platforms are highly-susceptible to precipitation, particularly due to overexposure of motors which are often necessary for heat dissipation. Low temperatures can influence the measurements made by critical IMU sensors and have a significant impact on battery performance. Some of the newest platforms are equipped with battery warmers which can raise the battery temperature to a safe level prior to flight. However, the warmers also consume energy. Windy conditions affect UAV stability and flight endurance. Stability is typically most affected by gusting wind. However, at very high payloads even low wind can cause

instability. This is because the UAV cannot commit additional power to resisting the wind force. It may also be necessary to consider that the UAV may hold in a tilted position while resisting wind. This may affect operations depending on the payload and operations being performed. Most weather conditions which bear consideration affect the UAV flight performance and sensor mechanics. Weather conditions will also affect the quality of data collected. For example, sunlight and its positioning will influence collected imagery. As mentioned previously, luminance-invariant features make SfM robust to basic changes in lighting, but dark shadows can still affect results. Sunlight will also affect imagery data used for other analyses, such as those discussed later in this chapter. An overcast day with moderate light is preferred.

Reconnaissance: It has been demonstrated that UAVs are powerful tools for documenting site geometry by collecting images for use in SfM model generation. However, during the course of reconnaissance efforts the UAV was found to be a useful tool for decision making and fundamental understanding of specific sites. At a debris flow site in Nepal, the UAV was used to investigate the source of debris flow material. The UAV mission was not part of the original site investigation plan and the results of the mission fundamentally changed the interpretation of the debris flow event. The perspective provided by the UAV can be used to identify features that would not normally be visible to a person on the ground or may not be clear from satellite imagery. For example, while investigating a 150 m high landslide, the multimode nature of the failure was not immediately obvious to reconnaissance personnel on the ground. The failure modes and documentation of a failed wedge were only confirmed once investigated using a UAV. The UAV is useful for collecting imagery at dangerous sites such as steep landslide deposits. However, in order to produce a high-accuracy model, a distribution of GCPs are necessary which, with current technology, requires them to be placed by a person at the site. Autonomous methods for performing

all required operations in dangerous scenarios are needed to optimize the safety of personnel and data quality (*e.g.* Greenwood et al., 2018).

Table 3-1: Sites in Hawaii surveyed by UAV

Site	Location	Description
Kauhola Point Lighthouse	N20° 14.770' W155° 46.280'	6-10 m tall eroding sea cliff.
Sapphire Cove	N20° 09.733' W155° 53.906'	Complex rock structure on coastline.
Cobble Beach	N20° 09.622' W155° 53.897'	Beach covered in basalt cobbles
Small Awini Landslide	N20° 11.612' W155° 43.355'	Shallow landslide caused by 2006 Kiholo Bay earthquake.
Large Awini Landslide	N20° 10.950' W155° 43.694'	Deep landslide caused by 2006 Kiholo Bay earthquake.

Table 3-2: Sites in Nepal surveyed by UAV

Site	Location	Description
Debris Flow	27° 57' 11.6" N 85° 32' 41.6" E	Debris fan of rainfall-mobilized landslide debris.
Rockfall	27° 57' 48.6" N 85° 32' 3.0" E	Construction site damaged by rockfall.
Landslide 1	28° 10' 48.8" N 85°19' 56.8" E	Goldzong landslide near Syapru Besi.
Landslide 2	28° 1' 28.3" N 85° 11' 26.5" E	Failures on vertical cliff with waterfall.
Landslide 3		Grouped landslides on Trishuli River.
Landslide 4	27° 56' 26.1" N 85° 33' 5.3" E	Two roadside landslides outside of Timbu.
Landslide 5	28° 0' 34.6" N 85° 10' 56.6" E	Adjacent rainfall and coseismic landslides.
Landslide 6	27° 57' 53.0" N 85° 32' 27.0" E	Landslide north of Timbu.
Landslide 7	27° 57' 29.6" N 85° 32' 27.8" E	Landslide near debris flow site.
Landslide 8	27° 55' 59.8"N 85° 33' 24.5" E	Roadside landslide between Timbu and Melamchi.
Landslide 9	27° 56' 39.8" N 85° 32' 59.7" E	Soil Terrace south of Timbu.
Landslide 10	27° 50' 39.9" N 85° 35' 0.0" E	Soil terrace near Melamchi
Landslide 11	27° 59' 58.2" N 85° 11' 3.2" E	Landslide along Trishuli River near Betrawati.
Landslide 12	27° 56' 48.1" N 85° 32' 56.7" E	Soil terrace near Timbu.
Landslide 13	27° 50' 50.5" N 85° 35' 14.2" E	Broken-up failure and finer-grained landslide near Melamchi.
Landslide 14	27° 56' 27.5" N 85° 33' 13.0" E	Structurally-controlled failure south of Timbu.
Landslide 15	27° 43' 49.9" N 85° 37' 50.1" E	Soil Terrace and deep landslide along Idrawati River.

Table 3-3: Selected sites mapped using UAV-enabled SfM

Site ID	Site Description	Location	Total Flight Duration, (min:sec)	Approximate Camera Distance from Target (m)	3D Area (m^2)	Average GSD (cm/pixel)
1	Cliff	Hawaii, USA	60	10	700	0.4
2	Cobbles	Hawaii, USA	8	6	345	0.2
3	Coastline	Hawaii, USA	9:00	13	1320	0.4
4	Rockslide 1	Nepal	5	40	3500	1.7
5	Rockslide 2	Nepal	10	28	10000	1.2
6	Complex or Rockslides	Nepal	9	200	329100	10.8
7	Terrace failure	Nepal	4	20	1400	0.9
8	Debris flow	Nepal	13:26	57	60700	2.5
9	Rockfall sloped area	Lefkada, Greece	38:50	114	1223160	5.0
10	Egkremnoi Landslide Area	Lefkada, Greece	41:10	143	637000	6.3
11	Platys Yalos Landslide 2	Lefkada, Greece	15	183	935835	6.9
12	Rockfall	Cephalonia, Greece	13:10	150	340900	7.1
13	Lixouri Port	Cephalonia, Greece	11:20	93	87300	3.9
14	Argostoli Port	Cephalonia, Greece	19:27	84	129000	3.9
15	Failed Campaneli	Cephalonia, Greece	11:40	10	154	0.5
16	Fault Rupture site	New Zealand	12	50	135600	2.3
17	Landslide site	New Zealand	28	94	654365	3.7
18	Scoured Bridge	Greece	30	18	5382	0.7
19	Irrigation Dam Collapse and flooded area mapping	Greece	70	62	390000	2.15
20	Anonymous Archaeological Site	Greece	125	61	759000	2.3
21	Retaining wall	Patras, Greece	9:20	40	30890	2.1
22	Levee	St. Louis, MO, USA	27	36	42000	1.6
23	Sub-urban area	Marousi, Greece	8	54	87344	1.7
24	Cliffed historical site	Chios, Greece	7	83.5	58000	2.15
25	Quarry	Penteli, Greece	10	55	72000	2.8
26	Moira landslide	Achaia Greece	40	120	790000	3.9

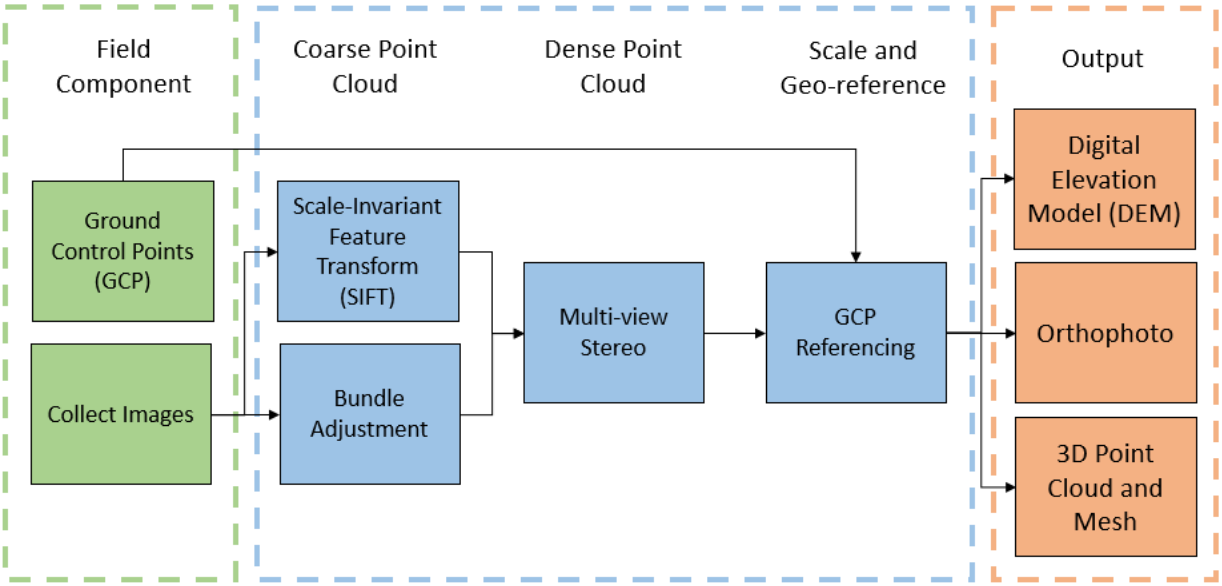

Figure 3-1: 3D imaging with SfM workflow

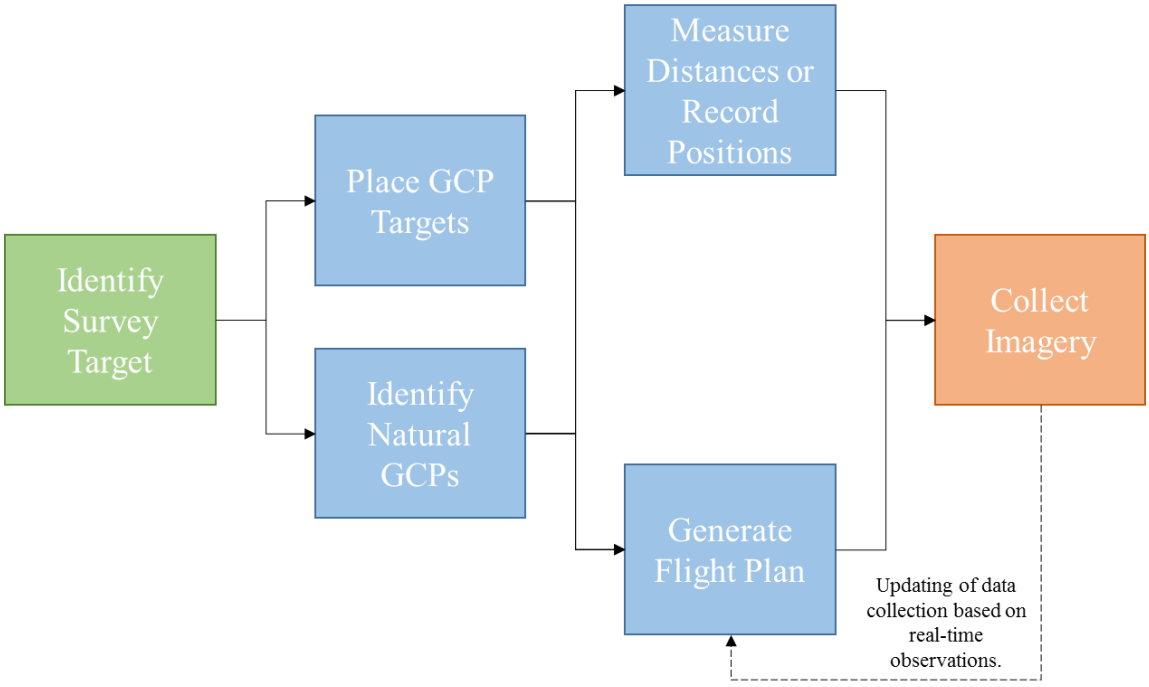

Figure 3-2: Procedure for performing geotechnical aerial survey

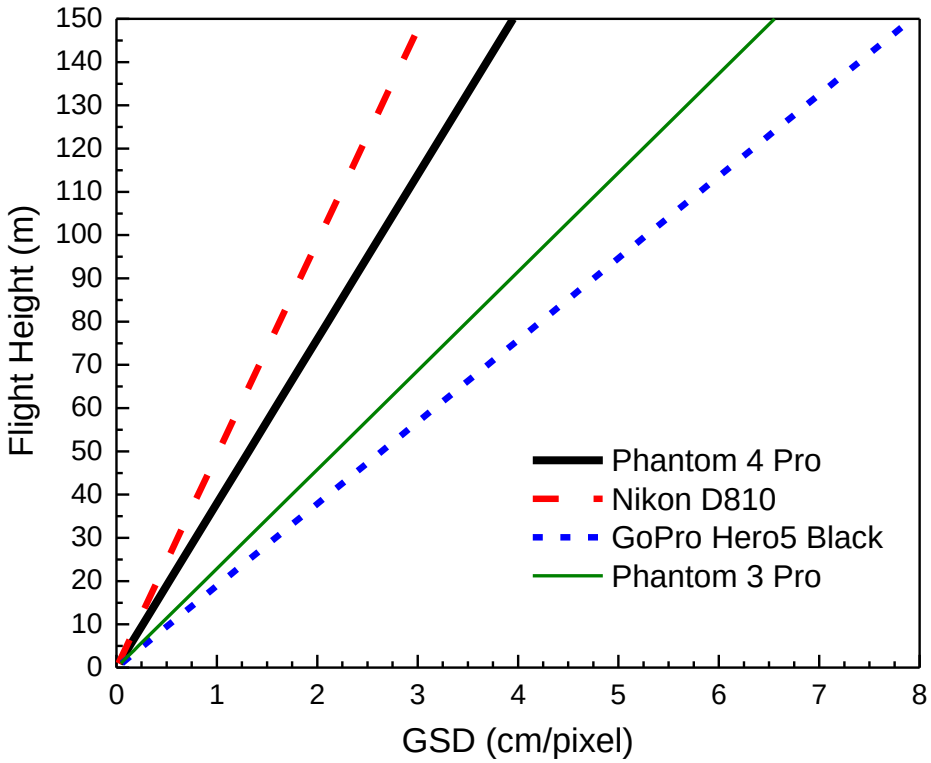

Figure 3-3: Maximum flight height to achieve GSD values for different cameras

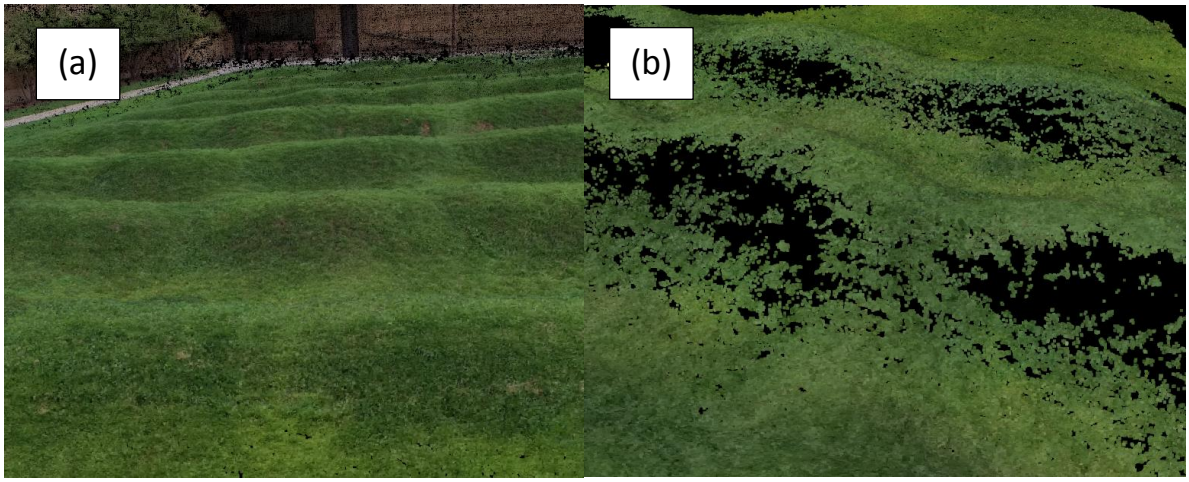

Figure 3-4: Grass-covered wavefield (crests are approximately 2 m apart) 3D point cloud produced with (a) oblique images and (b) without oblique images

Figure 3-5: Example of GCP visible in a UAV-collected image

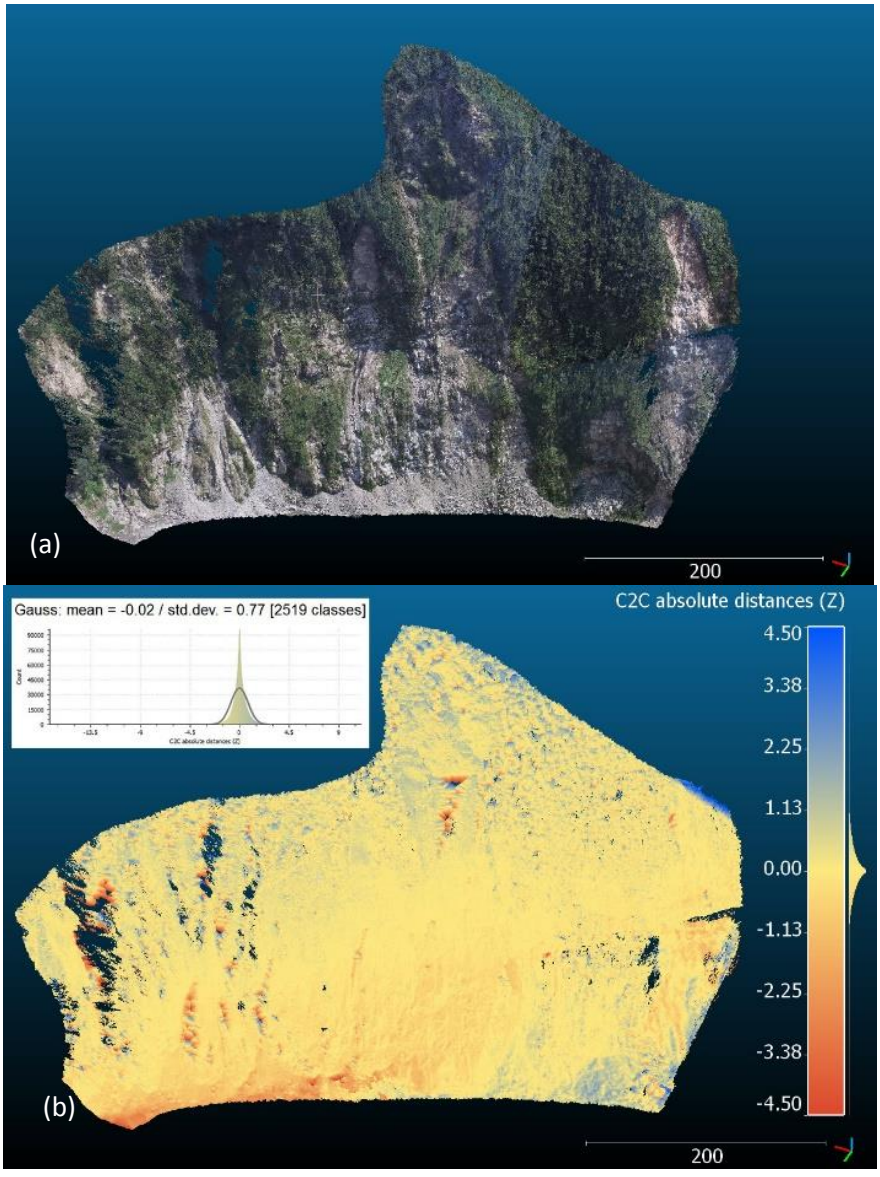

Figure 3-6: (a) SfM 3D point cloud (in meters) and (b) cloud-to-cloud distance comparison between UAV-SfM and terrestrial LiDAR

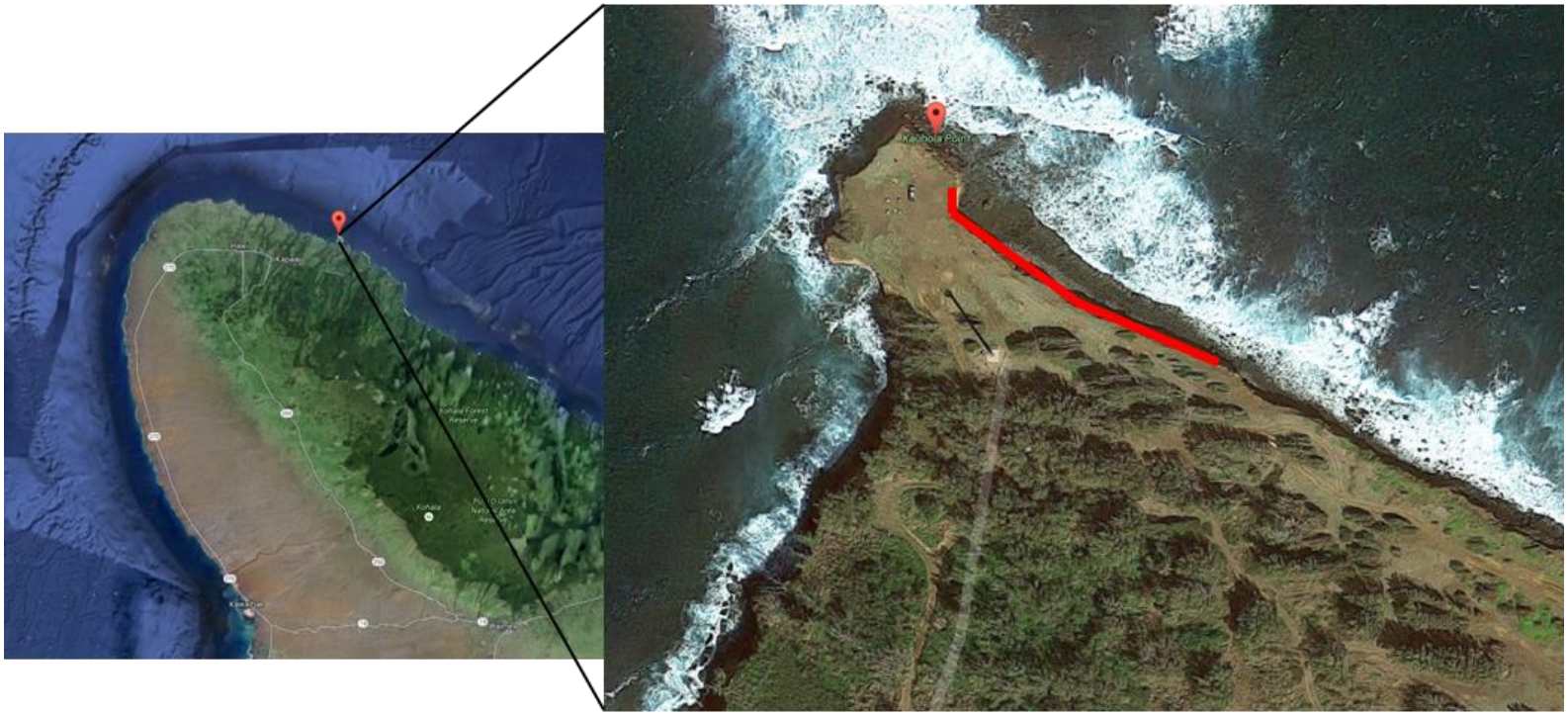

Figure 3-7: Satellite image of Kauhola Point with red line indicating survey area

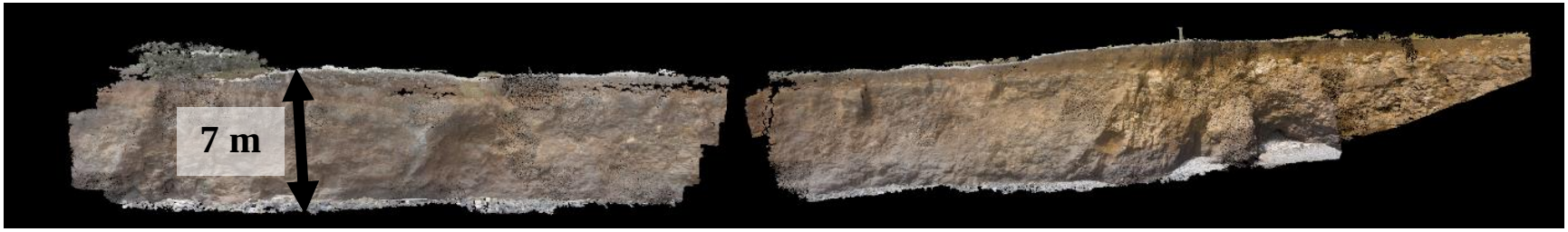

Figure 3-8: Disjointed 3D model of eroding Kauhola Point cliff

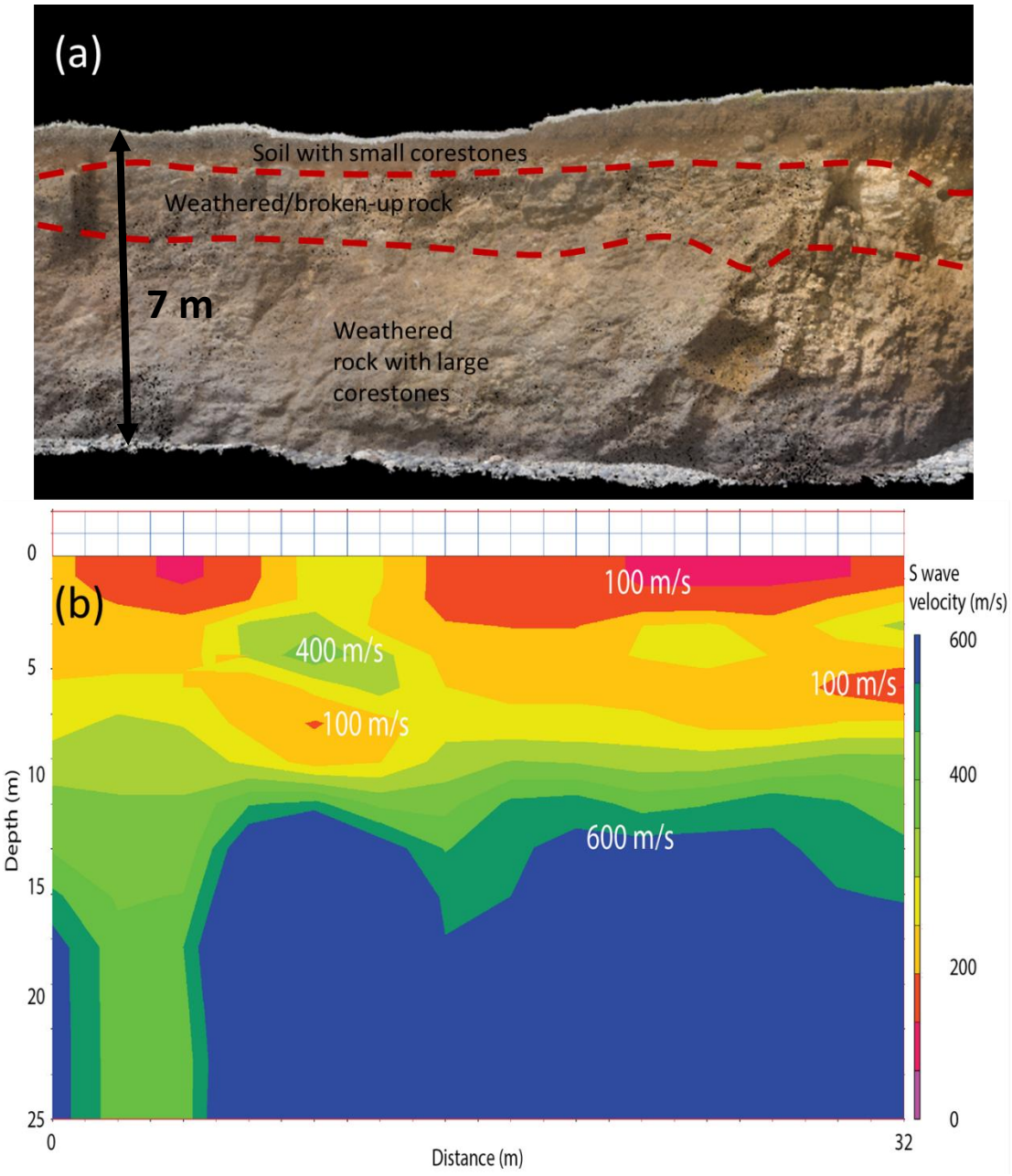

Figure 3-9: (a) Stratigraphy interpretation from 3D model and (b) 2D Vs profile

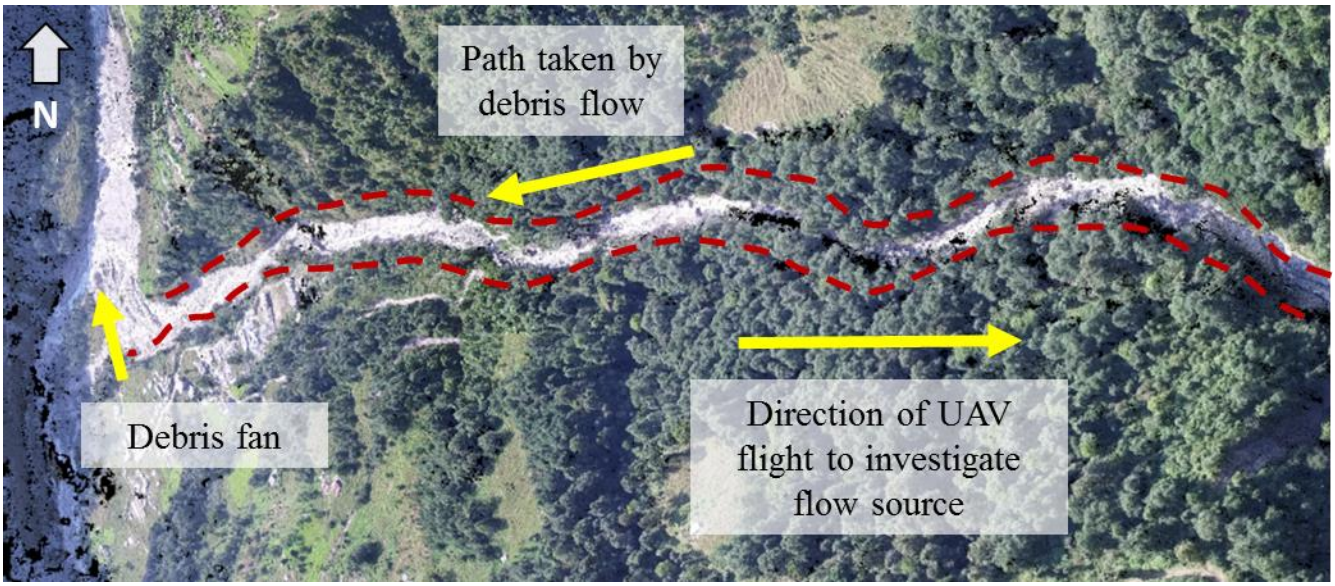

Figure 3-10: Channel followed by UAV to investigate source of debris flow

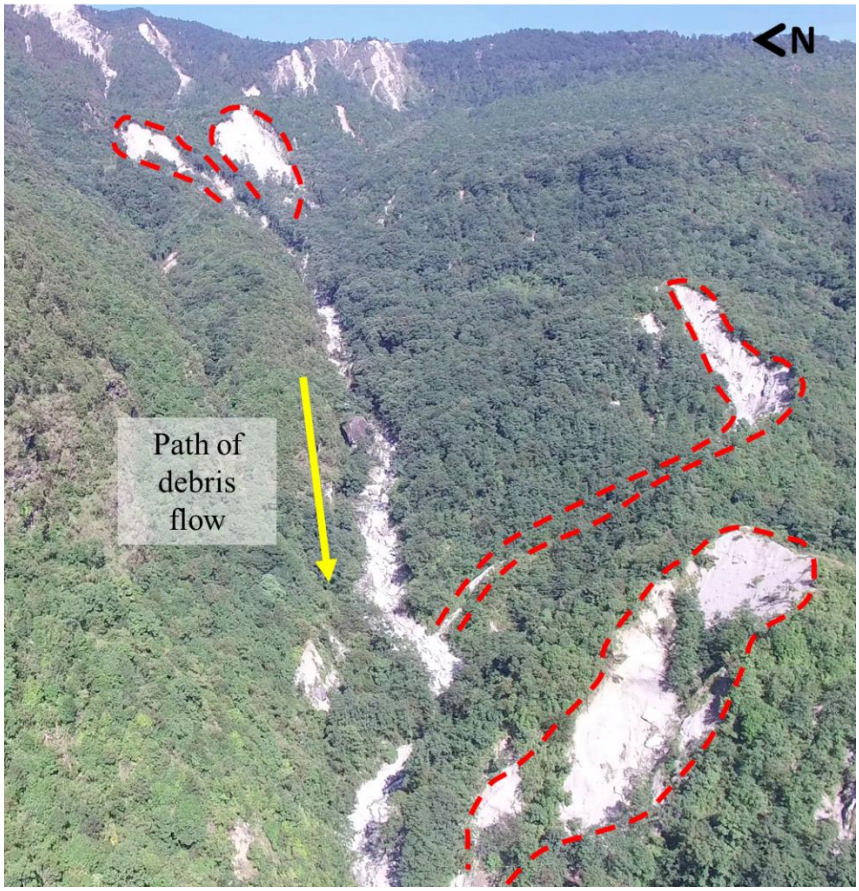

Figure 3-11: Debris flow sources identified by UAV reconnaissance

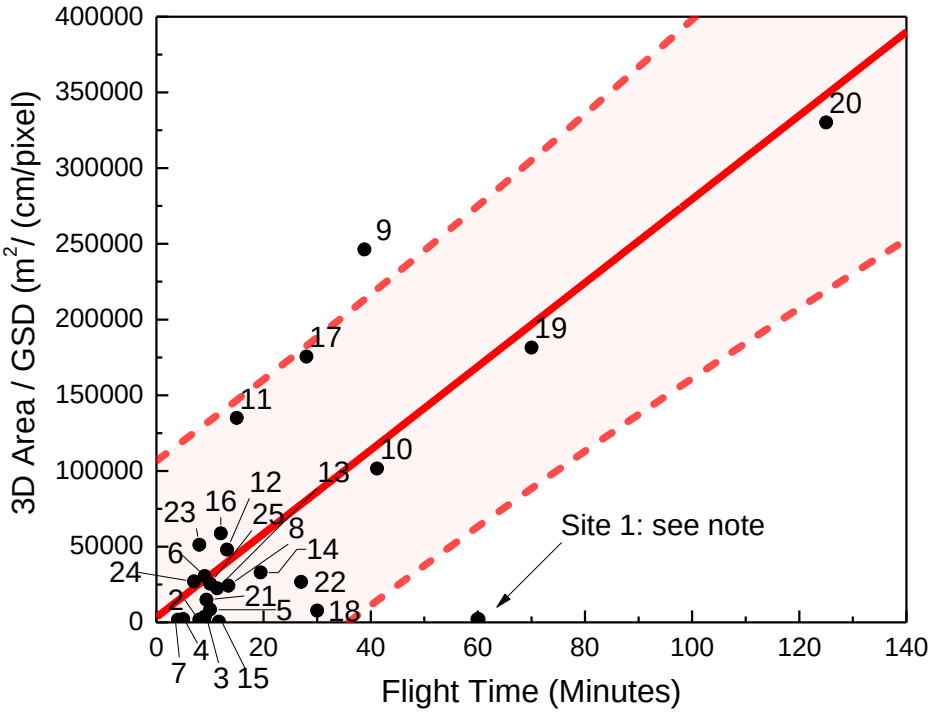

Figure 3-12: Survey area normalized by GSD as a function of flight time for aerial surveys of 26 different sites

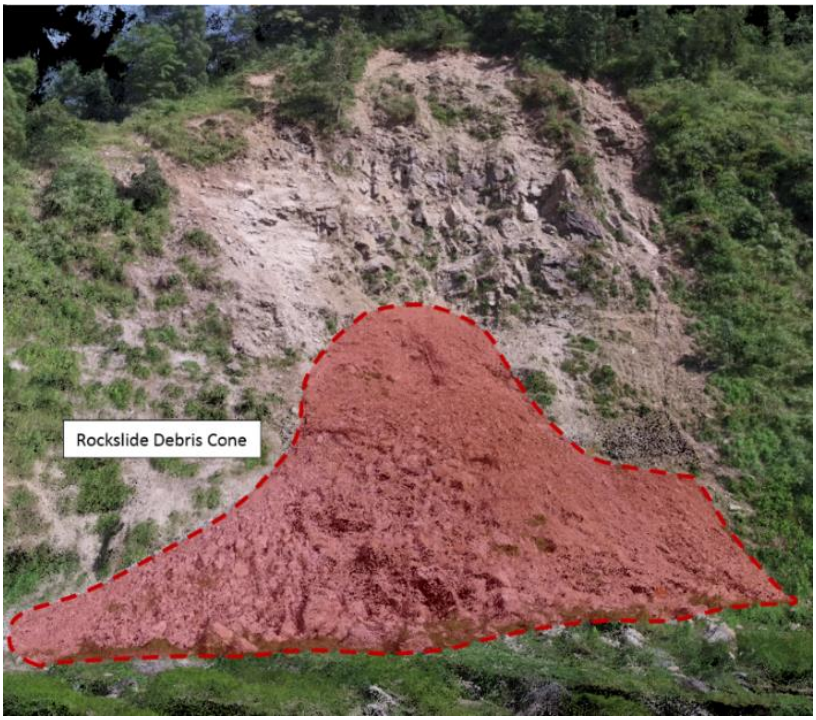

Figure 3-13: Point cloud overview of landslide with debris cone delineated

Figure 3-14: GCPs placed at the landslide toe

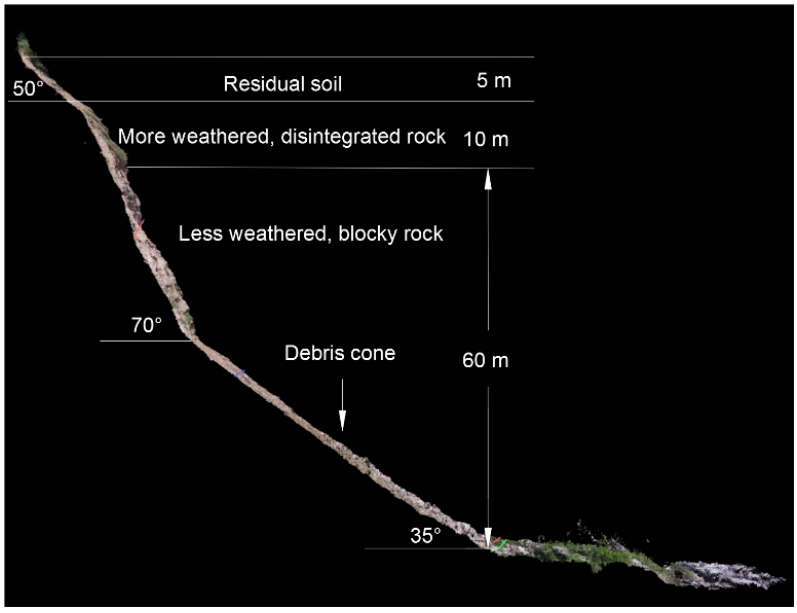

Figure 3-15: Cross-section through centerline of the landslide and annotated with point cloud measurements

Figure 3-16: Satellite images of Small Awini Landslide (a) about 1 month after the 2006 Kiholo Bay earthquake and (b) in January 2014

Figure 3-17: UAV-collected image at top of landslide scarp showing alternating stratigraphy

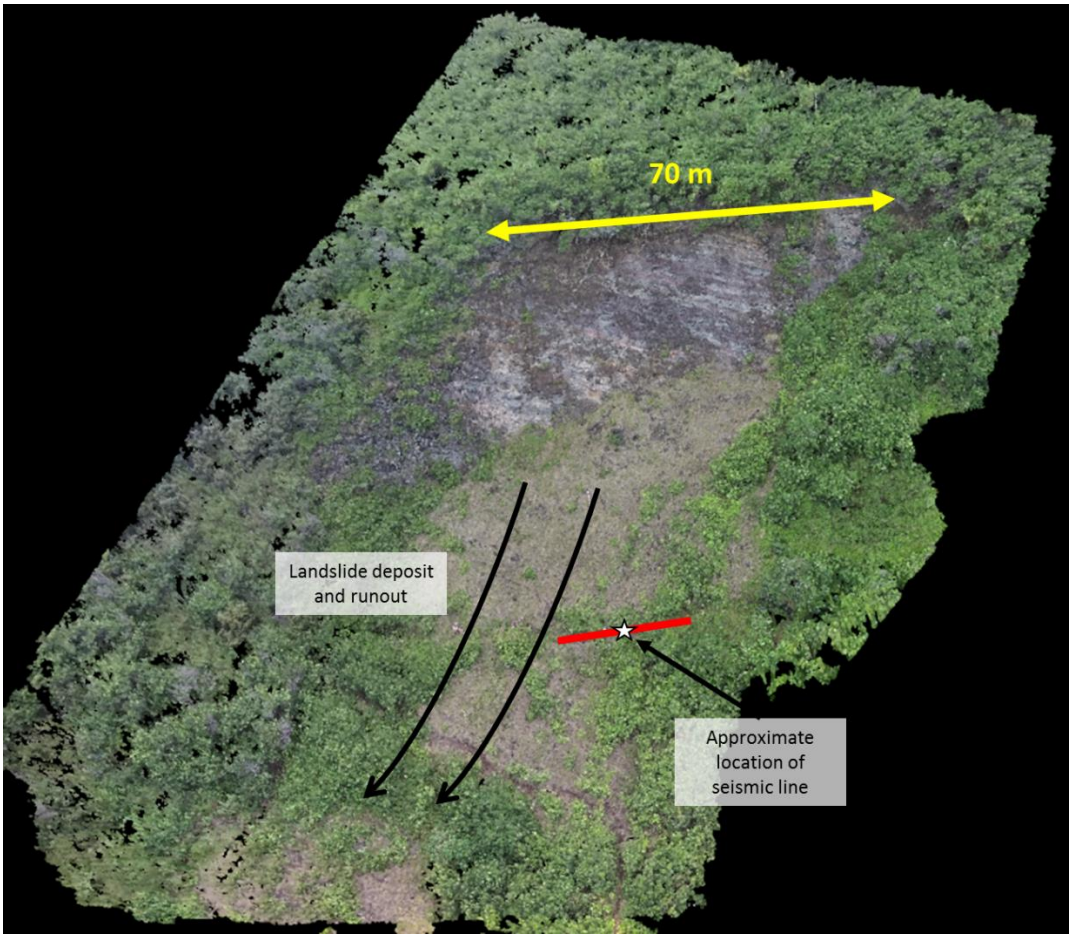

Figure 3-18: Location of shear wave velocity profile on landslide deposit

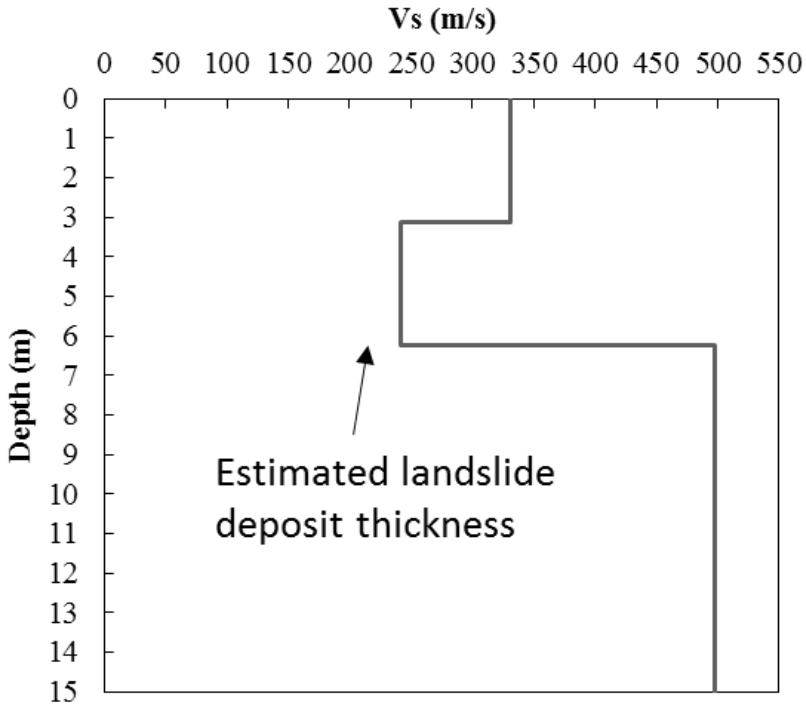

Figure 3-19: Shear wave velocity profile on landslide deposit

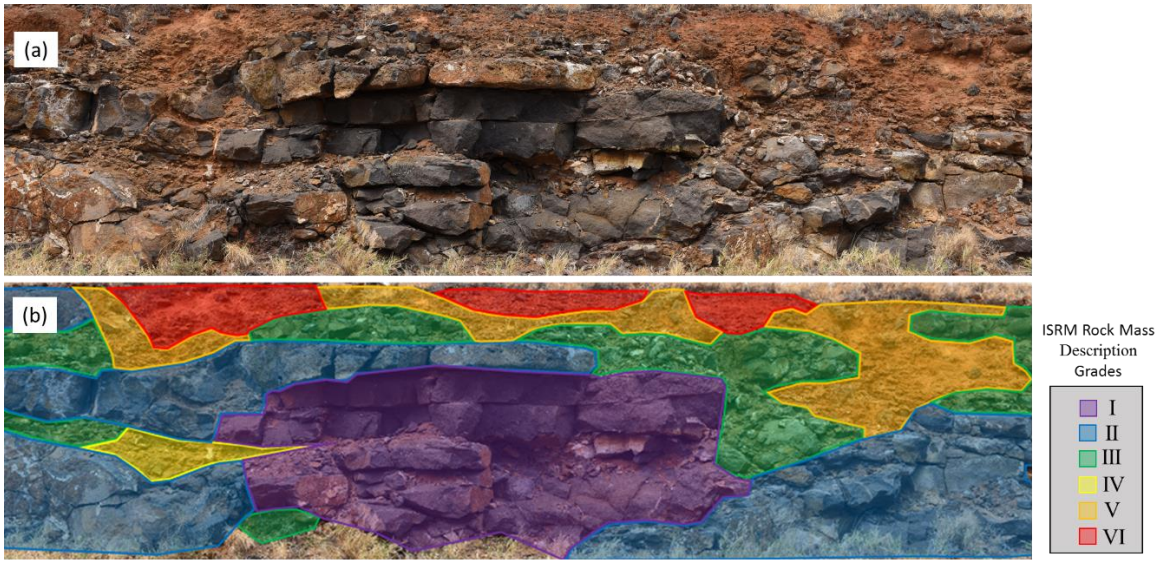

Figure 3-20: Example of visual rock mass classification using the ISRM (1978) approach applied to a 4 m vertical cut

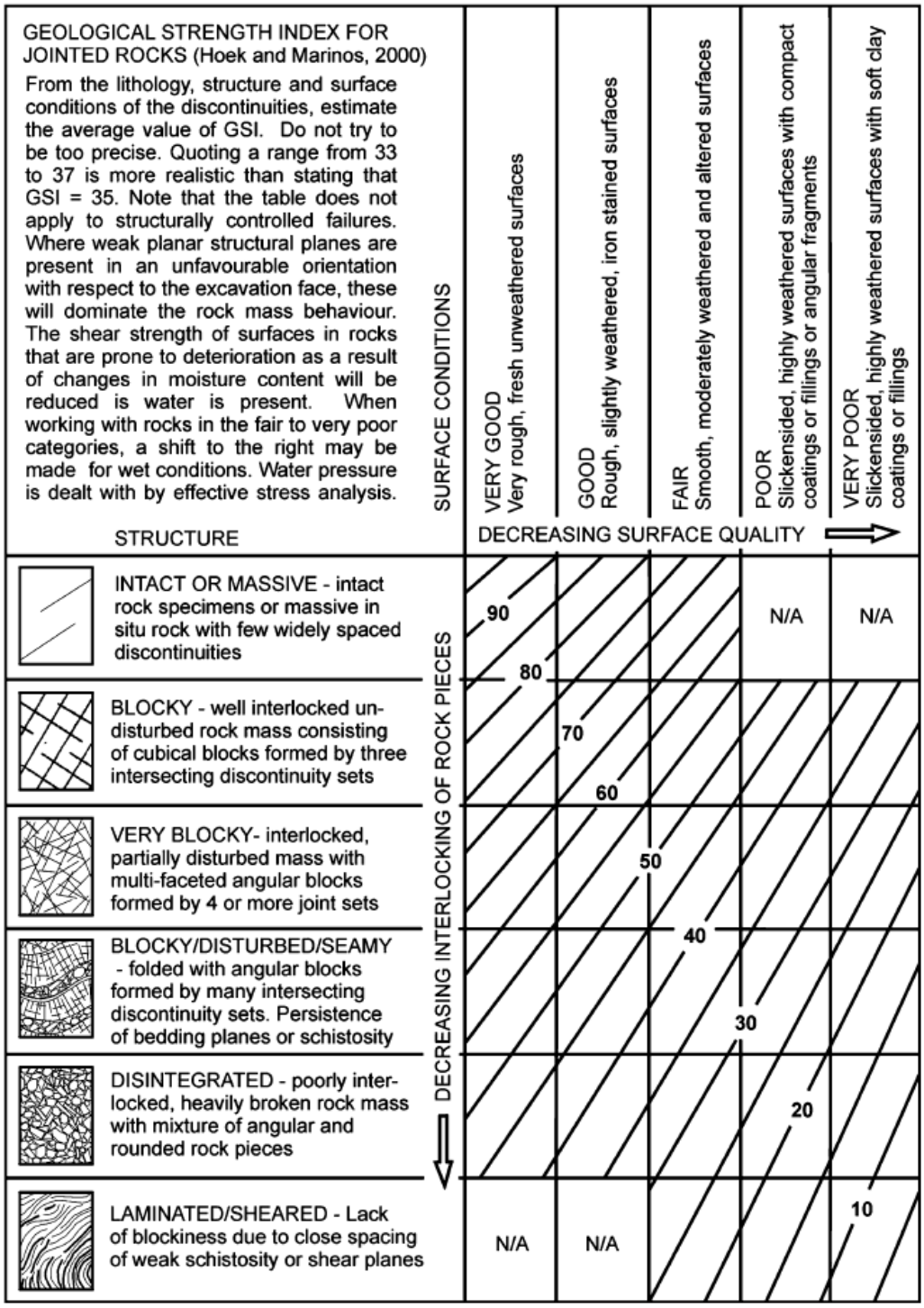

Figure 3-21: Chart used to assign GSI values for a rock mass (from Marinos et al., 2005)

Figure 3-22: Photo of landslide back-scarp revealing weathering profile

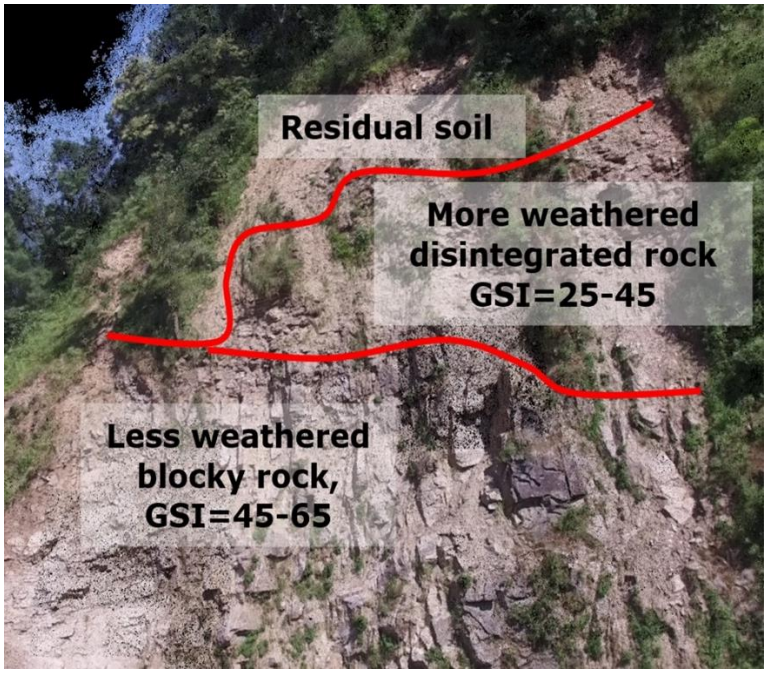

Figure 3-23: Spatial GSI allocation on landslide scarp

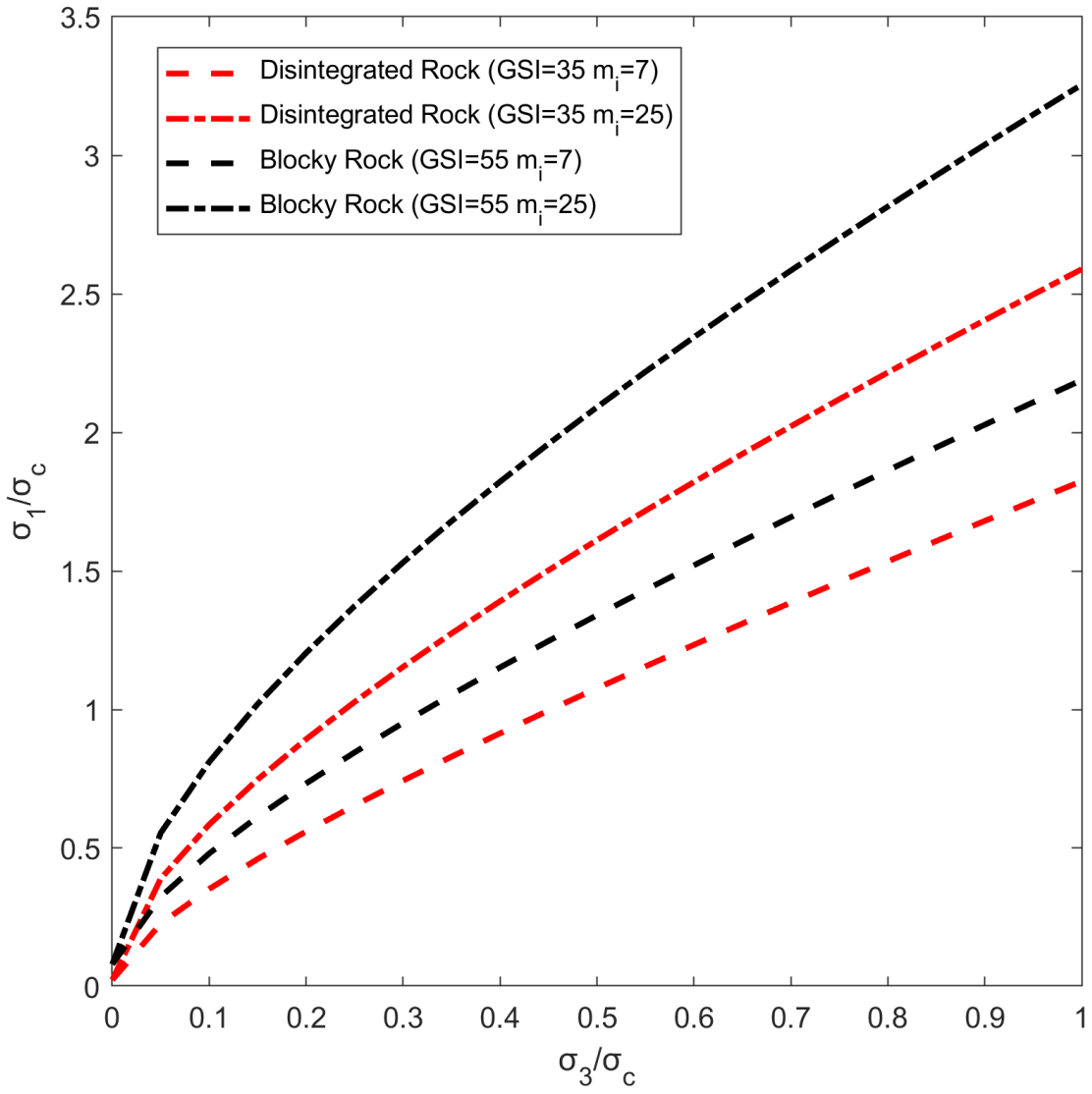

Figure 3-24: Hoek-Brown failure criterion using information derived from SfM data and point cloud

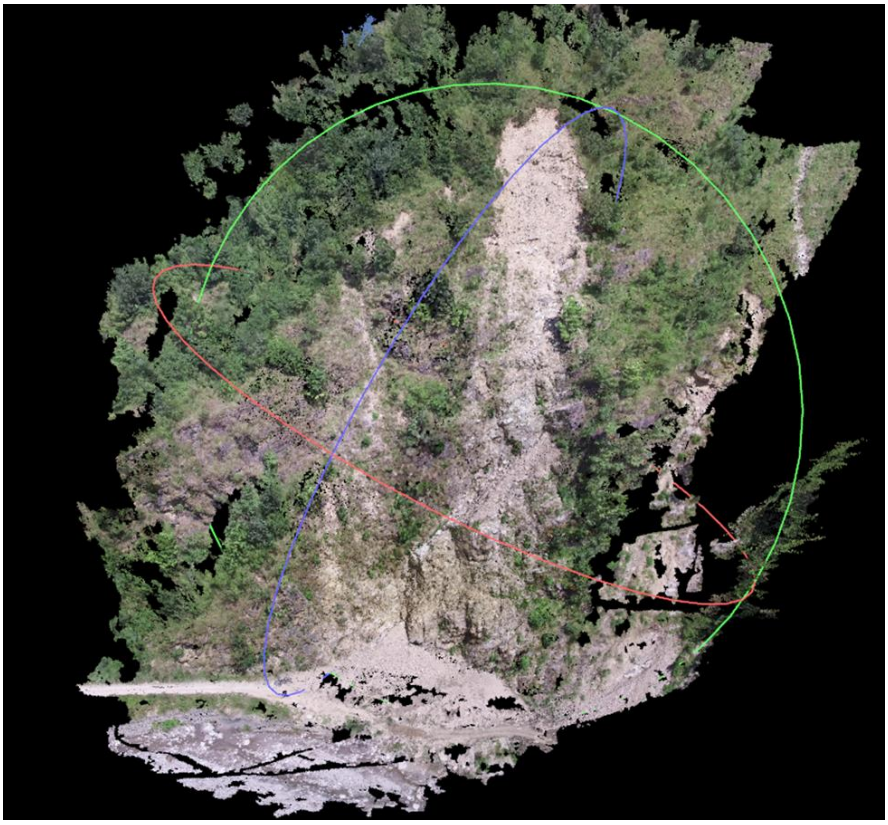

Figure 3-25: Point cloud overview of structurally-controlled landslide

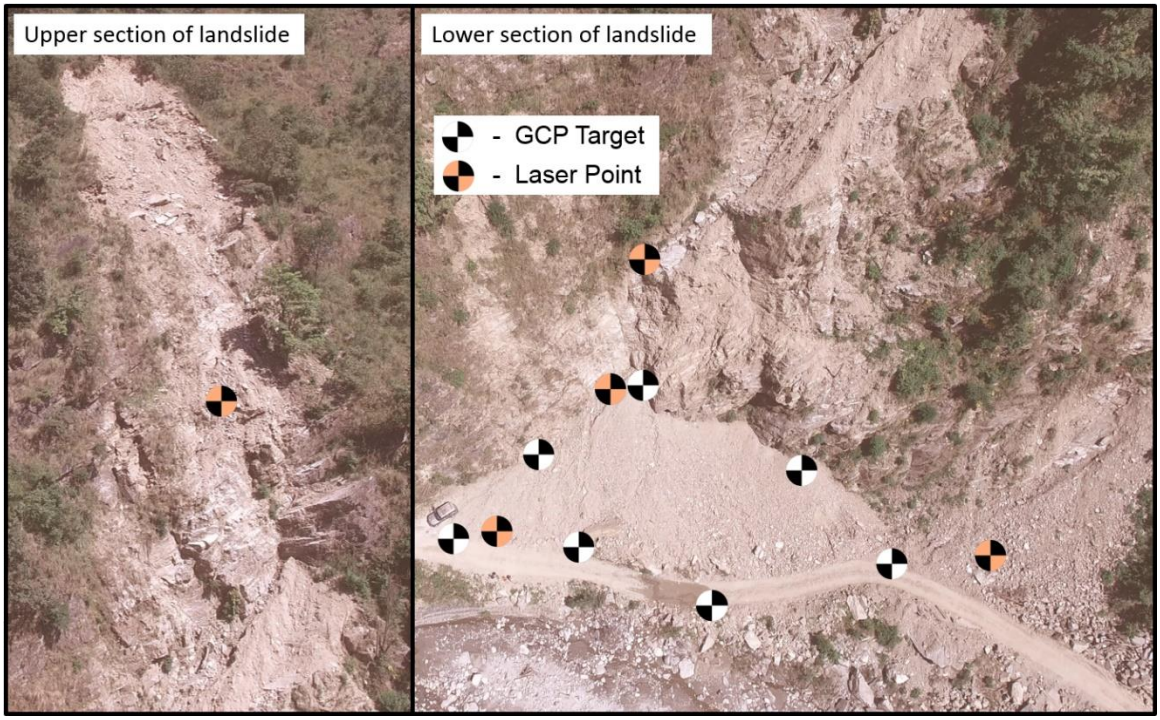

Figure 3-26: Distribution of GCP and laser points used for SfM scaling

Figure 3-27: Illustration of foliation controlling failure and measurement location in 3D point cloud

Figure 3-28: Structurally-controlled, wedge failure observed about 50 m upslope

3.4 References

Bemis, S. P., Micklethwaite, S., Turner, D., James, M. R., Akciz, S., Thiele, S. T., and Bangash, H. A. (2014). "Ground-Based and UAV-Based Photogrammetry: A Multi-scale, High-Resolution Mapping Tool for Structural Geology and Paleoseismology." *Journal of Structural Geology*, 69, 163-178.

Clark, M. K., S. Gallen, A. J. West, D. Chamlagain, K. Roback, K. Lowe, N. Niemi, W. Greenwood, J. Bateman, D. Zekkos. (2015). "Coseismic landslides associated with the 2015 Gorkha earthquake sequence in Nepal." (Invited) *Eos Trans., Fall Meet. Suppl.*, Abstract Session S42C-02.

Collins, B. D., and R. W. Jibson. (2015). "Assessment of existing and potential landslide hazards resulting from the April 25, 2015 Gorkha, Nepal earthquake sequence." U.S. Dept. of the Interior, U.S. Geological Survey, Open-File Report 2015-1142, August 2015.

Cook, K. L. (2017). "An evaluation of the effectiveness of low-cost UAVs and structure from motion for geomorphic change detection." *Geomorphology*, 278, 195-208.

Furukawa, Y., and Ponce, J. (2007). "Accurate, Dense, and Robust Multi-View Stereopsis." *Proceedings, IEEE Conference on Computer Vision and Pattern Recognition (CVPR)*, 17–22 June, Minneapolis, USA, pp. 1–8.

Furukawa, Y., Curless, B., Seitz, M., and Szeliski, R. (2010). "Clustering View for Multi-View Stereo." *Proceedings, IEEE Conference on Computer Vision and Pattern Recognition (CVPR)*, 13–18 June, San Francisco, USA, pp. 1434–1441.

Galetzka, J., D. Melgar, J. F. Genrich, J. Geng, S. Owen, E. O. Lindsey, X. Xu, Y. Bock, J.-P. Avouac, L. B. Adhikari, B. N. Upreti, B. Pratt-Sitaula, T. N. Bhattarai, B. P. Sitaula, A. Moore, K. W. Hudnut, W. Szeliga, J. Normandeau, M. Fend, M. Flouzat, L. Bollinger, P. Shrestha, B. Koirala, U. Gautam, M. Bhatterai, R. Gupta, T. Kandel, C. Timsina, S. N. Sapkota, S. Rajaure, and N. Maharjan. (2015). "Slip pulse and resonance of the Kathmandu basin during the 2015 Gorkha earthquake, Nepal." *Science*, 349, 1091-1095.

Gansser, A. (1964). "Geology of the Himalayas." Wiley Interscience, London.

Greenwood, W., Zekkos, D., Clark, M. K., Lynch, J. P., Bateman, J., and Chamlagain, D. (2016a). "UAV-Based 3-D Characterization of Rock Masses and Rock Slides in Nepal." *50th US Rock Mechanics/Geomechanics Symposium*, Houston, TX.

Greenwood, W. W., Zhou, H., Zekkos, D., and Lynch, J. (2018). "Experiments using a UAV-Deployed Impulsive Source for Multichannel Analysis of Surface Waves Testing." *Geotechnical Earthquake Engineering and Soil Dynamics V*, ASCE, Austin, TX.

Gruszczynski, W., Matwij, W., and Cwiakala, P. (2017). "Comparison of Low-Altitude UAV Photogrammetry with Terrestrial Laser Scanning as Data-Source Methods for Terrain Covered in Low Vegetation." *ISPRS Journal of Photogrammetry and Remote Sensing*, 126, 168-179.

Hashash, Y. M. A., Tiwari, B., Moss, R. E. S., Asimaki, D., Clahan, K. B., Kieffer, D. S., Dreger, D. S., Macdonald, A., Madugo, C. M., Mason, H. B., Pehlivan, M., Rayamajhi, D., Acharya, I., and Adhikari, B. (2015b). "Geotechnical Field Reconnaissance: Gorkha (Nepal) Earthquake of April 25 2015 and Related Shaking Sequence." *GEER Association Report No. GEER-040*, 7 August 2015.

Hoek E., and E. T. Brown. (1980). "Empirical strength criterion for rock masses." *J. Geotech. Engng. Div., ASCE* 106(GT9), 1013-1035.

Hoek, E., Carranza-Torres, C., and Corkum, B. (2002). "Hoek-Brown Failure Criterion – 2002

Edition." *Proc. NARMS-TAC Conference*, Toronto, 1, 267-273.
ISRM. (1978). "Suggested methods for the quantitative description of discontinuities in rock masses." *International Journal of Rock Mechanics and Mining Science & Geomechanics Abstracts*, 15, 319-368.
Jahanshahi, M. R., Chen, F. –C., Ansar, A., Padgett, C. W., Clouse, D., and Bayard, D. S. (2017). "Accurate and Robust Scene Reconstruction in the Presence of Misassociated Features for Aerial Sensing." *Journal of Computing in Civil Engineering*, 31(6), DOI: 10.1061/(ASCE)CP.1943-5487.0000702.
Kargel, J. S., G. J. Leonard, D. H. Shugur, U. K. Haritashya, A. Beyington, E. J. Fielding, K. Fujita, M. Geertsema, E. S. Miles, J. Steiner, E. Anderson, S. Bajracharya, G. W. Bawden, D. F. Breashears, A. Byers, B. Collins, M. R. Dhital, A. Donnellan, T. L. Evans, M. L. Geai, M. T. Glasscoe, D. Green, D. R. Gurung, R. Heijenk, A. Hilborn, K. Hudnut, C. Huyck, W. W. Immerzeel, J. Liming, R. Jibson, A. Kääb, N.R. Khanal, D. Kirschbaum, P. D. A. Kraaijenbrink, D. Lamsal, L. Shiyin, L. Mingyang, D. McKinney, N. K. Nahirnick, N. Zhoutong, S. Ojha, J. Olsenholler, T. H. Painter, M. Pleasants, K. C. Pratima, Q. I. Yuan, B. H. Raup, D. Regmi, D. R. Rounce, A. Sakai, S. Donghui, J. M. Shea, A. B. Shrestha, A. Shukla, D. Stumm, M. van der Kooij, K. Voss, W. Xin, B. Weihs, D. Wolfe, W. Lizong, Y. Xiaojun, M. R. Yoder, and N. Young. (2016). "Geomorphic and geologic controls of geohazards induced by Nepal's 2015 Gorkha earthquake." *Science*. 351, DOI: 10.1126/science.aac8353.
Le Fort, P. (1986). "Metamorphism and magnetism during the Himalayan collision." *Geological Society, London*, Special Publications. 19.1, 159-172.
Lowe, G. D. (1999). "Object Recognition from Local Scale-Invariant Features." *International Conference on Computer Vision*, Corfu, Greece, pp. 1150-1157.
Lowe, G. D. (2004). "Distinctive Image Features from Scale-Invariant Keypoints." *International Journal of Computer Vision*, 60(2), pp. 91-110.
Manousakis, J., Zekkos, D., Saroglou, F., and Clark, M. (2016). "Comparison of UAV-Enabled Photogrammetry-Based 3D Point Clouds and Interpolated DSMs of Sloping Terrain for Rockfall Hazard Analysis." *Int. Arch. Photogramm. Remote Sens. Spatial Inf. Sci.*, XLII-2/W2, 71-77, DOI: 10.5194/isprs-archives-XLII-2-W2-71-2016.
Marinos V., P. Marinos, E. Hoek. (2005). "The geological strength index: applications and limitations." *Bull. Eng. Geol. Environ.*, 64, 55-65
Meng, X., Currit, N., and Zhao, K. (2010). "Ground Filtering Algorithms for Airborne LiDAR Data: A Review of Critical Issues." *Remote Sensing*, 2, 833-860.
Moss, R. E. S., E. M. Thompson, D. S. Kieffer, B. Tiwari, Y. M. A. Hashash, I. Acharya, B. R. Adhikari, D. Asimaki, K. B. Clahan, B. D. Collins, S. Dahal, R. W. Jibson, D. Khadka, A. Macdonald, C. L M. Madugo, H. B. Mason, M. Pehlivan, D. Rayamajhi, and S. Uprety. (2015). "Geotechnical effects of the 2015 magnitude 7.8 Gorkha, Nepal earthquake and aftershocks." *Seismological Research Letters*. 86(6), 1514-1523.
NSET. (2015). National Society for Earthquake Technology – Nepal. 25 May 2015, < http://www.nset.org.np/eq2015/>.
Pirotti, F., Guarnieri, A., and Vettore, A. (2013). "Ground Filtering and Vegetation Mapping using Multi-Return Terrestrial Laser Scanning." *ISPRS Journal of Photogrammetry and Remote Sensing*, 76, 56-63.
Pix4D. (2017), "Pix4Dmapper 3.2 User Manual." *Version 3.2*, Pix4D SA.
Roback, K., Clark, M. K., West, A. J., Zekkos, D., Li, G., Gallen, S. F., Chamlagain, D., and Godt,

J. W. (2018). “The Size, Distribution, and Mobility of Landslides Caused by the 2015 M_W7.8 Gorkha Earthquake, Nepal.” *Geomorphology*, 301, 121-138.

Robertson, J., and H. Koontz. (2015). “Magnitude 7.8 earthquake in Nepal and Aftershocks.” 12 May 2015, <http://www.usgs.gov/blogs/features/usgs_top_story/magnitude-7-8-earthquake-in-nepal/>.

Schelling, D. (1992). “The tectonostratigraphy and structure of the eastern Nepal Himalaya.” *Tectonics*, 11(5), 925-943.

Siebert, S., and Teizer, J. (2014). “Mobile 3D Mapping for Surveying Earthwork Projects Using an Unmanned Aerial Vehicle (UAV) System.” *Automation in Construction*, 41, 1-14.

Snavely, N., Seitz, S. M., and Szeliski, R. (2008). “Modeling the World from Internet Photo Collections.” *International Journal of Computer Vision*, 80(2), 189-210.

Stumpf, A., Malet, J.-P., Kerle, N., Niethammer, U., and Rothmund, S. (2013). “Image-based Mapping of Surface Fissures for the Investigation of Landslide Dynamics.” *Geomorphology*, 186, 12-27.

Tong, X., Liu, X., Chen, P., Liu, S., Luan, K., Li, L., Liu, S., Liu, X., Xie, H., Jin, Y., and Hong, Z. (2015). “Integration of UAV-Based Photogrammetry and Terrestrial laser Scanning for the Three-Dimensional Mapping and Monitoring of Open-Pit Mine Areas.” *Remote Sensing*, 7, 6635-6662.

Von Voigtlander, J., Clark, M. K., Zekkos, D., Greenwood, W. W., Anderson, S. P., Anderspn, R. S., and Godt, J. W. (2018). “Strong variation in weathering of layered rock maintains hillslope-scale strength under high precipitation.” *Earth Surface Processes and Landforms*, https://doi.org/10.1002/esp.4290.

Westoby, M. J., Brasington, J., Glasser, N. F., Hambrey, M. J., and Reynolds, J. M. (2012). “‘Structure-from-Motion’ Photogrammetry: A Low-Cost, Effective Tool for Geoscience Applications.” *Geomorphology*, 179, 300-314.

Zekkos, D., Clark, M., Whitworth, M., Greenwood, W., West, J., Roback, K., Li, G., Chamlagain, D., Manousakis, J., Quackenbush, P., Medwedeff, W., and Lynch, J. (2017). “Observations of landslides caused by the April 2015 Gorkha earthquake in Nepal based on land, UAV and satellite reconnaissance.” *Earthquake Spectra*, 33(S4) S1-S20.

Zekkos, D., Manousakis, J., Athanasopoulos-Zekkos, A., Clark, M., Knoper, L., Massey, C., Archibald, G., Greenwood, W., Hemphill-Haley, M., Rathje, E., Litchfield, N., Medwedeff, W., Van Dissen, R. J., Ries, W., Villamor, P., Langridge, R. M., and Kearse, J. (2018). “Structure-from-Motion Based 3D Mapping of Landslides & Fault Rupture Sites during 2016 Kaikoura Earthquake Reconnaissance.” *Eleventh U.S. National Conference on Earthquake Engineering*, 25-29 June, Los Angeles, CA.

CHAPTER 4

Processing of UAV-Derived 2D and 3D Imagery Outputs for Rock Mass Characterization

In this chapter, image processing techniques have been developed using UAV-enabled imagery as input with the goal of characterizing rock mass structure. The aim is to leverage the results of SfM 3D modeling to better characterize site conditions in geotechnical engineering practice with a focus on semi-automatic or automatic processing routines. It is envisioned that these computations will be executed on-board the UAV in the future and used for field decisions. The 3D model developed using SfM provides a wealth of information; 3D geometry is one piece of information that is extracted from the image set to produce outputs which are useful for qualitative and quantitative observations and to inform further data collection and for quantitative analysis. In Chapter 3, 3D point clouds were used to manually identify discontinuity sets and their orientations which is essential for stability analyses of these rock masses. In addition to manual procedures, semi-automated procedures for identifying and analyzing 3D point clouds of rock masses exist, but have significant limitations (Lato and Vöge, 2013; Vasuki et al., 2014; Riquelme et al., 2015; Chen et al. 2016 among others). In general, it is computationally intensive to operate in 3D. In some cases it may be more efficient to operate in 2D and relate back to 3D, as necessary. For example, fractures visible in 2D images may not be apparent in 3D because the 3D models always have a lower resolution than the source imagery.

First, a fracture detection method for rocks, that can be fully- or semi-automated, for 2D images is developed and presented. The fracture detection performance is assessed on three image sets representative of different image types and sources. Next, the SfM point cloud is projected onto an image plane to provide information on the depth of certain points and features. The re-projection of the point cloud onto an image generates a color-depth image (*i.e.* RGBD). To leverage the incorporation of 3D information to the image, an updated version of the simple linear iterative clustering (SLIC) algorithm for segmenting the RGBD images has been developed. The depth images contain information from other camera perspectives, which is important for verifying results from 2D images of complex 3D structures. The updated SLIC algorithm is then synthesized with results produced by the fracture detection algorithm to map pixels identified as fractures in 2D for further 3D analysis (*i.e.* identification of discontinuity sets via plane segmentation).

4.1 Development of a 2D Fracture Detection Algorithm

In this section, a fracture detection algorithm was developed for the purpose of mapping the distribution of fractures in images of rock masses for assessing strength properties and identifying discontinuity sets. Many crack detection algorithms have been designed for use with concrete structures and pavements (Jahanshahi and Masri, 2013; Torok et al., 2014; Wu et al., 2014; Jiang and Tsai, 2015; Valença et al., 2017 among others). In general, concrete crack detection algorithms are designed to accurately and robustly delineate cracks on flat surfaces with minimal change in color or texture, and high contrast between the crack and concrete. These conditions are uncommon when assessing rocks. It is also desirable to extract information from images that may have relatively low resolutions due to being collected far away from the target (*i.e.* by UAV), which most crack detection algorithms are not designed for. Some recent crack

detection algorithms designed for concrete structures and pavements are shown in Table 4-1. Recent examples of discontinuity detection and analysis in rocks focus on fully- or semi-automated processes in 3D imaging outputs (*e.g.* point clouds) are also shown in Table 4-1. Chen et al. (2016) used a variation of K-means to cluster in a DSM and then optimized the segmentation and fit planes using random sample consensus (RANSAC) to acquire discontinuity set orientations. Discontinuities are identified based on exposed surfaces in the rock mass and are grouped accordingly. If discontinuity surfaces are not clearly exposed or cannot be simplified as a plane, they will not be detected. Lato and Vöge (2012) similarly detected discontinuities based on exposed planar surfaces using an automated method. The approach used point clouds to find planar surfaces considered natural discontinuities in the rock mass and intentionally ignored unnatural fractures, such as those caused by blasting. Riquelme et al. (2015) improved on previously-developed approaches to defining discontinuity sets and estimating their spacing. All 3D points were classified relative to discontinuity sets and each set was fit by parallel planes. Persistence of fractures was ignored but could potentially be considered depending on the user application. These example methods from the literature focus on identifying sets of discontinuities in exclusively 3D datasets. The relative advancements in operating on 3D data sets have outpaced 2D image processing approaches for discontinuity assessment in recent years due to the growing popularity of SfM in geosciences and the desire to robustly estimate discontinuity set orientations in 3D. The referenced procedures perform well for accurately quantifying the spacing and orientation of discontinuity sets that are clearly discernable in 3D point clouds and DSMs. As observed in Chapter 3 when performing manual discontinuity set interpretations, there is visual information contained in the source imagery that is not captured in the 3D point cloud or DSM. Additionally,

it may be impractical or uneconomic to collect imagery at such a high resolution to resolve complete planes in a DSM, particularly in post-earthquake reconnaissance.

The purpose of developing the method proposed in this section is to perform computationally efficient fracture detection on images of various rock masses and of varying resolutions that may be encountered by UAV-based data collection. It will also be demonstrated that the proposed method is easily integrated with established computer vision methodologies and workflows. The method described in this section attempts pixel-wise identification of fractures in rock masses. The fractures can, when SfM or equivalent 3D modeling is performed, be related back to the 3D point cloud and used to augment other discontinuity analysis procedures, such as those in Table 4-1. The semi-automated fracture detection procedure is outlined starting with an input image in Figure 4-1. The basic procedure computes the image gradient, estimates a gradient threshold, detects candidate fractures, and then performs morphological filtering to help remove false positives. The procedure can be fully-automated, or semi-automated by manually updating control parameters or activating optional algorithm components. The optional components for noise removal are a Gaussian filter and a modified version of Otsu's threshold (Otsu, 1979). The advantages and disadvantages of applying the filter and conditions where the modified Otsu's threshold is beneficial are discussed after the base algorithm is described.

For implementation, the fully-automated procedure is recommended for real-time processing of sub-images, or specific image segments. This is recommended because image processing is computationally intensive and dramatically affected by image size, and the control parameters may need to be adjusted for different parts of the image especially if the image covers a large area (*e.g.* site orthophoto). While the computations performed in these algorithms are rapid and fairly robust, the subsequently discussed segmentation operations applied to full-size images

take significantly more computational effort. For large, full-size images, the complete, semi-automated approach is recommended as a post-processing methodology.

The fracture detection method is prepared for integration with other 2D and 3D processing methods. Figure 4-2 shows the framework followed where the 2D fracture detection process is synthesized with 3D information, when available, to analyze rock surface roughness and the characteristics of individual fractures detected in 2D images as discussed later in this chapter. When RGBD images from SfM are available, pixels classified as fractures coinciding with depth (*i.e.* 3D) points can be transformed back to 3D and merged with the existing 3D point cloud. This means that binary fracture classification is applied to the 3D points. Manual measurements of discontinuity orientation and spacing, as performed in Chapter 3, can then be performed. Alternatively, the fracture-labeled point cloud can be combined with 3D processing techniques such as the discontinuity analyses discussed previously.

4.1.1 Image Gradient

The gradient of an image describes the pixel-wise change in intensity in some direction across an image. Intensity is the numerical representation of light for a pixel. For example, in a 24-bit RGB image, the intensity of each color channel (*i.e.* red, green, blue) is a value on [0,255]. Each pixel is described by a vector containing the intensity of each color channel. When converted to grayscale, each pixel is described by a scalar which is the magnitude of the RGB pixel vector. Image gradients have many uses, including being the fundamental basis for many edge detection methods developed over several decades. Roberts (1963) developed one of the earliest gradient-based edge detectors. Other, more complex, edge detection methods have also been developed. The Canny edge detector (Canny, 1986) has been arguably the most popular edge detection

algorithm since its inception and sparked the development of similar edge detectors such as Deriche (1987).

The gradient of an image can be defined as the partial derivative of intensity with respect to the vertical or horizontal axis. As the basis for this fracture detection algorithm, the image gradient is approximated using central finite difference method. For an input image of arbitrary size, the vertical or horizontal gradient is estimated by convolving a central difference operator with the grayscale image. Equation 4-1 estimates the image gradient in the vertical direction (d_y) of a grayscale image (I).

$$d_y = \begin{bmatrix} 1 \\ 0 \\ -1 \end{bmatrix} * I \tag{4-1}$$

The gradient in the horizontal direction (d_x) can similarly be estimated by convolving the transpose of the kernel in equation 4-1 with the image. The two gradient images, vertical and horizontal, can be combined to provide the gradient magnitude (d) and direction (θ) in equations 4-2 and 4-3 respectively.

$$d = \sqrt{{d_x}^2 + {d_y}^2} \tag{4-2}$$

$$\theta = \tan^{-1}\left(\frac{d_y}{d_x}\right) \tag{4-3}$$

Gradient values that exceed a certain threshold become classified as an edge and are candidates to be classified as fractures by the algorithm. Figure 4-3 shows examples of the gradient operations performed on a sample image.

4.1.2 Estimation of Gradient Threshold

Pixels are potentially classified as fractures if the gradient for a given pixel exceeds a threshold value. Effective selection of that threshold is critical for the fracture detection process.

For example, Figure 4-4 shows the effect of two different gradient thresholds for classifying pixels as potential fractures. It is possible to iteratively find a threshold value by manually checking a range of values, but it is desirable to perform a gradient selection automatically. Automatic selection of a gradient threshold is performed using the following method adapted from Groenewald et al. (1993) and Wang (2011):

1. Select initial threshold (T) guess (10 is recommended for most rock images).
2. Generate a pixel-wise binary map (b) based on the threshold.
    a. $b(x,y) = 1\ ,\ \forall\ x,y\ such\ that\ d(x,y) > T$
3. Calculate the mean gradients values of fracture (d_f) and background (d_b) pixels:
    a. $d_f = \frac{\sum d(x,y)}{\sum b(x,y)}\ ,\forall\ x,y\ such\ that\ b(x,y) = 1$
    b. $d_b = \frac{\sum d(x,y)}{\sum b(x,y)}\ ,\forall\ x,y\ such\ that\ b(x,y) = 0$
4. Estimate a new threshold as a linear combination of the mean gradient values:
    a. $T = k_f d_f + k_b d_b$ where $k_f + k_b = 1$
5. Return to Step 2 and repeat until threshold value converges.
6. Output vector of 10 potential thresholds within $T \pm 0.15T$

Figure 4-5 shows an example of automatic threshold selection applied to a photo of a brick wall. Figure 4-5a shows a photo of the brick wall and Figure 4-5b shows the brick wall with the gradient threshold (T=4.6) applied, note that pixels exceeding the threshold are black in this example (reverse of the detailed algorithm). Figure 4-5c shows the convergence of the automatic threshold selection on a value. When the final threshold value is estimated, a set of ten evenly spaced potential threshold values is considered within ±15% of the convergence value. Generally, the lowest threshold from this set is then used for fracture detection. This makes the fracture map

more sensitive to noise and as a result increases the false positive rate. However, many of the small false positives and noise can be removed through morphological filtering which is performed following initial pixel classification and described in a subsequent section. The set of potential threshold values is then used to create a multi-threshold fracture map where pixels are rated based on their relative likelihood of being a component of a fracture. The multi-threshold fracture map is not subjected to the subsequently discussed morphological filtering. A rating is assigned to each pixel proportional to the fraction of potential thresholds it meets. For example, for a set of ten potential thresholds, each pixel detected by the five lowest thresholds receives a rating of 0.5 (*i.e.* detected by 50% of the threshold values). The multi-threshold fracture map is not used directly for quantitative analysis, but is useful for making observations of the rock mass or on the sensitivity to the gradient threshold. Significant spatial changes in pixel rating are indicative of the image needing further manual, or automatic as discussed later, segmentation. Additionally, the multi-threshold fracture map could be used to manually select a threshold value from the output threshold vector, rather than using the lowest threshold value. Figure 4-6 shows an example image from a marble quarry and an annotated example of a multi-threshold fracture map. In Figure 4-6, white pixels were detected for 100% of the threshold values in $T \pm 0.15T$. The pixels become darker (gray) as they are detected in fewer of the threshold values. Black pixels are not detected using any of the thresholds.

The primary control parameter for the algorithm is the value of k_b, and by extension k_f. Lowering k_b will reduce the expected threshold for an image, and therefore increase the number of fracture candidate pixels. A starting value of $k_b = 0.3 - 0.4$ is suggested for most cases. A higher value (0.4 - 0.5) may be needed for bright images with widely spaced fractures. A value lower than 0.2 is not recommended because the threshold selection may not converge. Figure 4-7 shows the

effect of k_b on a sample image where green pixels have been classified as fracture. In Figure 4-7, the k_b value is lowest (0.2) for Figure 4-7a and increases to 0.5 in Figure 4-7d. In Figure 4-7a the threshold value is too low and only the most distinct fractures are detected. In Figure 4-7b the threshold selection is nearly optimal; nearly 100% of the fracture lengths are captured without any false positives. In Figure 4-7c and Figure 4-7d, the threshold is too low and false positives begin to contaminate the image, primarily caused by the surface texture of the rock.

4.1.3 Morphologic Filtering

Following the selection of the gradient threshold and generation of a pixel-wise fracture candidate map, noise and small features are removed using a series of morphological operations. The first operation removes objects smaller than 4% of the smaller image dimension in pixels for a 4-way connected neighborhood (*i.e.* ignoring diagonal pixel contacts). Figure 4-8 illustrates 4-way and 8-way pixel connectivity neighborhoods. Objects in the binary image are defined as independent clusters of pixels maintaining the defined connectivity (4-way or 8-way). Removing objects smaller than 4% of the smallest image, or region, dimension removes stray pixels, small clusters of noisy pixels, and weakly-connected fragments. Figure 4-9a shows a potential fracture map after removing the small objects. The second morphological operation shrinks the remaining objects to a minimal thickness (one pixel in most cases) while maintaining 8-way connectivity so that individual objects are not fragmented. Figure 4-9b shows a potential fracture map after thinning objects. The third and final operation removes objects smaller than 10% of the smaller image, or region, dimension in pixels for an 8-way connected neighborhood. This operation is performed to remove remaining small, stray objects. The 8-way neighborhood is used because of the thinning function applied in the previous step. Using a 4-way neighborhood would remove

significant portions of detected fractures. Figure 4-9c shows a potential fracture map after the second round of object removal. The fraction of the maximum image dimension (*i.e.* 4%; 10%) can be adjusted manually by the user if necessary. These values were found to perform well with the segments of UAV-collected images used in this study. The morphological filtering does inevitably remove some information such as smaller fractures, discontinuous delineation of larger fractures, and weak connections in larger fractures. The most significant effect is the removal of noise and false positives caused by irregular surfaces, staining, and other natural features. For simple images with large aperture fractures and smooth, low-noise rock surfaces, the removal of small objects may not be necessary. However, for natural rocks, situations with such images are rare. In fact, higher-resolution imagery which senses textured rock surfaces well, will very likely need such morphological filtering.

4.1.4 Additional Fracture Detection Components

Morphological filtering is the final step of the main fracture detection algorithm. The final binary image shows the network of pixels classified as fractures. Additional, optional, components have also been implemented into the algorithm to address more complex rock masses and a wider range of input images. Gaussian filters are commonly used in edge and crack detection methods in order to remove noise from the image prior to processing. Figure 4-10 demonstrates the effect of applying a Gaussian filter to images before they are used in the fracture detection method. The Gaussian filter is useful for removing noise such as texture on rock surfaces. The filter is not useful for images that do not have dramatic contrast between fracture and rock surface. As the filter removes surface texture, which is effectively noise, it also has a smoothing effect on fracture edges. The smoothing makes the intensity change at the fracture edge more gradual and therefore reduces

the gradient along the edge, thus making the fracture more difficult to detect. Figure 4-11a and Figure 4-11b show a fracture before and after blurring respectively. It is apparent from Figure 4-11a and Figure 4-11b that several changes have occurred: noise has been reduced, the overall intensity of image has decreased, and apparent width of the fracture has increased from approximately 4-5 mm to 7-8 mm. In some cases, fractures that are 2-4 pixels wide may become undetectable by the algorithm. In Figure 4-11c, the smoothing of the intensity values around the fracture is quantified. Figure 4-11d similarly shows the change in the fracture signature within the image vertical gradient. Application of a Gaussian filter is recommended for high-resolution images (GSD < 5 mm) with high-contrast fractures. The filter can be activated by the user if necessary for other cases where noise becomes overly disruptive. A filter can also be coupled with high values of k_b, which will be most sensitive.

Other natural features on rock surfaces can also cause issues in fracture detection. Abrupt changes in color, or brightness, can create distinct intensity changes in the surface of rocks. Surface staining, caused by chemical weathering processes, is one such feature. Figure 4-12 shows different degrees of staining on the exposed surface of a weathered basalt rock mass. The result manifests as a signature within the image gradient very similar to fractures, often making them indistinguishable within the image gradient. The approach taken to remove these signatures is implemented prior to any gradient-based operations. Pixels unlikely to be fractures based on their intensity values are grouped and scaled to become more similar to other pixels, thereby simultaneously reducing, or removing gradient values for non-fractures and potentially increasing the gradient at the edges of fractures. Pixels that are likely to be part of a fracture will have very low intensity values, typically 0 – 30 (8-bit) depending on the image. The intensity values are image dependent and may also vary across a single image if lighting is non-uniform. In most cases,

the intensity threshold can be selected automatically by using a derivative of Otsu's method for image binarization (Otsu, 1979). Otsu's method assumes that a grayscale image can be divided into two classes (*i.e.* intensity bands) and searches for the threshold that divides the classes and minimizes intra-class variance. Otsu's method is most successful when the two classes have very distinctly separated peaks in the image histogram. For the images of interest here, the image histogram is dominated by non-fracture (*i.e.* rock surface) pixels which biases the threshold toward high intensities. The fracture portion of the histogram is often obscured by the presence of textures on the rock surface. For this example, it was found that scaling the Otsu threshold by a factor of 0.4-0.5 (O_s) provided the best results, and was used in the subsequent performance evaluation of basalt images in this chapter. A wider range of scaling factors may be suitable on depending the image (*i.e.* resolution, rock type, and lighting). This is typically best used with moderately to highly-fractured rock masses where the fracture component of the image histogram will distinctly peak separately from the rest of the image. For high intensity images of rocks with sparse fracturing, this is likely to fail, resulting in no fractures being detected. The modified Otsu's threshold was found to be very successful for isolating fractures in weathered rock masses. It did not succeed when applied to images of high-intensity rocks (*e.g.* marble, limestone). While fracture detection is fairly successful in these rocks without the modified Otsu's threshold, theoretically making it of no concern, this effect should be considered when integrating into an automated framework. Figure 4-13 shows an example of modified Otsu's threshold brightening on an image subjected to fracture detection. The original grayscale image is shown in Figure 4-13a. Figure 4-13b shows the image after all pixels above 50% of the image Otsu threshold are set equal to their mean intensity. Figure 4-13c and 4-13d show the final fracture detection for the unaltered and

altered images respectively. By comparing Figure 4-13c and 4-13d, it can be observed that the white staining on the surface of the rock is no longer triggering significant false positives.

4.1.5 Performance of Fracture Detection

The main functions of the method can be fully-automated and are most useful for images of rocks not affected by significantly variable discoloration caused by weathering conditions, image blurring, variable lighting conditions, and rocks with low contrast between fractures and the rock surface. An optional Gaussian filter and modified Otsu's threshold have been incorporated to address the complexities mentioned above and can be automated, or controlled by the user. The performance of the proposed methodology has been tested on sets of specific image types. The first image set was extracted from an orthophoto of a marble quarry wall in Dionysos, Greece shown in Figure 4-14. Portions of the wall were excluded from the analysis due to the existence of human-made objects such as cables. The quarry wall was then divided into 18 sections of interest for fracture detection. Each of the image sections was approximately 500x300 pixels. The images have a GSD of approximately 1 cm/pixel. The detected fractures are compared to a baseline manual interpretation of detectable fractures. Detectable fractures are those that are manually detected and have a width of at least 3 pixels. Narrower fractures may still be manually detectable, but are not expected to be detected by the fracture detection method. A fracture is considered detected if the majority of its detectable length is assigned as fracture. Figure 4-15a shows an example of automated fracture detection applied to a sample marble image. Figure 4-15b shows a simplified view of manual detection used as the baseline for establishing detection rates. In Figure 4-15a, two fractures where their full lengths have not been labeled by the automatic detection are highlighted. One (left) is an example of positive detection because at least 75% of the length has

been detected. The other (right) is an example where less than 75% of the length has been detected and therefore is not a positive detection. While this example appears to identify a fracture in the image, because less 75% of the total detectable length is identified, it is excluded from positive results in the subsequently discussed performance metrics.

In computer vision and other machine learning applications, it is desirable to assess classification performance using a receiver operating characteristic (ROC) curve. The ROC curve compares the true positive rate (also called sensitivity) to the false positive rate as a single parameter is varied. In this case, the false positive rate cannot be computed because the total number of true negatives cannot be known. This is because the accuracy assessment is performed on a fracture-by-fracture basis, for which the total number of true negatives is not defined. For this reason, a true ROC curve cannot be obtained. However, it is still of interest to compare the number of false positives to the true positive rate in a similar fashion. Since the number of true negatives is unknown for this assessment, it can be treated as an information retrieval problem. Performance of information retrieval is quantified independently of the number of true negatives by considering three different parameters. Precision, defined in Equation 4-4, is the correctly-identified fraction of the total detected fractures. Recall (or detection rate), defined in Equation 4-5, is the correctly-identified fraction of the total number of detectable fractures. Finally, the F-measure, defined in Equation 4-6, is double the harmonic mean of precision and recall. The F-measure is intended to quantify accuracy as a synthesis of precision and completeness.

$$Precision = \frac{TP}{TP+FP} \tag{4-4}$$

$$Recall = \frac{TP}{TP+FN} \tag{4-5}$$

$$F - measure = 2\left(\frac{Precision + Recall}{Precision \cdot Recall}\right) \tag{4-6}$$

Table 4-2 shows the results of fracture detection performed on the set of marble images while varying the parameter k_b. Low values of k_b did not perform well, successfully detecting less than 40% of fractures for values less than 0.4. About 60% of fractures were detected for k_b=0.5 and about 80% of fractures were detected for k_b=0.6. Additionally, at k_b=0.6, and to a lesser extent k_b=0.5, false positives significantly affect the results. False positives are interpreted as likely fractures in the binary image but are not manually selected fractures. For the marble, false positives are primarily caused by the predominantly horizontal foliation in the rock, which may also be of interest from a structural and strength perspective, but not a target of the methodology being tested. The marble image set required a low gradient threshold to perform well as indicated by the k_b=0.6 value for 80% success. This is due to the fracture pixels having higher than expected intensity values. This is caused by the generally coarse resolution of the orthophoto and blurring caused by image generation from the DSM. Raw images are generally best for performing fracture detection, but generating an orthophoto is useful when the desired perspective is unavailable in the raw imagery or the method needs to be applied over an area much larger than a handful of image. Figure 4-16 shows the true positive rate versus the total number of false positives for the marble images as k_b varies. The relative improvement of fracture detection decreases significantly above k_b = 0.5. Additionally, the total number of false positives increases significantly above k_b = 0.5. The precision-recall relationship for the marble images is shown in Figure 4-17. Recall did not improve significantly when k_b was increased above 0.4. The F-measure for fracture detection on the marble images for the tested values of k_b are shown in Table 4-3. These results indicate that for the marble image set, k_b = 0.4-0.5 was optimal. Some example outputs are shown in Figure 4-18 for k_b = 0.5. Most of the fractures are captured well in Figure 4-18. However, some remain partially, or fully, undetected; the width of these fractures is around 2-4 pixels.

The second image set was constructed from images collected of a vertically cut weathered basalt outcrop in Hawaii. Some example photos of the approximately 4 m high outcrop are shown in Figure 4-19. The GSD of the source imagery was on average 1.7 mm/pixel but it varies due to the complex 3D structure of the rock mass. For this image set, 28 sub-images of fractured basalt in varying weathering states were extracted. The main functions of the fracture detection algorithm could successfully identify fractures in the set of basalt images, but the presence of noise on the rock surfaces generated a large amount of false positives. The noise in the images was caused by the presence of discoloration due to weathering processes and vesicles within the rock. When the modified Otsu's threshold is applied to the images, fracture detection is more successful. Table 4-4 shows the detection results for 28 basalt images for six different combinations of control parameters O_s and k_b. The performance characteristics (precision, recall, and F-measure) of the different parameter combinations are summarized in Table 4-5. Figure 4-20 shows the detection rate as a function of false positives. Based on the results in Table 4-5, it can be observed that O_s was most influential on the detection rate. For O_s = 0.4 the detection rate was about 70% and for O_s = 0.5 the detection rate was about 86%. While the detection rate was roughly constant for O_s = 0.5, the amount of false positives generated increased as k_b increased, therefore it is recommended that a lower value of k_b be used. Based on this assessment, using a parameter combination of O_s = 0.5 and k_b = 0.3 is recommended for similar images. Figure 4-21 contains an example image subjected to fracture detection using each of the parameter combinations. For this example, the detection remained essentially unchanged as k_b was varied. Figure 4-22 shows four example outputs from fracture detection using k_b = 0.3 and O_s = 0.5. Using the modified Otsu's threshold made the images less sensitive to noise caused by surface texture and discoloration. The images in the basalt set are not extremely fractured. As the images, or regions, become more fractured, the

suggested value of O_s increases and approaches 1, where $O_s = 1$ is equivalent to binarization using Otsu's method. For images of highly-fractured, broken-up rocks, it is recommended that a higher value of O_s (0.6 – 1) be selected in order to best capture the fractures.

A third set of images comprised of generally lower resolution extracted from UAV-based and ground-based photos was also tested. The image set contains 28 images of various rock types (sandstone, limestone, basalt, etc.) and conditions (widely spaced fractures, highly-fractured, etc.). The set is not intended to capture performance on any particular type of rock. The performance of fracture detection on the image set is summarized in Table 4-6. The algorithm performed very well on images of highly fractured rocks for k_b = 0.4 - 0.5. The F-measure for different k_b values is shown in Table 4-7 and maximizes between k_b = 0.3 – 0.4. The fracture detection rate is compared to the total number of false positives in Figure 4-23 which indicates optimal performance around k_b = 0.4. Figure 4-24 shows the precision-recall relationship. The precision-recall relationship also indicates k_b = 0.3 – 0.4 is the best-performing parameter selection. Figure 4-25 shows example output for the fracture detection performed on three images with k_b = 0.4. The examples in Figure 4-25 demonstrate the automated algorithm applied to different fracture patterns, including a disintegrated rock.

4.1.6 Limitations and Practical Considerations

The automated fracture detection algorithm performed well when applied to a set of images without known special conditions such as discoloration due to weathering or intense surface texture. However, the generation of false positives may be of concern and could result in overly-conservative interpretations. When augmented with a Gaussian filter, or modified Otsu's thresholding to handle noise sources (weathered surfaces, texture, vesicles etc.), the performance

improves. Images may perform poorly if not properly segmented to separate regions of different brightness and pre-processing requirements. The algorithm was found to perform best in identifying fractures at least 3 pixels wide. However, in some brighter (*i.e.* higher intensity) rocks, thinner fractures could be detected due to high contrast. Fractures very close to 3 pixels width may also become segmented, meaning that their persistence is not captured due to width dropping below 3 pixels at certain points along the fracture length.

To address some of the issues previously mentioned (*e.g.* surface weathering and texture) and improve performance on special image cases, the fracture detection approach has been integrated with the simple linear iterative clustering (SLIC), also known as superpixels, image segmentation algorithm detailed by Achanta et al. (2012). SLIC is an unsupervised image segmentation algorithm which clusters pixels based on color, brightness, and spatial proximity. Specific functions can then be applied to all or some of the clusters, or superpixels. An example of SLIC applied to a sample image is shown in Figure 4-26. SLIC can be used to simplify an image into tiles for easier processing in computer vision applications. In Figure 4-26b each superpixel has been assigned its median RGB vector as a constant color. SLIC is further discussed and implemented in the following section. The segmentation performed by SLIC is effective at separating parts of an image affected by different lighting patterns. As previously mentioned, and demonstrated by the fracture detection performance, spatial changes in lighting play a significant role in selection of a gradient threshold and subsequent identification of fractures. The images can be segmented using SLIC, then pixel clusters are processed individually and reconstructed into a final fracture map. As an example, Figure 4-27 shows a section of weathered, vesicular basalt. The image was segmented using SLIC into 20 superpixels and fracture detection using $k_b = 0.4$ and $O_s = 0.5$ was applied. When processing a larger image and/or more broken-up rocks, a higher value

of O_s may be needed. The number of automatically detected fractures was compared to the number of manually counted fractures for each transect in Figure 4-28. The automatic detection tended to undercount the true number of fractures in the image. This is caused by automatic fracture detection missing thin fractures, which is an advantage of human interpretation over the automated algorithm. The point for T5 in Figure 4-28 shows that only 44% of fractures were detected. The significant under-detection was caused by several thin fractures not being clearly identified. The small fractures were not highlighted when the modified Otsu's threshold was applied and therefore not identified as fractures. These fractures were not thick enough to be easily detectable by the algorithm but were still visible for manual interpretation. It should be assumed that thin fractures (2-3 pixels wide) with lower contrast will be missed when applying the modified Otsu's threshold resulting in undercounting. The undercounting may be unconservative, as demonstrated by T5 in Figure 4-28.

A similar comparison between the fracture detection algorithm and manual fracture counting for a UAV-collected image of an angular blocky rock (GSI of 50 to 70) with good interlocking is presented. The GSI for this material is about 50 – 70. Fractures were manually counted along 14 vertical transects and compared to results of fracture detection with $k_b = 0.4$. The rock with detected fractures and delineated vertical transects is shown in Figure 4-29. Comparison with manual counting of fractures along the vertical transects is made in Figure 4-30. In general, the algorithm identifies the number of manually counted fractures within about 15%. Cases of both undercounting and overcounting are apparent in Figure 4-30. The cases of undercounting typically occur for fractures that have low contrast with the rock surface and are less than 3 pixels wide. Overcounting tends to be caused by edges on jagged surfaces protruding in 3D. Another source of overcounting is the attachment of false positives to true fractures. Because the false positive is

connected to the true fracture, it is not removed through post-detection filtering and will artificially increase the fracture count when intersecting the vertical transect. The jagged edges on protruding pieces of rock cause overcounting, but are useful for point cloud based discontinuity analyses that rely on using protruding surfaces to measure the strike and dip of discontinuities.

Fracture detection is applied to a third example in Figure 4-31. The image in Figure 4-31 is an orthophoto produced from 3D modeling of a vertical face in a quarry. The image is 4825 pixels wide and 7960 pixels tall. The GSD of the image is 6 mm/pixel, therefore it is not expected that we will detect fractures thinner than 1-2 cm. However, very thin (1 cm or less) fractures may be partially detected due to high contrast rock surface. Figure 4-31 also shows the results of applying fracture detection. The image was segmented into approximately 570 superpixels and a value of $k_b = 0.35$ was used. The fracture detection captures the major discontinuities effectively. The image was split into 13 vertical transects where fractures were manually counted and compared to the fracture detection algorithm results in Figure 4-32. In this case there is overcounting of fractures by the algorithm (about 15% in general). The overcounting is caused by small areas of surface staining and apparent edges in areas with jagged 3D blocks. The small fractures (*i.e.*, thin, low contrast) are partially detected. When partially detected, the existence of a fracture is noted, but the persistence of the fracture is not captured. Figure 4-33 shows an example of complete and partial detection of fractures on the quarry orthophoto. The fracture detection accuracy could be improved by further image segmentation and selection of regions where the modified Otsu's threshold should be applied. This would assist in removing false positive caused by discoloration. But, applying the modified Otsu's threshold does eliminate some smaller fractures from detection which resulted in undercounting of fractures in the earlier example of weather basalt.

4.1.7 Example Applications in Rock Mechanics

The detection of fractures in RGB images can be extended to practical applications such estimating rock strength parameters, rapid identification of low-strength areas, and correlation with other physical properties. In Figure 4-34, a basalt profile was subjected to fracture detection using O_s = 0.8 and k_b = 0.4 (note that detection is not sensitive to k_b when using O_s). The image was segmented into approximately 200 superpixels using SLIC. Each superpixel was processed separately and reconstructed into the original image. Figure 4-34a shows the image following fracture detection. The rock quality designation (RQD) (Deere and Deere, 1988) was computed automatically for 5 pixel wide (about 10 cm) vertical transects across the image. The RQD is a parameter measured, in practice, based on core recovery in drilling operations. RQD is an input parameter for the Rock Mass Rating (RMR) system and the Q-system for geomechanical classification of rocks. Both of these rating systems are used in practice for excavations, tunneling, and correlation with material properties (*e.g.* Young's modulus, compressive strength). The RQD is defined as the summed length of rock pieces recovered from the core that are greater than 10 cm, divided by the total drilling length (*i.e.* percentage of a drilling core made up of rock pieces 10 cm long or more). The RQD is also used by practitioners as a design parameter when constructing facilities on rock. Figure 4-34b shows the results of dividing the image into vertical transects and automatically computing the RQD. The black rectangular regions at the top of the profile in Figure 4-34b are excluded from the RQD computation because they consist primarily of soil. The RQD contours appear as vertical bars because RQD provides a constant value across the vertical length (or recovered core). Spatial distribution of the 10 cm pieces is ignored. Figure 4-35 shows a comparison between the automatic RQD and a manual check of eight different transects (labeled in Figure 4-34b). For the comparison, the automatic RQD value is taken as the average of

the cell containing the transect center and the two adjacent cells. Because the RQD only considers rock pieces 10 cm or larger, sparse false positives in the image do not affect the calculated value unless they appear in a piece close to the 10 cm limitation. Similarly, sparse false negatives do not affect the RQD value unless they split a rock into segments smaller than 10 cm. As observed in the basalt transect example in the previous subsection, the automatic procedure tended to undercount fractures in each transect, which translates to a higher reported RQD. While observing this bias, it should be noted that the data points are clustered in RQD = 0.6-0.8, which is due to the RQD of the imaged rock falling in the range of approximately 0.6-0.9.

The ability to automatically estimate RQD is useful, however, the RQD itself has many limitations. For example, it does not describe the spatial distribution of fractures or potential changes in material. Figure 4-36b shows contoured heat map of fractures per unit length (fractures/m) overlain on the rock profile. The rock mass, after fracture detection, was split into 50 cm square cells and the number of fractures per unit length was estimated within each cell. The purpose of this is to describe the spatial distribution of fracturing in the rock and automatically identify regions of intact, moderately fractured, and highly fractured rock. Highlighting these changes in fracturing quickly flags areas where changes in material type occurs or where more careful analysis is warranted (such as in 3D slope stability). The contours can be compared to a manual interpretation describing the rock mass using the ISRM (1978) rock mass classification system shown in Figure 4-36c. This example was shown briefly in Chapter 3. The ratings I through VI describe the rock as fresh, slightly weathered, moderately weathered, highly weathered, completely weathered, or residual soil. In general, the results agree well with the regions classified as I-II (fresh or slightly weathered) mapping to regions of mostly intact rock in the contours. However, the regions classified as, essentially, soil (V and VI) are detected as intact rock. Figure

4-37 shows the contours and profile separately and highlights instances where the heat map of fractures is accurately portraying conditions. The contours effectively capture different regions of intact rock and broken-up rock. The heat map also captures a region of seamy rock on the left side of the image. The results show that the fracture detection has value in automatically describing the distribution of rock structure and weathering along a surface. In Figure 4-38, areas where the contour mapping did not perform well are highlighted. Areas of soil have few detected fractures because, from the algorithm perspective, the soil has the appearance of a solid, textured surface. When using this approach, regions of rock and soil should be separated through a pre-processing, material type classification approach. Additionally, debris consisting of rock fragments is detected as a highly-fractured region, while in reality the fragments are lying over mostly intact rock. The filtering of surface debris could potentially be performed while considering 3D information (*e.g.* from a 3D point cloud) and deriving the visual properties unique to loose rock fragment debris.

A 2D shear wave velocity (V_s) profile and a 2D P-wave (V_p) velocity profile were also generated at this site (Greenwood et al., 2017; Von Voigtlander et al., 2018). The V_s profile was generated using the common midpoint cross-correlation (CMPCC) 2D imaging approach for multichannel analysis of surface waves (Park et al., 1999; Hayashi and Suzuki, 2004). Greenwood et al. (2017) also performed a delineation of GSI for the outcrop that was then used to update the layered earth model used in V_s inversion for the purpose of improving confidence in the results. The final V_s profile generated by Greenwood et al. (2017) is shown in Figure 4-39 overlain on the outcrop. It is difficult to produce a correlation between GSI and stress wave velocity in part because they are both significantly affected by scale. When assessing GSI or measuring stress wave velocity the sample size is a controlling factor for results. For example, if a small sample is considered, it will ignore widely spaced fractures that outsize the sample area (*i.e.* a wave will not

propagate through the fracture nor will it be considered for GSI allocation). A correlation for degree of fracturing and V_s for this outcrop could be developed using the results of the automatic fracture detection. It is expected that fracturing will vary as a function of V_s due to the low resolution of the V_s profile relative to fracture detection (and contouring). To assess this, the range of fracture frequency (minimum and maximum) within each of the V_s contours (Figure 4-39) is identified from Figure 4-36b. The previously discussed cases of poor rock structure evaluation by the automatic fracture detection are ignored for this assessment. The minimum and maximum fracture frequencies are also fit by power functions ($R^2 > 0.83$) in Figure 4-40. The minimum fracturing at 400 m/s in Figure 4-40 appears as an outlier. The large region at the center of the outcrop that is mostly intact, which is captured well by automatic fracture detection, and the V_s is lower than expected. This was observed by Greenwood et al. (2017) and is likely caused by changes in weathering behind the outcrop face. It is typically expected that weathering (and fracturing) will decrease behind an outcrop face. But increased fracturing is possible and dipping intact blocks could result in a lower than expected V_s. The derived correlation between V_s and fracture frequency can be used to estimate V_s in other sections of the outcropping rock if fracture detection is applied to those sections. The V_s was correlated to both the minimum and maximum observed fracturing frequency. The difference between minimum and maximum fracture frequency increases as V_s increases. Even if small areas of high-density fracturing exist, the V_s measurement involves sampling over a large area, so the extensiveness of intact rock will dominate the small area of high-density fracturing.

When a 3D point cloud is available, as it is with the quarry example, and the intrinsic and extrinsic camera parameters are known, the detected fractures can be transformed back onto the 3D point cloud through a reverse projection and 3D transformation. The process of transforming

and projecting 3D points onto an image is described in the following section. Once fracture-classified points have been placed on the 3D point cloud, the fracture orientation relative to the global coordinate system can be estimated. Additionally, parameters such as RQD and fracturing-correlated V_s or V_p can be mapped to the 3D point cloud. As this is performed, the point cloud becomes a virtual database of material properties that accounts for their spatial distribution.

4.2 Generation and Processing of RGBD Images using 3D Imagery

It is valuable to utilize the 3D information generated by SfM in the workflow. In this section, the 3D points generated by SfM are re-projected back onto the original images they were extracted from. This new information is layered into the RGB images to produce RGB-Depth (RGBD) images. RGBD images were used to analyze pavement distress by Jahanshahi et al. (2013b) and can be generated by depth sensors in conjunction with traditional cameras. This type of multimodal imagery which synthesizes multiple data types (*e.g.* visible color, depth, infrared, and other spectral bands) has become a popular research thrust as UAV-based spatial data collection has gained popularity across many different fields.

4.2.1 Generating RGBD Images

As a result of the SfM workflow described earlier in this chapter, a 3D point cloud is produced from a series of images with estimated camera locations. The camera locations and orientations could be known at the time of collection or could be estimated/updated during bundle adjustment. The extrinsic camera parameters are used to define a matrix which can translate the 3D points into the local coordinate system. The matrix (R) is defined as:

$$R = \begin{bmatrix} \cos\kappa & \sin\kappa & 0 \\ -\sin\kappa & \cos\kappa & 0 \\ 0 & 0 & 1 \end{bmatrix} \begin{bmatrix} \cos\varphi & 0 & -\sin\varphi \\ 0 & 1 & 0 \\ \sin\varphi & 0 & \cos\varphi \end{bmatrix} \begin{bmatrix} 1 & 0 & 0 \\ 0 & \cos\omega & \sin\omega \\ 0 & -\sin\omega & \cos\omega \end{bmatrix} \tag{4-7}$$

Where ω, φ, and κ are the yaw, pitch and roll angles of the camera about the *x*, *y*, and *z* axes in Figure 4-41 respectively. The matrices in Equation 4-7 can be altered as necessary to fit the definition of the coordinate systems. Figure 4-41 shows the local coordinate system of an arbitrary camera. The matrix *R* is then used to convert the 3D points into that specific image's local coordinates in equation 4-8. Equation 4-8 performs a translation followed by rotation of 3D points and then performs a perspective transformation using the camera intrinsic parameters.

$$\begin{bmatrix} x \\ y \\ z \end{bmatrix} = \begin{bmatrix} -f/s_x & 0 & c_x & 0 \\ 0 & -f/s_y & c_y & 0 \\ 0 & 0 & 1 & 0 \end{bmatrix} \begin{bmatrix} r_{11} & r_{12} & r_{13} & 0 \\ r_{21} & r_{22} & r_{23} & 0 \\ r_{31} & r_{32} & r_{33} & 0 \\ 0 & 0 & 0 & 1 \end{bmatrix} \begin{bmatrix} 1 & 0 & 0 & -P_x \\ 0 & 1 & 0 & -P_y \\ 0 & 0 & 1 & -P_z \\ 0 & 0 & 0 & 1 \end{bmatrix} \begin{bmatrix} X \\ Y \\ Z \\ 1 \end{bmatrix} \tag{4-8}$$

Where *X*, *Y*, and *Z* are coordinates of 3D points in the global (*i.e.* SfM) coordinate system, [P_x P_y P_z] is the camera position in the global coordinate system, and r_{ij} are the elements of *R*, *f* is the camera focal length, s_x and s_y are skew factors, c_x and c_y are the image center, and *x*, *y*, and *z* is the set of 3D points in the local coordinate system. The pixel coordinates on the image plane of each 3D point are defined by equations 4-9 and 4-10.

$$u = \left(\frac{x}{z}\right) \tag{4-9}$$

$$v = \left(\frac{y}{z}\right) \tag{4-10}$$

Where *u* and *v* are the pixel coordinates as defined in Figure 4-42, *x*, *y*, and *z* are the coordinates of the 3D points, and c_x and c_y are the image center in pixel coordinates. The multi-stage transformation from 3D global coordinates to image coordinates can be performed several equivalent ways. It is notable that any point can be projected onto the image plane, but may reside outside of the image itself. Such points are removed and a new image layer is populated with depth

values (the distance from the image plane to the object). If any pixel is assigned more than one depth value, meaning that more than one point was projected onto that pixel, the closest point is assigned to the pixel and the others are discarded. Figure 4-43 shows an example of an RGBD image where the green pixels overlain on the image represent points where a depth value has been assigned. When reverting SfM points back onto a source image, the lateral resolution of the depth points will never match the resolution of the image. In order for the lateral resolution to match (*i.e.* have a depth value in every pixel), each pixel should have been used in the generation of a 3D point. The RGBD images have a variety of uses. As an example, Figure 4-43 shows the profile of a vertical cross-section taken from center of the RGBD image. This is useful because a detailed 2D profile can be produced by defining a transect in an image without needing to operate on the 3D point cloud.

4.2.2 Framework for Depth-Enabled Superpixels

As described in the previous section of this chapter, the SLIC segmentation algorithm is useful for clustering portions of a rock mass image for independent processing. The SLIC algorithm performs clustering on 2D color images. With the addition of a depth component to the image, it is desirable to use this information to enhance the image segmentation and perform additional sub-processing utilizing the new image mode. The original SLIC algorithm has been adapted for use with RGBD images. The updated SLIC algorithm is similar to the original algorithm in Achanta et al. (2012) which is shown in Figure 4-44. There are two major differences between the updated version presented here and the original. The cluster feature vector is now defined as: $C_k = [l_k,a_k,b_k,x_k,y_k,z_k]^T$. And a distance measure to compare the depth component of the image with color and spatial proximity was developed. When performing iterative clustering, SLIC

computes a distance measure (D) between a pixel and a potential cluster. If a pixel-to-cluster D value is less than the value for the pixel's original cluster, the pixel is assigned to the new cluster (described in Figure 4-44). The distance measure is calculated based on the computed Euclidean distances between the pixel and cluster for the color (d_c) and spatial proximity domains (d_s). These respective metrics are defined by equation 4-11 and 4-12. Equation 4-13 is then used to calculate the pixel-cluster distance metric.

$$d_c = \sqrt{\left(l_c - l_p\right)^2 + \left(a_c - a_p\right)^2 + \left(b_c - b_p\right)^2} \tag{4-11}$$

$$d_s = \sqrt{\left(y_c - y_p\right)^2 + \left(x_c - x_p\right)^2} \tag{4-12}$$

$$D = \sqrt{\left(\frac{d_c}{N_c}\right)^2 + \left(\frac{d_s}{N_s}\right)^2} \tag{4-13}$$

Where N_c and N_s are normalization factors for the respective distance metrics; l_c a_c b_c and l_p a_p b_p are cluster and pixel color parameters in CIE-L*a*b color space respectively; x_c and y_c are the column and row designation of the cluster center; x_p and y_p are the column and row designation for the pixel. These factors are the expected maximum values for the respective distance metrics. N_s is defined as the maximum spatial search distance (S):

$$S = \sqrt{N/k} \tag{4-14}$$

Where N is the total number of pixels in the image and k is the desired, or target, number of superpixels. N_c is more complex as the maximum expected distance in the color domain is not necessarily known and difficult to define. Achanta et al. (2012) provided 1 – 40 as the range of possible values for N_c and recommended using 10 – 40. This normalization factor could then be used as a control parameter to alter the relative importance of color with respect to spatial proximity. Higher values reduce the relative importance of color compared to spatial proximity

and result in more regularly-shaped clusters. Lower values minimize the relative importance of spatial proximity and do not constrain the cluster shapes. If irregular clusters are expected, as is expected with rock masses, a lower value of N_c should be used. For example, Figure 4-45 shows the impact of changing N_c, note that using a large value forces more regular shapes and does not conform as well to the rock structure. Now that a new image mode, namely depth, has been introduced a new distance metric (d_d) is needed:

$$d_d = \sqrt{\left(z_c - z_p\right)^2 + \left(z_c - z_p\right)^2} \tag{4-15}$$

The distance metric for comparing pixels to potential clusters then becomes:

$$D = \sqrt{\left(\frac{d_c}{N_c}\right)^2 + \left(\frac{d_s}{N_s}\right)^2 + \left(\frac{d_d}{N_d}\right)^2} \tag{4-16}$$

Where N_d is the depth component normalization factor, which is similarly defined as the maximum expected depth distance metric between pixels and potential clusters. This is more difficult to describe than N_c because the range of values is unknown. However, the normalization factor must be tied, in some way to the scale of the image and the physical distances expected. To capture physical characteristics, a definition of N_d is proposed in equation 4-17.

$$N_d = K \cdot GSD \tag{4-17}$$

Where GSD is the ground sampling distance of the image and K is a constant. Based on initial testing of the effect of segmentation weighting on cluster contents (*i.e.,* color and depth distribution), K = 5-20 is recommended. For a GSD of 5 mm, the expected maximum value of d_d would then be 25 – 100 mm. When selecting a value for K, the expected surface variations on the rock and the desired cluster size should be considered. If a very irregular surface is expected, especially with significant variations expected within a cluster, a large value of K should be used. If cluster sizes will be small and lack discontinuities and significant surface variations within them,

a small value of K should be used. In general, large variations will not be expected across small spatial distances. The selection of K could also be used to control the influence of depth data relative to color. For example, if the reliability of the depth data is low, its potential influence can be mitigated by using a large K. Figure 4-46 shows the histograms of depth values contained between equivalent clusters for SLIC outputs with and without considering depth (*i.e.* RGBD versus RGB) for two different values of N_c. When the RGBD SLIC method is used, intra-cluster variance of depth decreases. In general, RDGB clustering improves the depth variance between equivalent clusters, as expected. However, the RGBD clustering may actually increase the intra-cluster variance of depth in some clusters (*e.g.* 1 out of 25 total clusters) as a result of improving all of the surrounding clusters. In those cases, the variance of depth for that cluster increases when depth is considered. Figure 4-47 shows the effect of altering K on the resulting clusters. Very low values of K, maximize the weight of depth data in the clustering. Low values may also bias clustering towards regions with higher resolutions. The resolution of the depth layer within the RGBD image will not, in general, be constant when produced from SfM results. It will be dependent on the spatially-variant resolution of the point cloud and how those points project onto the image (*i.e.* how much those pixels contributed to model generation).

4.2.3 Estimation of Surface Roughness

Following manual selection of a small region on the surface of the rock within an RGBD image, or after RGBD clustering with SLIC, an estimation of surface roughness within the superpixel can be made. To do this, a plane is fit to the depth information embedded in the image region. Roughness is then estimated by calculating the deviations from the plane. An affine fit to a plane for this data can be performed by considering the mean-shifted 3D points:

$$A = [X \quad Y \quad Z] - mean[X \quad Y \quad Z] \tag{4-18}$$

Equation 4-18 forces the assumption that the mean of the points will fall on the plane. The plane which fits the points in $[X\ Y\ Z]$ is orthogonal to the first eigenvector of A^TA. A planar surface can be described completely by a unit normal vector to the plane. Figure 4-48 shows an example of fitting a plane to a relatively flat surface of a vesicular basalt. Figure 4-48a shows the location of pixels containing a depth component. The planar fit to those depth points is shown in Figure 48b. Following the planar fit, Figure 48c shows the histogram of point deviations from the plane and the resulting value of RMS roughness (2.9 mm). While the spatial resolution of the depth component of the RGBD image may be sufficient to observe depth of features at the surface of the material, the 3D information derived from SfM is unlikely to be capable of properly capturing the depth similarly to larger areas concealed by shadows. When combined with outputs from fracture detection, identified fractures (classified pixels) can be removed from the roughness computation to filter erroneous results when analyzing a single block. Observing spatial changes in the surface roughness could provide an additional indicator of changing weathering states and rock types. For the case of broken up rock masses, measuring deviations from a plane could provide 3D information on the size of fragments. Additionally, the estimated surface roughness can be mapped back to the 3D point cloud and included in the point feature vectors containing material properties and characteristics. The roughness value may be useful when known for planar surfaces used in 3D discontinuity analysis such as examples in Table 4-1 which do not quantify the roughness of discontinuities (*e.g.* joint roughness) which is important for understanding the strength properties of the discontinuity.

4.2.4 Isolation of Discontinuities

As discussed earlier, it is of interest to delineate fractures and subsequently describe the structure of a rock mass in order to spatially assign strength parameters. To do this, information about the weathering state of discontinuities is also needed. Regions around fractures identified by the detection approach described earlier can be selected to analyze them. The information that can be extracted about the fracture is primarily a function of the density of the depth layer in the RGBD image. Figure 4-49 shows the RGBD data for an isolated fracture. Figure 4-49a shows an example of a detected fracture where all pixels between the fracture edges have also been classified through post-processing. Figure 4-49b shows the depth mode of the image, corresponding pixel color has been assigned to the 3D points and the fracture is visible. Figure 4-49c similarly highlights the detected fracture pixels mapped to the 3D points. In Figure 4-49d the same highlighted fracture is shown from a different perspective. The dashed lines bound points identified as being part of the fracture in 3D analysis but were missed in 2D fracture detection. This is caused by the perspective of the camera used to obtain the image, which obscures the bottom internal edge of the fracture. However, this information can be resolved through incorporating additional camera perspectives as demonstrated by the 3D points in Figure 4-49. With the fracture isolated, it is possible to make observations on its aperture and roughness. It appears from Figure 4-49d that a value for depth of the fracture could be interpreted from the RGBD data. However, the depth is unlikely to be accurate due to the lack of color information within the fracture and the lack of available internal camera views. The credibility of SfM points within a fracture must be independently verified. A useful quantification of fracture depth could be acquired from other methods, such as Jahanshahi et al. (2013).

4.2.5 Mapping Detected Fractures to 3D Points

Pixels classified as fracture and also containing a depth component can be transformed back into 3D and overlain on the point cloud. Figure 4-49a shows an example of a section of rock containing detectable fractures. After detection, the points coinciding with depth values are transformed back to 3D points in Figure 4-49b. The reverse transformation of a single depth image back to its original point cloud is not necessarily a trivial problem. Some translational information may be lost during forward projection onto the image. The result is that when transformed back to 3D space in global coordinates, the points are translated away from the original point cloud. This can be managed with different approaches. If there are no known tie points or the translation cannot be determined, the entire set of 3D points (not just those classified as fracture) can also be pushed through a reverse transformation. The full set of points will share a coordinate system with the reverse transformed fracture points and can be overlain in the new coordinate system. Additionally, by using the full set of points in the reverse transformation, the translation needed to align with the original point cloud can be determined as the translation minimizing the error between the original and reverse transformed point clouds. Alternatively, if there are known geotagged points within the reverse transformed data, determining the residual translation is trivial. If more information is needed such as scaling and additional rotation of the point cloud, the scale and rotation matrix can be estimated by iteratively solving for the operations that minimize the error between point clouds.

As another example, Figure 4-50a shows a photo of a rock mass that was part of a complex of landslides caused by the 2015 Gorkha earthquake in Nepal. The exposed rock structure in Figure 4-50a is about 20 m high. A 3D point cloud was generated of this site and a subset of 3D points pertaining to the rock mass has been transformed and projected onto the image in Figure 4-50b. This shows that if only a subset of points are needed, such as if a material classification has been

performed and one of those materials requires further characterization, point subsets can be processed separately. Fracture detection was applied with k_b = 0.4 which generated Figure 4-51a. The RGBD pixels assigned the fracture were then transformed back into 3D space and merged with the original point cloud. This can be performed for any number of images covering the entire rock mass. The 3D points with a fracture designation are highlighted in Figure 4-51b. It can be observed by comparing Figure 4-51a to Figure 4-51b that some of the detected fractures have lost some of their shape or continuity after transformation. This is because only the pixels containing depth information (*i.e.* pixels that have a corresponding point in 3D) can be mapped back to the point cloud. Now, each of the points has a binary label classifying it as fracture constituent or not. The assigning a fracture designation to the 3D points allows for easier identification of some fractures that were not previously apparent in the point cloud. Doing this allows for easier interpretation of fracture orientation in 3D, as performed in Chapter 3, because the fractures have been highlighted. Additionally, fractures not previously identifiable in the 3D imagery are labeled and can have their orientations measured, which was previously not possible. However, there were still fractures visible in the point cloud that were not detected in 2D as a result of incomplete recall. The labeled 3D points can then be subsequently included in 3D analysis methods, such as potentially automated estimations of rock strength parameters (*e.g.*, GSI) or with other discontinuity assessments such as those that measure orientation on planar faces. In Figure 4-51b, examples of discontinuity sets were measured based on the fracture designations in 3D and strike/dip was reported and can be used for stability analysis. For example, the discontinuity labeled with a dip of 40° and striking at 90° is the bottom plane consisting of a set of three discontinuities that form a wedge. The wedge, which dips away from the rock face would be the

target of a structurally-controlled stability analysis and could fail similarly to the earthquake-induced wedge failure observed in Chapter 3 at another landslide site in Nepal.

4.3 Summary and Recommendations for 3D-Enabled Image Processing Framework

In this chapter, image processing techniques have been introduced for assessing the structure of a rock mass. The synthesized workflow integrating the described techniques was summarized in Figure 4-2. When the semi-automated fracture detection method is used, the user can tune the algorithm to handle complex characteristics of rock masses such as surface texture and discoloration. The presented fracture detection algorithm, as outlined in Figure 4-1, has two optional pre-processing components. First, a Gaussian filter can be applied to the image to remove noise associated with grains, minerals, and other texture on the surface of the rock. However, using the filter, which is standard in many edge detection procedures, was found to be detrimental for images that do not have high contrast between fracture and rock surface, and for images where the fracture width is close to the 3 pixel minimum due to a smoothing effect on fracture edges. The filter is recommended for higher-resolution images (GSD < 5 mm) with high-contrast fractures. Alternatively, the filter can be manually activated by the user to address cases of disruptive noise on the rock surface. When used, the filter may need to be coupled with higher values of k_b (0.4 - 0.6). The second optional pre-processing component uses a modified version of Otsu's threshold for image binarization. The Otsu's threshold is computed on the grayscale image and scaled by a factor O_s. Pixels with intensity values above the threshold are assigned a constant value (*e.g.* median of all pixels). Performing this function was found to greatly improve fracture detection performance on images of weathered, vesicular basalt. For the basalt image set, $O_s = 0.5$ was found to perform the best and was significantly more influential on results than k_b. However, when used

with large images that include high-density fracturing, larger values of O_s (0.6-0.9) is recommended. It is recommended that the modified Otsu's threshold be used if it is specifically noticed that the images will need the pre-processing or to address results with high false positive rates and high-contrast fractures. The fracture detection method should be applied to segmented images, either manually or automatically (*e.g.* SLIC) because control parameters may need adjustment across the image. However, the algorithm can be applied to full images of any size if desired. The fracture detection was used to estimate RQD in vertical transects across an image. The RQD estimate is fairly resilient to noise, for the examples tested, but provides an overestimate by 10-15%. A heat map of detected fracture density was compared to a manual classification. The heat map was useful for quickly identifying areas of intact, moderately fractured, and highly fractured rock. However, soil appeared similar to intact rock in the results. A pre-processing method to segment soil and rock is needed because the two material categories must be handled separately. The heat map described the spatial distribution of fracturing in the rock mass well and was compared to a 2D V_s profile conducted along the top of the outcrop. The minimum and maximum fracture frequency was correlated to V_s for the 2D profile contours.

It has been shown that depth images (RGBD) can be produced by reducing SfM point clouds and synthesized with traditional 2D image processing. The depth images contain information from other camera perspectives which is important for verifying results from 2D images of complex 3D structures. An updated version of SLIC (superpixels) for RGBD images was developed but will require additional validation with currently undeveloped baseline datasets before being extended to other applications than what has been covered here. The RGBD images can be generated by projecting 3D points onto a SfM input image, orthophoto generated from a DSM, or a newly acquired image. The relative weighting of image depth for clustering was tied to

the GSD of the image scaled by a factor (K = 5-20). The selection of K can be made based on the relative uncertainty of the depth data, desired influence, or *a priori* knowledge of the rock structure. When clustering was performed on RGBD images, the intra-cluster variance of decreased and resulted in clusters more closely following the 3D structure of the rock. The methodology in Figure 4-2 synthesizes the 2D fracture detection with 3D information, when available, to analyze rock surface roughness and the characteristics of individual fractures detected in 2D images. Using the same principles that allowed for the RGBD images to be generated from SfM point clouds, the depth-enabled pixels contained in detected fractures within each image can be transformed back to 3D and attached to the 3D point cloud. The fracture orientations (strike/dip) and spacing can then be measured, the 3D spatial density of fracturing can be estimated, or the labeled 3D points can be used in further 3D rock structure analyses. The reverse transformation back to the 3D point cloud from 2D images can translate additional information as well including V_s, fracture frequency, surface roughness, GSI, and RQD among many others. When mapped back to the 3D points, the point feature vectors store information about these material properties and characteristics. The properties can then be combined with other point cloud outputs or propagated through other 3D-based analyses. The connection of external information also causes the point cloud to act as database for spatially-distributed data. This is useful for managing large databases of earthquake-affected sites such as landslides. The individual components of the framework are designed to be open-ended for integration with other 2D/3D image processing techniques developed outside of this study.

Table 4-1: Recent crack and discontinuity mapping approaches

Reference	Data Type	Material
Vasuki et al. (2014)	DSM	Widely spaced rock joints.
Lato and Vöge (2013)	DSM	Natural fractures in rocks.
Chen et al. (2016)	Point Cloud	Planar surfaces in rock masses.
Riquelme et al. (2015)	Point Cloud	Discontinuity sets in rock masses.
Valença et al. (2017)	Image and Point Cloud	Concrete.
Wu et al. (2014)	Image	Pavements.
Torok et al. (2014)	Mesh	Severely damaged concrete.
Jiang and Tsai (2015)	Image with depth	Pavements.
Jahanshahi and Masri (2013)	Image and Point Cloud	Concrete.

Table 4-2: Performance of fracture detection on marble images

IMG ID	Detectable Fractures	k_b=0.2	k_b=0.3	k_b=0.4	k_b=0.5	k_b=0.6
M1	21	3	4	9	15	21
M2	10	0	3	5	7	10
M3	11	0	3	7	9	11
M4	19	2	4	8	11	14
M5	28	5	13	15	23	28
M6	28	3	6	8	15	16
M7	15	3	4	6	8	9
M8	17	2	6	7	10	12
M9	18	2	3	8	11	12
M10	25	1	2	4	8	14
M11	32	0	7	10	15	22
M12	14	2	3	4	8	10
M13	9	2	2	5	6	7
M14	18	2	2	3	4	10
M15	12	0	4	7	10	12
M16	14	0	0	3	6	14
M17	18	1	3	11	16	18
M18	14	3	5	7	8	14
Total:	323	31	74	127	190	254

Table 4-3: F-measure for five values of k_b in marble images

k_b				
0.2	**0.3**	**0.4**	**0.5**	**0.6**
0.17	0.36	0.53	0.58	0.47

Table 4-4: Performance evaluation of basalt images

IMG ID	Detectable Fractures	O_s=0.4 k_b=0.3	O_s=0.4 k_b=0.4	O_s=0.4 k_b=0.5	O_s=0.5 k_b=0.3	O_s=0.5 k_b=0.4	O_s=0.5 k_b=0.5
BA1	8	6	6	7	7	7	7
BA2	7	3	3	3	5	5	5
BA3	6	4	4	4	6	6	6
BA4	5	2	2	2	4	5	5
BA5	5	4	4	4	4	4	4
BA6	5	3	3	3	5	5	5
BA7	4	1	1	1	1	1	1
BA8	4	2	2	2	2	2	2
BA9	8	7	8	8	8	8	8
BA10	3	3	3	3	3	3	3
BA11	5	3	4	4	5	5	5
BA12	8	4	4	5	6	7	7
BA13	5	5	5	5	5	5	5
BA14	6	5	5	5	6	6	6
BA15	7	3	3	3	4	5	5
BA16	14	11	12	12	12	12	12
BA17	7	4	4	4	6	6	6
BA18	8	5	5	5	7	7	7
BA19	6	3	3	4	6	6	6
BA20	7	5	5	6	6	6	6
BA21	4	1	1	1	2	2	2
BA22	15	10	10	11	11	11	11
BA23	7	5	5	5	6	6	6
BA24	5	5	5	5	5	5	5
BA25	1	1	1	1	1	1	1
BA26	6	4	4	4	5	5	5
BA27	6	5	5	5	6	6	6
BA28	10	9	9	9	10	10	10
Total:	**182**	**123**	**126**	**131**	**154**	**157**	**157**

Table 4-5: Fracture detection rates in basalt images for six different combinations of control parameters

Parameters	$k_b = 0.3$ $O_s = 0.4$	$k_b = 0.4$ $O_s = 0.4$	$k_b = 0.5$ $O_s = 0.4$	$k_b = 0.3$ $O_s = 0.5$	$k_b = 0.4$ $O_s = 0.5$	$k_b = 0.5$ $O_s = 0.5$
Precision	0.77	0.73	0.72	0.52	0.46	0.41
Recall	0.68	0.69	0.72	0.85	0.86	0.86
F-measure	0.72	0.71	0.72	0.64	0.60	0.56

Table 4-6: Performance of third image set

IMG ID	Detectable Fractures	$k_b = 0.2$	$k_b = 0.3$	$k_b = 0.4$	$k_b = 0.5$
H2	4	3	4	4	4
H3	11	5	10	11	11
H4	11	3	7	10	11
IDL	3	2	2	3	3
K1	6	4	4	5	6
K2	9	7	9	9	9
L5	6	2	6	6	6
L6	14	3	11	14	14
NP1	13	9	12	13	13
NP4	12	8	10	12	12
NP5	16	8	14	15	16
NZ1	15	5	7	15	15
NZ2	81	18	48	71	77
NZ3	43	17	31	43	43
NZ4	40	12	29	36	40
NZ5	11	3	5	7	8
NZ10	9	1	2	9	9
NZ11	16	0	0	10	16
NZ12	19	2	3	6	16
NZ13	8	2	4	8	8
NZ17	10	0	1	5	9
NZ18	17	2	11	13	15
NZ21	14	1	3	9	14
S1	47	11	26	44	46
S2	13	5	11	13	13
S3	13	3	9	13	13
S7	15	4	9	13	15
S8	7	2	3	7	7
Total	483	142	291	424	469

Table 4-7: F-measure for third image set

k_b			
0.2	**0.3**	**0.4**	**0.5**
0.44	0.71	0.77	0.64

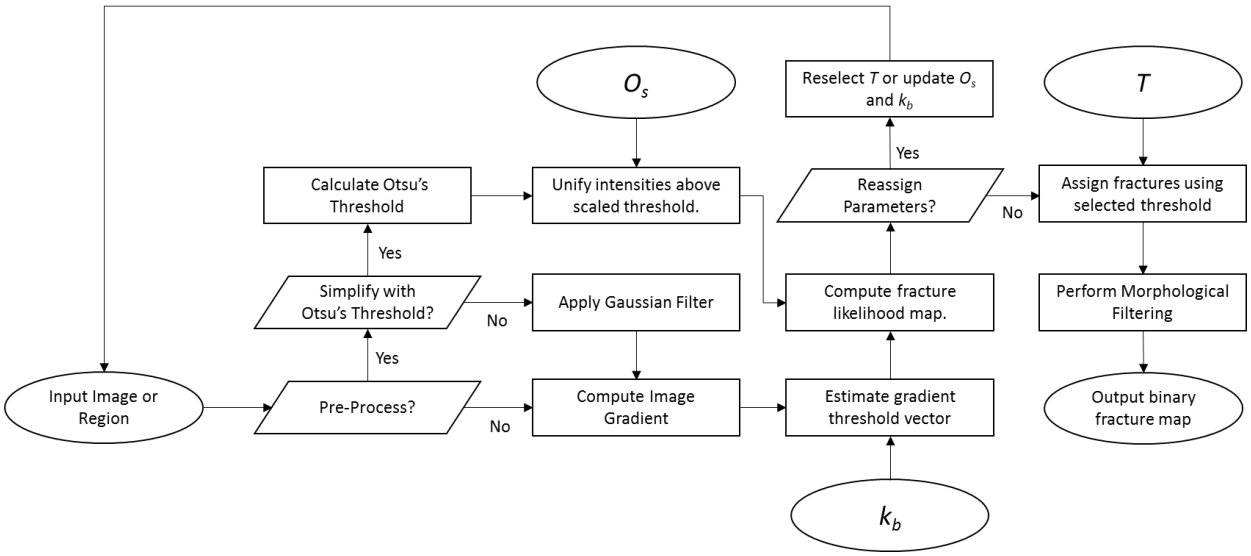

Figure 4-1: Developed computation sequence fracture detection method

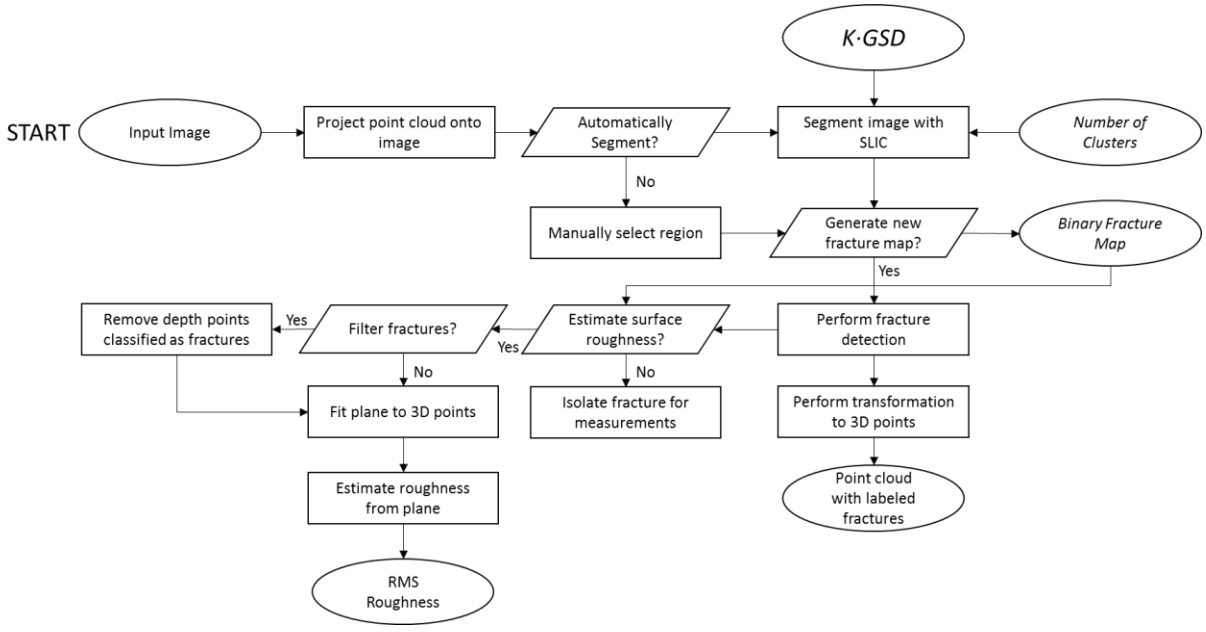

Figure 4-2: 3D-enabled image processing framework

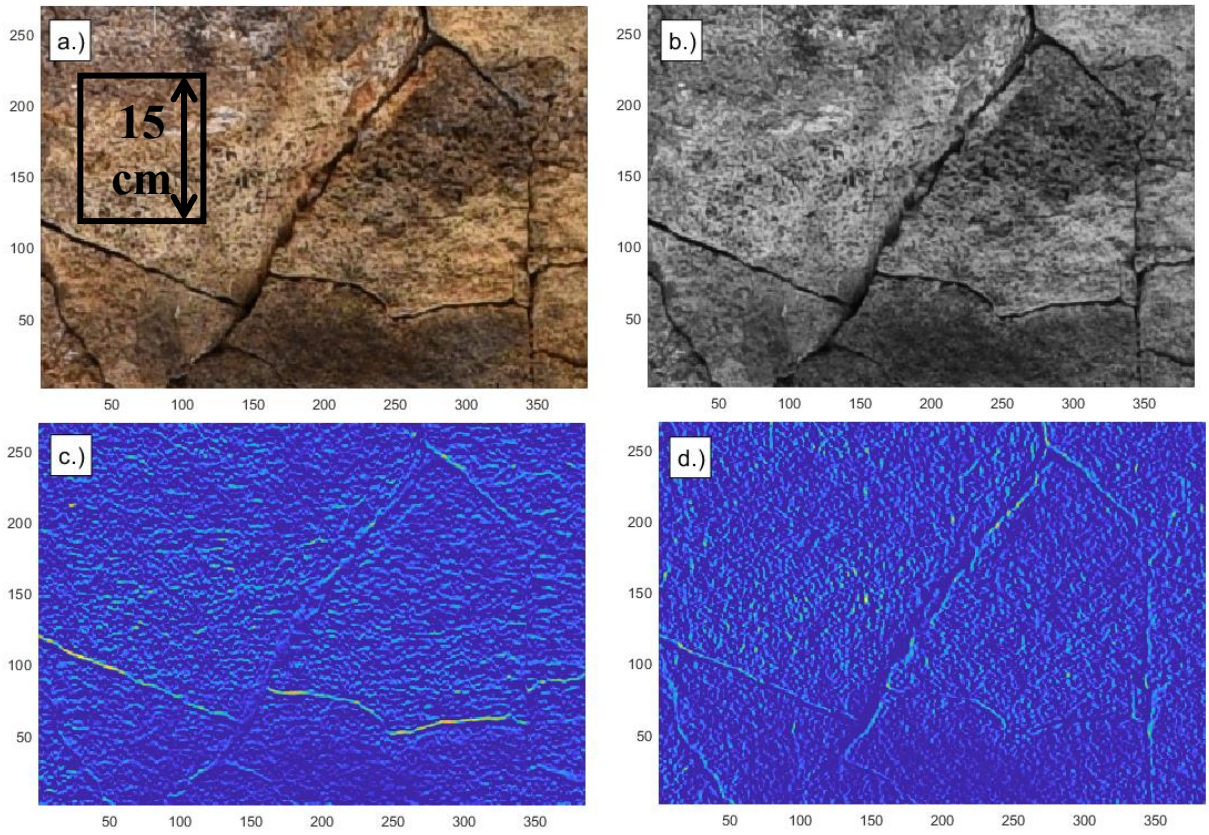

Figure 4-3: (a) Sample image; (b) grayscale image; (c) vertical image gradient; and (d) horizontal image gradient

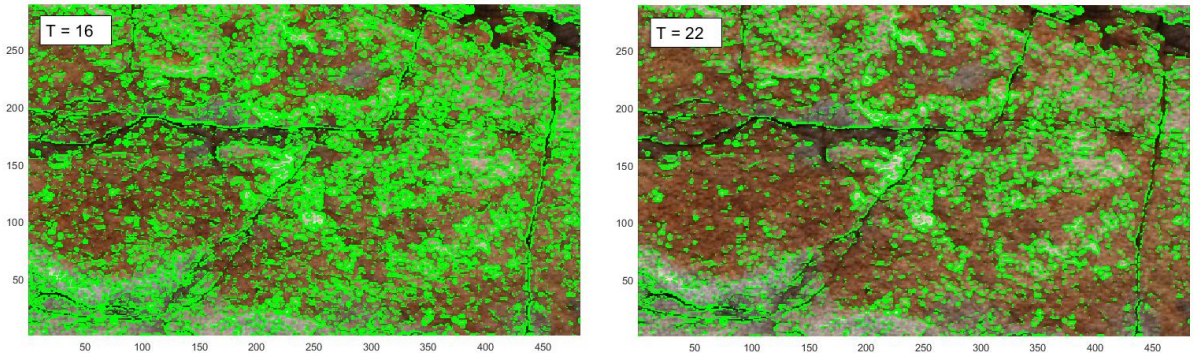

Figure 4-4: Effect of increasing gradient threshold

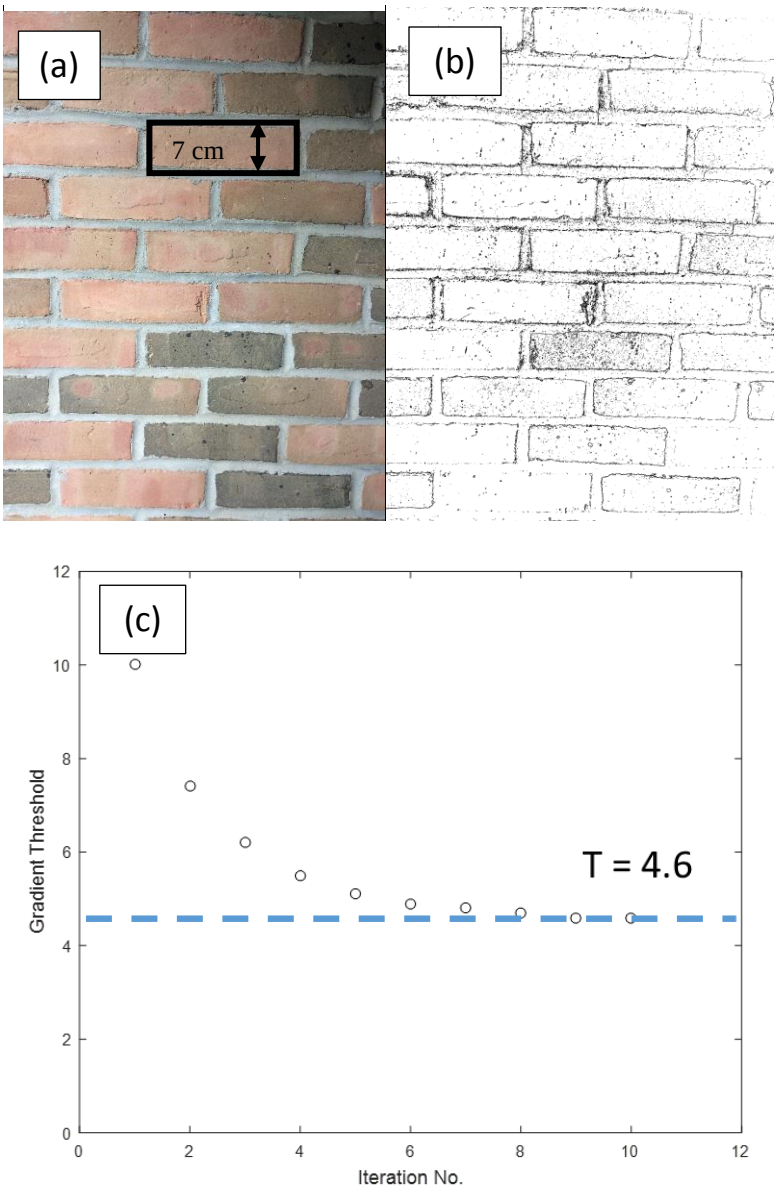

Figure 4-5: (a) Photo of brick wall; (b) binary image of brick wall generated with threshold T; and (c) convergence of threshold value

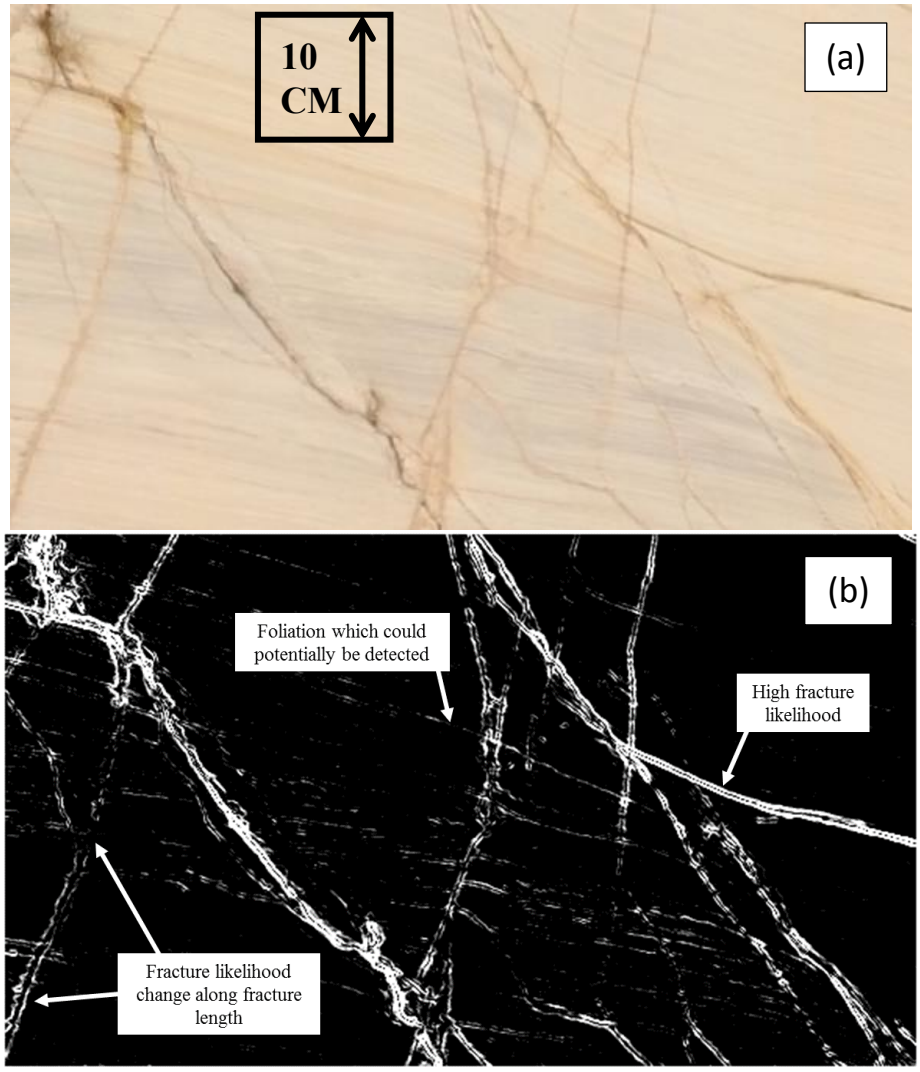

Figure 4-6: Example multi-threshold potential fracture map

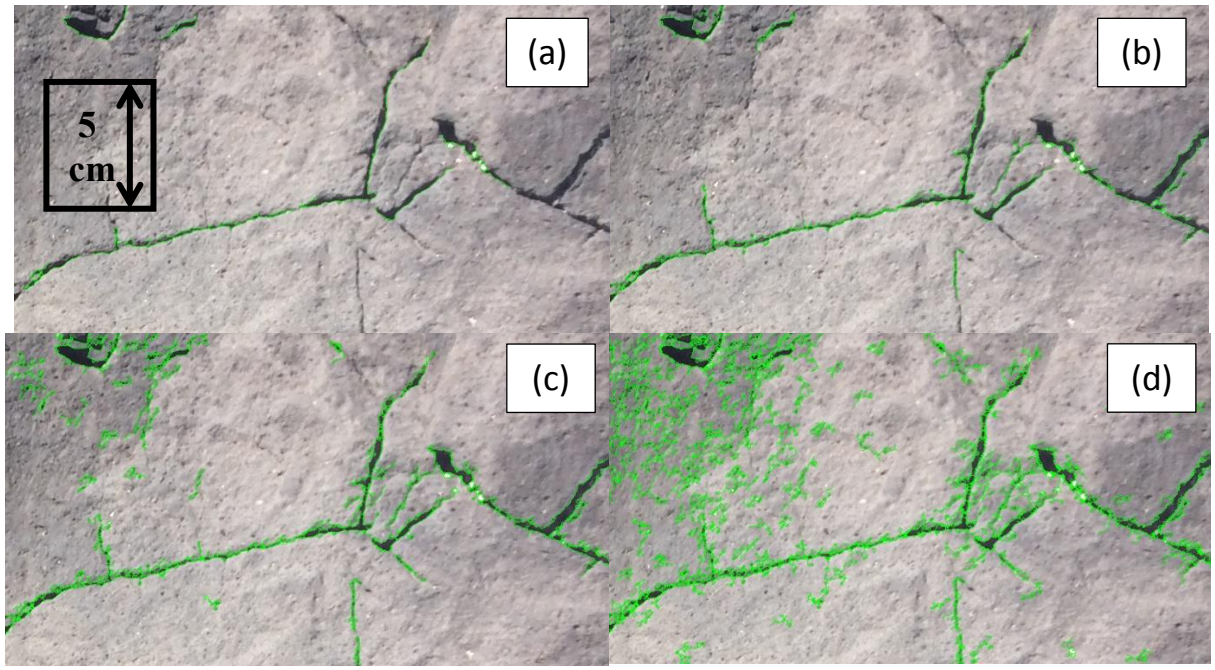

Figure 4-7: Effect of k_b on sample images: (a) k_b = 0.2; (b) k_b = 0.3; (c) k_b = 0.4; (d) k_b = 0.5

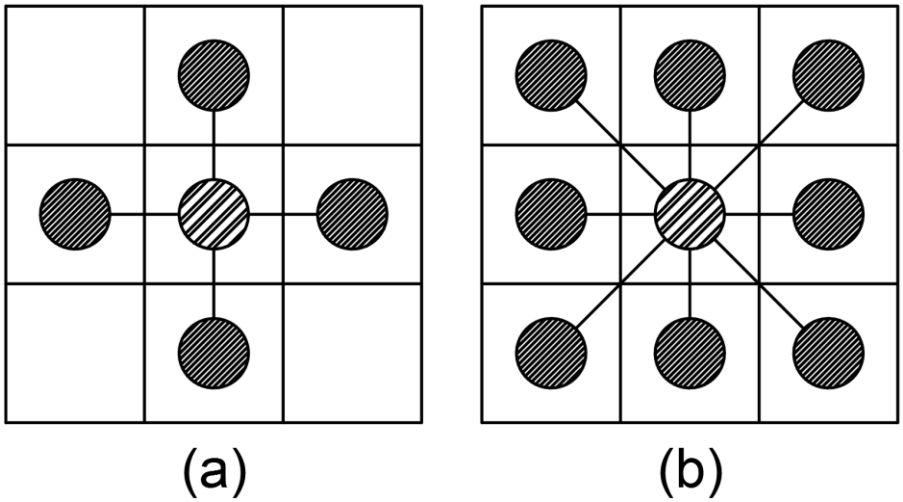

Figure 4-8: (a) 4-way and (b) 8-wayconnectivity neighborhoods

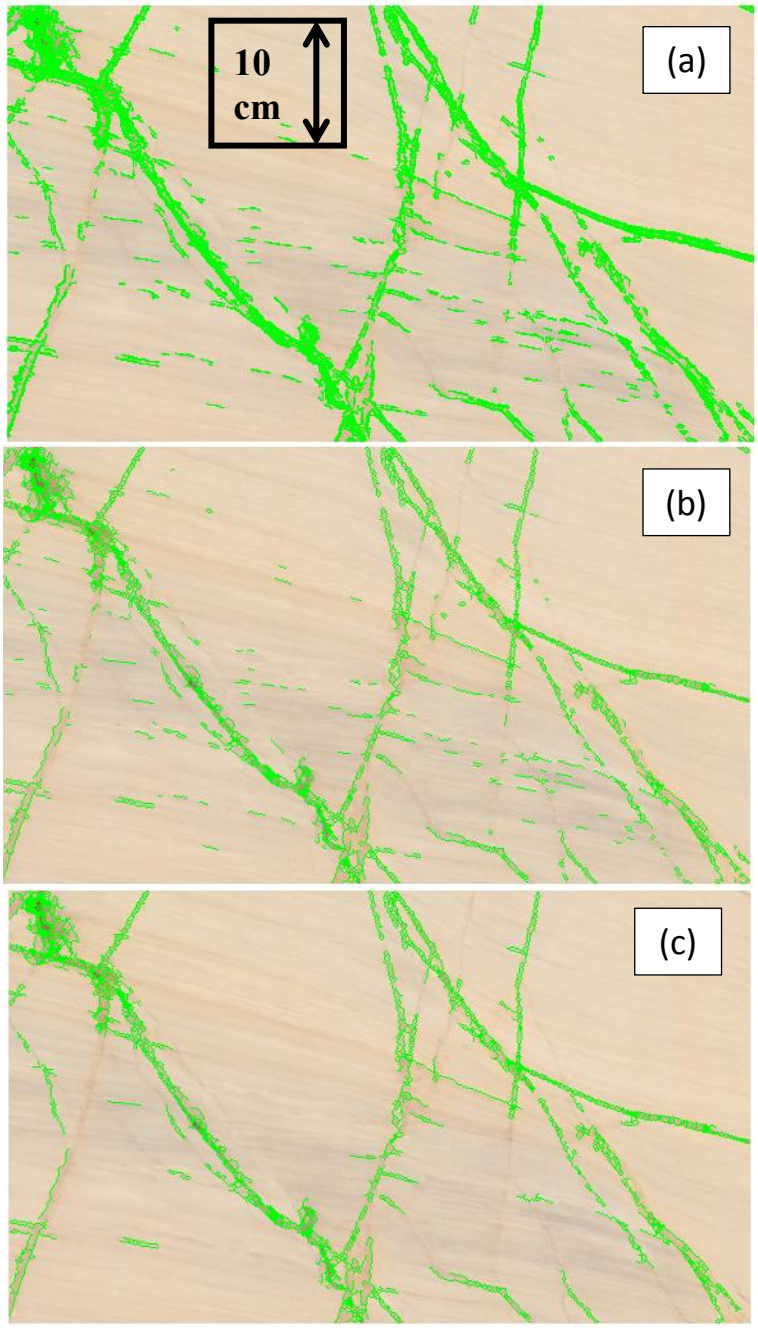

Figure 4-9: Example marble image (M1) subjected to (a) first morphologic filtering step; (b) binary object thinning; and (c) second morphologic filtering step

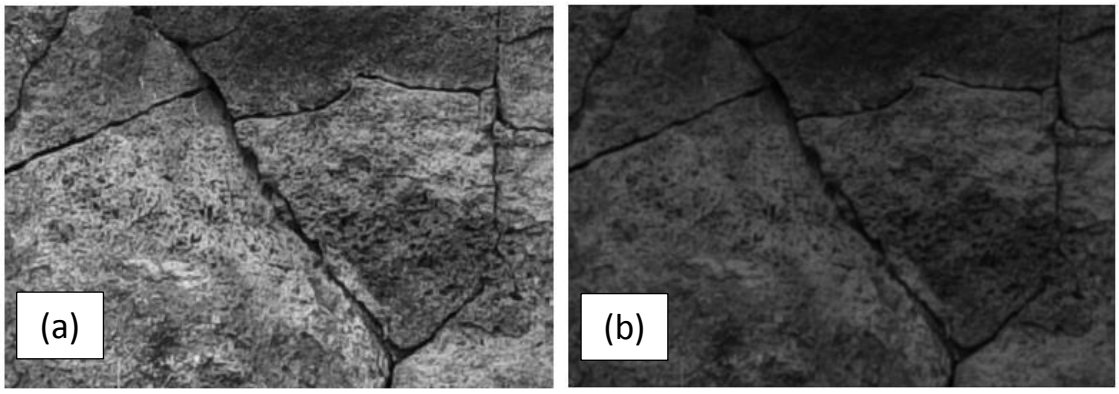

Figure 4-10: Sample image (a) before applying Gaussian filter and (b) after

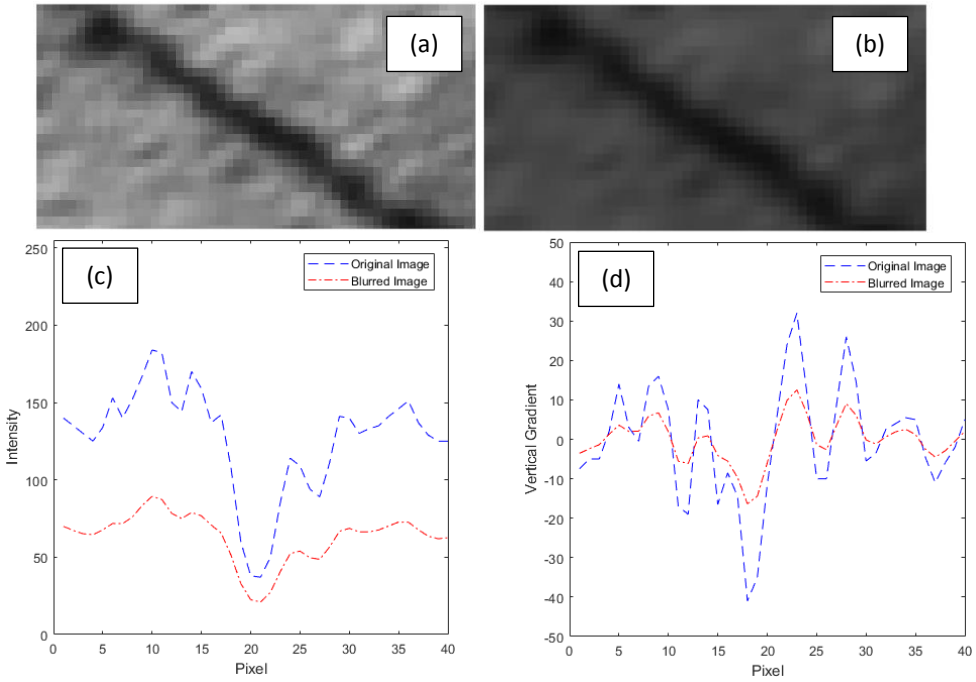

Figure 4-11: Effect of blurring on fractures: (a) unfiltered fracture; (b) filtered fracture; (c) intensity across fracture; and (d) vertical gradient across fracture

Figure 4-12: Examples of staining of weathered basalt

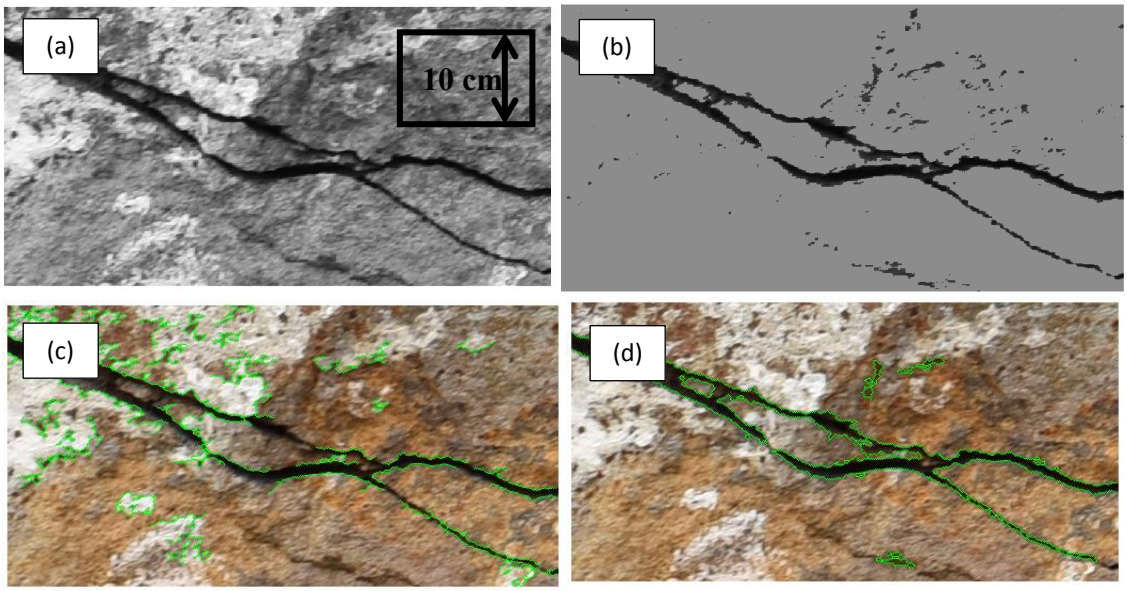

Figure 4-13: (a) Unaltered grayscale image; (b) image altered using modified Otsu's threshold (O_s = 0.5); (c) final fracture detection of unaltered image; (d) final fracture detection of altered image

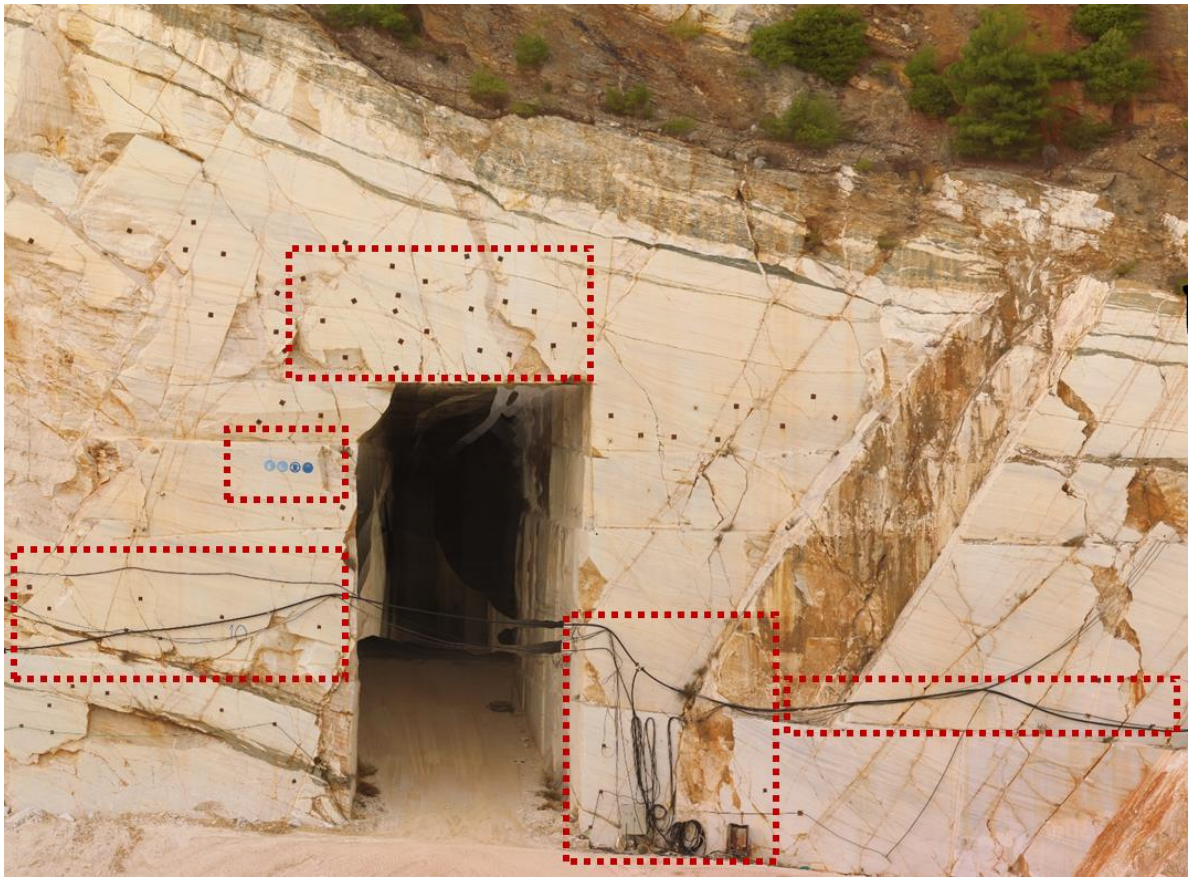

Figure 4-14: Orthophoto of marble quarry wall with human-made objects highlighted

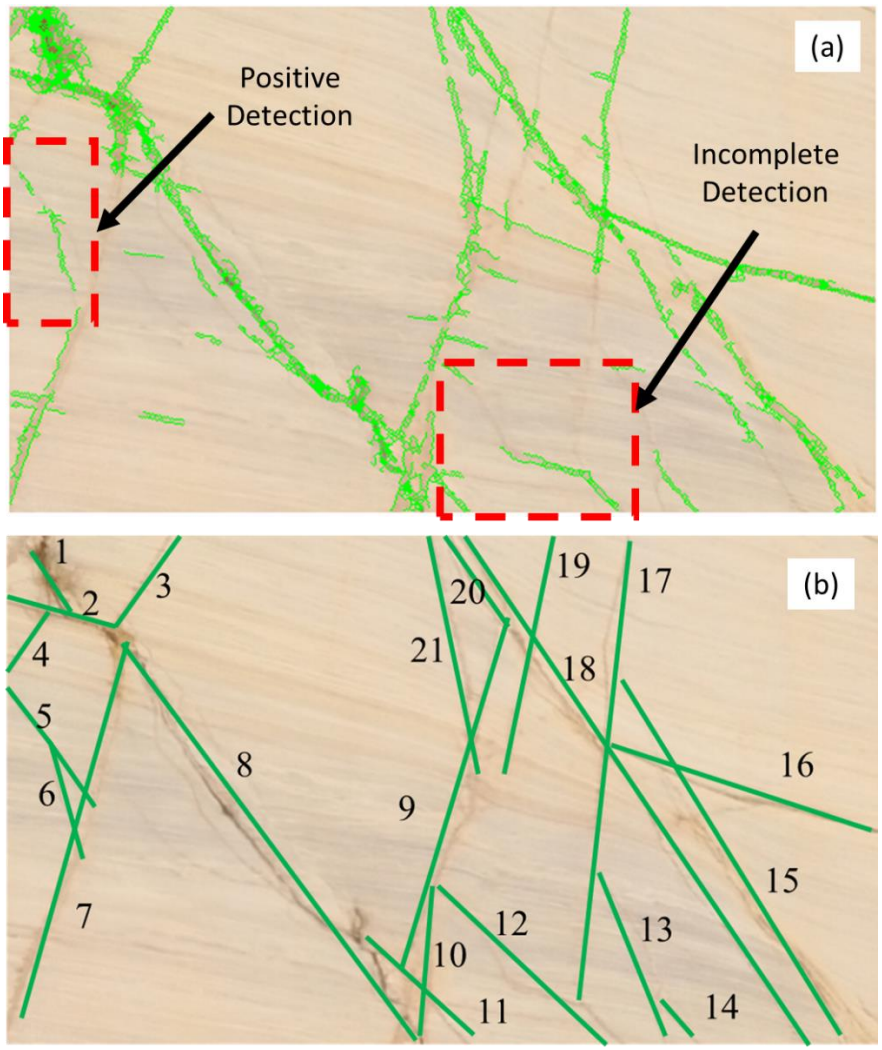

Figure 4-15: (a) Example of automatic fracture detection performed on a marble image (M1) with examples of a positive detection and incomplete detection of fractures; and (b) simplified labeling of manually-detected fractures

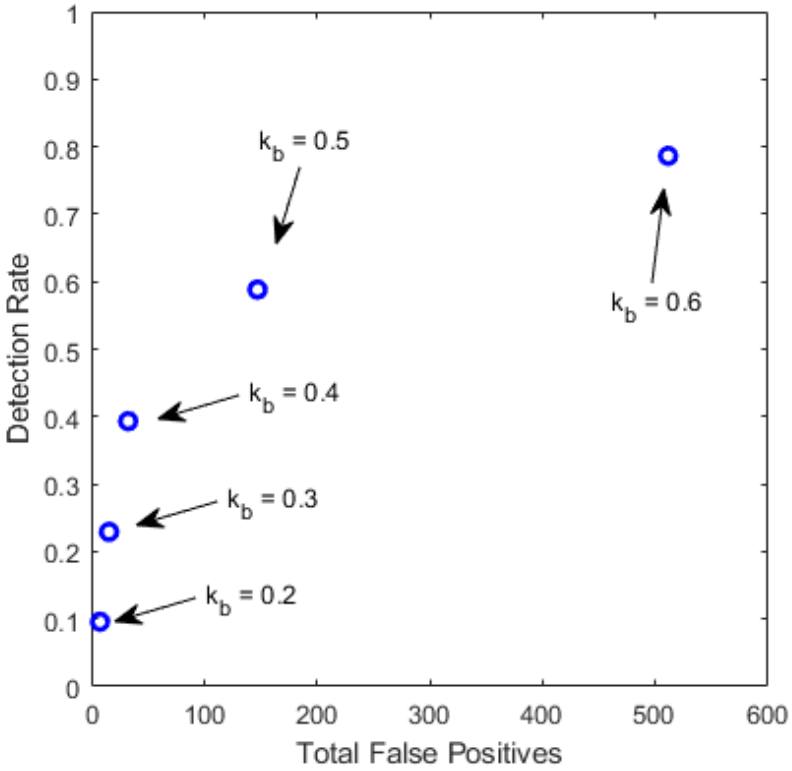

Figure 4-16: True positive rate as function of total false positives for marble orthophoto images

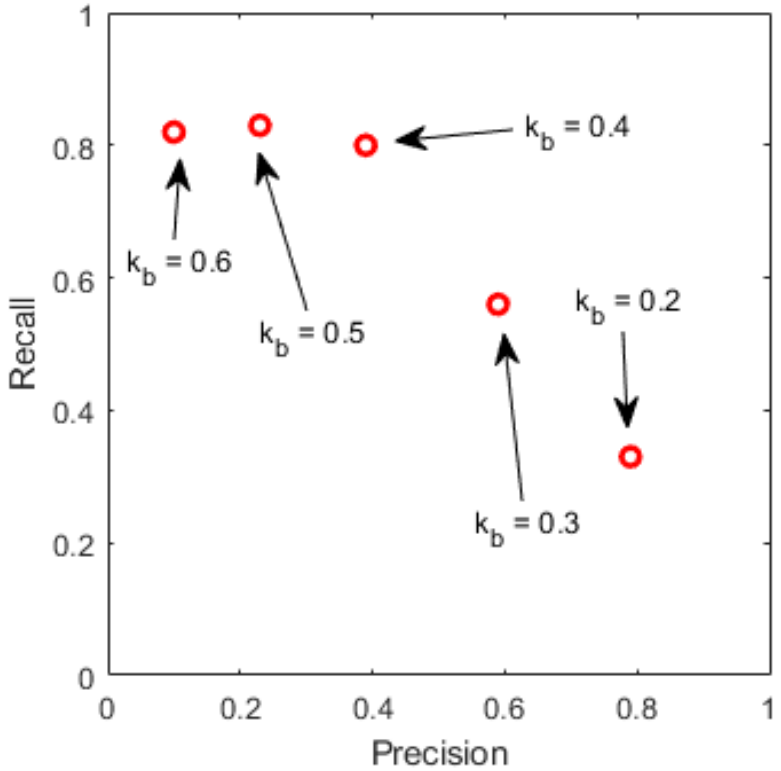

Figure 4-17: Precision-Recall Relationship for marble orthophoto images

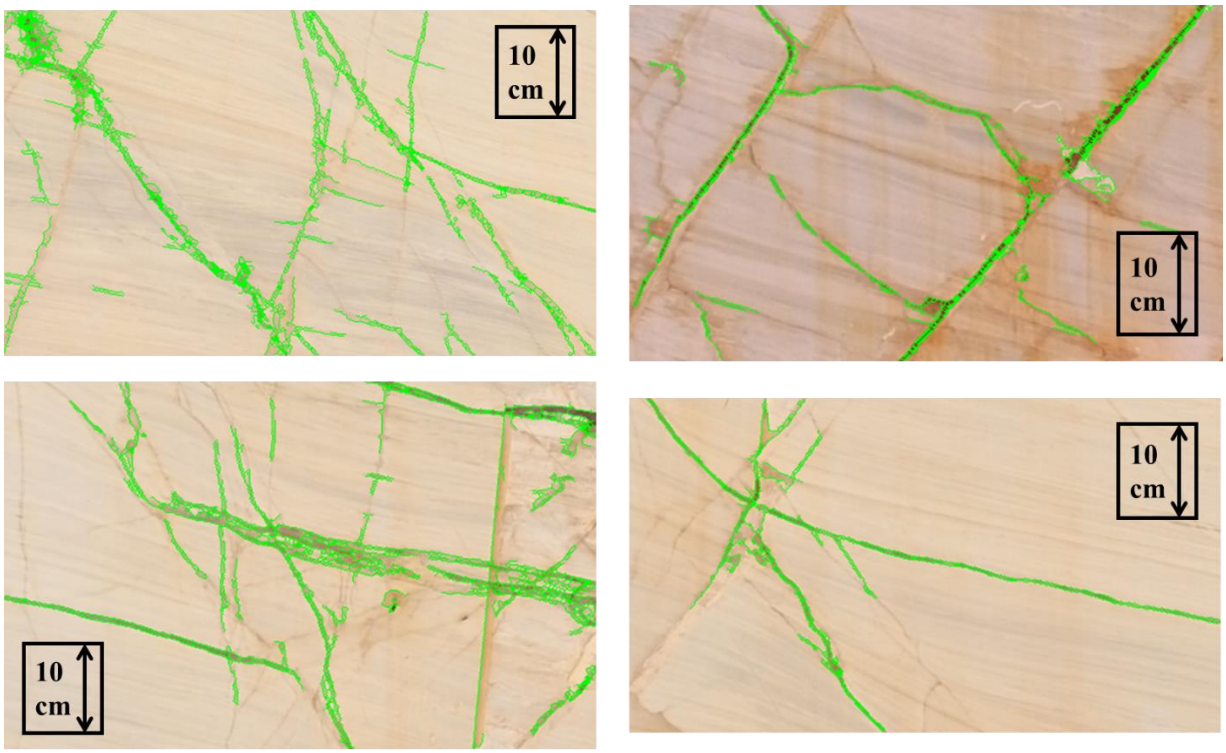

Figure 4-18: Example output from fracture detection on four marble images with k_b=0.5

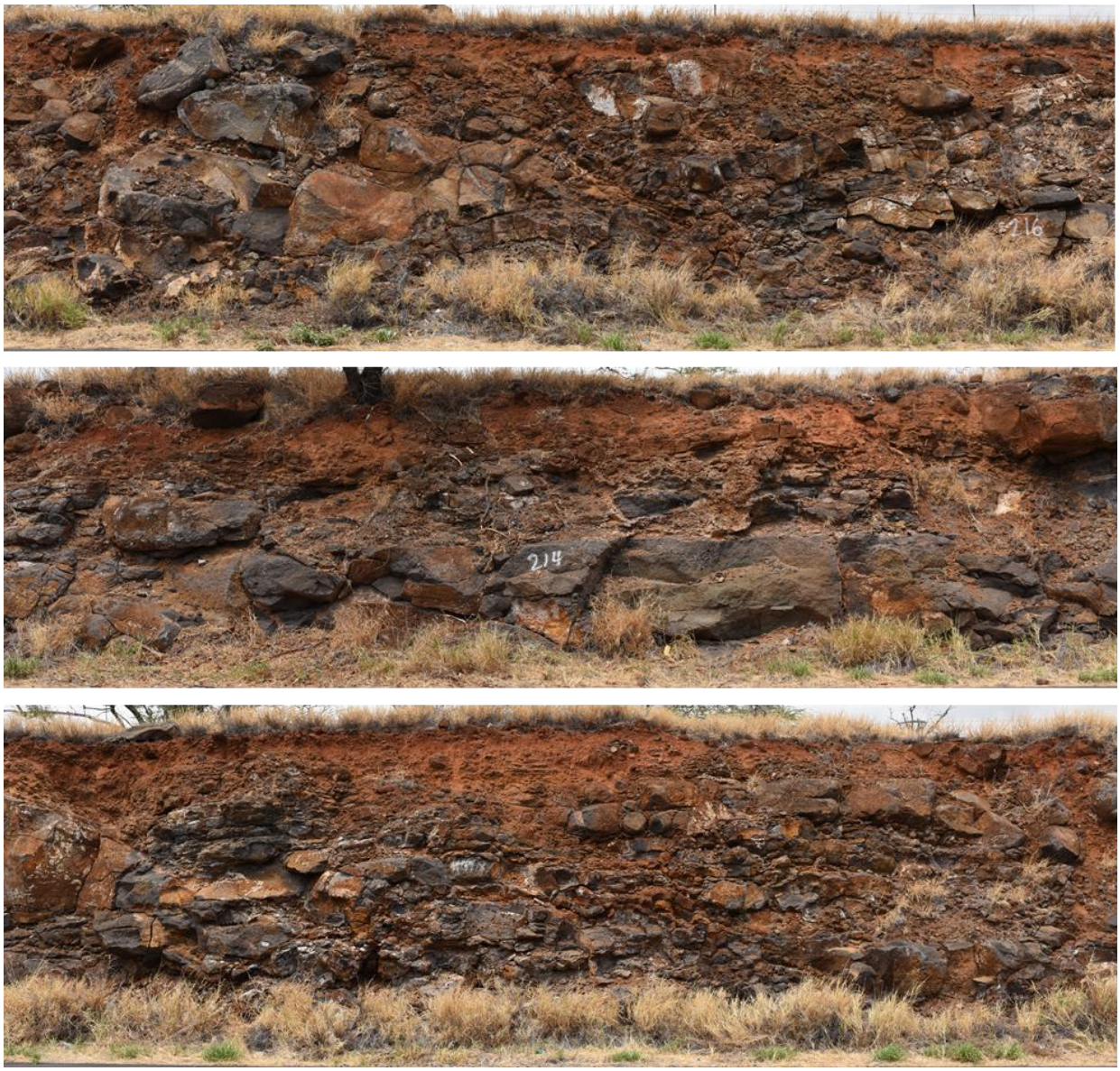

Figure 4-19: Example photos of a roughly 4 m high basalt outcrop in Hawaii

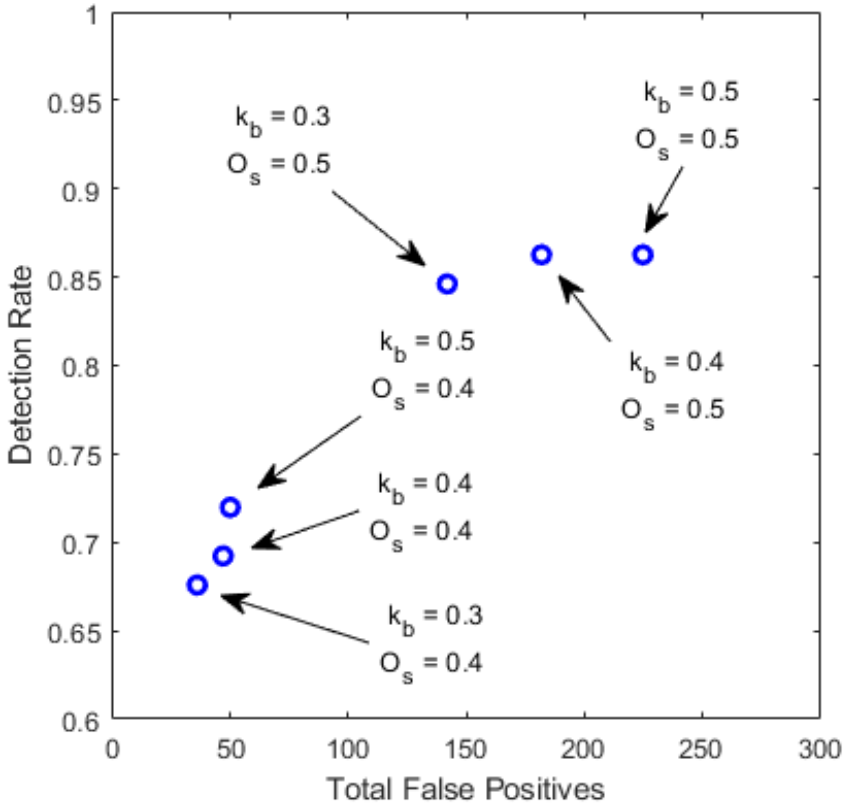

Figure 4-20: Detection rate as a function of false positives for basalt images

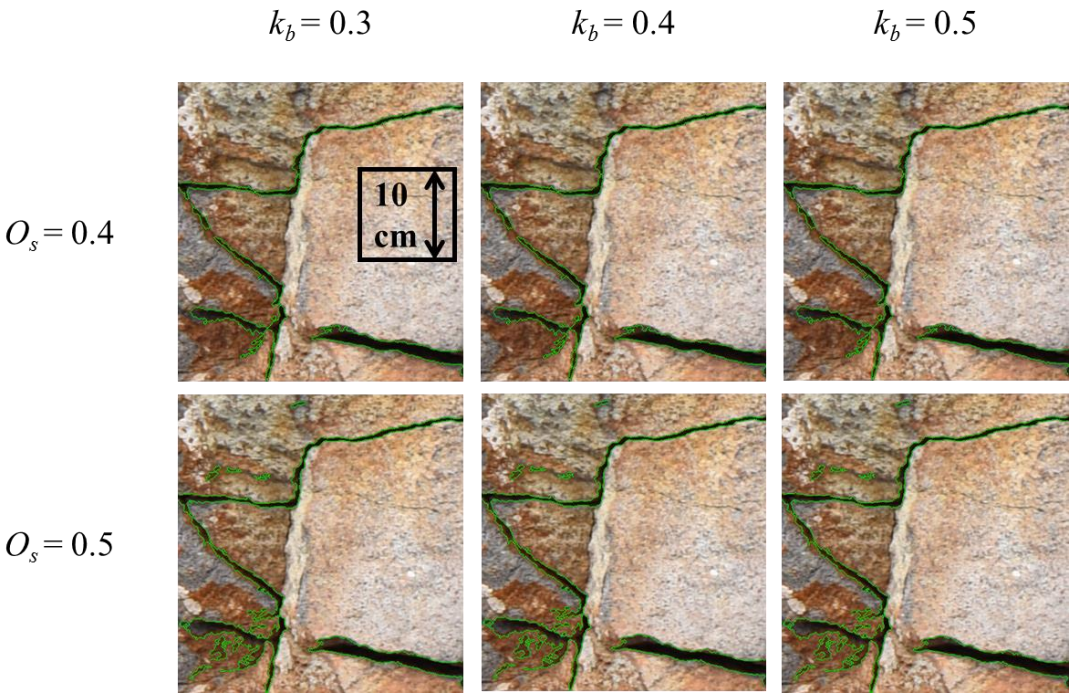

Figure 4-21: Example of single basalt image subjected to different control parameters

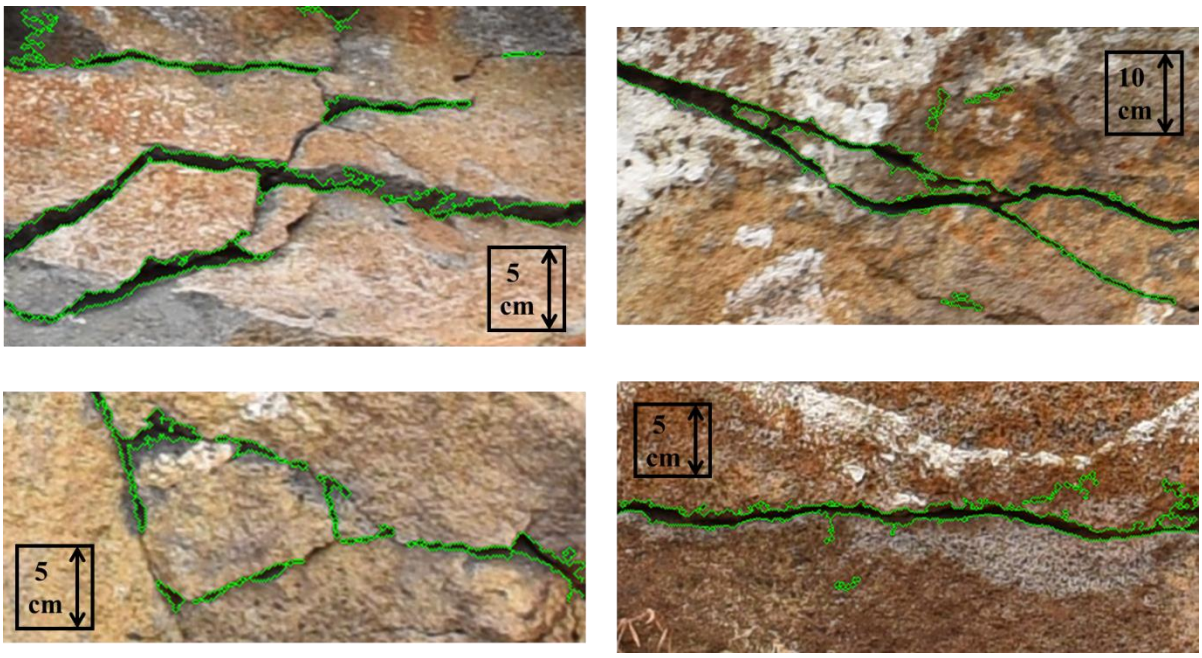

Figure 4-22: Example output from fracture detection on four basalt images

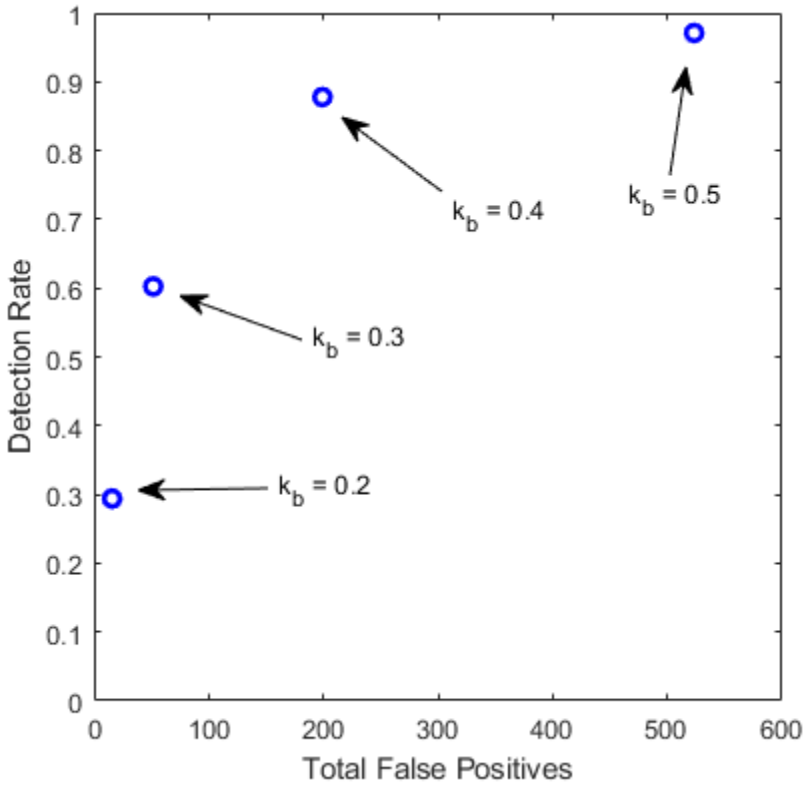

Figure 4-23: Detection rate as a function of false positives for the third image set

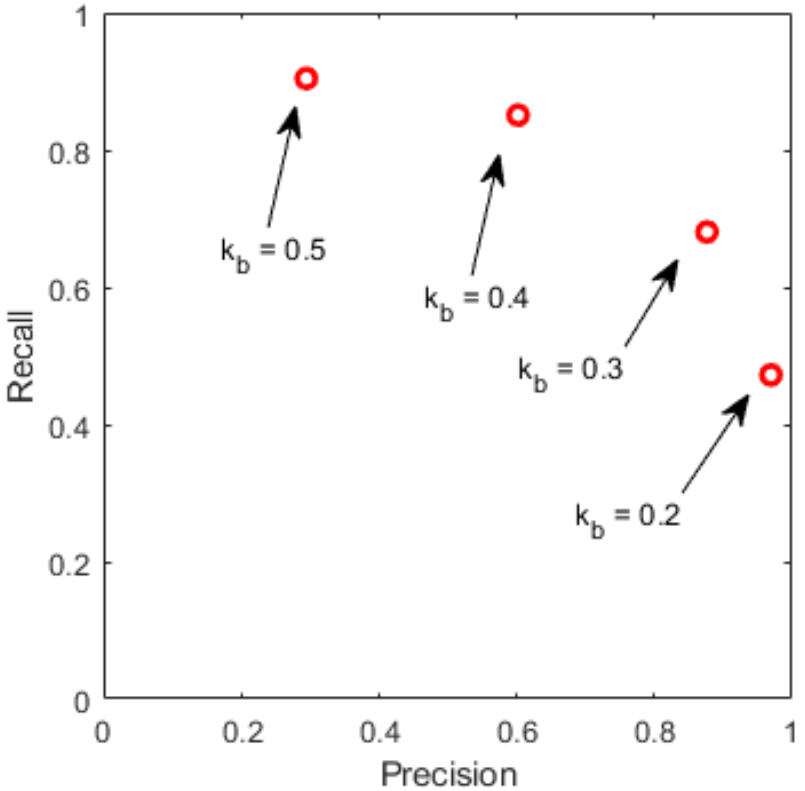

Figure 4-24: Precision-recall relationship for third image set

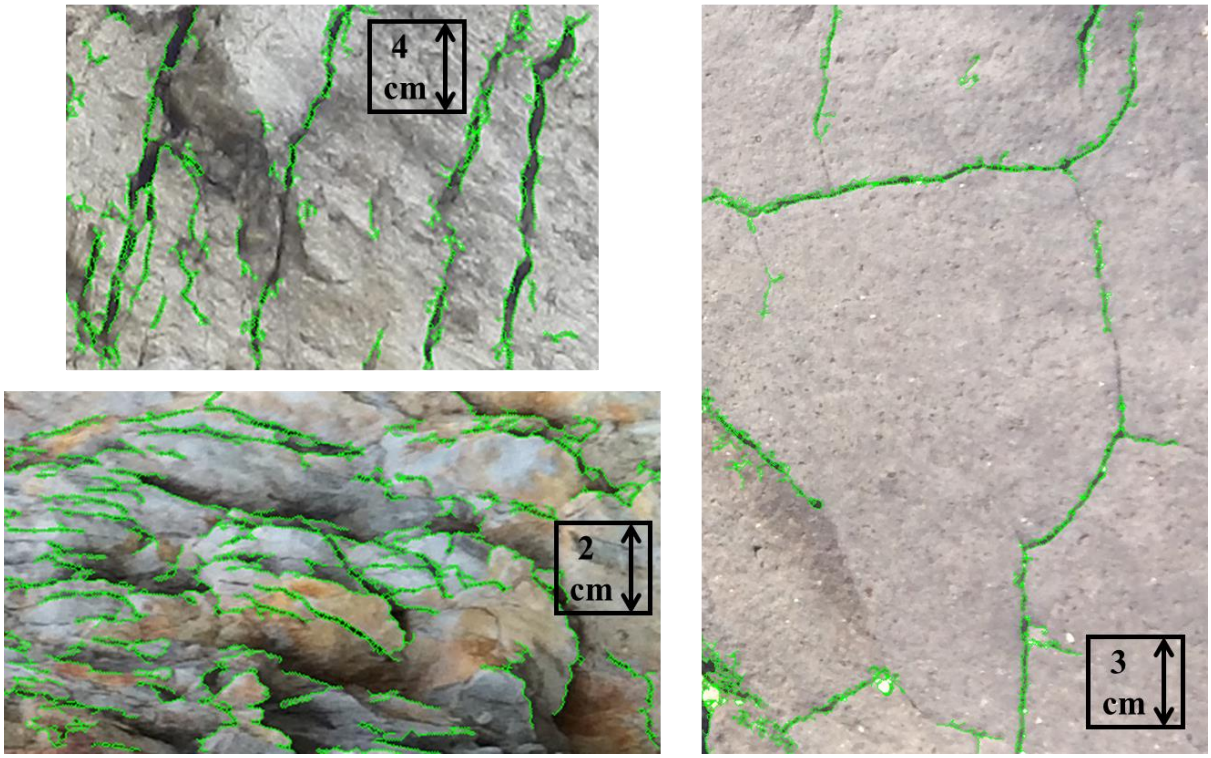

Figure 4-25: Output from fracture detection performed on three examples from the third image set with k_b = 0.4

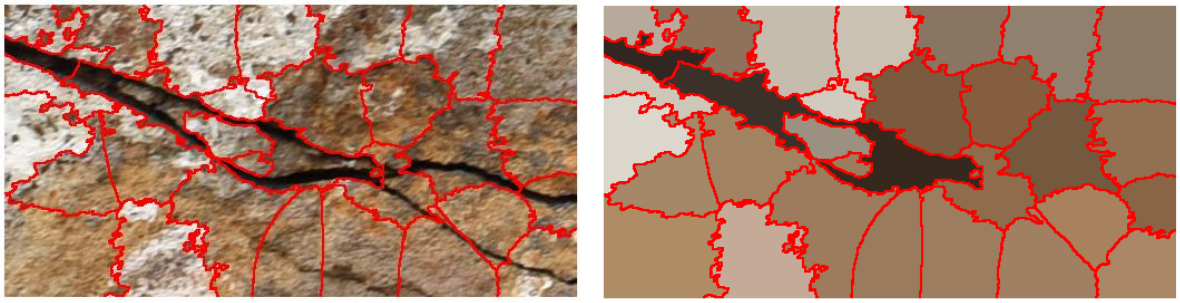

Figure 4-26: (a) SLIC (N_c=10) applied to a sample image and (b) median function applied to the superpixels

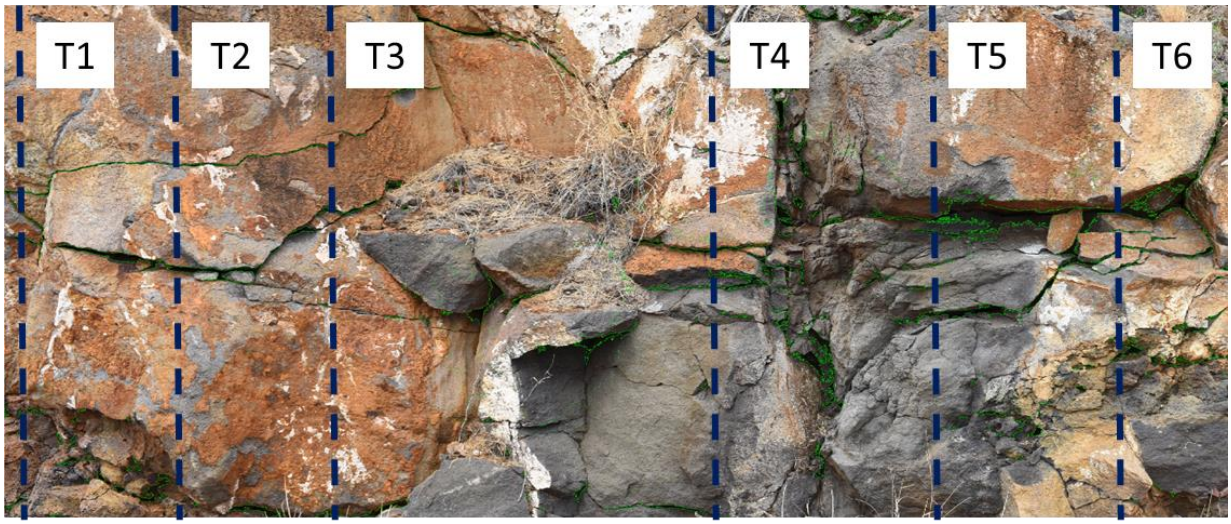

Figure 4-27: Sample transects for manual fracture counting, approximate height is 2 m

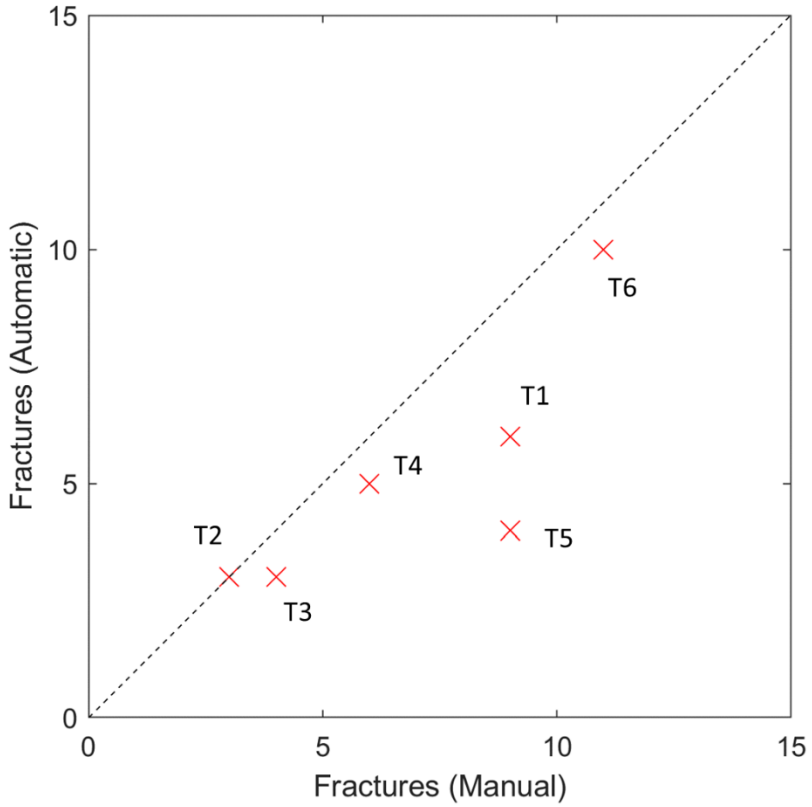

Figure 4-28: Automatic fracture detection versus manual fracture counting for transects in Figure 4-27

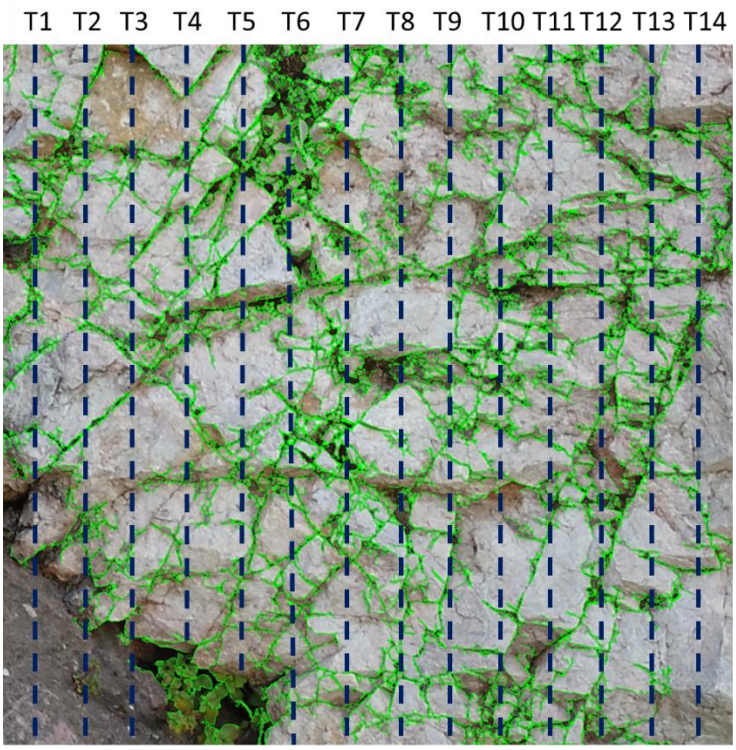

Figure 4-29: Transects used to assess fracture detection of interlocked angular blocky rock with k_b=0.4

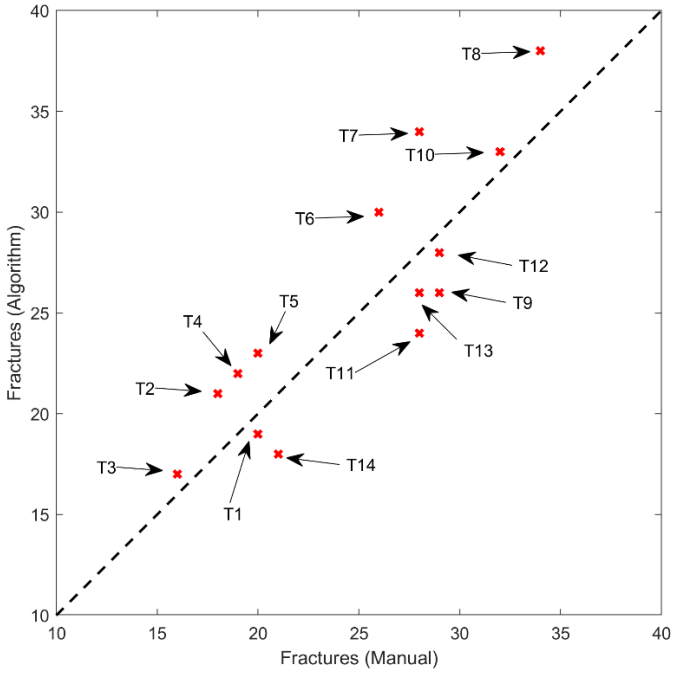

Figure 4-30: Results of fracture detection compared to manual fracture counting for transects in Figure 4-29

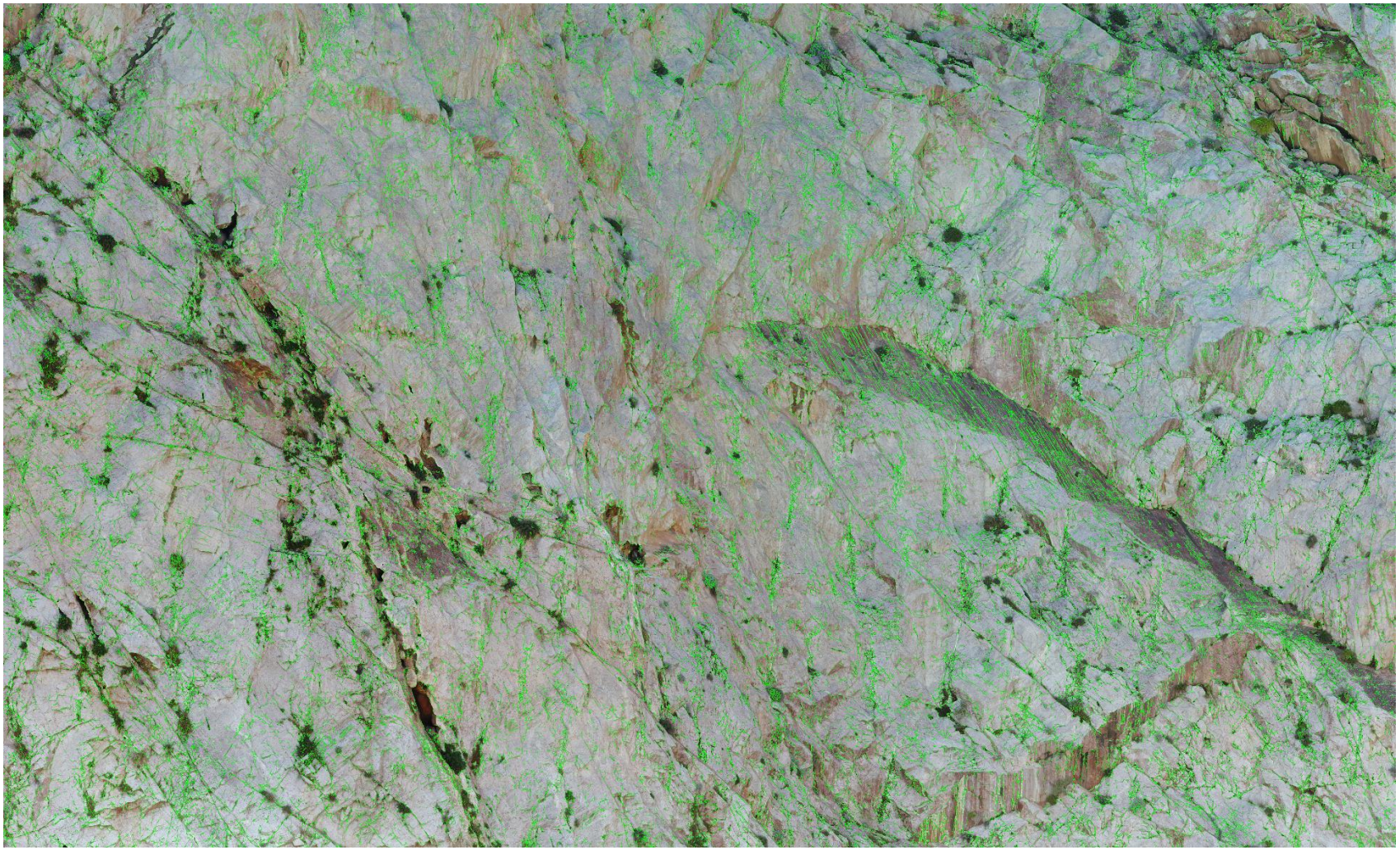

Figure 4-31: Fracture detection with k_b = 0.35 applied to the marble quarry orthophoto

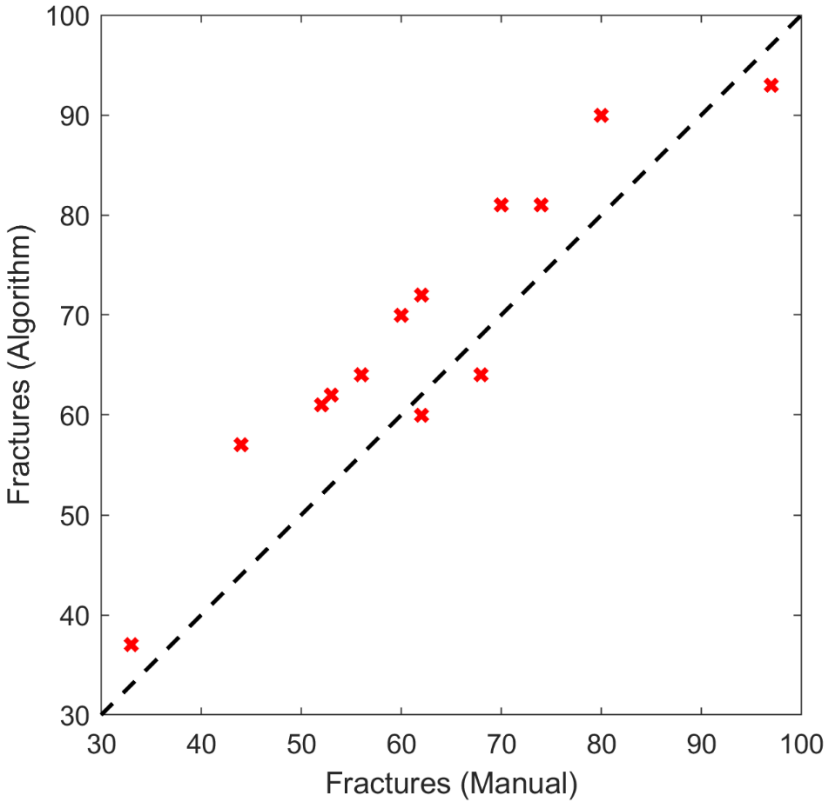

Figure 4-32: Comparison of fracture detection results to manual counting for the quarry orthophoto

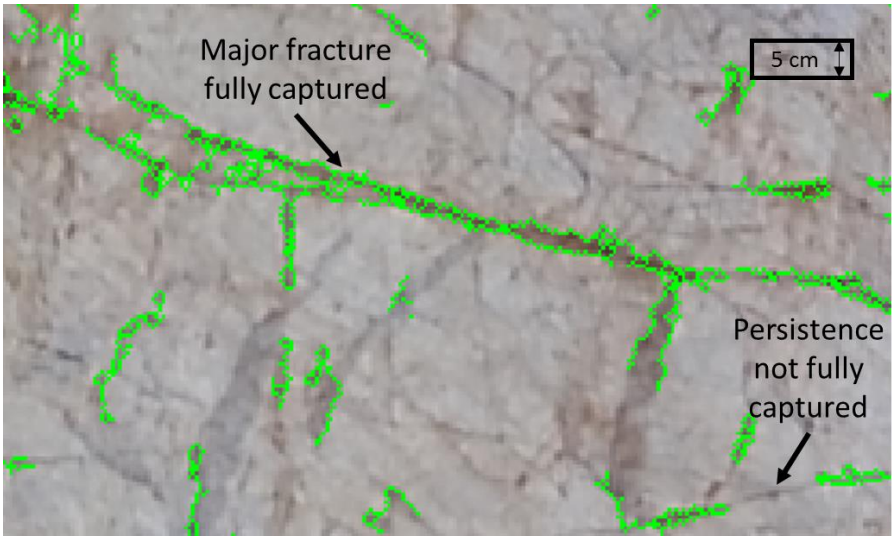

Figure 4-33: Example of fracture detection; narrowest fractures are not detected, or are partially detected

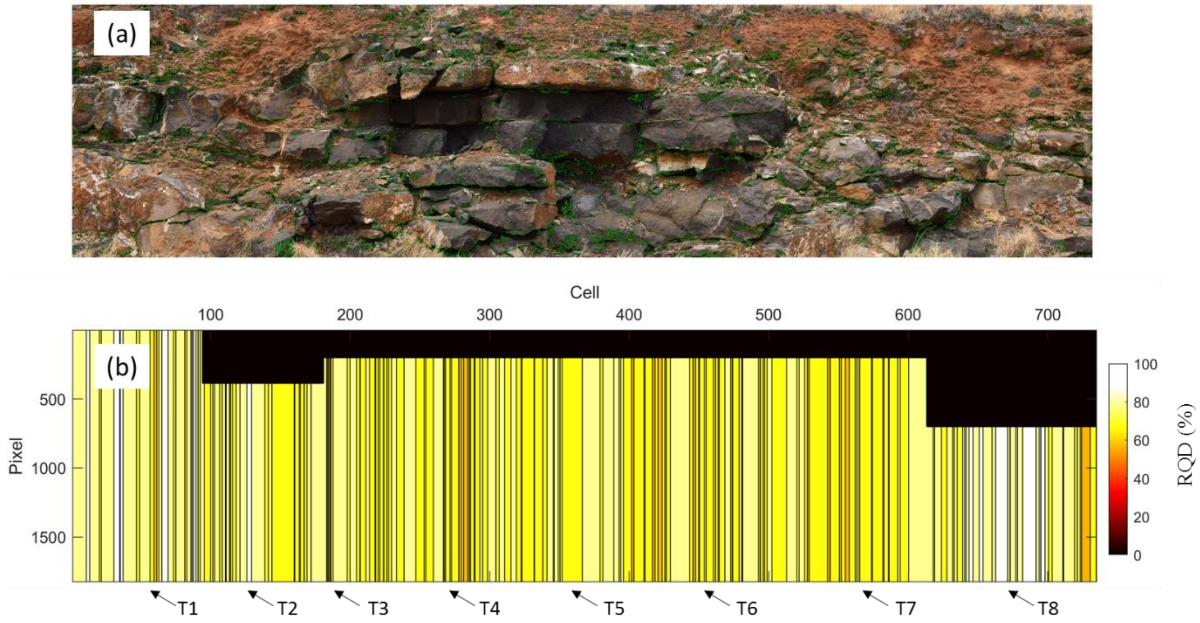

Figure 4-34: (a) Profile subjected to fracture detection (green pixels), and (b) automatic RQD computation on 10 cm wide vertical transects

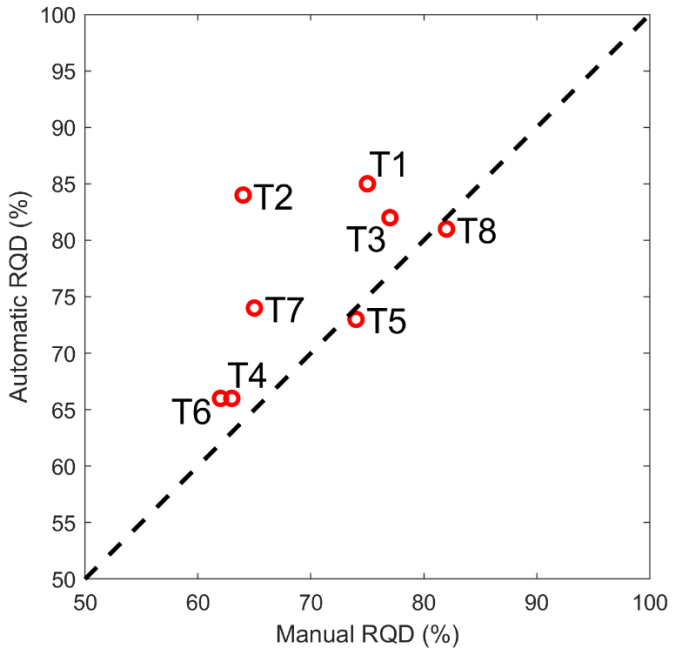

Figure 4-35: Comparison between automatic RQD and manual RQD calculations for vertical transects labeled in Figure 4-34; automatic values are the average of three closest cells

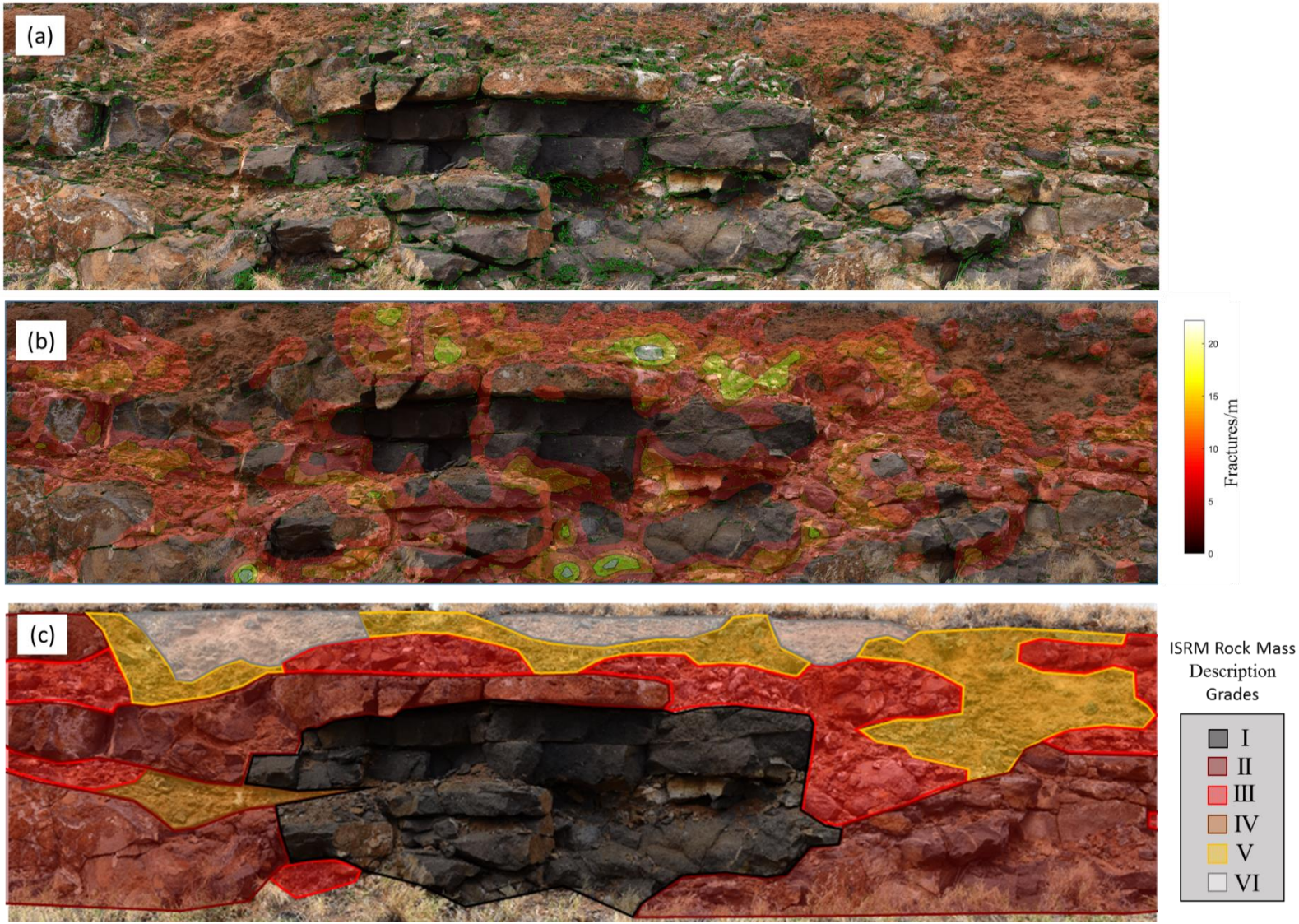

Figure 4-36: (a) Profile subjected to automatic fracture detection; (b) contours indicating fracture density (fractures per meter) overlain on photo of profile; and (c) manual classification of profile using the ISRM (1978) system

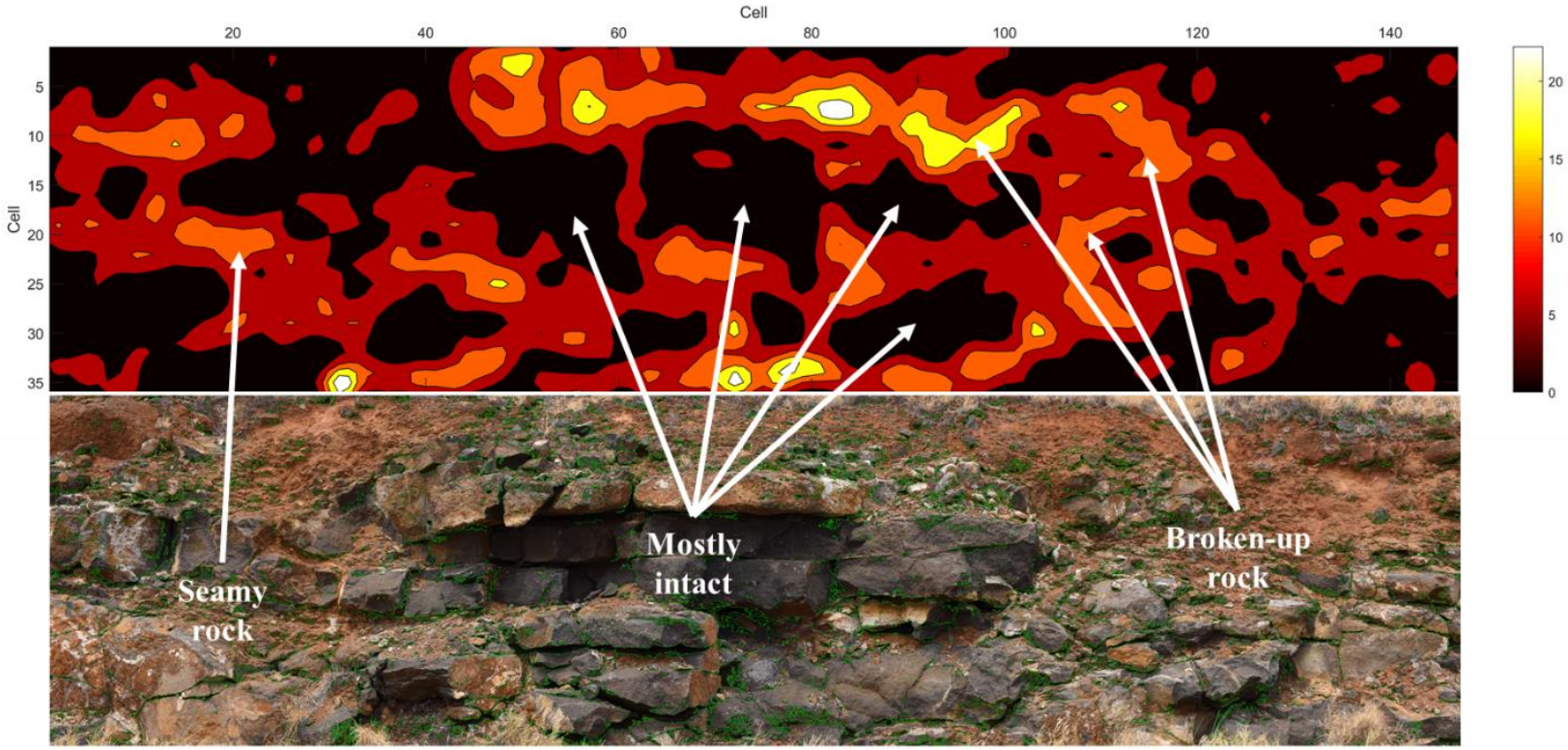

Figure 4-37: Heat map of fractures per meter and profile; examples of good performance are highlighted

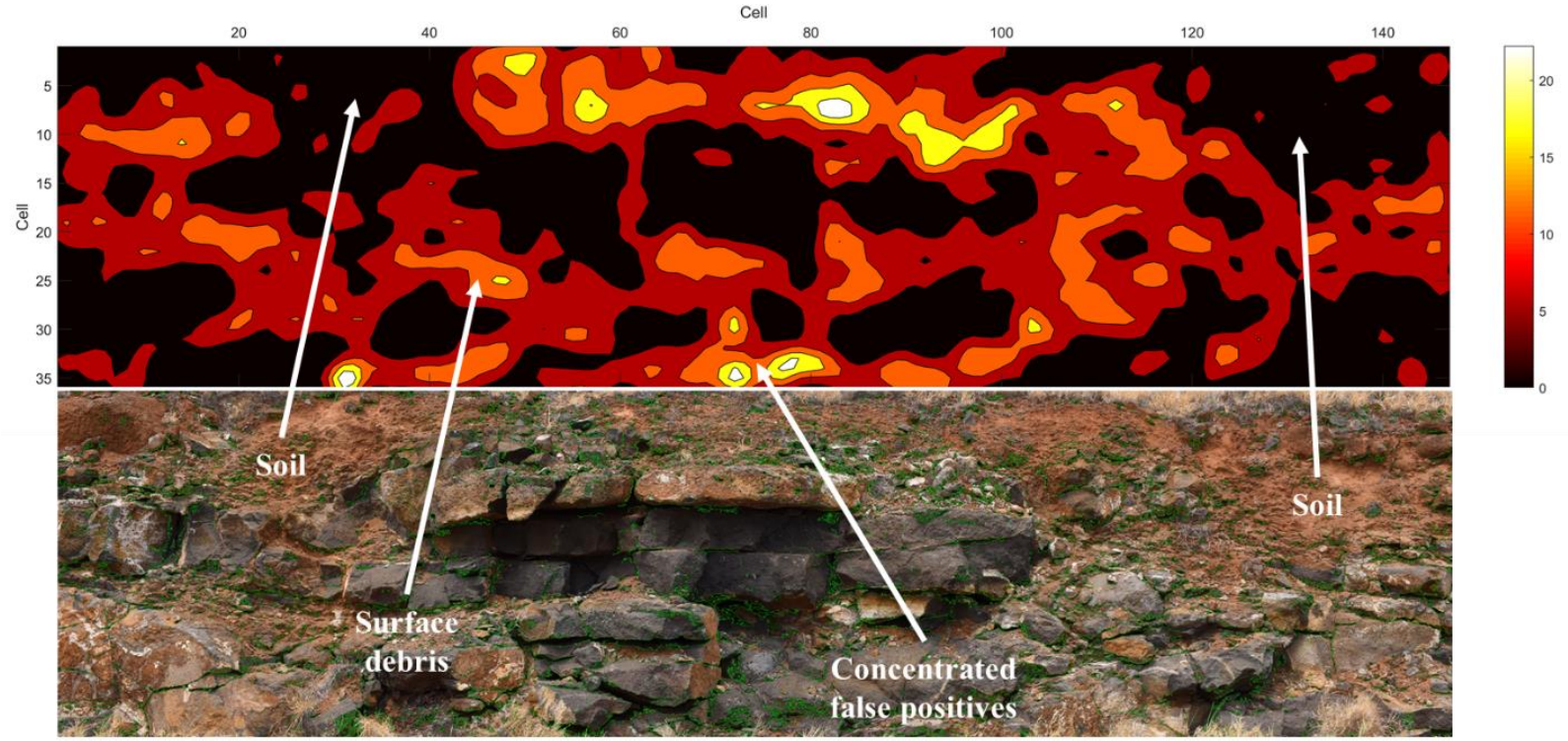

Figure 4-38: Heat map of fractures per m and profile; examples of erroneous results are highlighted

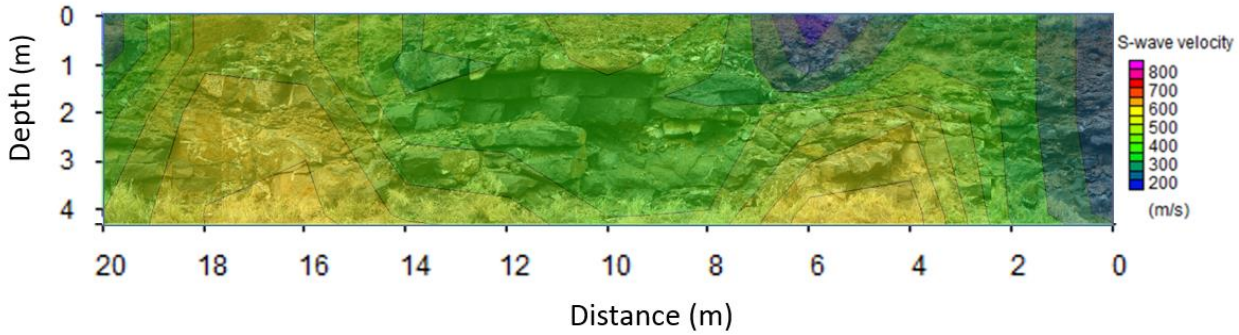

Figure 4-39: 2D V_s contours generated by MASW testing above outcrop

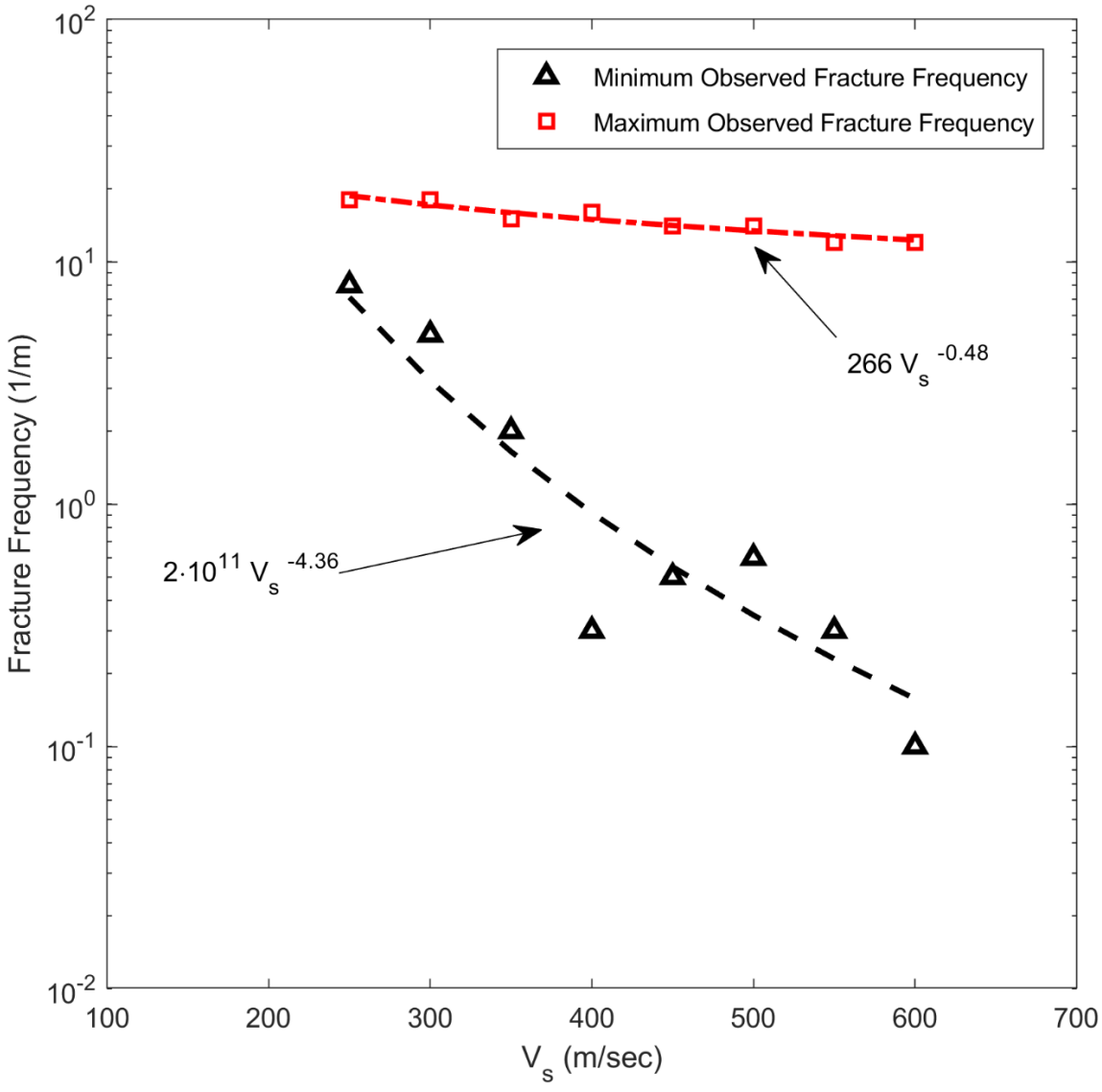

Figure 4-40: Correlation between approximate minimum and maximum fracture frequency and V_s generated by 2D MASW test

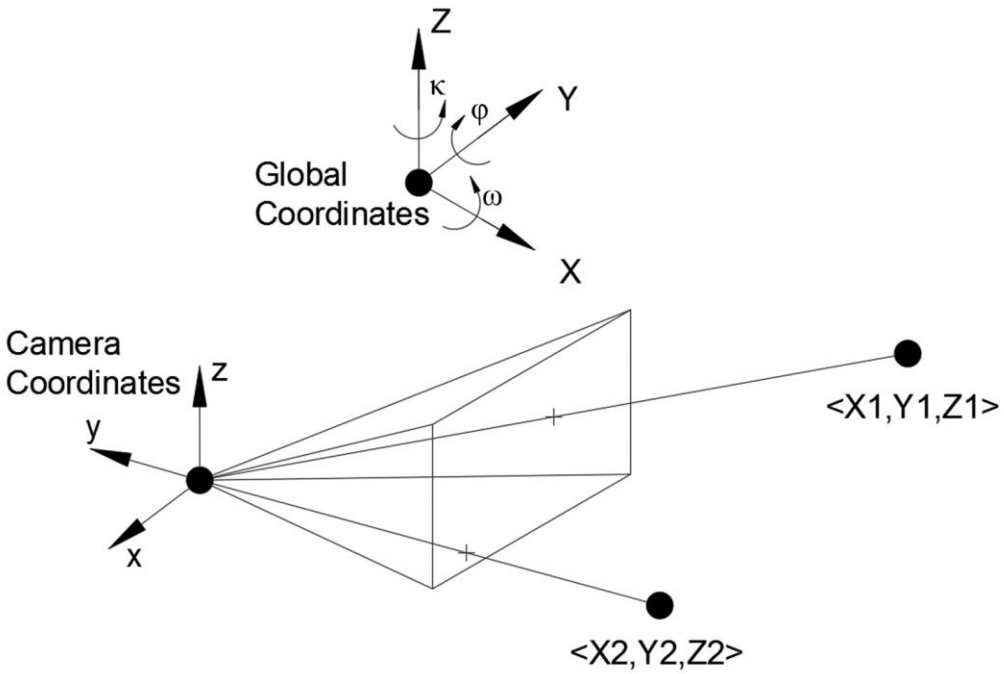

Figure 4-41: Example of camera and global coordinate systems

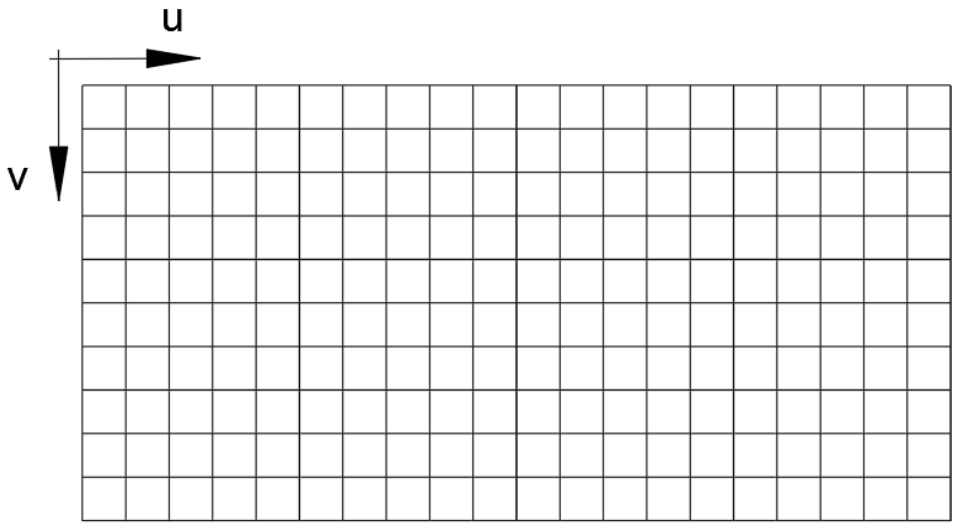

Figure 4-42: Pixel coordinate system

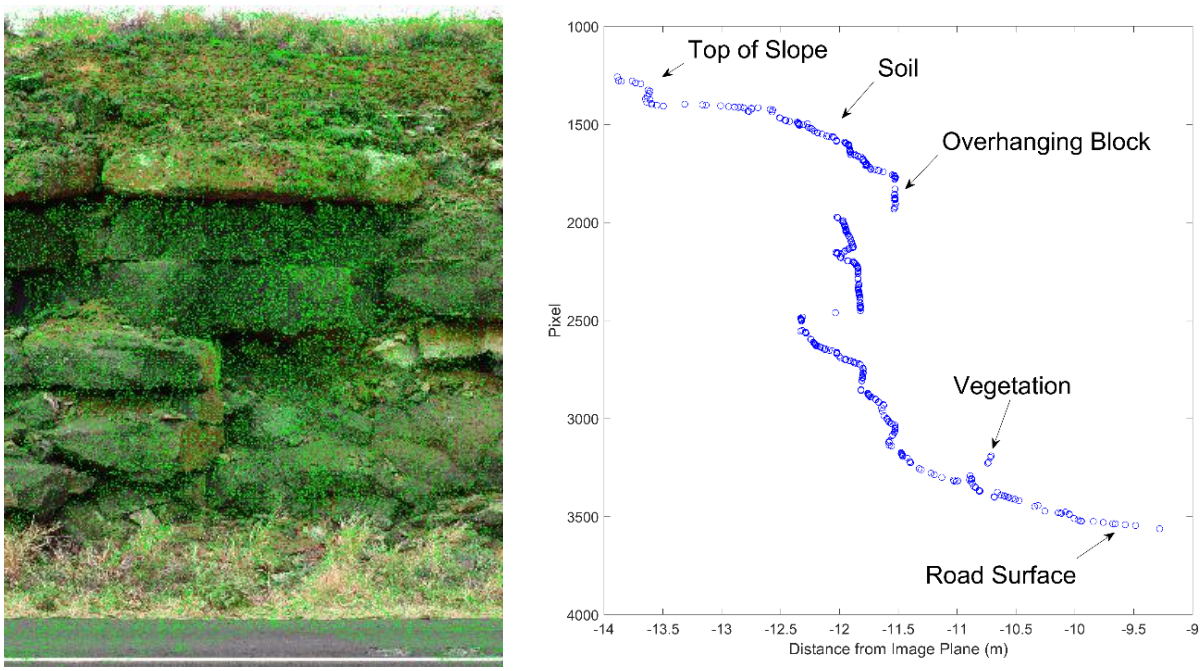

Figure 4-43: Slope profile derived from RGBD image

Algorithm 1 SLIC superpixel segmentation

/ Initialization */*

Initialize cluster centers $C_k = [l_k, a_k, b_k, x_k, y_k]^T$ by sampling pixels at regular grid steps S.

Move cluster centers to the lowest gradient position in a 3×3 neighborhood.

Set label $l(i) = -1$ for each pixel i.

Set distance $d(i) = \infty$ for each pixel i.

repeat

  / Assignment */*

  for each cluster center C_k **do**

    for each pixel i in a $2S \times 2S$ region around C_k **do**

      Compute the distance D between C_k and i.

      if $D < d(i)$ **then**

        set $d(i) = D$

        set $l(i) = k$

      end if

    end for

  end for

  / Update */*

  Compute new cluster centers.

  Compute residual error E.

until $E \leq$ threshold

Figure 4-44: SLIC Procedure (from Achanta et al., 2012)

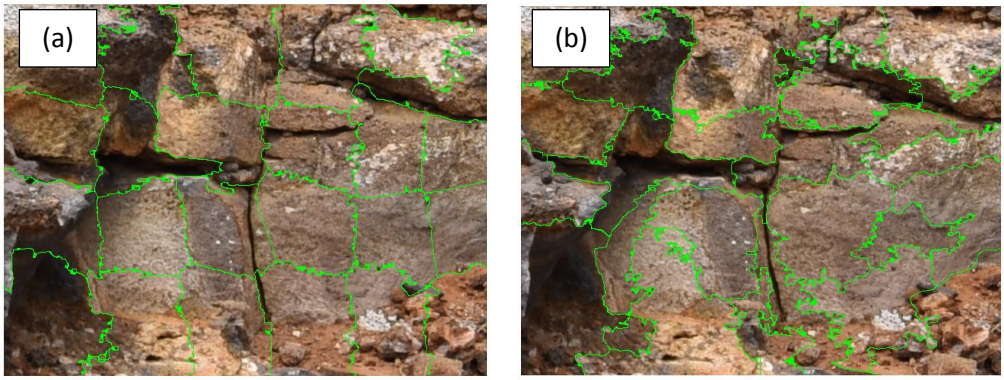

Figure 4-45: Impact of changing N_c in the original SLIC algorithm for an image; (a) N_c=40 and (b) N_c=10

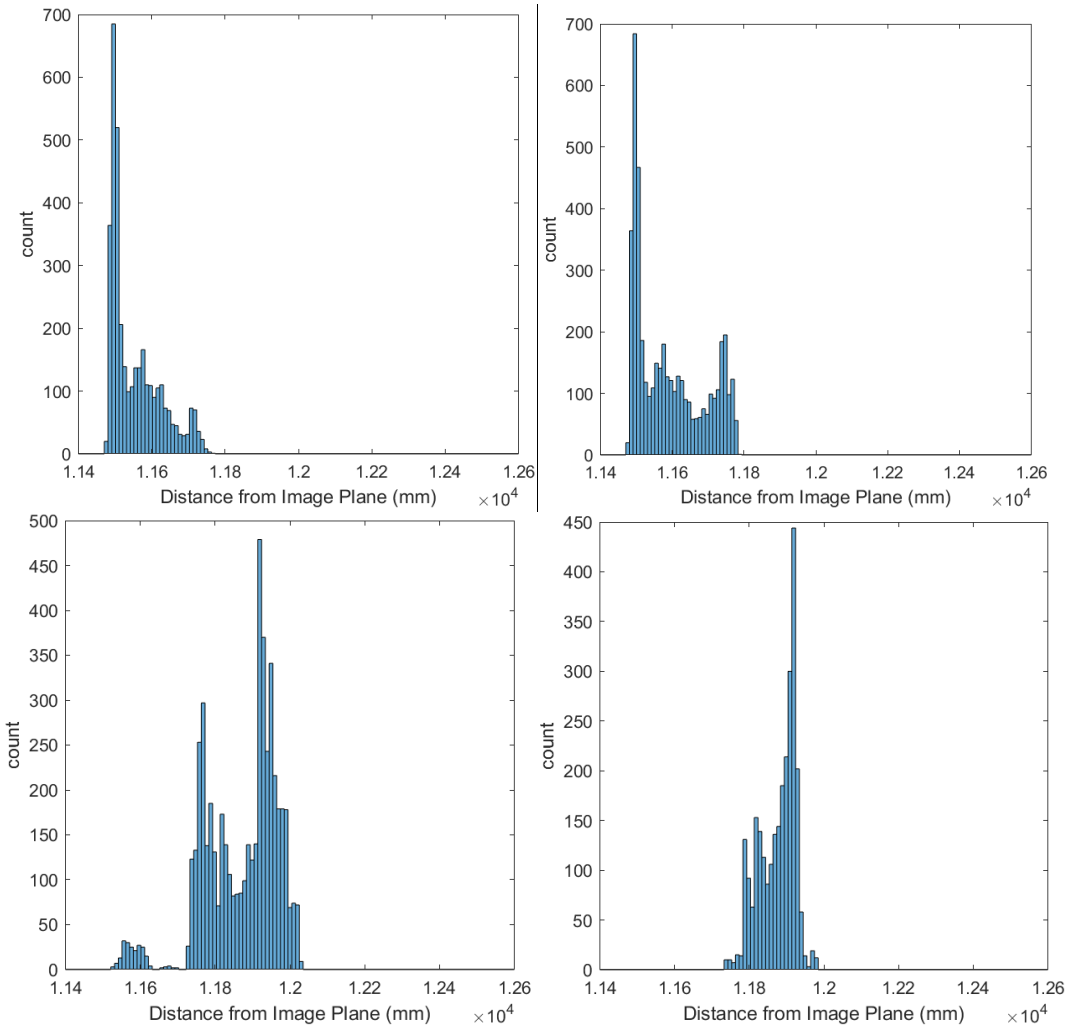

Figure 4-46: Comparison between depth values within a single cluster for RGB (left) versus RGBD (right) SLIC for two equivalent clusters with K=10 and N_c=10 (top) and N_c=40 (bottom)

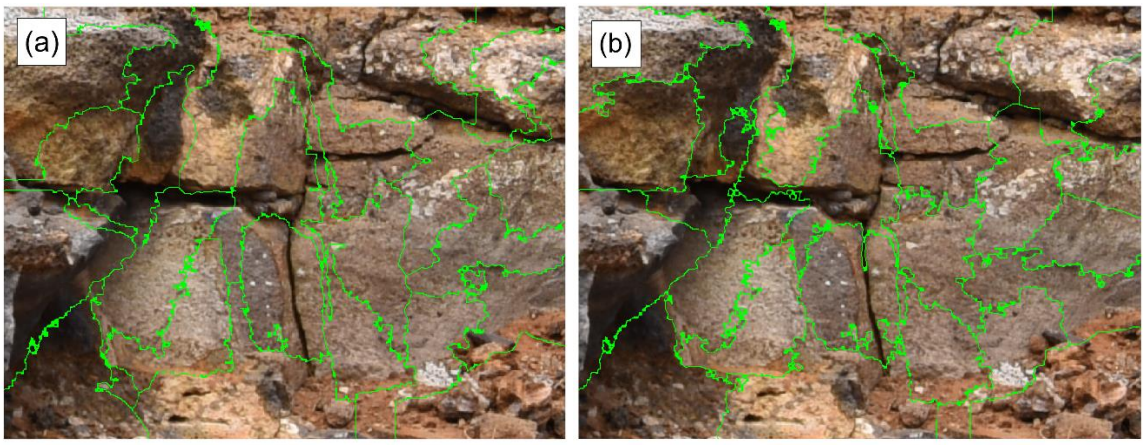

Figure 4-47: Impact of *K* on clustering; (a) *K*=5, and (b) *K*=10

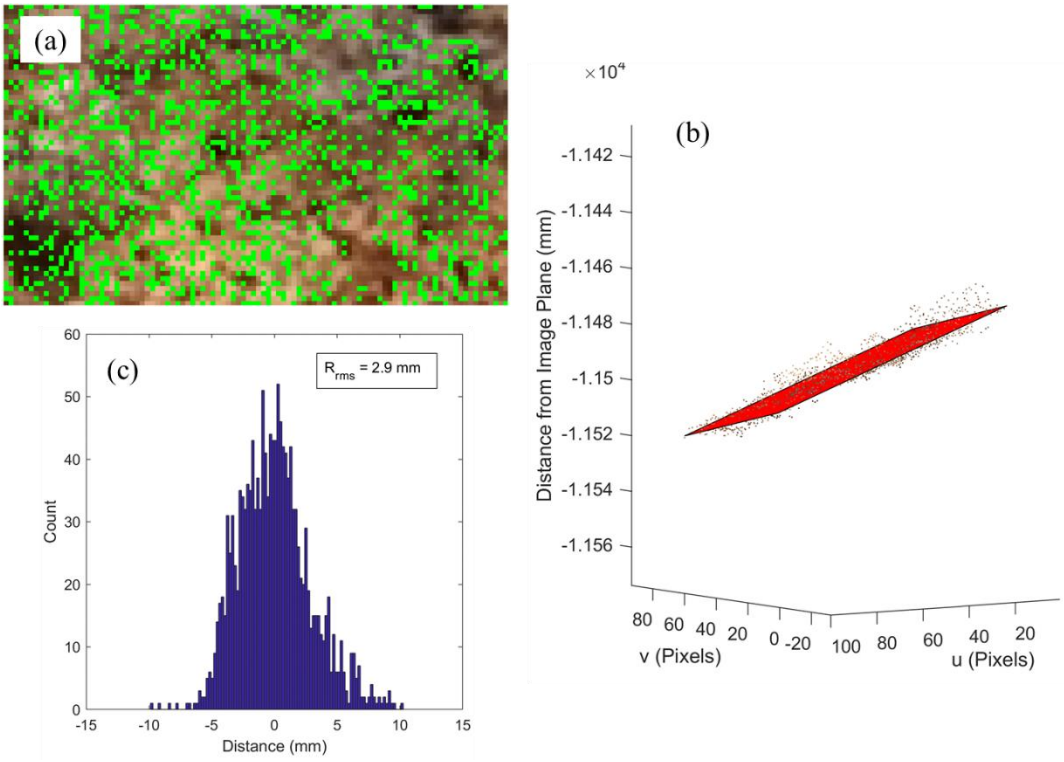

Figure 4-48: (a) Manually-segmented region of RGBD image; (b) planar fit to points, and (c) estimation of surface roughness

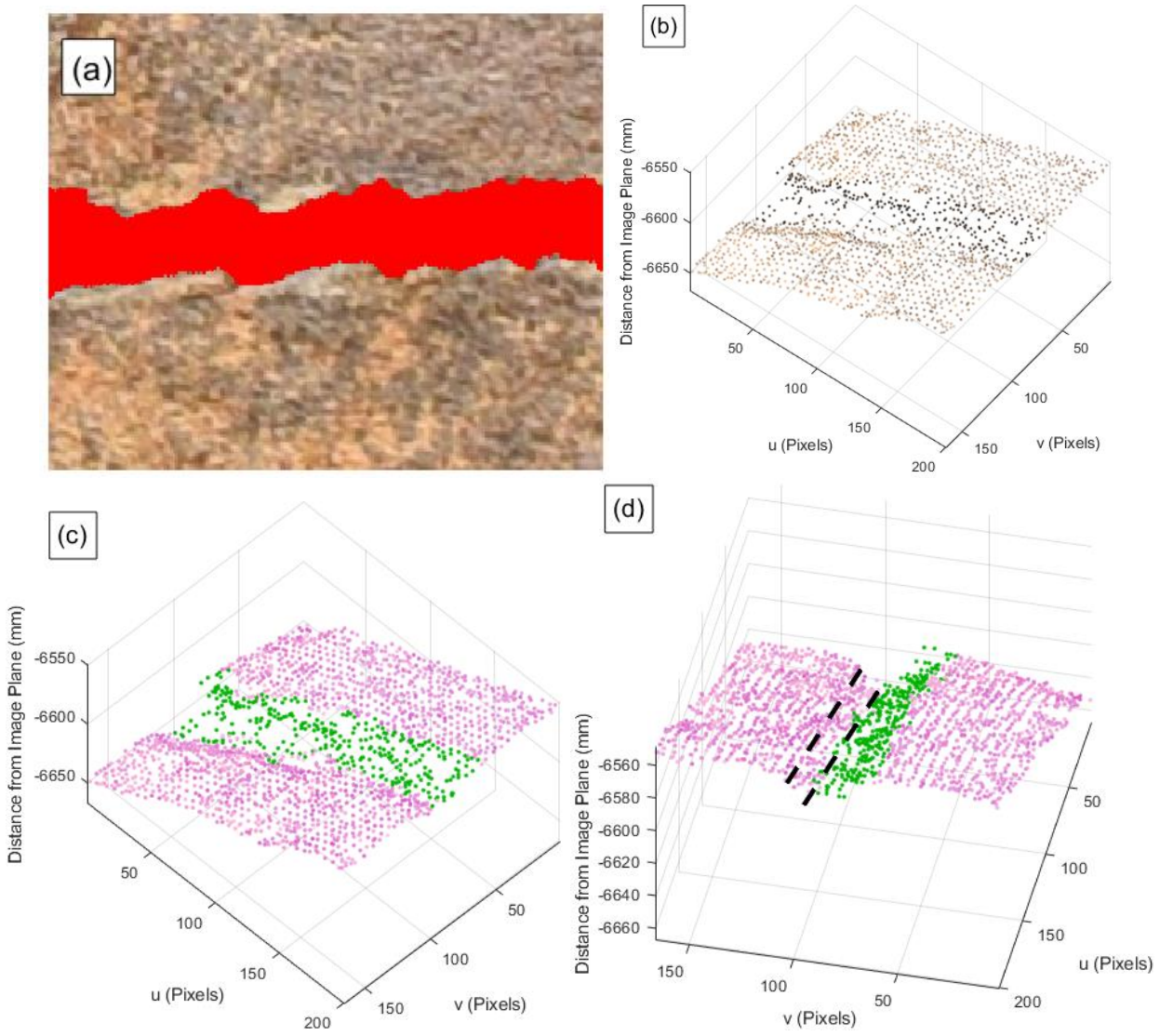

Figure 4-49: (a) Image of detected fracture (internal pixels have also been classified); (b) visualization of RGBD data for the image; (c) classified fracture pixels mapped to the depth points; and (d) highlight of depth points identified as fracture in 3D but missed in 2D detection

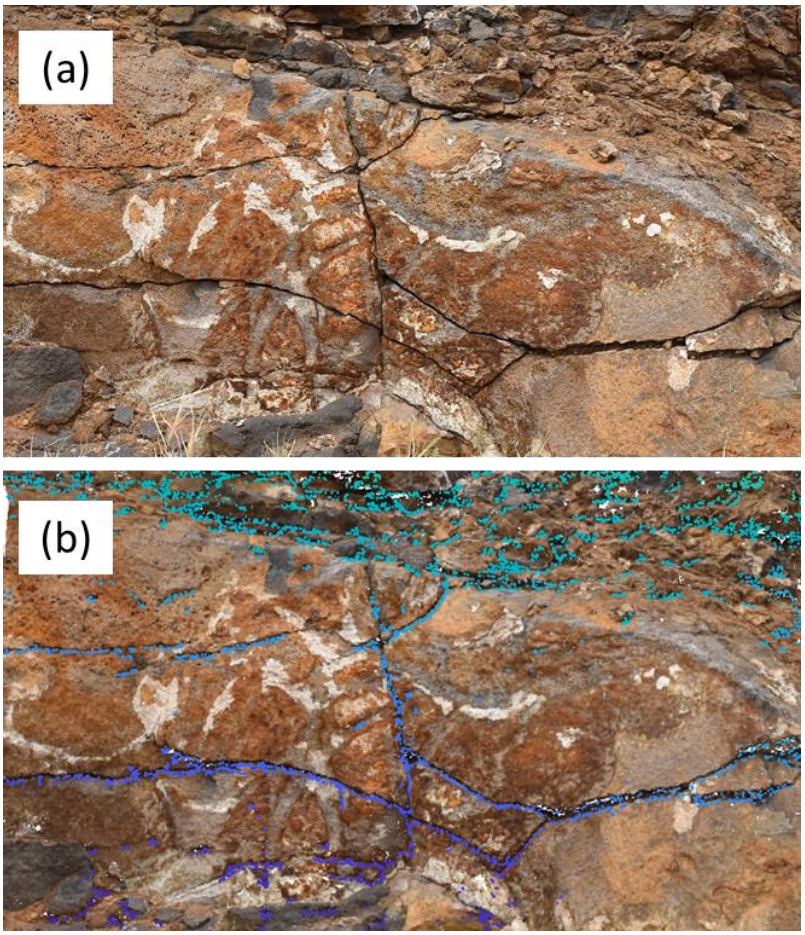

Figure 4-50: (a) Photo of fractured rock; (b) fracture detection results transformed to 3D point cloud

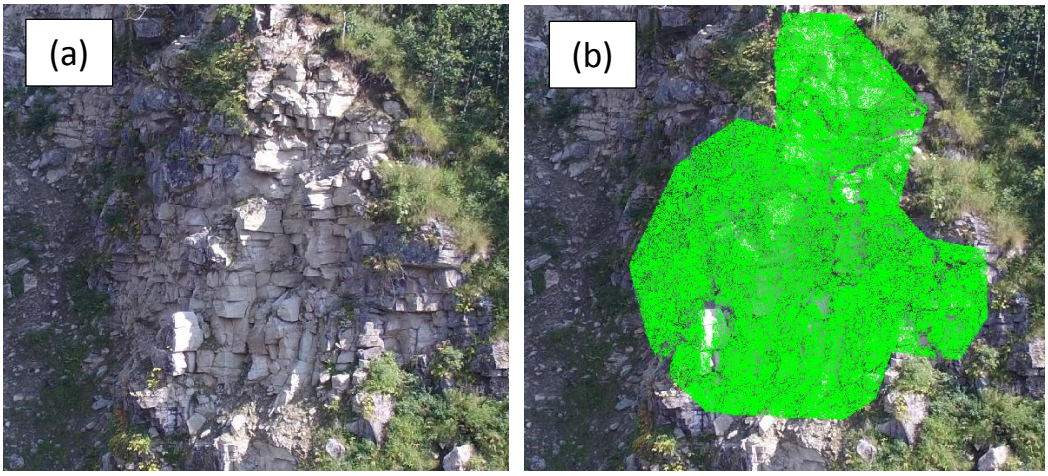

Figure 4-51: (a) Photo of a blocky rock mass; (b) 3D points projected to image plane

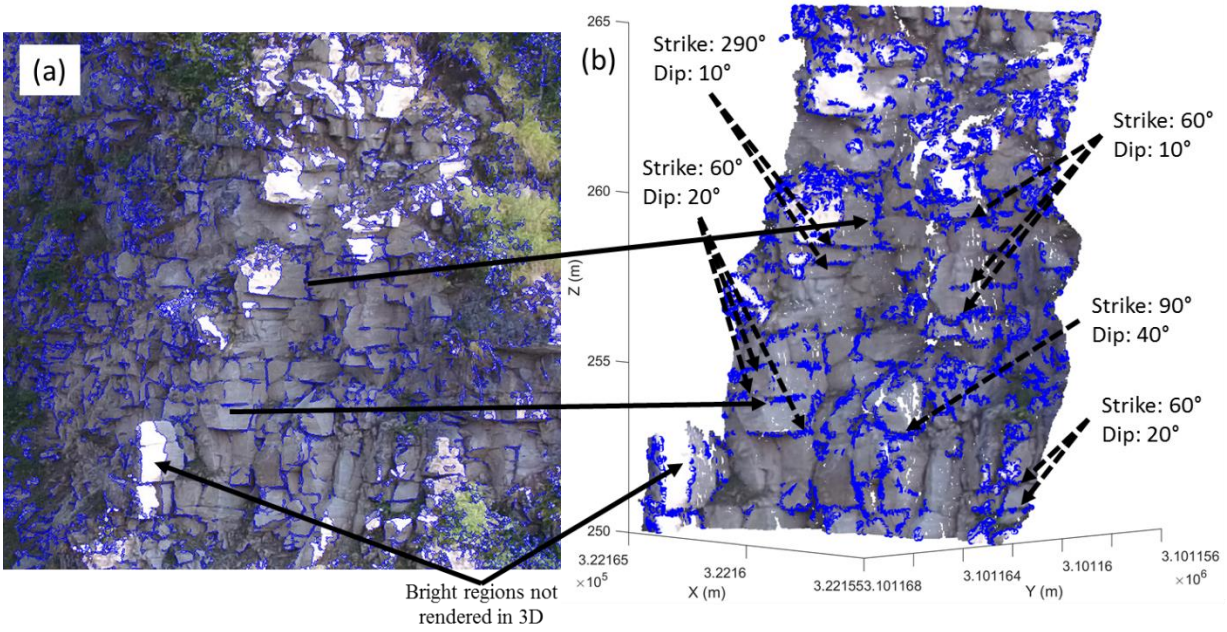

Figure 4-52: (a) Fractures identified in 2D and (b) transformed back to 3D (points are exaggerated)

4.4 References

Achanta, R., Shaji, A., Smith, K., Lucchi, A., Fua, P., and Süsstrunk, S. (2012). "SLIC Superpixels Compared to State-of-the-Art Superpixel Methods." *IEEE Trans. Pattern Anal. Mach, Intell.*, 34(11), 2274-2282.

Canny, J. A. (1986). "Computational Approach To Edge Detection." *IEEE Trans. Pattern Analysis and Machine Intelligence*, 8(6), 679–698.

Chen, J., Zhu, H., and Li, X. (2016). "Automatic Extraction of Discontinuity Orientation from Rock Mass Surface 3D Point Cloud." *Computers & Geosciences*, 95, 18-31.

Deere, D. U., and Deere, D. W. (1988). "The Rock Quality Designation (RQD) Index in Practice." In *Rock Classification Systems for Engineering Purposes*, Kirkaldie, L. Ed., ASTM STP 984.

Deriche, R. (1987). "Using Canny's Criteria to Derive a Recursively Implemented Optimal Edge Detector." *Int. J. Computer Vision, Vol. 1*, 167–187.

Greenwood, W. W., Zekkos, D., Clark, M. K., and Lynch, J. P. (2017). "Data Fusion of Digital Imagery and Seismic Surface Waves for a Rock Road Cut in Hawaii." *3rd International Conference on Performance-based Design in Earthquake Geotechnical Engineering*, 17-20 July, Vancouver, BC.

Groenewald, A. M., Barnard, E., and Botha, E. C. (1993). "Related Approaches to Gradient-Based Thresholding." *Pattern Recognition Letters*, 14, 567-572.

Hayashi, K., and Suzuki, H. (2004). "CMP Cross-Correlation Analysis of Multi-Channel Surface-Wave Data." *Exploration Geophysics*, 35: 7-13.

ISRM. (1978). "Suggested methods for the quantitative description of discontinuities in rock masses." *International Journal of Rock Mechanics and Mining Science & Geomechanics Abstracts*, 15, 319-368.

Jahanshahi, M. R., and Masri, S. F. (2013). "A New Methodology for Non-Contact Accurate Crack Width Measurement through Photogrammetry for Automated Structural Safety Evaluation." *Smart Materials and Structures*, 22, 035019.

Jahanshahi, M. R., Jazizadeh, F., Masri, S. F., and Becerik-Gerber, B. (2013). "Unsupervised Approach for Autonomous Pavement-Defect Detection and Quantification Using an Inexpensive Depth Sensors." *Journal of Computing in Civil Engineering*, 27(6), DOI: 10.1061/(ASCE)CP.1943-5487.0000245.

Jiang, C., and Tsai, Y. J. (2015). "Enhanced Crack Segmentation Algorithm Using 3D Pavement Data." *Journal of Computing in Civil Engineering*, 30(3), 04015050.

Lato, M. J., and Vöge, M. (2012). "Automated Mapping of Rock Discontinuities in 3D Lidar and Photogrammetry Models." *International Journal of Rock Mechanics & Mining Sciences*, 54, 150-158.

Otsu, N. (1979). "A threshold Selection Method from Gray-Level Histograms." *IEEE Transactions on Systems, Man, and Cybernetics*, 9(1),62-66.

Park, C.B., Miller, R.D., and Xia, J. (1999). Multichannel analysis of surface waves." *Geophysics*, 64(3), 800–808.

Riquelme, A. J., Abellán, A., and Tomás, R. (2015). "Discontinuity Spacing Analysis in Rock Masses using 3D Point Clouds." *Engineering Geology*, 195, 185-195.

Roberts, L. G. (1965). "Machine Perception of Three Dimensional Solids." *Optical and Electro-Optical Information Processing*, M.I.T. Press, 159-197.

Torok, M. M., Golparvar-Fard, M., and Kochersberger, K. B. (2014). "Image-Based Automated 3D Crack Detection for Post-Disaster Building Assessment." *Journal of Computing in Civil Engineering*, 28(5), A4014004.

Valença, J., Puente, I., Júlio, E., González-Jorge, H., and Arias-Sánchez, P. (2017). "Assessment of Cracks on Concrete Bridges using Image Processing Supported by Laser Scanning Survey." *Construction and Building Materials*, 146, 668-678.

Vasuki, Y., Holden, E. –J., Kovesi, P., and Micklethwaite, S. (2014). "Semi-Automatic Mapping of Geological Structures using UAV-based Photogrammetric Data: An Image Analysis Approach." *Computers & Geosciences*, 69, 22-32.

Von Voigtlander, J., Clark, M. K., Zekkos, D., Greenwood, W. W., Anderson, S. P., Anderspn, R. S., and Godt, J. W. (2018). "Strong variation in weathering of layered rock maintains hillslope-scale strength under high precipitation." *Earth Surface Processes and Landforms*, https://doi.org/10.1002/esp.4290.

Wang, W. (2011). "Rock Fracture Image Segmentation Algorithms." In *Image Segmentation*, G. P. Ho Ed., pp. 459-488.

Wu, L., Mokhtari, S., Nazef, A., Nam, B., and Yun, H. –B. (2014). "Improvement of Crack-Detection Accuracy Using a Novel Crack Defragmentation Technique in Image-Based Road Assessment." *Journal of Computing in Civil Engineering*, 30(1), 04014118.

CHAPTER 5

UAV-Enabled Characterization Imaging using Multichannel Analysis of Surface Waves

As discussed in Chapter 2, UAV implementation in civil engineering has focused on remote sensing using optical cameras, LiDAR, and other sensing systems such as wireless sensor networks. The remote sensing focus of most UAV implementations has led to dramatic improvements to geometric documentation at sites, as has been shown in Chapter 3. It was also identified in Chapter 3 that even as geometric documentation of sites continues to advance rapidly, remote methods for subsurface characterization have not advanced significantly. Chapter 2 identified that existing work on remote subsurface sensing using UAVs has been limited and is the focus of this chapter. First, an open-source MASW data processing code written in Matlab was developed. The function of the code is to provide a framework for performing MASW computations through a UAV platform. The fundamental components are described and examples are provided. An on-board data analysis framework is one of many components that will contribute to developing an autonomous system for performing *in situ* seismic surface wave tests. Next, an actuation implementation is made where UAVs are used to deploy the impulsive source for MASW tests. For this implementation, two UAVs were modified to lift and drop various masses to generate Rayleigh surface waves. This is intended to highlight the use of UAVs for physical interaction with the ground for subsurface sensing. The contributions of this chapter are part of the vision for remote, autonomous subsurface mapping to be coupled with image-based surface

mapping which will be critical for remote site characterization in post-earthquake geotechnical reconnaissance.

5.1 Surface Wave Methods Background

Surface wave methods (SWM) have become useful techniques for geotechnical site characterization over the past several decades. SWM are used to estimate a shear wave velocity (V_s) profile in the subsurface. The V_s is a key input parameter for subsurface characterization and seismic response analysis. The V_s is a fundamental engineering parameter which describes the stiffness of a geomaterial. The V_s of a material is related to the material's small-strain shear modulus (G_{max}) and mass density (ρ) by Equation 5-1.

$$V_s = \sqrt{G_{max}/\rho} \tag{5-1}$$

The V_s has been used for a variety of tasks in geotechnical engineering including liquefaction susceptibility assessment (Andrus and Stokoe, 2000), foundation settlement estimation (Sheehan et al., 2010), spatial variability of stiffness assessment (Greenwood et al., 2015), fault zone mapping (Duffy et al., 2014), karst and subsurface cavity identification (Nasseri-Moghaddam et al., 2005), and seismic site response analyses (Kramer, 1994). V_s also has many uses for general material characterization and stiffness assessment (Stokoe and Santamarina, 2000). For these reasons V_s investigations are valuable for site characterization, particularly in areas prone to seismicity. Several active-source techniques have been established such as spectral analysis of surface waves (SASW), multi-offset phase analysis (MOPA), and multichannel analysis of surface waves (MASW). Active-source SWM generally rely on the same fundamental physics governing the propagation of Rayleigh surface waves in a layered half-space. Passive methods, such as microtremor analysis method (MAM), which uses spatial autocorrelation to

estimate surface wave dispersion in background vibrations at low frequencies (Okada, 2003), can be combined directly with active-source methods (Park et al., 2005; Sahadewa et al., 2012). MAM is best used with a nonlinear array (e.g. circular) to avoid the effects of dominant noise direction which requires array reconfiguration (Sahadewa et al., 2012).

5.1.1 Rayleigh Wave Dispersion

Rayleigh surface waves induce particle motion to different depths in the ground as a function of their wavelength. If material properties vary as a function of depth, different wavelength Rayleigh waves will travel at different velocities. This results in dispersion of different frequency waves as they propagate along the ground surface. The recorded phase offset of different frequency waves is used to develop a relationship between phase velocity and frequency (or wavelength) called a dispersion curve. The dispersion curve is then used to estimate a V_s profile. Several methods for acquiring the dispersion curve are available but generally provide the same results with some variability introduced by user interpretation. Many of the available dispersion methods for active and passive sources are listed in Table 5-1. For the active-source dispersion methods listed in Table 5-1, they are all capable of resolving higher mode dispersion curves. Considering energy concentration in higher modes is important for modeling velocity inversions and identifying low-velocity layers in the subsurface. As noted by Garafolo et al. (2016), when inverting the dispersion curve some users model the effective, or apparent, dispersion curve which consider how energy would theoretically split between modes. For the V_s profiling performed in this chapter, the Park et al. (1998) phase-shift transform method is used for dispersion analyses and the Xia et al. (2003) inversion approached is used with consideration for higher modes when appropriate. The dispersion curve is the best way to make direct comparisons between sets of data.

However, in practice, it is most useful to develop the V_s profile for use in further analysis and design.

5.1.2 Dispersion Curve Inversion

Many different inversion approaches have been developed for surface wave inversion. Major differences in interpretation arise depending on the approach and inversion algorithm used to estimate the V_s profile from the dispersion curve. Table 5-2 summarizes several of the available inversion techniques and the underlying algorithms. The general workflow for surface wave dispersion curve inversion is detailed in Figure 5-1.

The selection of the inversion method has a much stronger influence over the final V_s model than the dispersion method (Garafalo et al., 2016). For example, increasing the number of inversion variables reduces computational efficiency and increases the number of possible solutions presented. Global search methods are typically inefficient and can produce unreasonable results. Dispersion curve misfit can be difficult to quantify and a least squares solution may not produce a result that is closest to truth or a reasonable dispersion curve match. Correct identification of higher mode dispersion curves is necessary in most algorithms which utilize them. The combination of the inversion method used and user bias may result in significant differences in the inversion results for a single dispersion curve (Cox et al., 2014).

The convergence of the inversion solution can be improved with the inclusion of additional data which introduce constraints to the model. Inversion methods have been introduced that utilize additional information available in the raw data other than Rayleigh wave dispersion. These methods include borehole, penetration, or other stratigraphic data, joint inversion of Rayleigh wave dispersion with P-wave refraction (Piatti et al., 2012; Boiero and Socco, 2014), Rayleigh wave

attenuation (Lai et al., 2002), and Love wave dispersion (Joh et al., 2006). For the case of joint inversion methods, the intent is to introduce constraints to the V_s model. For some of the examples mentioned above, *a priori* information is pulled from the raw data and introduced to the inversion procedure. The information required (e.g. P-wave first arrivals, surface wave attenuation) may be contained within the same seismic recording. However, these methods have not gained much traction because they are highly dependent on the quality of the data used for joint inversion.

Generally, *a priori* information, when available, is used to set up the initial model and/or constrain the inversion. The setup of the initial model typically has a strong influence on the final model (Socco et al., 2010). Recent research efforts have focused on quantifying uncertainty and constraining the V_s model in cases where no *a priori* information is available. Recently, significant effort has been placed into assessing uncertainty and managing surface wave inversion without *a priori* knowledge. Cox and Teague (2016) implemented a layer parametrization method for surface wave inversion when *a priori* stratigraphy information is unavailable. The inversion is performed with different layer thickness multipliers until the most reasonable V_s profile is determined. Griffiths et al. (2016a) introduced a dispersion approach to assess a site's dispersion uncertainty based on many inversion results. With respect to uncertainty, particular interest has been taken on the impact of inversion uncertainty on seismic site response analyses (Foti et al., 2009; Comina et al., 2012; Griffiths et al., 2016b). In general, confidence in surface wave inversion results is improved when *a priori* information is utilized, but it is not always available.

5.1.3 Generalized Field Procedure in this Study

In this study, *in situ* V_s measurements were performed using the MASW technique (Park et al., 1999). A linear array of 16 surface 4.5 Hz geophones are used to measure Rayleigh waves

generated by a sledgehammer. The hammer strike is offset from the array about 15-20% of the total array length to avoid the influence of near field effects (Yoon and Rix, 2009). Hammer strikes are stacked 5-10 times to improve the signal to noise ratio. Geophone spacing is adjusted depending on the desired depth of investigation and near-surface resolution. Longer arrays are capable of measuring longer wavelengths, and therefore have greater maximum investigation depths. Arrays with closely spaced geophones are able to measure higher frequency waves and therefore can resolve thinner layers near the surface. The same array is used to measure lower frequency (<10 Hz) Rayleigh waves in the background noise. It is notable that the frequencies recorded will vary somewhat depending on the V_s of the materials at the site. For example, higher frequencies will be recorded at a rock site with low weathering compared to a typical soil site when using the same array geometry. A typical testing program for a given location at a site may include a combination of 3 m spacing passive, 3 m spacing active, and 1 m spacing active tests, depending on the goal of the investigation.

2D V_s profiling was performed using the same field setup as the 1D profiling. However, after a sufficient number of hammer strikes have been stacked, the geophone array is shifted by one sensor spacing in the same direction the array is oriented. This is repeated until a sufficient length has been covered to produce the desired 2D V_s profile. A 2D V_s profile is produced from this data using the common midpoint cross-correlation (CMPCC) method (Hayahsi and Suzuki, 2004). CMPCC considers sensor groups in the 2D profile data collection with common midpoints and extracts dispersion characteristics from them. The CMPCC method was developed to provide improved spatial resolution, particularly at the extents of the array, relative to traditional 2D profiling methods (*e.g.* Xia et al., 2000).

5.2 Open-Source Computer Dispersion Code:

An open-source code (Matlab) was developed for the purposes of analyzing surface wave data collected using traditional methods as well as the UAV tests discussed later in this chapter. The primary function of the code is to extract Rayleigh wave dispersion curves from data collected in the field and outline the framework for UAV-based MASW computations.

5.2.1 Dispersion of Multichannel Data:

The code reads raw data from active MASW tests and uses the Park et al. (1998) algorithm (phase-shift transform) to develop a phase velocity-frequency spectrum. The spectral peaks are then automatically selected as initial guesses for points in the dispersion curve. The selected spectral peaks can then be manually adjusted by the user. An example output from the code is shown in Figure 5-2. The selected dispersion points in Figure 5-2e are selected automatically from Figure 5-2d but require additional processing to be finalized for modeling (*e.g.* points at 10 Hz and 30 Hz). The required inputs for the dispersion analysis are: number of sensors, sensor time histories, sensor locations, sampling frequency, source location, number of files for signal stacking, dispersion frequency range, and phase velocity range. Theoretical dispersion curves can then be computed for a given earth model (V_s, V_p, ρ) for comparison with the experimental dispersion curve if desired. The earth model can then be updated using an inversion algorithm but is not presently implemented in the code. Ideally, the user could integrate their inversion approach of choice. UAV-based MASW operations are expected to be performed of surface wave dispersion. Analysis of data quality in phase velocity-frequency spectrum is expected to be basis for on-board operational decision-making. Other functionality has been incorporated to complement the initial dispersion analysis which is documented in the following subsections.

5.2.2 Estimation of Spatial Variability:

It is critical to understand the inherent variability of soil properties. The coefficient of variation (COV) is the ratio of the standard deviation (SD[X]) to the expected value (E[X]) of a sample set. COV is mathematically defined in Equation 5-2.

$$COV = {SD[X]}/{E[X]} \tag{5-2}$$

COV has been used to quantify variability in several different soil properties (Phoon and Kulhawy, 1999; Vipulanandan et al., 2007; Alshibli et al., 2009; Chen and Kulhawy, 2014). COV has also been applied to V_s profiles, generated using the same methods, at soil and rock sites (Stokoe et al., 2004a; Stokoe et al., 2004b; Lin et al., 2008; Cox et al., 2011; Wong et al., 2011; Cox et al., 2012). A similar approach to these examples was applied by our research team to five different waste materials in a total of 26 locations (Greenwood et al., 2015). One-dimensional V_s profiling was performed at multiple locations in each type of waste material and COV profiles were estimated. In this implementation, the V_s profiles developed are fit to a log-normal distribution (*i.e.* $V_s \sim \text{Lognormal}(\mu,\sigma^2)$) then ±SD and median profiles are calculated. Based on these statistical V_s profiles, a COV profile is then calculated. The COV is calculated for a lognormal distribution in Equation 3-5:

$$COV = \sqrt{e^{\sigma^2} - 1} \tag{5-3}$$

The COV profile provides a quantification of material variability as a function of depth. An example of the statistical analysis performed at a soil site is shown in Figure 5-3. Similarly, a log-normal distribution can model dispersion curves for the multiple site tests. Assessing the dispersion curve variability quantifies site variation but does not relate directly to specific depths in the subsurface unless the dispersion curves are inverted into V_s profiles.

5.2.3 Modeling of Profiles:

The median profiles derived from the statistical analysis can then be approximated using a hyperbolic model through curve fitting. The curve can then be used as an estimated shear wave velocity versus depth estimate for subsequent analyses such as seismic site response. If multiple tests are performed at a site, the variability estimate generated through statistical analyses can be propagated through seismic site response analyses. The empirical model is defined by Equation 5-4.

$$V_s = V_{si} + \frac{z}{\alpha_{V_s} + \beta_{V_s} \cdot z} \tag{5-4}$$

Where V_s is the shear wave velocity (m/s) and z is the depth (m). Parameters V_{si}, α_{Vs}, and β_{Vs} describe the shape of the curve. Parameter V_{si} is the initial shear wave velocity value for the model (*i.e.* V_s near the surface of a given material). Parameter α_{Vs} controls the initial slope of the curve. Larger values manifest as sharper increases in V_s near the surface. Parameter β_{Vs} controls the maximum model value the curve will asymptotically approach. The inverse of β_{Vs} is the difference between the surface V_s (V_{si}) and the maximum V_s. This means that for $\beta_{Vs} = 0$ there is no maximum value and the model will simply increase linearly with depth, this is apparent by observing that Equation 4-5 becomes a linear model for $\beta_{Vs} = 0$. Figure 5-4 shows an example of applying the empirical model. The median profile shown in Figure 5-3 is fit to the model using nonlinear lest squares regression. Weighted regression can also be performed if there is greater confidence at some depths in the profile (*e.g.* lower uncertainty, secondary data is available, etc.) or a specific depth range is the fit target. This empirical model was used by Greenwood et al. (2015) for a range of waste materials in containment facilities including regional municipal solid waste (MSW), bioreactor degraded MSW, a hazardous waste landfill, construction and demolition waste,

municipal water treatment sludge, and MSW incineration ash. The parameters for models fit to mean profiles in those materials is shown in Table 5-3.

5.2.4 Rayleigh Wave Attenuation:

Attenuation analyses of the input geophone time histories can be performed by converting to displacement time histories. Rayleigh surface waves propagating in geomaterials exhibit both geometric and material damping. The Bornitz Equation (Equation 5-5) synthesizes both of these factors to model the attenuation of vibrations at the ground surface (Bornitz, 1931).

$$A_2 = A_1\sqrt{r_1/r_2}\, e^{-\alpha(r_2-r_1)} \tag{5-5}$$

Where A_1 and A_2 are the vibration amplitudes at two distances away from the vibration source, r_1 and r_2 are the respective distances of the amplitudes from the source, and α is the coefficient of attenuation. The Bornitz Equation has been used for many years to estimate the attenuation of construction vibrations (Dowding, 2000). However, the attenuation of Rayleigh surface waves in geomaterials is frequency-dependent. This means that for different frequency vibrations analyzed by Equation 5-5, the attenuation coefficient will be different. Additionally, because Rayleigh waves induce particle motion as a function of wavelength, as soil properties vary with depth the attenuation of different frequency waves will change because a different set of material is sampled. To consider this effect, attenuation analyses that incorporate frequency effects are integrated with the code.

The first approach was proposed by Athanasopoulos et al. (2000) and originally used with SASW test results. The Athanasopoulos et al. (2000) method considers the attenuation of the frequency domain between two sensors where the coherence function is greater than 0.99. For this

frequency range, the function provided in Equation 5-6 is then fit to the ratio of the Fourier amplitudes of the two sensors.

$$\frac{W_2}{W_1} = \sqrt{r_1/r_2}\, e^{-\alpha_0 f(r_2 - r_1)} \tag{5-6}$$

Where W_1 and W_2 are the Fourier amplitudes of the sensors, r_1 and r_2 are the distances of the sensors from the source, f is the frequency of vibration, and α_0 is the frequency-independent attenuation coefficient which is extracted from the curve fitting. Figure 5-5 shows an example of this approach applied to a soil site. The frequency-independent attenuation coefficient can be used to estimate the coefficient of attenuation for a specific frequency simply by multiplying by that frequency (Hz).

The second implemented approach is similar to that proposed by Athanasopoulos et al. (2000) and takes advantage of all data generated by a multichannel array. The attenuation of each frequency generated by the source is considered across the entire array by transforming the recorded geophone signals into the frequency domain. The decay of Fourier amplitudes at each frequency is observed as a function of distance from the source. Equation 5-6 is then fit to the data to derive the coefficient of attenuation as a function of frequency. An example of curve fitting for two frequencies is shown in Figure 5-6. An example of an attenuation-frequency curve produced from MASW testing at the site discussed in the following section is shown in Figure 5-7. Figure 5-7 clearly shows the frequency dependence of Rayleigh wave attenuation. It is expected that α will decrease as frequency decreases due to higher-frequency waves attenuating more quickly in dissipative material such as soil. The overall trend of the curve in Figure 5-7 demonstrates this, however, there is an apparent increase in α below 19 Hz. The coefficient of attenuation approximately doubles from 19 Hz (α_{19}=5.23E-3 1/m) to 18 Hz (α_{18}=1.01E-2 1/m) which is not expected. Assuming measurement locations at r_1=10 m and r_2=50 m, the vibrations amplitudes of

the 18 Hz and 19 Hz waves would attenuate to approximately 30% and 36% of their respective initial amplitudes. This unexpected trend below 19 Hz is likely caused by amplitude peaks in passive recordings which often occur in the range of 13-18 Hz (the affected frequencies) at this site. There is also a phase velocity increase trend occurring in the dispersion curve for this site in the affected frequency range as will be observed in the later dispersion analysis. The sharp velocity increase is indicative of a material change (*e.g.,* bedrock interface) that can also affect the attenuation estimate. When Rayleigh wave velocity has been found as a function of frequency (*i.e.* dispersion curve) and inverted into a V_s profile, the Rayleigh attenuation curve can also be inverted into a shear damping (D_s) profile (used in seismic site response) or jointly inverted with the V_s profile (Rix et al., 2000; Lai et al., 2002). The primary functions used to perform the operations and analyses described in this section are summarized in Table 5-4.

5.3 Surface Wave Methods Using UAV-Delivered Impulse Sources:

In this section, the use of a UAV for dropping a payload to generate Rayleigh surface waves is investigated. The study was performed to investigate the feasibility and limitations of using UAV-delivered payloads as well explore the differences between signals generated by a sledgehammer and different shape (or mass) payloads.

5.3.1 Limitations of Surface Wave Methods

The depth of investigation for a V_s profile produced using SWM is governed by the lowest frequency of the dispersion curve. In many cases, it is desirable to increase the depth of investigation. It is important to note that layer resolution will decay as depth increases in the V_s profile. In MASW, two factors control the lowest frequency measured in the dispersion curve: the

source must have sufficient energy to propagate the lowest frequency wave to the end of the array, and the sensor array must be long enough to detect the dispersion of the lowest frequency wave. The latter can be achieved by increasing sensor spacing and/or adding new sensors to the end of the array. The most common way of measuring dispersion for lower frequency waves is to use a passive-source SWM, but passive methods can be negatively impacted by other noise sources and sites where the background vibrations are insufficient.

The most commonly used active source is a sledgehammer. The sledgehammer is generally capable of generating frequency content as low as 10-15 Hz depending on site conditions. Similar types of active sources have been developed, such as automatic trip hammers. Electromagnetic oscillators have been used to control the input wave frequency. Vibroseis trucks can similarly deliver a frequency-controlled input such as a frequency sweep. They have been used to great success for generating low frequency waves and conduct V_s profiling to significant depths (*e.g.* Stokoe et al., 2004b). Depending on the unit, a minimum frequency as low as 0.1 – 1 Hz can be achieved but with low input force. The vibroseis shown in Figure 5-8 has a minimum frequency of 17 Hz at maximum input force. However, they have difficulty accessing sites and are costly to mobilize. For large-scale testing programs, explosives have been used for wave generation but are also costly. The studies conducted in this chapter use a UAV-dropped weight to improve on the energy input and frequency content of the hammer while introducing while also providing mobility. Figure 5-8 compares the fundamental characteristics of surface wave generators.

5.3.2 UAV Platforms:

Two UAV platforms were used to lift and drop a weight for generating surface waves. In an initial testing program, a DJI Phantom 3 Professional (P3P) quadrotor was used. Some P3P

specifications are shown in Table 5-5. The P3P contains an integrated camera and triaxial gimbal. To incorporate a payload-release system and maximize payload capacity, the camera-gimbal system was removed. The custom payload release system consisted of a mechanical servo that was mounted to a carbon fiber composite platform attached to the UAV landing gear. The payload-release mechanism used a 48 kg-cm mechanical servo to hold the payload. The servo was powered by a 7.4V battery and communicated through a Futaba S.Bus2 wireless receiver. When the payload was ready to be a released, an independent wireless transmitter delivered a signal to the receiver on the UAV. The mass connected to arm of the servo was then released upon clockwise rotation of the arm.

Following the initial testing program with the P3P, the payload-release system was installed on a DJI Matrice 600 Pro (M600P) hexarotor UAV. Some specifications of both P3P and M600P are shown in Table 5-5. The M600P UAV is capable of carrying a much larger mass to greater altitudes. The M600P uses a robust flight control system leveraging data from a set of three inertial measurement units (IMU) and three GPS receivers. The M600P was originally developed to carry 1-2 heavy cameras for industrial imaging applications. The UAV platforms and payload-release components are shown in Figure 5-9. For the purposes of this study several different weights were tested. The weights used in this study are shown in Figure 5-10 and their associated properties are shown in Table 5-6.

5.3.3 Site Layout and Equipment

UAV-enabled MASW tests were performed at the Scio Flyers Model Aircraft Club in Scio Township, MI. The site and the designated UAV test area is shown in Figure 5-11. For comparing the signals generated by UAV-dropped weights and a sledgehammer, a linear array of sixteen

Geospace GS-11D 4.5 Hz geophones spaced at 3 m was placed. Geophone locations were marked for repeated testing. The source target was placed at an offset of 7.6 m from the first geophone in the array. This layout at the test site is shown in Figure 5-12. A 5.4 kg Dytran modal hammer instrumented with a load cell was used to compare with UAV-dropped weights. Geophone signals were converted using a Geometrics ES-3000 seismograph and recorded on a Panasonic field laptop. A closer view of the drop weight impact area is shown in Figure 5-13. Previously established 2D MASW subsurface imaging was used to perform an initial evaluation of the site to assess if the site was a good candidate for baseline testing and prototype operations. The 2D V_s profile is shown in Figure 5-14. The V_s at the site increases from approximately 240 m/sec (800 ft/sec) near the ground surface to over 600 m/sec (2000 ft/sec) at over 15 m (50 ft) depth. The investigated cross-section at the site does not contain significant lateral variations or velocity inversions. The lack of lateral variations and velocity inversions is beneficial for developing the test method before extending to more complex sites.

5.3.4 Initial Testing Program – Low Energy Input

The initial testing program was executed to demonstrate that a UAV-delivered payload could be used as the impulsive source for surface wave testing. The initial program was also used to refine testing procedures and explore some of the limitations associated with using a UAV for surface wave generation. The field testing procedure is generally conducted using 3 personnel: the pilot and 2 visual observers:

- After the sensor array is placed and data recording is prepared, pre-flight UAV checks are performed.

- The drop weight is attached to the UAV and the UAV is flown to the desired altitude above the impact target.
- The weight is released and data recording (f_s = 2 kHz) is simultaneously initiated. The payload release is operated by either the pilot or one of the visual observers.
- When data recording has been completed, the UAV is landed and the impact location of the weight is marked.
- The test is then repeated as required.

Trials were repeated until a set of 8 stackable signals were acquired for the C1 and C2 (identified in Figure 5-10) weights when dropped from 6 m and 12 m. Stacked signals were then used in the Park et al. (1998) dispersion method to generate dispersion curves. Figure 5-15 compares the stacked time domain signals at the first geophone in the sensor array for the UAV to the hammer. The hammer clearly generates the largest amplitude signal. As expected, the 0.5 kg weight dropped from 6 m produced the lowest amplitude signal. To investigate the effect of mass and altitude, Figure 5-16 shows the mean drop frequency content for the UAV-generated signals at the first geophone. An example of recorded ambient vibrations at the site is also displayed. As drop altitude and mass are increased, the amplitudes of frequencies beyond 20 Hz increase systematically. When considering the 0.5 kg mass dropped from 6 m, doubling the drop altitude or increasing the mass by 50% produced similar results. Therefore as energy of the input source is increased, the signal is scaled across all generated signal frequencies. The UAV-deployed sources performed well at generating high-frequency signals. The predominant frequency of the signal remained the same (55 Hz) as mass and drop altitude increased. To assess the influence of mass and altitude on generating lower frequency (<10 Hz) signals, the frequency content of the stacked

signals is considered. Figure 5-16 demonstrates that for masses less than 1 kg as the drop altitude and mass are increased, the broadband performance of the UAV-deployed source improves, but remains at lower amplitudes than that of the sledgehammer. Figure 5-17 shows the frequency content of the stacked P3P UAV-generated signals compared to the stacked sledgehammer-generated signal over the 5-20 Hz frequency range. Increasing the mass by 50% to 0.75 kg and doubling the altitude to 12 m, the Fourier amplitudes between 5-20 Hz increased by a factor of approximately 2. However, as indicated by the Fourier spectrum of the background noise, the signal-to-noise-ratio (SNR) of the UAV-generated signals is very low and requires significant signal stacking to perform a reliable dispersion analysis at low frequencies.

5.3.5 MASW with M600P – High Energy Input

Following the initial testing program, the payload-release system was installed on the larger M600P UAV to assess:

- At what mass/altitude is the drop weight equivalent to the hammer-generated signal?
- Can enough energy be transmitted at low enough frequencies to outperform the hammer?
- Is the low-frequency signal adequate to perform deeper investigations (i.e. longer arrays, lower frequencies)?
- Can a signal with high enough SNR at low frequencies be generated to remove the need for signal stacking?

The drop weight tests performed using the M600P are summarized in Table 5-7. The P_IMU weight listed in the first row of Table 5-7 was instrumented with an IMU containing a triaxial geophone and a triaxial gyroscope. The sensors were recorded with a single-board computer and transmitted wirelessly to a nearby laptop computer. The purpose of instrumenting this weight was to better understand the motion of the weight during impact and transmission of energy into the ground. Based on initial proof-of-concept tests using the instrumented plate, the weight exhibits a significant amount of motion following impact at 10-20 m drop heights and decreases at greater drop heights as more shearing of the surface soil occurs. The impact of mass, shape, size, and altitude are observed by comparing the signal generated at the first geophone and discussed in the following sections. The size of the mass carried is limited by the payload capacity of the UAV. For the purposes of this study, the practical payload limit was found to be about 7 kg. It is also important to note that carrying a maximum payload on a multirotor UAV has a detrimental impact on flight performance including flight time, velocity, flight stability, and response to wind. Without carrying the drop mass payload, the UAVs used in this study can have a flight duration exceeding 30 minutes. The duration carrying the mass has a significant impact on the expected battery life of the UAV. For the tests covered in this study, flight durations at maximum payload were kept to less than 2 minutes. The total flight duration for a single drop were approximately 3 minutes. Eight or more drops could then be performed on a single battery charge. While carrying the 7 kg payload, the maximum flight duration is approximately 16 minutes. However, this is dramatically affected by upward motion. While ascending with the 7 kg payload, the expected flight duration decreases to approximately 11 minutes.

5.3.6 Accuracy of Dropped Weights

Figure 5-18 shows drop weight landing locations for both the P3P and M600P platforms (91 total points). The square located at the origin of the Figure 5-18, represents the size of the striking plate used with the sledgehammer source. All hammer strikes occur within this footprint. During flight, the UAV uses adaptive control to maintain position above the drop target. The UAV reacts to wind by tilting in the direction of the wind source (equivalent to motion in the opposite direction of the wind) and returning to its original position if forced in translation. It becomes more difficult for the UAV to respond to external forces as the payload capacity increases toward maximum lift, as is the case when carrying a 7 kg payload. This can result in temporary movement away from the held position. Additional movement away from the drop target can occur as the observed GPS location of the UAV changes (*i.e.* drifts). In the case of drifting GPS observations, the UAV is not forced out of position, but moves as it attempts to keep its interpreted position constant. Lateral translation of the UAV with respect to the drop target is the primary cause of weight landing inaccuracy. The accuracy of weight drops from the UAV are measured from the center of the striking plate. Approximately 75% of the drops from M600P occurred within 1.2 m radially of the plate origin. Approximately 75% of the drops from P3P occurred within 1 m radially of the plate origin. There are a number of factors which impact the accuracy of the drop which are difficult to completely isolate, but were observable during testing and in the results:

- Wind (sustained or gusts)
- User experience
- Platform/Flight Control System
- Positioning Accuracy
- Smoothness of Payload Release

- Altitude

The effects of drop inaccuracy on surface wave dispersion must be considered. A drop was not considered for dispersion analysis if the weight landing location was more than 1.5 m East/West or North/South from the target (3% of the array spread length). In general, inaccuracy of the weight landing location can result in three scenarios:

- Source offset laterally from the array
- Source axial offset is shorter
- Source axial offset is longer

Each of the above scenarios have a different potential impact on the measured surface wave dispersion and therefore the interpretation of soil properties. If a source is offset laterally from the array, the distance from the source to the sensors increases as a function of the angle of incidence. For small lateral offsets, this change is very small, but can be accounted for if necessary. If the lateral offset is very large, the wavefront will not be perpendicular to the sensor array axis. If the axial offset is shorter than the target, several issues may arise. If the source becomes too close, the near-source sensor(s) will be influenced by near-field effects. It is also possible that the induced vertical particle velocities could exceed the capabilities of the sensor, depending on the geophones selected for testing. If the source axial offset is greater than the target, surface waves may attenuate prior to reaching the end of the sensor array. Dispersion of the waves over significantly different distances could also render signal stacking inappropriate. However, it was observed that the small changes on wave travel distance did not have a noticeable impact on the ability to stack signals and interpret surface wave dispersion. This was judged by comparing the dispersion curves generated by the UAV to those generated by the hammer and by comparing single drop dispersion curves as discussed subsequently. While the fundamental assumptions of the SWM remain

unviolated, such as a planar wavefront and sufficient offset distance, the drop-weight signals may be stacked and compared for dispersion analysis. However, these variations in weight impact location will introduce additional uncertainty into the dispersion analysis. Figure 5-19 shows five interpreted multimodal dispersion curves from individual drops from 60 m using the S1 weight. Drop location was not accounted for in the analysis. This was repeated for the individual drops from 60 m using the P2 weight. The COV for the dispersion points at each frequency was less than 4% for both cases. These results do not separately account for the uncertainty associated with the MASW technique. Dispersion curves developed from drop weight data is discussed further in a subsequent subsection,

5.3.7 Source Characterization

Source characterization for the purposes of SWM is done by considering the signal recorded by the closest geophone to the source and comparing it to a baseline signal generated by a hammer. To account for effects of weather and seasonal changes, the hammer signals are recorded for new testing periods as necessary. Figure 5-20 shows examples of seasonal changes to the multimodal dispersion signature at the test site. Seasonal changes affect the V_s and therefore dispersion of surface waves in shallow strata. Most notably, there was a dominance of higher mode surface waves from about 27-40 Hz in the fall and winter months. The majority of seasonal changes occurred approximately in the top 5 m as indicated by the dispersion curves. Below 18 Hz, the dispersion remains virtually unchanged.

When a hammer and striking plate are used as the energy source for surface wave methods, the source input location does not change between stacks or trials. When a trigger is used to initiate recording for wired sensors, the time syncing of signals is not an issue. Signals can therefore be

directly stacked in the time domain. For the UAV, the weight does not land in the same location for each stack or trial and the time between release and impact will vary as a function of UAV altitude. Individual signals must be corrected to account for this before they can be stacked. Signals can be time-synced manually by time-shifting to align common points in the waveform (e .g. first break or first peak). In many cases, the waveforms can be aligned automatically by identifying the time of peak amplitude or through cross-correlation of the signals. Assuming all sensor channels are synced with each other, this is done by just considering one channel (typically the first). Figure 5-21a shows the signals generated by five individual hammer strikes; the mean signal is shown as a thicker red line. The figures that follow show mean (red line) Fourier amplitudes for five hammer and five UAV drop signals. As shown in Figure 5-21a, the hammer signal is highly repeatable at high frequencies. This can also be observed at lower frequencies as shown in Figure 5-21b, but the repeatability decreases below 15 Hz as the SNR increases. An example of background noise recorded during these tests is also shown for comparison. The amplitude of the individual hammer signals is approximately the same as the recorded background noise at 5-7 Hz. Figure 5-21c and Figure 5-21d show the signals for the 4.7 kg weight dropped from 15 m over the same frequency ranges. It can be observed that while the low frequency signal is approximately the same, the UAV signal is less repeatable than the hammer above 15 Hz. This was not judged to be problematic, as explained subsequently, as long as the SNR is high enough.

Figure 5-22 illustrates that the higher-energy combination of a greater mass and drop altitude used with the M600P UAV can generate a signal comparable to the sledgehammer. The phase-velocity frequency spectra for the stacked sledgehammer and UAV-deployed 4.7 kg mass at 15 m are shown in Figure 5-23a and Figure 5-23b respectively. Figure 5-23c shows the frequency content of stacked signals at the first and last geophones in the array. Figure 5-23d

shows the interpreted multimodal dispersion curves. The dispersion curves for the UAV-deployed 4.7 kg mass released from 15 m was within 10% of the sledgehammer source dispersion curve, indicating that the same type of surface wave data is generated. These results demonstrate the feasibility of performing active MASW testing using a mass dropped by a UAV in the field. While the signals generated in the above results approximately reproduce the hammer signal, it is desirable to maximize energy input, particularly at low frequencies. In the example shown, the frequency content at 5-7 Hz is about the same as the content of the background noise.

Figure 5-24 shows the 5-20 Hz frequency content of individual and mean signals for weight drops from 30 and 60 m using different weights. The data shows that as altitude/mass increase, the repeatability of the signal improves at low frequencies. Based on the data in Figure 5-24, the 7 kg plate and sphere dropped from 60 m produce the most repeatable and highest energy results. It was observed experimentally that, from a rigid body dynamics perspective, the spherical weight contacts the ground the same way consistently. The plate often impacts the ground at an angle and, occasionally, strikes the ground along an edge. The data presented in Figure 5-24c does not contain signals generated by the plate striking the ground along its edge, thus not capturing this effect. While edge-first contact is uncommon, it reduces the expected reliability of the signal generated by the plate.

Figure 5-25 shows the stacked (5x) time domain signals of the 4.7 kg and 7 kg plates with their respective stacked hammer-generated signals. To better understand how the signal is affected by increasing energy via drop height and mass, the signals are compared directly in the frequency domain. Figure 5-26 compares the frequency content of mean signals generated by the 4.7 kg plate-shaped weight (P1) to the mean hammer-generated signals. The 7 kg plate (P2) is similarly compared in Figure 5-27. In Figure 5-26a and Figure 5-26b, it can again be seen that the 4.7 kg

plate dropped from 15 m closely resembles the signal generated by the hammer. Increasing the drop height to 30 m approximately doubles the signal amplitudes in the 5-10 Hz range. The greatest improvements to the signal occur in 5-40 Hz, the frequencies used in dispersion analysis with this data. As expected, in Figure 5-27, the 7 kg plate dropped from 60 m generated the highest amplitude signal. The mean signals for the 7 kg plate show significant improvement over the hammer for frequencies below 60 Hz. In the 60-100 Hz band, the signal is similar for all three sources. Figure 5-28 compares the frequency content of stacked signals generated by the plate-shaped weights for 5-20 Hz. Figure 5-28 demonstrates the effect of stacking for improving the SNR at low frequencies.

A comparison is made for the spherical weights (S1 and S2), both are 7 kg. Figure 5-29 shows the mean or individual signals for the spherical weights compared to the hammer-generated signal. Extensive conclusions about the signal generated by the small sphere cannot be drawn from Figure 5-26 because only two trials were performed. The small sphere dropped from 15 m does perform comparatively well versus the large sphere trial dropped from 20 m at less than 10 Hz. Only two trials were performed using the small sphere because it was found to be impractical for repeated testing. Figure 5-30 shows photos taken of the impact location of the small sphere trials. When dropped from 15 m the sphere penetrated the ground about 9 cm. When dropped from 30 m the sphere entered the ground about 15 cm. The diameter of the sphere is 12.7 cm, this meant that when dropped from 30 m the sphere was completely below the ground surface after impact. In both cases it was extremely difficult to remove the sphere from the ground, which significantly reduced the efficiency of field testing. If a UAV were to perform multiple drops by retrieving the weight following impact, it would not be practical with a sphere of similar size and mass at this site. It is still of interest to consider the effect of surface area of the weight. A, roughly, equivalent

force is applied over a smaller footprint when using a smaller surface area weight. However, this also causes additional shearing of the ground which requires energy that is not transferred into wave propagation. This effect will also likely influence high and low frequencies differently. The available results for the smaller sphere suggest that a smaller surface area may be more desirable, especially at lower heights when it is more likely to be practical. However, when released from large heights, the smaller sphere will be less affected by drag. It is also worth considering that a longer contact time of the impulse would theoretically promote concentration of the frequency response to lower frequencies which would be beneficial in this application. The mean signals generated by 7 kg plate and spheres are compared in Figure 5-31. The stacked signals for 7 kg plate and spheres are compared in Figure 5-32. As shown in Figures 5-28 and Figure 5-29, the 7 kg large sphere outperforms the 7 kg plate when dropped from 60 m in terms of frequency content.

When discussing the effects of ground-shearing caused by the spherical weights at this site, it is important to consider the effects of the ground surface type on the impact. At the test site, the weight directly impacted grass-covered topsoil. When applying this technique in practice, many other conditions will be encountered such as compacted soil, frozen ground, and outcropping rock among many others. For example, if the surface soil is frozen the weight will cause less shearing and potentially recoil more. This may negatively impact the generation of low frequency waves. Similarly, when impacting an outcropping rock surface the weight will cause less shearing (likely in the form of fracturing) and recoil more. In this case the generation of low frequencies may also be diminished. However, this may be less of a concern at rock sites where the same depth of investigation can be achieved at higher frequencies (due to the high velocity material). The effect of different surface soils and their response to drop weight impact should be explored empirically to develop recommendations for the application of this method to different site types. While the

testing for this study was partially performed during winter months, very little was conducted while the ground was frozen. Testing was extended into winter months largely due to warmer-than-usual temperatures and UAV battery performance is poor in temperatures below freezing. When testing was performed during cold periods when the ground may have been partially frozen, no significant changes in weight impact were observed. The recoil of the weight is not a concern. It was experimentally observed that the second impact does not affect the interpreted surface wave dispersion. This is because the second hit is very low amplitude so the signal attenuates after a short propagation distance and the surface waves generated by the primary impact have propagated a significant distance prior to the second impact occurring. Similar double hits occur often in conventional surface wave testing when using hammers. It should be noted that for drops using spherical weights from 15 m and higher, no recoil was observed.

5.3.8 Dispersion Analysis

In earlier subsections it was demonstrated that the UAV-dropped weight could be used as a hammer replacement for MASW dispersion analysis using the same processing workflow by stacking signals to improve SNR. Subsequently, it was also demonstrated that the generated signal could be improved by increasing the mass and/or release height of the weight beyond a combination of 4.7 kg released from 15 m. One objective of attempting surface wave generation with a larger, 7 kg, weight was to attempt a surface wave dispersion analysis without using signal stacking. The motivation behind eliminating signal stacking in UAV-enabled MASW of active-source SWM is derived from the fundamentals of UAVs discussed in Chapter 2. Resource conservation is paramount in UAV planning and operational optimization. As previously mentioned, carrying a near-maximum payload on a multirotor UAV has a detrimental impact on

flight performance. Minimizing the time committed to carrying the payload will assist in optimizing resource expenditure. With this in mind, eliminating or significantly reducing the need for signal stacking could be the difference between testing one versus multiple sites on a single resource unit (*i.e.* batteries). Alternatively, this would promote multiple array tests at a single site allowing for site dispersion uncertainty assessments (*e.g.* Griffiths et al., 2016).

Dispersion analyses were performed on individual drops from weights committing the most energy. This has already been briefly demonstrated in the earlier section on drop weight accuracy. Figure 5-33 shows examples of phase velocity-frequency spectra generated using the Park et al. (1998) method using a single drop versus 5 stacked signals. Figure 5-34 shows the dispersion curves produced from individual weight drops using 7 kg and 4.7 kg weights with multiple trials. The mean, standard deviation, and COV were calculated as a function of frequency for each set of dispersion curves. The dispersion curves developed from 7 kg sources had a minimum frequency of 10-11 Hz. The minimum frequency, as described earlier is not necessarily limited by the energy source, but by the array geometry. Here, the 7 kg weights generate surface waves at frequencies below 10-11 Hz (content down to 5 Hz and potentially lower), but the array length limits the minimum dispersion curve frequency. The COV for intra-modal dispersion points for the 7 kg plate and sphere dropped from 60 m did not exceed 4% at any frequency. The 7 kg plate dropped from 30 m produced similar results with generally higher COVs and significantly greater uncertainty with respect to the fundamental to first higher mode transition. The dispersion curves produced from 4.7 kg plates dropped from 15 m and 30 m were less reliable and had a minimum frequency of 12-13 Hz. In Figure 5-35, the mean dispersion curves derived from individual dispersion curves generated by 7 kg weights dropped from 60 m are compared to the baseline stacked hammer-generated dispersion curve. Interestingly, the dispersion for the hammer source

had greater energy concentration in the first higher mode between 25-30 Hz relative to the 7 kg weights. However, the first higher mode is still visible for 25-30 Hz in the 7 kg weight phase-velocity, as observed in Figure 5-33 for the large sphere, and therefore will not have a significant impact on multimodal Rayleigh wave inversion.

5.3.9 Depth of Investigation

The preceding analysis of dispersion curves developed with UAV-dropped payloads showed that for that array configuration, the 7 kg weights dropped from 60 m produced a dispersion curve with a minimum frequency of 10 Hz versus 11 Hz for the hammer. While this does demonstrate the UAV source resulting in a greater depth of investigation, it is a difference of only 1 Hz and further testing is warranted. It can be observed in Figure 5-33 that further increasing energy will not improve depth of investigation because the array configuration prevents measuring dispersion at lower frequencies than 10 Hz (for the velocities observed at this site). To address this, a new configuration was set by doubling the spacing to 6 m (90 m spread length). Due to spatial constraints at the site, the array was rotated and aligned perpendicular to the 3 m spacing array. The source target was offset from the array by about 13.7 m.

The stacked time domain signals recorded at the first and last geophones are shown in Figure 5-36. In Figure 5-36a, the UAV-deployed weight has the highest amplitude, as expected based on previous testing. In Figure 5-36b it can be seen that the SNR for the UAV is greater than that of the hammer. The mean frequency domain signals recorded at the first geophone are shown in Figure 5-37. The energy contained in the UAV signal begins to increase rapidly at around 10 Hz. The hammer signal does not increase more rapidly until around 20 Hz. This is a slightly different result than previous testing and an indicator that the minimum frequency for hammer-

generated signals will be higher. Figure 5-38 similarly shows the stacked frequency domain signals at the first geophone. For 5-10 Hz, the stacked UAV signal is about 1.5 - 2x the stacked hammer signal. The phase velocity-frequency spectra produced from the dispersion analysis are shown in Figure 5-39. The UAV spectrum clearly shows the fundamental mode dispersion curve dominating from about 8 – 20 Hz with some content in the first higher mode. The hammer spectrum appears to show more content in the first higher mode. In fact the fundamental mode dispersion curve is difficult to identify. The hammer, again, appears to have a minimum frequency of around 11 Hz. The dispersion curves interpreted from the spectra are shown in Figure 5-40. By assuming that the depth of investigation for an MASW test is approximately one half of the longest wavelength, which is associated with the lowest frequency in the dispersion curve, the theoretical depth of investigation for the hammer is approximately 20 m. The depth of investigation for the UAV is approximately 70 m, more than triple the hammer. This is demonstrated empirically in Figure 5-41 where the dispersion curves have been inverted into V_s profiles. It can be seen that the depth of the UAV-produced profile is approximately 3x the depth of the hammer-produced profile, as predicted. The UAV-dropped weight also appears to generate usable content at frequencies lower than 8 Hz; the amplitude of the signal in 5 - 8 Hz is consistent. Figure 5-42 shows the SNR for both stacked and unstacked signals generated by the UAV with 7 kg large sphere and the hammer. The SNR for the UAV remains consistent between 5-10 Hz. The SNR for the unstacked UAV signals performs better than the stacked hammer for 13-20 Hz. The dispersion of lower frequencies can, again, not be measured with this array configuration because the increasing velocity causes the wavelength to outsize the array below 8 Hz. If the V_s at this site was lower at depth, frequencies below 8 Hz would be usable with the 90 m array.

When a longer array is used, signal stacking was used to achieve an appropriate SNR (Figure 5-42). Figure 5-43 shows the theoretical range of depth of investigation values for the dispersion curve derived from the 90 m geophone array. Extending the array allows for longer wavelengths to be interpreted and therefore increases depth of investigation. Because of this, it is of interest to predict the maximum propagation distance of the low frequency waves generated by the UAV-dropped weight. Doing this provides a recommendation of the maximum usable array for the UAV-dropped weight at this site and potentially similar sites. The maximum allowable array length increases as SNR is improved by signal stacking. Signal stacking improves the SNR by the square root of the number of stacks and is subject to diminishing returns. Figure 5-44 illustrates this concept by showing the improvement to SNR provided by signal stacking and the incremental benefit provided as the number of stacks increases. In conventional MASW testing, typically no more than 8-10 stacks are acquired due to the low incremental benefit of additional stacks. For the M600P UAV, 8-10 stacks is approximately what could be performed using a 7 kg weight dropped from 60 m. In general, 8 stacks can be assumed the maximum if additional battery resources are needed for returning to base following weight drops. Considering these factors, the results for the 90 m array can be extrapolated to estimate the maximum array length that could be used with 8 stacks of the 7 kg large sphere dropped from 60 m. Based on test results at this site, the coefficient of attenuation for 5 Hz Rayleigh waves is $3.72 \cdot 10^{-3}$ 1/m. By assuming a mean input for a 7 kg drop for 60 m stacked 8 times and the mean background vibration amplitude at 5 Hz observed at this site, the 5 Hz wave could be propagated approximately 120 m while maintaining an appropriate vibration amplitude over the background noise (SNR = 20). As a conceptual exercise, if the dispersion curve in Figure 5-40 is extrapolated to 5 Hz, the phase velocity would be approximately 2000 m/sec. In order to measure this imagined dispersion, the array would need

to be about 200 m long at this site, or that sensors must be spaced that far apart. To measure the dispersion of 5 Hz waves with a 120 m long array, the phase velocity at 5 Hz would need to be less than 1200 m/sec. Clearly, this is an unlikely scenario at this site because this velocity is exceeded at 8 Hz. However, the 120 m array could extend the dispersion curve to as low as 5.5 - 6 Hz at this site assuming the phase velocity continues to increase on its current trajectory at 8 Hz. In general, a 120 m array capable of measuring 5 Hz vertical vibrations could be used to generate a V_s profile to a maximum depth of about 80 - 120 m depending on site conditions.

5.3.10 Attenuation of Peak Vibrations

The impact of a given mass released from a specific height onto the ground has similarities to the deep dynamic compaction ground improvement technique. It is of interest to compare the induced peak vibrations to other instances of large weights dropped onto the ground surface. Typically, the peak particle velocity (PPV) of a ground vibration is measured as a vector sum of vibrations measured on three axes. In the absence of triaxial sensors, it is often appropriate to estimate the PPV generated by vertical vibratory sources as the maximum of the vertical component (Dowding, 2000). Drop weight tests can be performed to assess the attenuation properties of a site to estimate the expected peak vibrations during construction activity. Figure 5-43 shows the estimated (average of trial weight drops) PPV of the hammer and UAV-introduced vertical impact sources. The results displayed in Figure 5-43 indicate the same conclusions already drawn in signal comparisons between the different sources, for example, it is clear that the 4.7 kg plate released from 15 m is a good approximation of the hammer-induced vibrations. These results also demonstrate that a UAV-deployed drop weight may be useful for assessing the attenuation of construction vibrations prior to construction initiating.

Some examples of drop weight-induced peak vibrations are taken from the literature and compared with the UAV vibrations data in Figure 5-44. The lines shown in Figure 5-44 are pseudo-attenuation curves developed by Woods and Jedele (1985) for construction vibrations at a set of sites. The identifiers for the lines match the site designations in the original reference (*i.e.* M1, M2, M5, O1, NC1) and have details provided in Table 5-8. The curves are essentially straight-line approximations of PPV attenuation (in a log-log scale). These approximations are most appropriate over short distances where PPV attenuation is approximately linear within log-cycles. The impact source used to generate the lower M5 line (two drop heights were used at site M5) has approximately the same potential energy as a 7 kg weight released from 60 m. To better understand how the induced peak vibrations relate to input energy, they can be shown as a function of scaled distance. This is often done with vibrations recorded from deep dynamic compaction and blasting applications (Dowding, 2000). The distance of the vibration sensor from the source is normalized by the square root (or occasionally, cube root) of the source energy. In Figure 5-45, the UAV-induced vibrations have been normalized by the square root of their potential energy at the point of release. The hammer-induced vibrations were normalized using input energy from instrumented hammer's load sensor. It should be noted that the potential energy at the point of release is not the true amount of energy imparted to the ground. Other factors during falling of the weight to ground and the impact characteristics affect how much energy is imparted to the ground. Additionally, not all energy at impact is transferred into small-strain vibrations. A certain amount of energy is dissipated by permanent displacement of soil at the impact location and recoil of the weight following impact. If energy from different sources was uniformly transmitted into ground vibrations upon impact, the points in Figure 5-45 would more closely appear on the same curve. The separation of different sources in the figure indicates that they have different apparent energy

transmission efficiencies. With respect to this concept, Figure 5-45 indicates that the 4.7 kg plate dropped from 15 m (lowest potential energy) and the 5.4 kg hammer are the most efficient. The least efficient sources are the 7 kg plate and sphere dropped from 60 m. This is likely because the 7 kg sources (highest potential energy) caused the most permanent ground displacement and exhibited the most drag during free fall.

5.3.11 Drop Weight Recommendations

Recommendations for practical implementation as a result of this study on UAV-dropped weights as impulse sources for MASW are made in this subsection. From the initial testing program using small drop weights (< 1 kg), it was concluded that a small mass object is appropriate for testing where only high frequency surface waves transmitted across short distances are of interest. While the amount of energy in the seismic source is much lower than a hammer, it is still sufficient for high frequency dispersion analysis (>20 Hz). However, most surface wave applications desire lower frequency surface waves because increasing the depth of investigation (which is proportional to the largest measured wavelength) is beneficial or required. In the second phase of this study, where larger mass (4 -7 kg) weights were dropped from the M600P UAV, the UAV-delivered source was found to be approximately comparable and significantly more powerful than the hammer source depending on the parameters adopted. For the mass/height combinations tested in this study, the approximate threshold parameters for improving the signal beyond what the 5.4 kg hammer could generate was 4.7 kg mass released from 15 m, potential energy of about 700 J.

The 7 kg circular plate weight (P1) was compared to 7 kg large (S2) and small (S1) spherical weights to observe the effects to changing shape and size of the weight. It was found that

the large spherical weight had lower impact uncertainty than the plate and outperformed the plate for the frequencies of interest for surface wave dispersion. The large sphere was found to be a better choice from a practical perspective than the small sphere. The small sphere, at this site, was extremely difficult to remove from the ground after impact even when dropped from heights of 30 m or less. The distance the sphere penetrates the ground and the overall amount of ground displacement at the location of impact will vary depending on the site for a given energy input. The small sphere may be useful at sites with stiff surfaces.

While limited, the data collected for the small sphere indicated improved performance over the plate and large sphere, practical considerations aside. This perceived performance increase is potentially caused by a combination of the smaller surface area and other potential factors, however, this requires further investigation. From the perspective of this application, retrieving a weight buried in the subsurface is impractical. However, if repeated weight drops are not necessary, and recovery of the weight is not required, the small sphere could be advantageous. In fact, applications attempting to embed an object in the subsurface will find this to be a useful trait. The small sphere was also found to have an advantage over the large sphere in windy conditions. As previously discussed, when carrying a maximum payload, the UAV is highly susceptible to being displaced by wind. This is because the UAV does not have the ability to drive additional power to the motors to react to the wind. When carrying the large sphere the cross-sectional area of the UAV subjected to wind is significantly increased. This resulted in aborted tests when carrying the large sphere in the same conditions the 7 kg plate and small sphere could be dropped without issue.

5.3.12 Conclusions and Future Work

The UAV experiments performed in this research were motivated by a desire to develop a high mobility energy source for performing MASW tests. From a broader perspective, the development of a UAV-deployed impact source can be considered the first step in developing a semi-autonomous, or fully-autonomous, UAS for subsurface imaging in remote or dangerous environments. The results of the investigation demonstrated that UAV-dropped weights could outperform a hammer for energy input below 10 Hz. The signal generated by the UAV-deployed weight could be used to perform a dispersion analysis without the need for signal stacking for an array length of 45 m. Signal stacking was used with a 90 m array which generated a dispersion curve with a minimum frequency of 8 Hz that more than tripled the maximum depth of the V_s profile relative to the hammer. Based on observations of the background noise at the test site and estimated frequency-dependent attenuation, the maximum array length that could be used with 8 stacks of a 7 kg sphere dropped from 60 m was approximately 120 m. The maximum usable array length will vary as a function of ground surface conditions (weight impact), subsurface conditions (shear wave velocity), background noise, vibration sensors, and data acquisition characteristics.

As a result of the experimentation, specific conclusions and observations were made which contribute to developing recommendations for best practice. It was found that for an array spread length of 45 m, source location deviations of less than 3% of the total array length had no significant impact on surface wave dispersion measurements. The hammer source, at this site, had similar energy content to dropping a 4.7 kg circular plate from 15 m (approximate potential energy of 700 J). However, to achieve a surface wave dispersion test without signal stacking, a 7 kg circular plate or sphere needed to be released from 30-60 m. Following experimentation with different weight shapes and sizes, the large sphere was found to be more efficient and practical

than the circular plate and small sphere. The impact of the spheres is more reliable and eliminates the risk of an undesirable impact angle. When acceptable impacts were achieved with the plate, the generated signal was as consistent as the sphere. However, the plate had a poor impact rate of around 20%, meaning that about every 1 out 5 drops did not generate the desired data. Future tests performed at sites with hard surfaces (*e.g.* rock sites) or inclined ground may find that sphere travels undesirably post-impact due to less shearing of the material and increased recoil. For drops above 15 m, the small sphere penetrated completely below the ground surface rendering the sphere difficult to retrieve. This slowed the process of repeated testing and would be incompatible with UAV-based weight retrieval. While the large sphere was found to be the best option for weight drops, its size (8.5 in diameter) increased the UAV's susceptibility to wind. For cases of testing in windy conditions, it is recommended that weight with small cross-sectional areas perpendicular to the wind direction be used. Alternatively, using a lower mass drop weight will free resources allowing the UAV to react to the wind more easily and remain stable. Another consideration as greater drop heights are explored is the effect of drag on the drop weight. A sphere will outperform a plate with respect to drag, but other shapes, such as an airfoil, could also be considered. In addition to continuing to explore the effects of drop weight shape, size, and contact area on surface wave generation at different sites, research directions have been identified in the following areas to improve the UAV-based surface wave tests.

Wireless/mobile geophones: The mobility of the UAV has been established, however the sensor array needs to provide equivalent mobility for practical application. Additionally, the sensors must be capable of communicating with the UAV and repositioning if directed.

Payload retrieval: Some observations were made in this study about how the shape and size of the drop weight would affect its recoverability. For signal stacking or repeated testing at a

site, such as for dispersion uncertainty assessments, the ability of the UAV to efficiently recover the drop weight.

Autonomy and Decision Making: To promote the development of a semi- or fully-autonomous UAV-based surface wave test, a decision-making framework in the context of SWM must be developed for the UAV. This includes deciding what size weight to use, how high to release it from, checking the landing location of the weight, verifying data is collected, and that the collected data is sufficient among many other components.

Table 5-1: Various available surface wave dispersion techniques

Reference	Source Type	Method
Forbriger (2003)	Active	Fourier-Bessel Expansion Coefficients
Park et al. (1998)	Active	Phase-Shift Transform
McMechan and Yedlin (1981)	Active	Frequency-Slowness Transform
Nolet and Panza (1976)	Active	Frequency-Wavenumber Transform
Zywicki (1999)	Passive	Frequency Beamformer
Aki (1957)	Passive	Spatial Autocorrelation
Bettig et al. (2001)	Passive	Modified Spatial Autocorrelation
Maranò et al. (2012)	Passive	Wavefield Decomposition
Asten (2006)	Passive	Smoothed Coherency-Frequency Spectra Spatial Autocorrelation

Table 5-2: Examples of surface wave inversion algorithms

Reference	Type	Basis
Xia et al. (2003)	Deterministic	Levenberg-Marquardt Method
Wathelet et al. (2004)	Global	Neighborhood Algorithm
Luke and Calderon-Macias (2007)	Deterministic	Simulated Annealing
Supranata et al. (2007)	Deterministic	Levenberg-Marquardt Method
Maraschini and Foti (2010)	Global	Monte Carlo
Maraschini et al. (2010)	Deterministic	Steepest-Descent Method
Leong and Aung (2013)	Global	Generalized Reduced Gradient Method

Table 5-3: Empirical model for various waste materials in containment facilities

Material	V_{si} (m/s)	α_{Vs} (s)	β_{Vs} (s/m)	Max. Depth (m)
MSW (Zekkos *et al.*, 2014)	89	0.08	0.0062	30
Michigan MSW	90	0.19	0.0025	30
Northern California MSW	75	0.07	0.0040	35
Southern California MSW	110	0.09	0.0047	60
Bioreactor MSW	65	0.21	0.0093	10
Hazardous Waste	140	0.15	0.0010	40
C&D	123	0.11	0.0049	25
Water Treatment Sludge	43	0.11	0.0267	5
MSW Incineration Ash	475	0.05	0.0013	40

Table 5-4: Primary Matlab functions to perform operations described in this section

Function	Description
GeoRead( )	Detects number of channels and imports raw sensor data from files.
Dispersion( )	Performs Park *et al.* (1998) dispersion analysis to compute phase velocity-frequency spectrum.
Limitation( )	Imposes spatial restrictions on the dispersion analysis.
Dispersion_Curve( )	Automatically selects spectral peaks for initial guess at experimental dispersion curve.
Disp_Fig( )	Generates output display of dispersion analysis.
LogNormal_Fit( )	Fits a set of profiles to a lognormal distribution.
Empirical_Fit( )	Fits the empirical shear wave velocity model to a profile.
Alpha_0( )	Performs Athanasopoulos et al. (2000) attenuation analysis to estimate frequency-independent attenuation.
Attenuation_Curve( )	Estimates frequency-dependent attenuation curve.

Table 5-5: Characteristics of UAVs used for releasing weights

	Aircraft Weight	Diameter	Maximum Velocity	Maximum Flight Time
Phantom 3 Professional	1.3 kg	59 cm	16 m/sec	23 min.
Matrice 600 Professional	9.5 kg	113 cm	18 m/sec	32 min.

Table 5-6: Physical characteristics of drop weights used for Rayleigh wave generation

Weight ID	UAV	Shape	Diameter	Height	Material	Mass
C1	P3P	Cylinder	4.5 cm	3.8 cm	Steel	0.5 kg
C2	P3P	Cylinder	7.6 cm	6.3 cm	Aluminum	0.75 kg
P1	M600P	Plate	20 cm	2 cm	Steel	4.7 kg
P2	M600P	Plate	20 cm	3 cm	Steel	7 kg
S1	M600P	Sphere	22 cm		Polyurethane	7 kg
S2	M600P	Sphere	13 cm		Steel	7 kg

Table 5-7: Summary of Drop-Weight Trials used for MASW using M600P UAV

ID	Shape	Altitude : Trials
P_IMU	Plate	30 m : 1 24 m : 3 15 m ft : 7
P1	Plate	30 m : 8 24 m : 1 15 m : 8
P2	Plate	30 m : 10 60 m : 4
S1	Sphere - Large	60 m : 11 20 m : 1
S2	Sphere - Small	30 m : 1 15 m : 1

Table 5-8: Details of drop weight vibration sites (modified from Woods and Jedele, 1985)

Site	Soil Type	Potential Energy	Frequency Range (Hz)	Coefficient of Attenuation (1/m)
M1	Sand	3300 kJ	5 - 10.5	0.0066 - 0.0082
M2	Clay	500 kJ	8.5 - 17	0.0135
M5	Clay	8 kJ (2 ft drop) 4 kJ (1 ft drop)	12 - 33 30 - 48	0.0335
O1	Clay	700 kJ	9 - 12	0.0161
NC1	Sand	2 kJ	20 - 40	0.0338

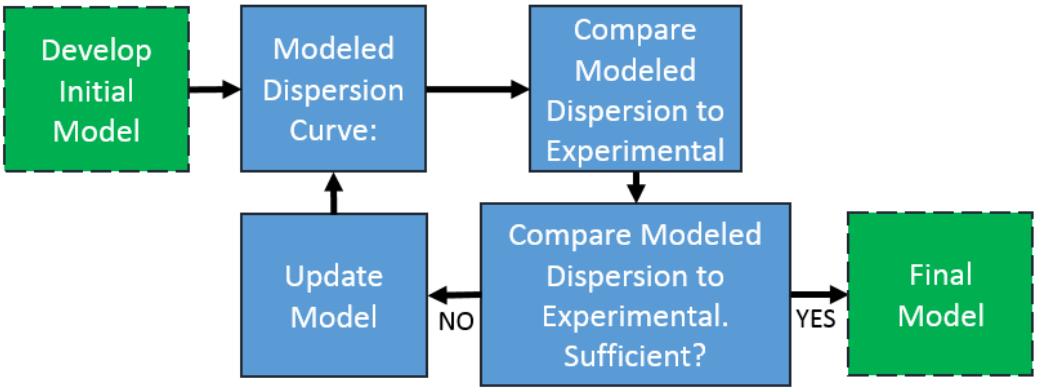

Figure 5-1: Generalized workflow for surface wave inversion algorithms

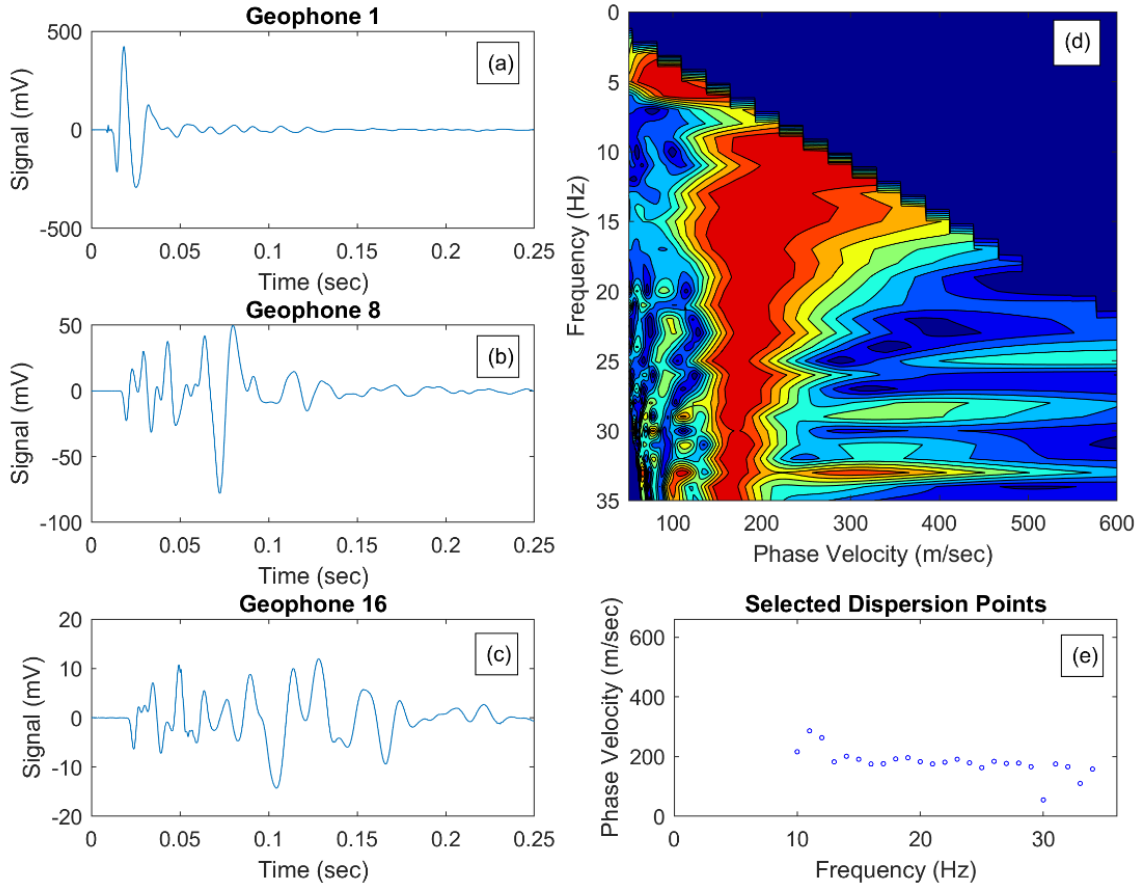

Figure 5-2: Sample output from dispersion code including sensor recordings for (a) the first, (b) eighth, and (c) sixteenth geophones in the array; (d) velocity-frequency spectrum; and (e) automatically selected spectral peaks

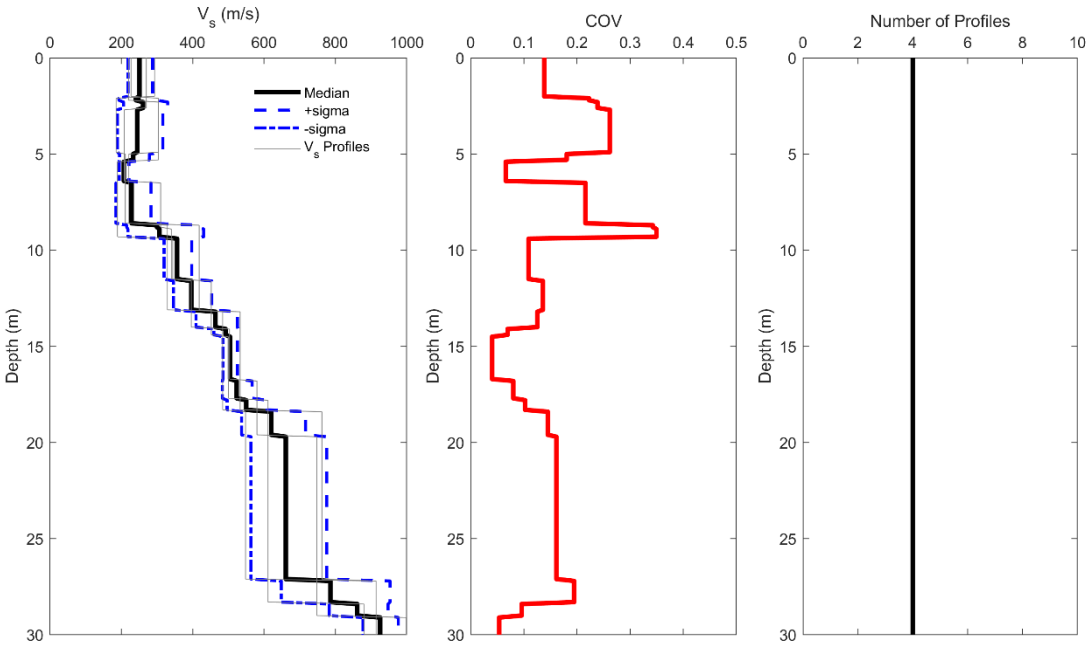

Figure 5-3: Variability assessment of four V_s profiles at a soil site

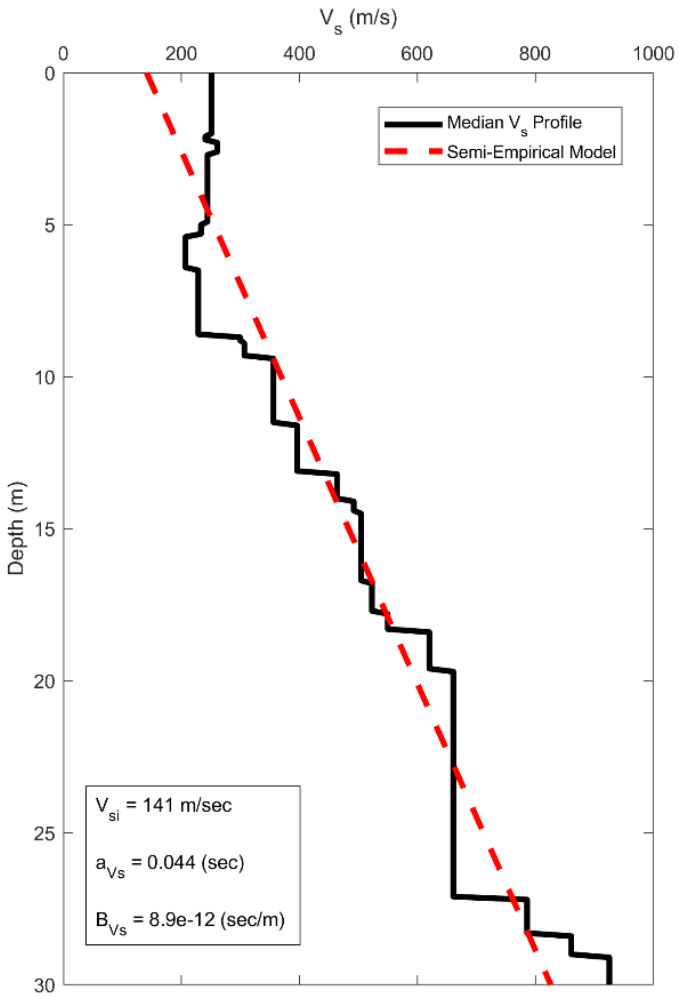

Figure 5-4: Median profile from Figure 5-3 with model fit

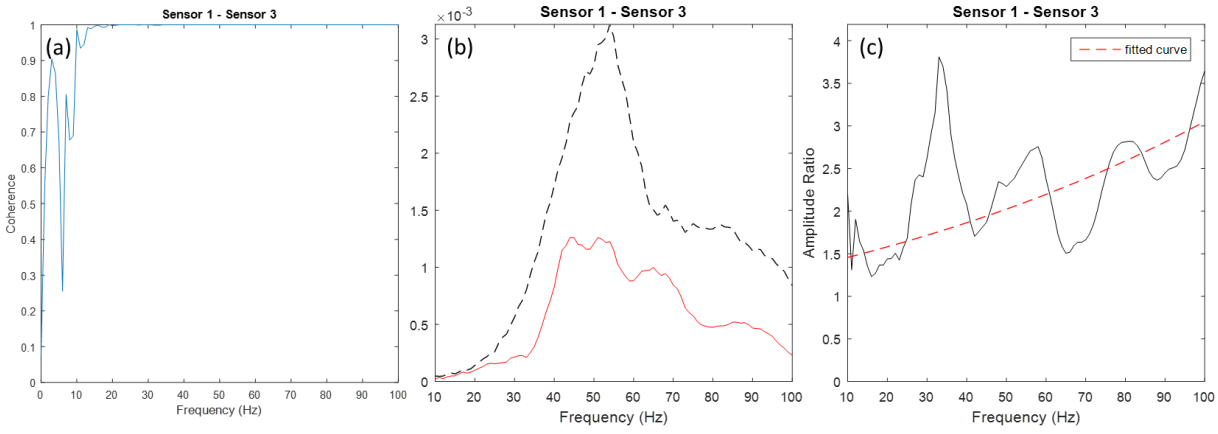

Figure 5-5: (a) Coherence function; (b) frequency domain comparison; and (c) fitting of curve described by Equation 5-6

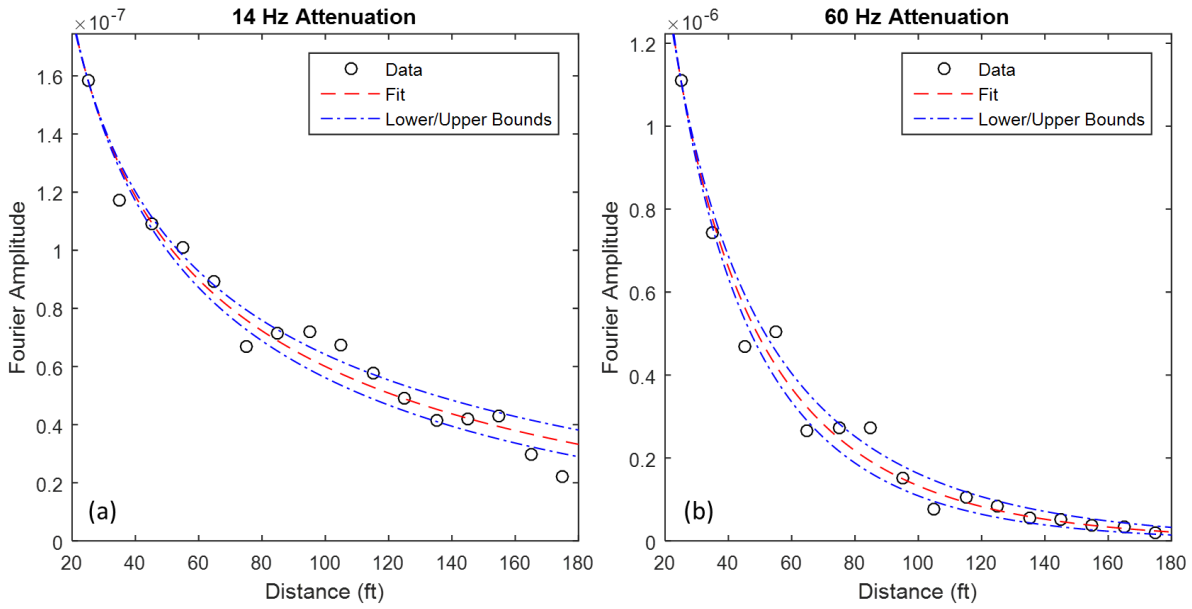

Figure 5-6: Examples of attenuating active-source signals at (a) 14 Hz and (b) 60 Hz as a function of distance from the source

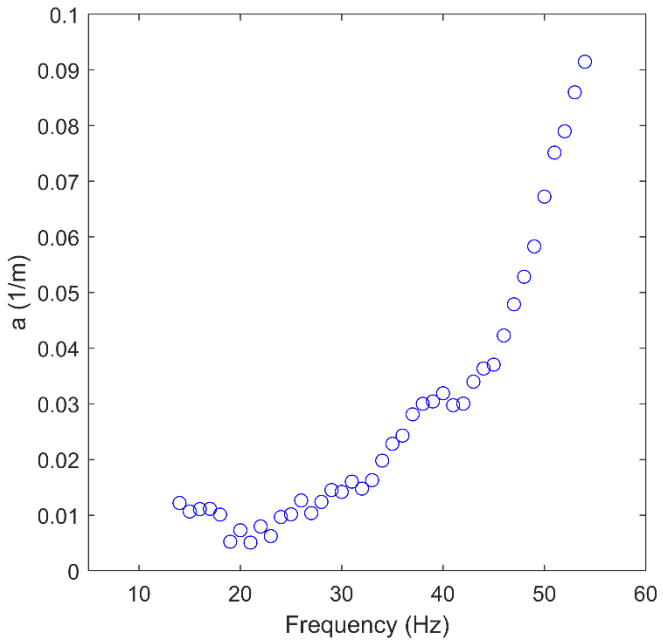

Figure 5-7: Rayleigh wave coefficient of attenuation as a function of frequency derived from MASW data collected at the UAV test site

Figure 5-8: Fundamental comparison of seismic surface wave sources

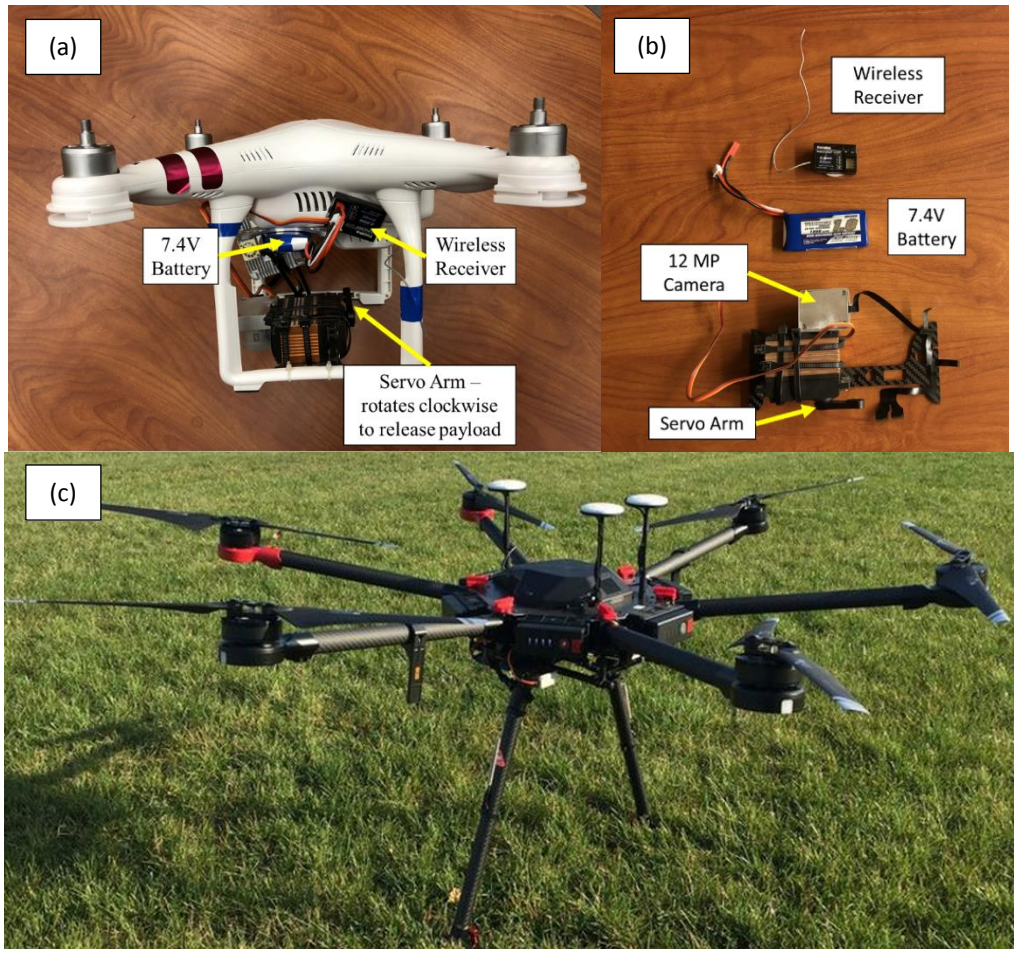

Figure 5-9: (a) Phantom 3 Professional with payload release attached; (b) payload-release system components; and (c) Matrice 600 Pro UAV

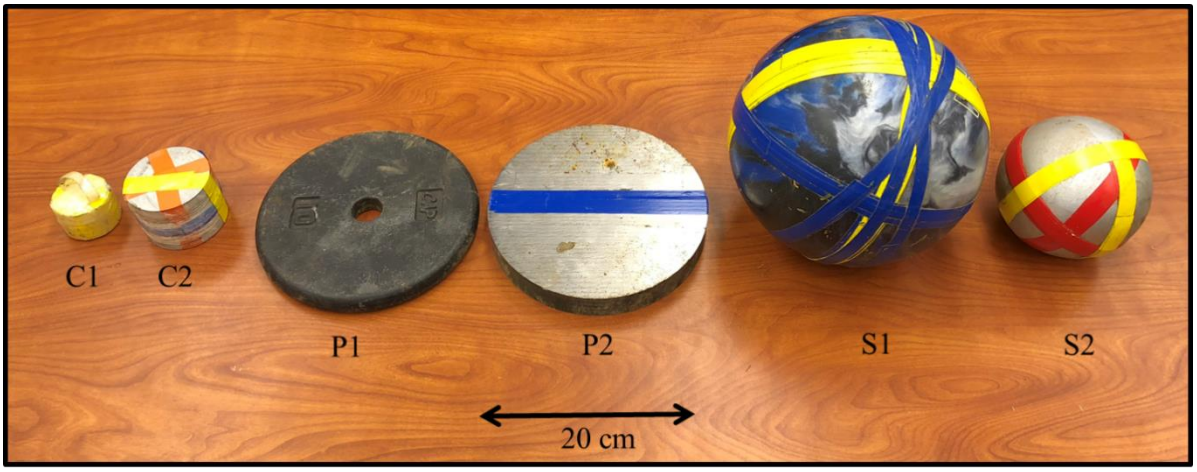

Figure 5-10: Drop Weights used in this study; labels correspond to Table 5-6

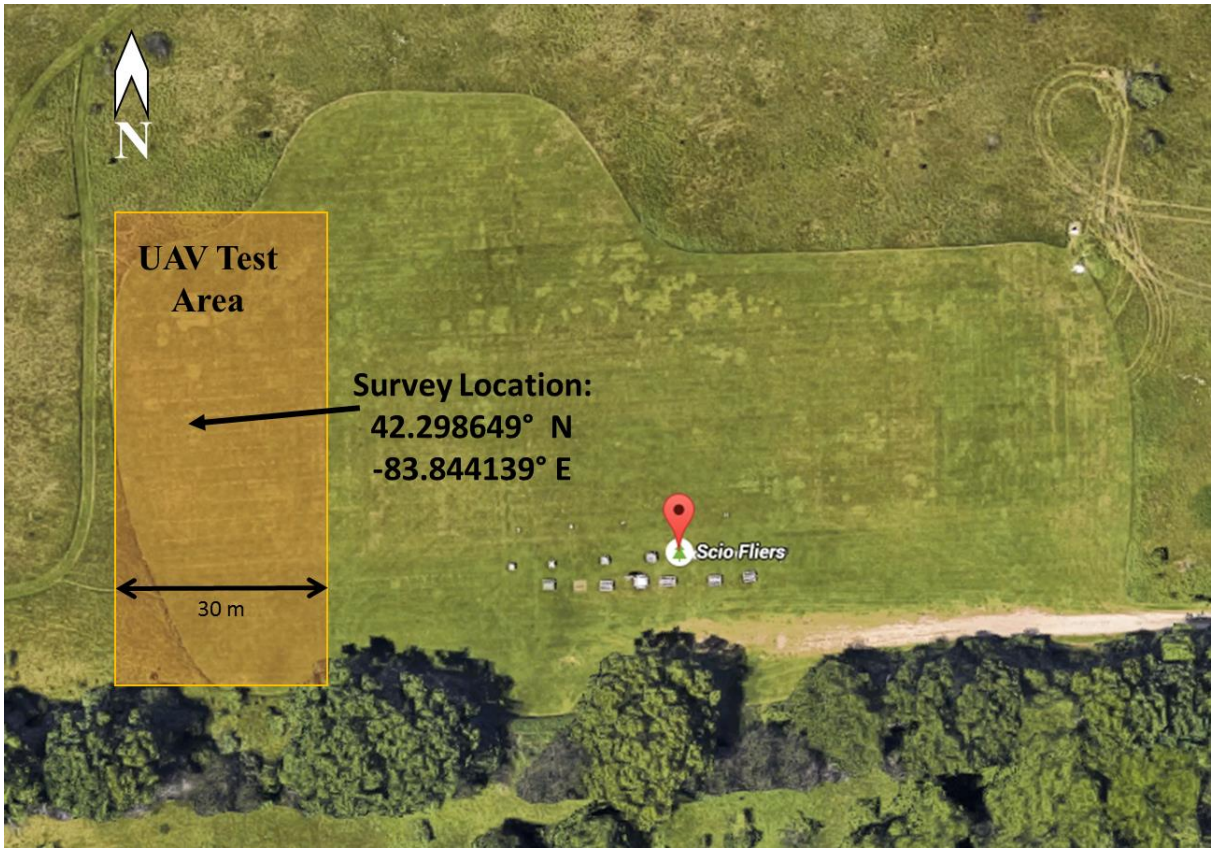

Figure 5-11: UAV-MASW test site location

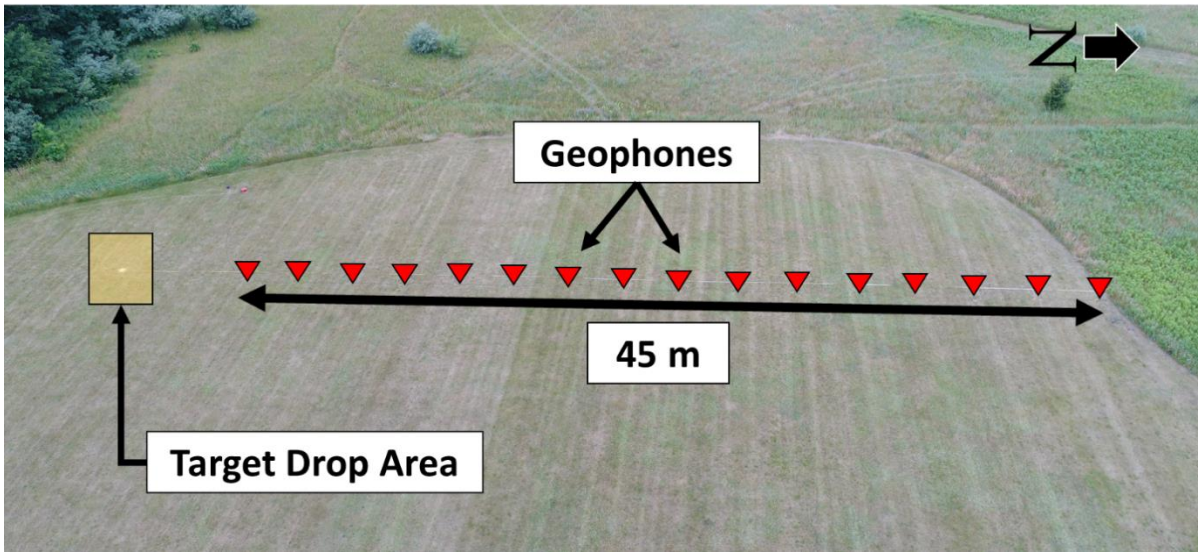

Figure 5-12: Aerial photo showing layout of sensors at the test site

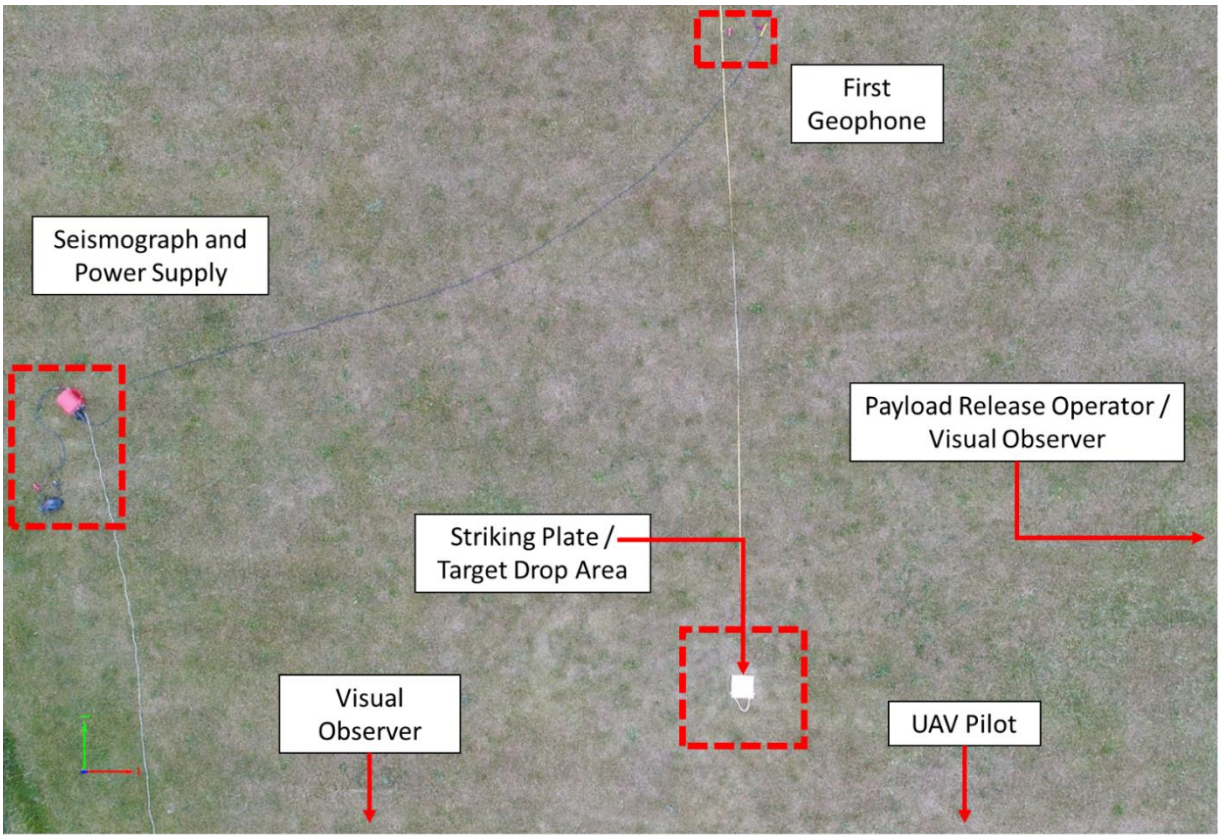

Figure 5-13: Aerial photo of equipment and target weight drop area

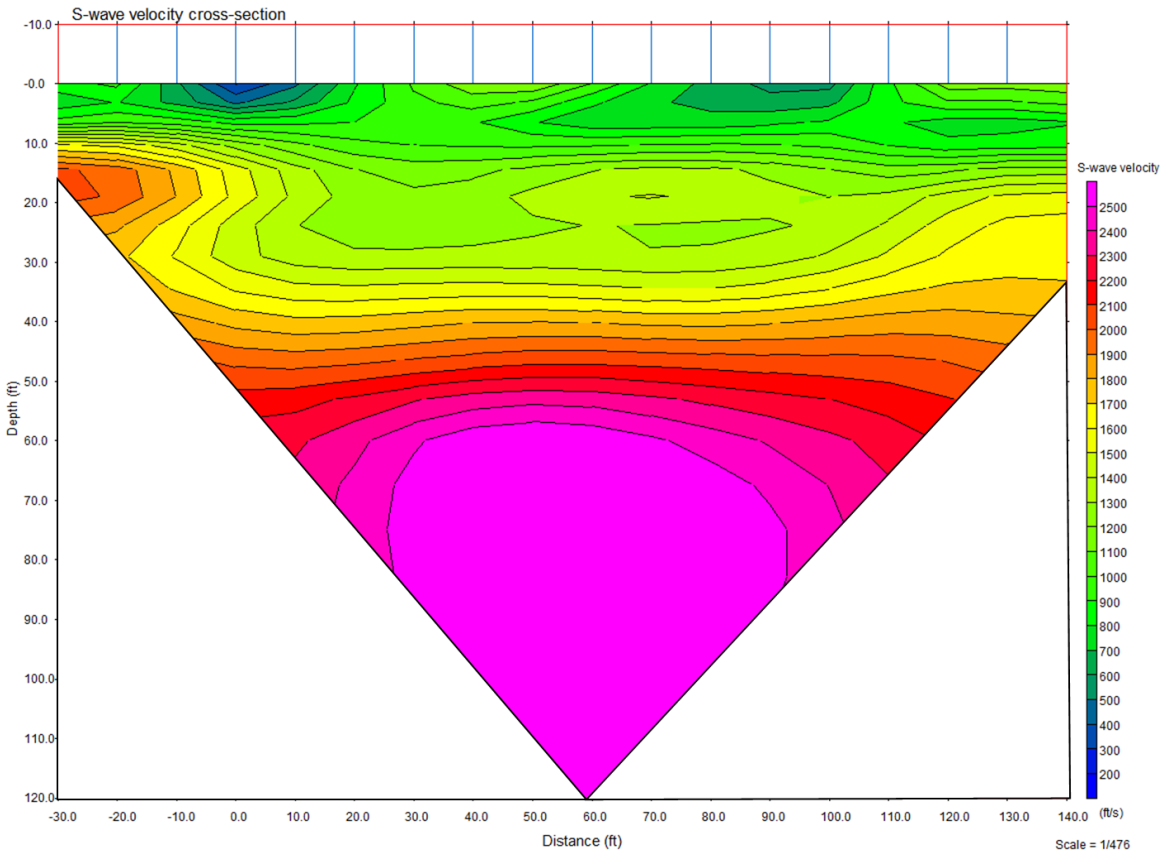

Figure 5-14: 2D Shear wave velocity cross-section produced using CMPCC MASW method

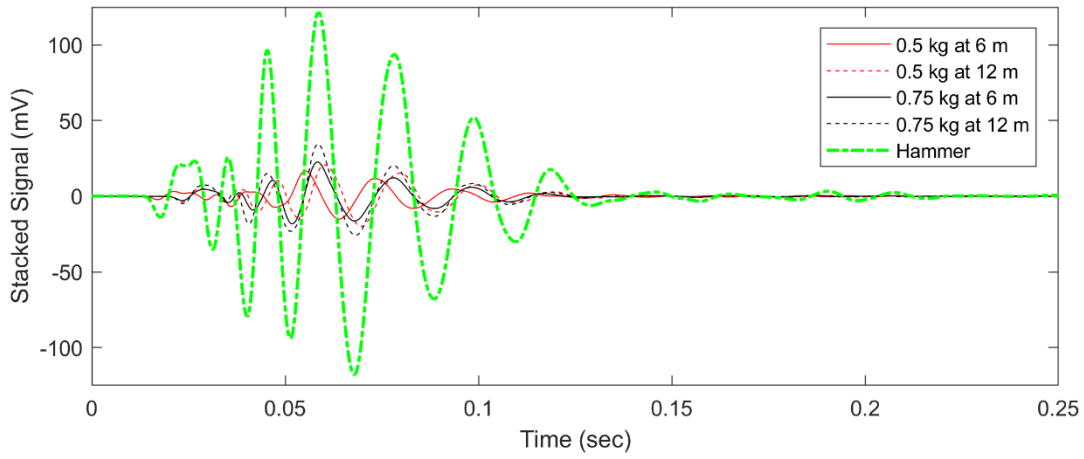

Figure 5-15: Time histories at first geophone of stacked signals for P3P UAV (8 stacks) and hammer sources (5 stacks)

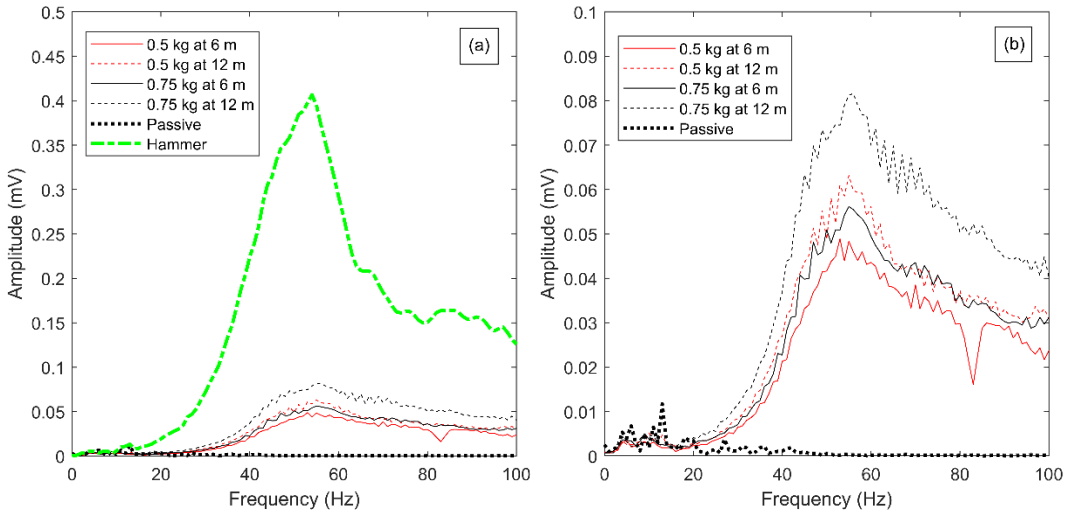

Figure 5-16: Frequency content of mean signals generated by P3P UAV (a) compared to the mean hammer signal and (b) compared to background noise

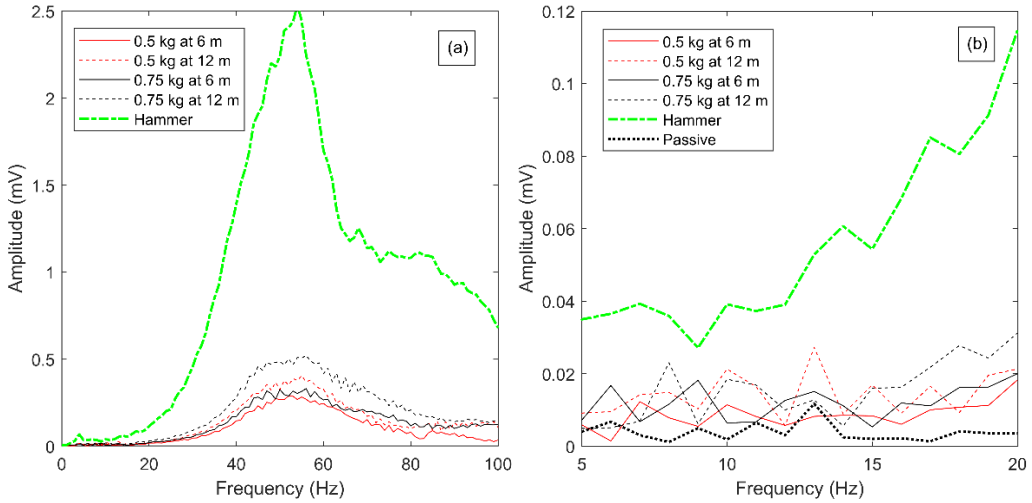

Figure 5-17: (a) Frequency content of stacked signals generated by P3P UAV (8 stacks) and hammer (5 stacks) and (b) at low frequencies

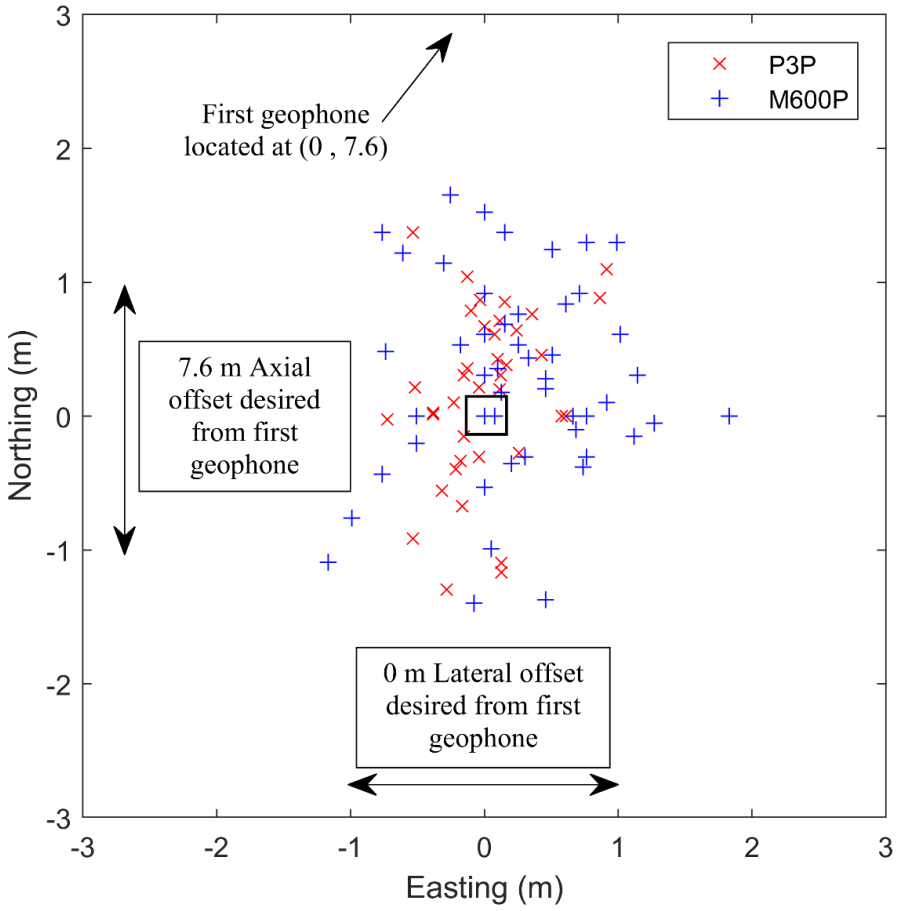

Figure 5-18: Weight landing locations for P3P and M600 UAVs; northing and easting measured from the center of the drop target

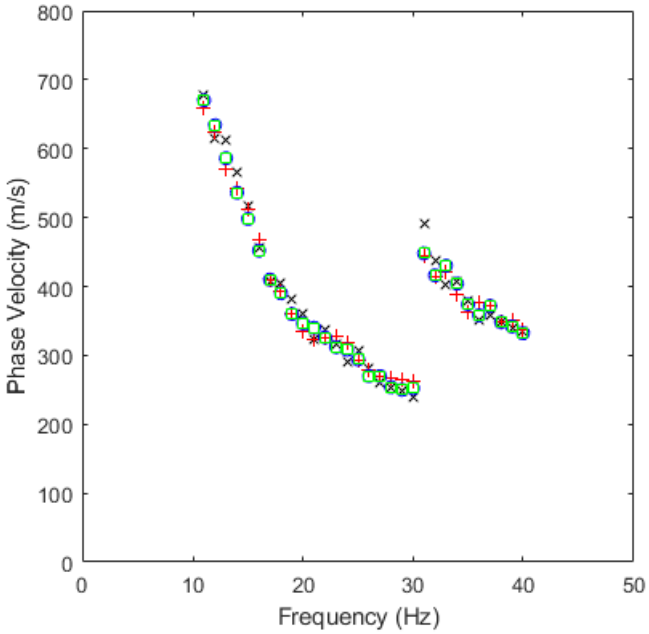

Figure 5-19: Interpreted dispersion curves from single drops using the S1 (large sphere) from 60 m

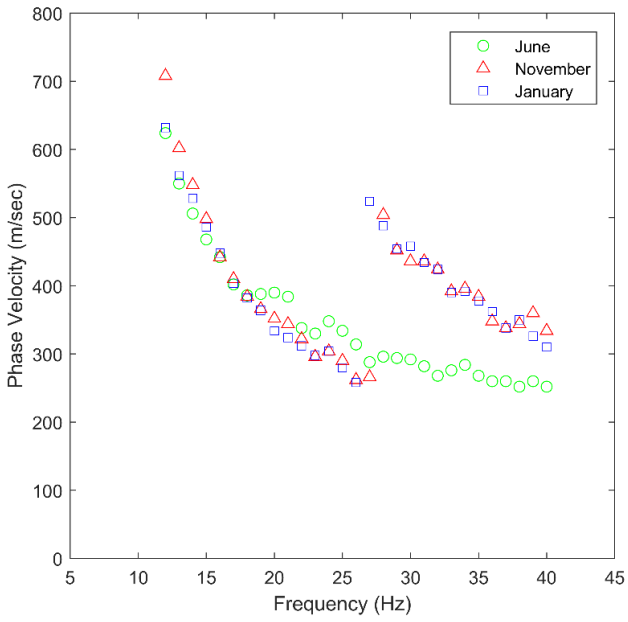

Figure 5-20: Hammer-generated dispersion curves indicating seasonal effects on subsurface properties at the test site

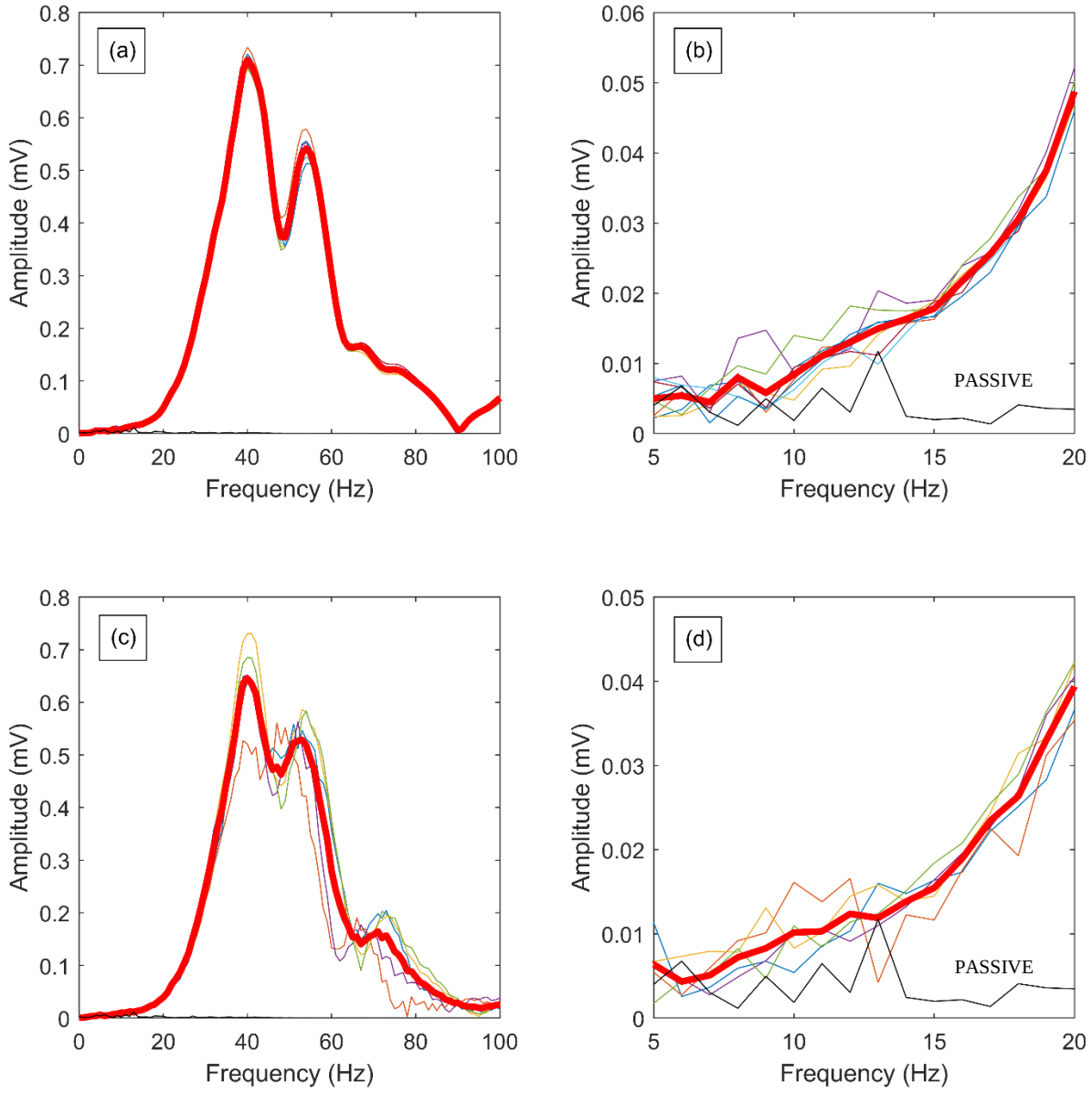

Figure 5-21: Individual and mean signals for (a) 5.4 kg hammer; (b) low frequency 5.4 kg Hammer; (c) 4.7 kg weight dropped from 15 m; (d) and low frequency 4.7 kg weight dropped from 15 m

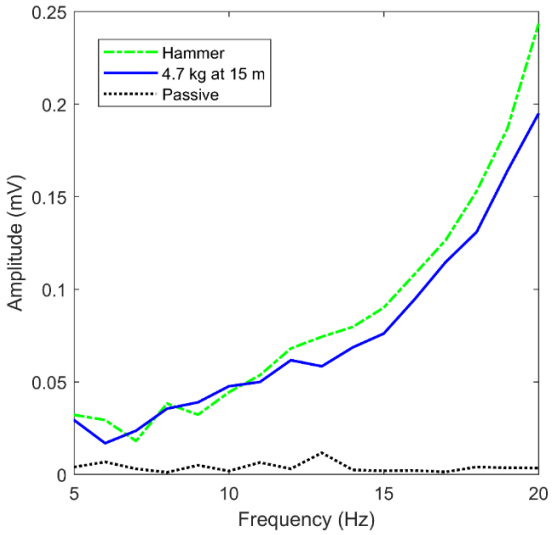

Figure 5-22: Frequency content (5 - 20 Hz) of sledgehammer signals (5 stacks) at the first geophone compared to the M600P UAV (5 stacks)

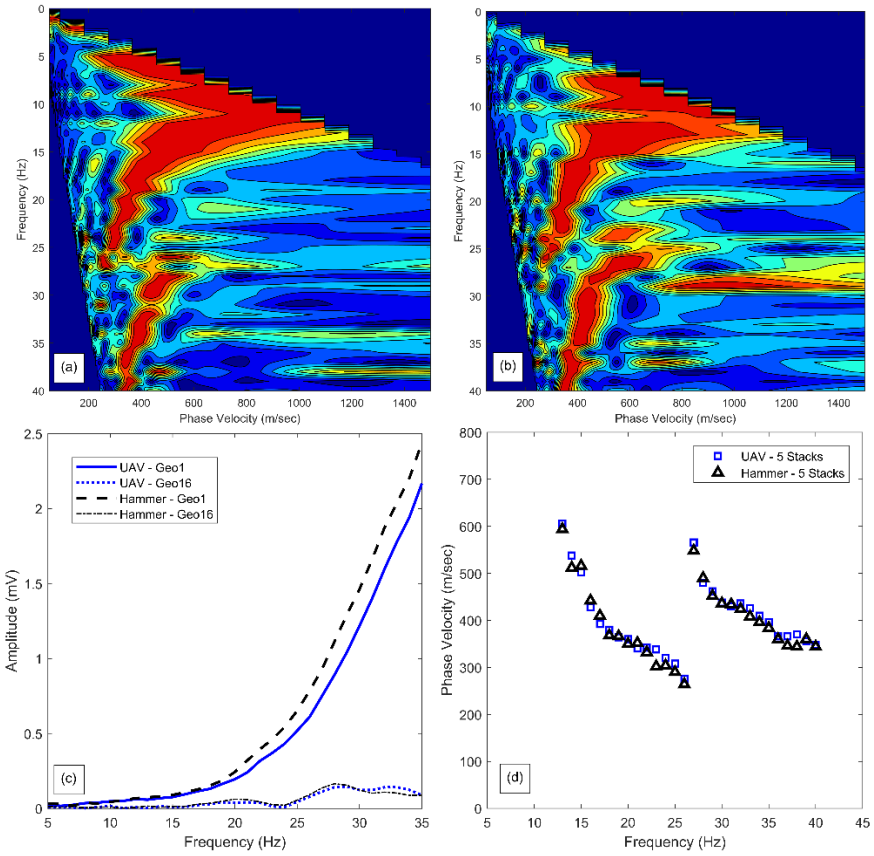

Figure 5-23: Phase velocity-frequency spectra for (a) 4.7 kg mass dropped from 15 m (stacked 5 times); and (b) 5.4 kg sledgehammer (stacked 5 times); (c) frequency domain of stacked sledgehammer and UAV-generated signals; and (d) dispersion curves

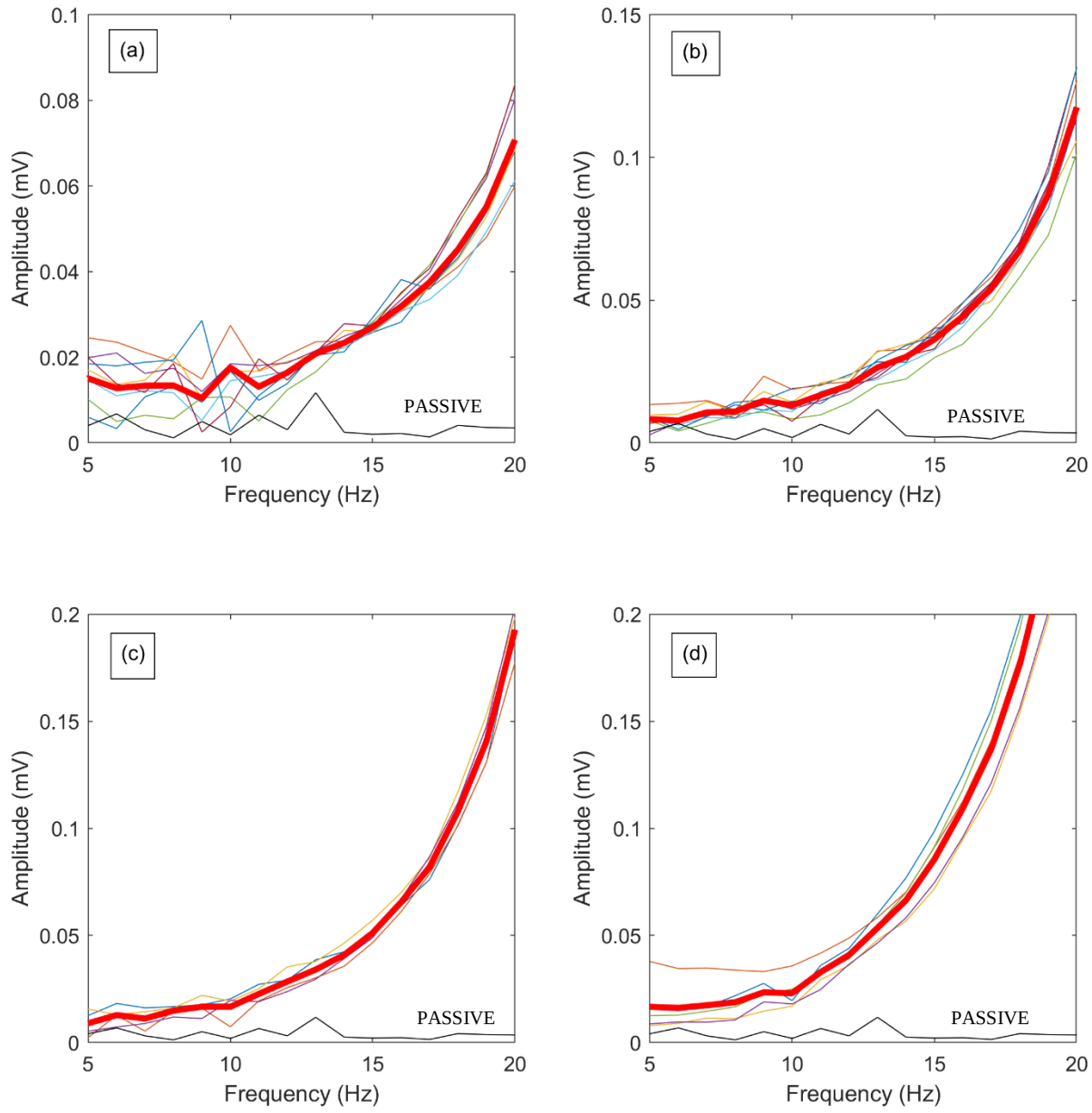

Figure 5-24: Individual and mean signals for (a) 4.7 kg plate from 30 m; (b) 7 kg plate from 30 m; (c) 7 kg plate from 60 m; and (d) 7 kg large sphere from 60 m

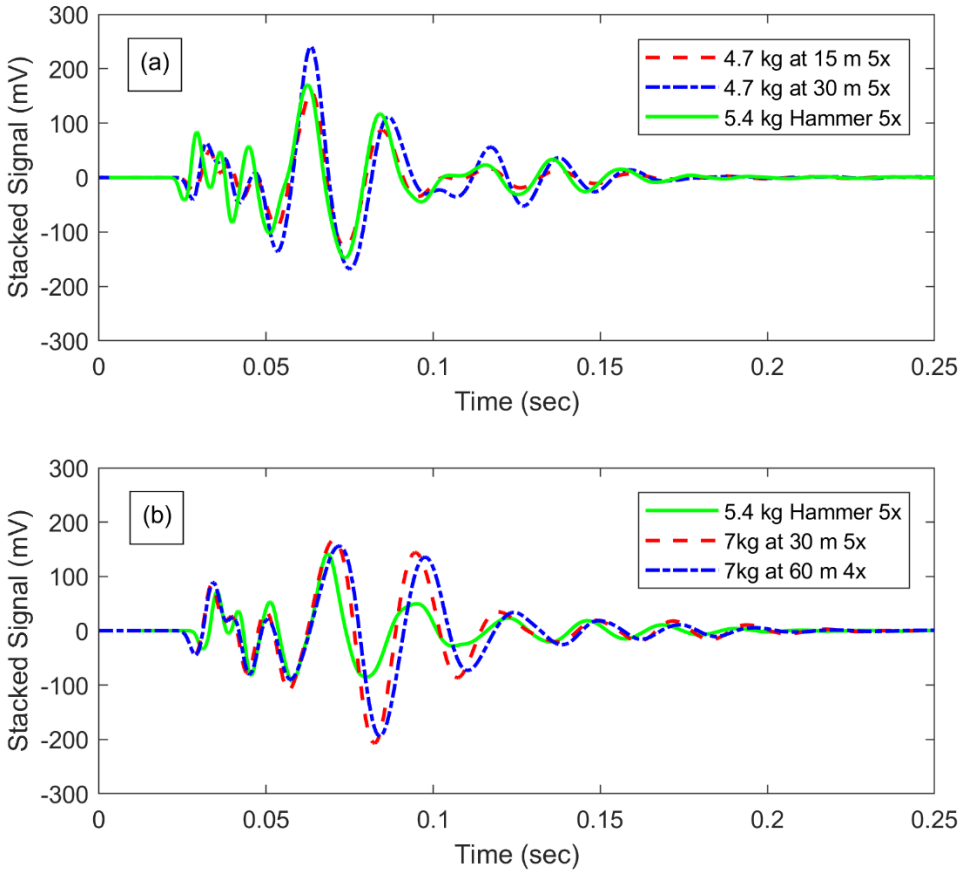

Figure 5-25: Comparison of stacked time domain signals for (a) 4.7 kg plates and (b) 7 kg plates versus hammer

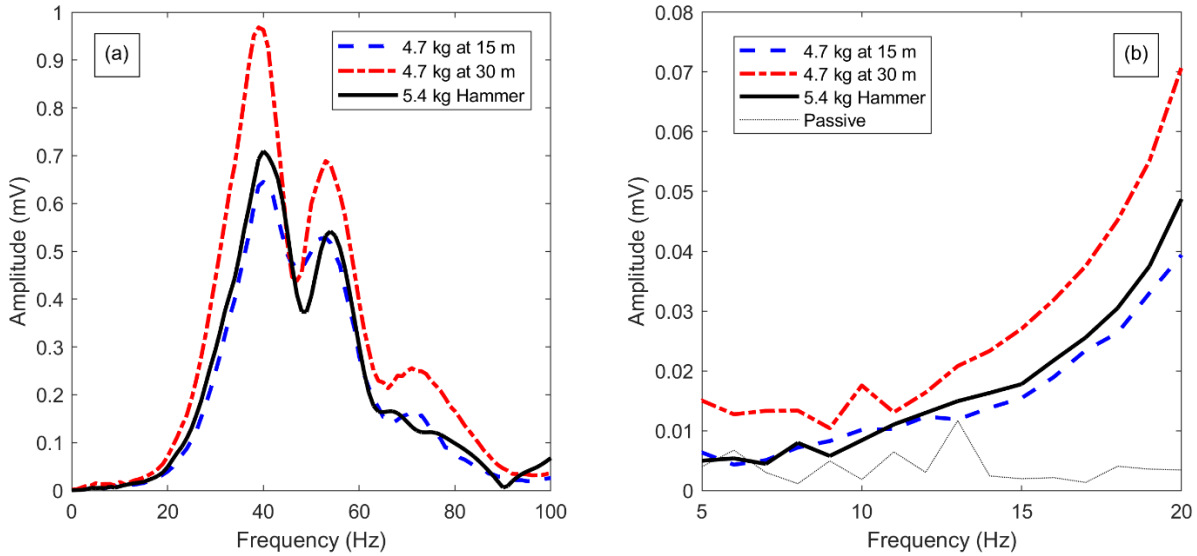

Figure 5-26: Comparison of mean frequency domain signals for (a) 4.7 kg plates and hammer; and (b) at low frequencies

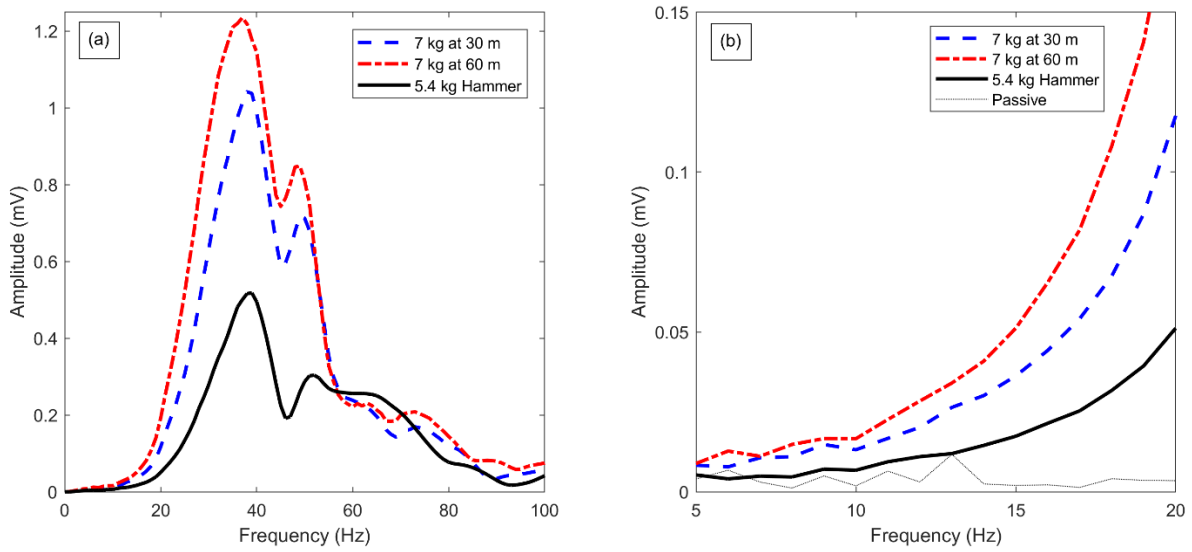

Figure 5-27: Comparison of mean frequency domain signals for (a) 7 kg plates and hammer; and (b) at low frequencies

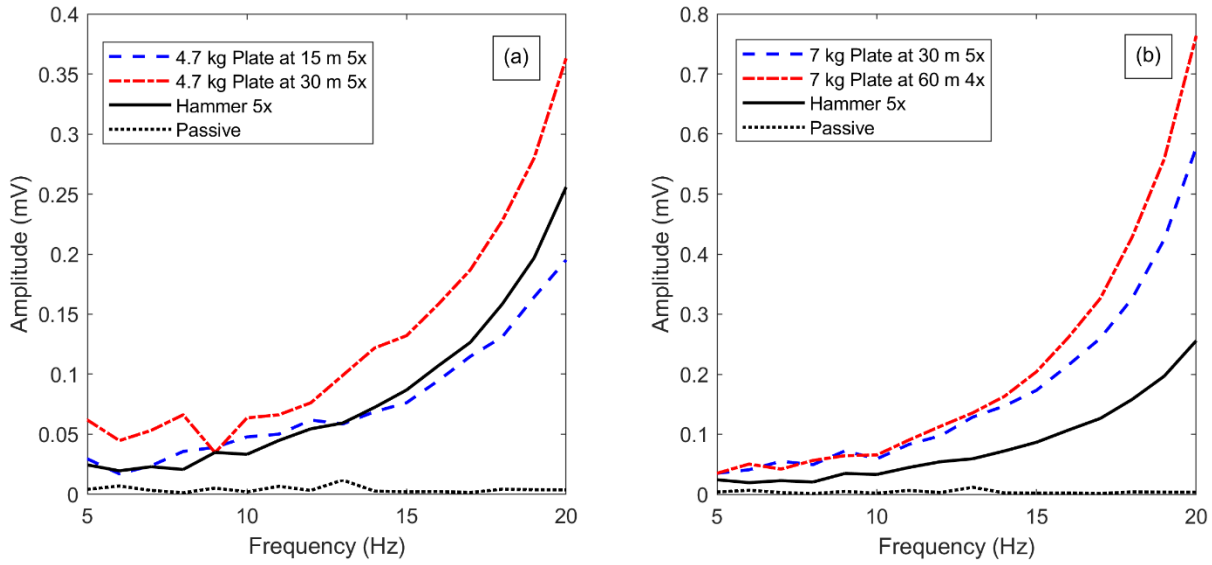

Figure 5-28: Comparison of stacked signals in the frequency domain for (a) 4.7 kg plates with hammer; and (b) 7 kg plates with hammer

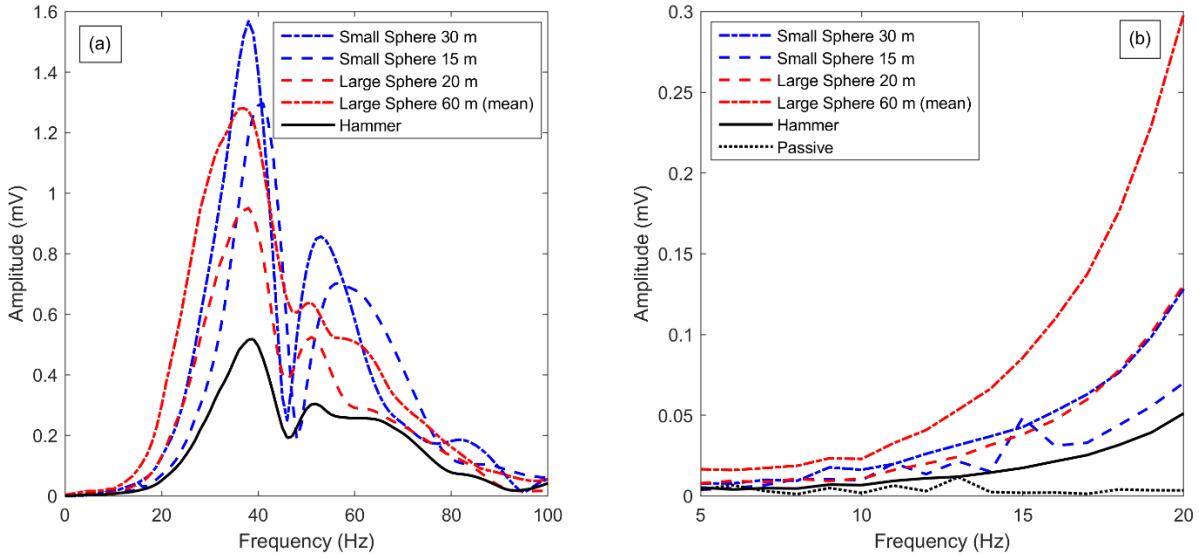

Figure 5-29: Frequency content of signals generated by (a) 7 kg spherical weights; (b) and at low frequencies

Figure 5-30: Impact craters of small spherical 7 kg weight (S1) dropped from (a) 15 m and (b) 30 m

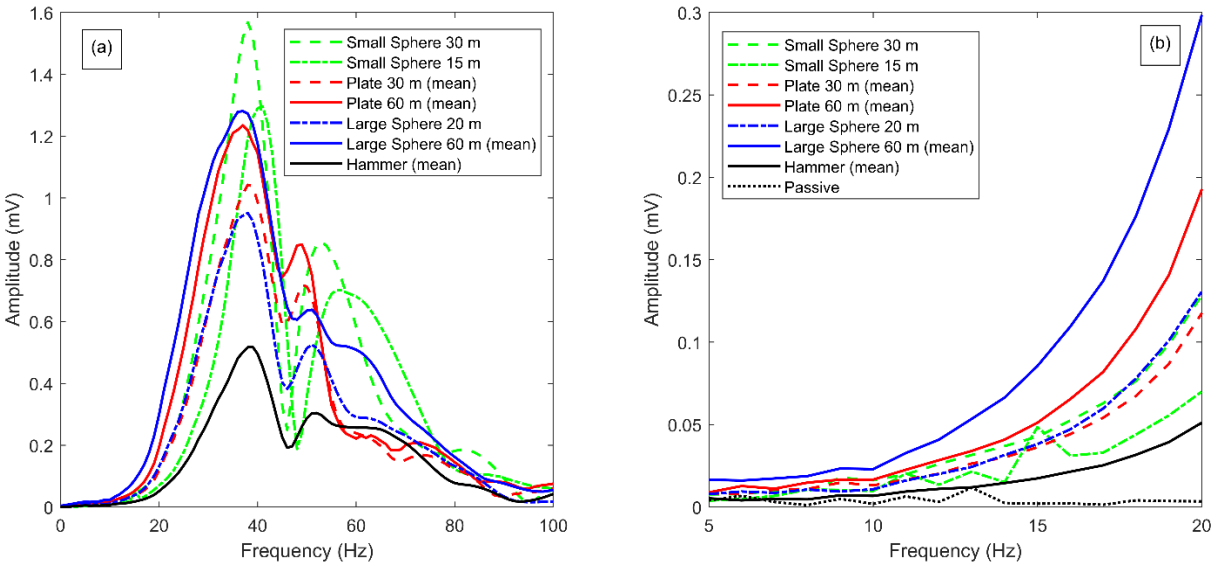

Figure 5-31: Individual and mean signals generated by (a) 7 kg weights and hammer; and (b) at low frequencies

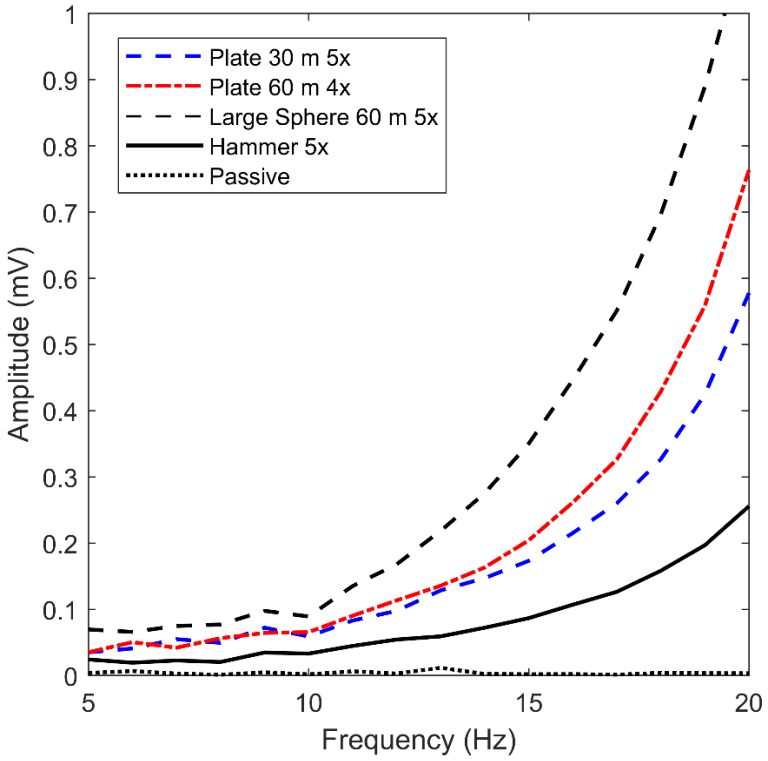

Figure 5-32: Stacked signals generated by 7 kg weights and hammer

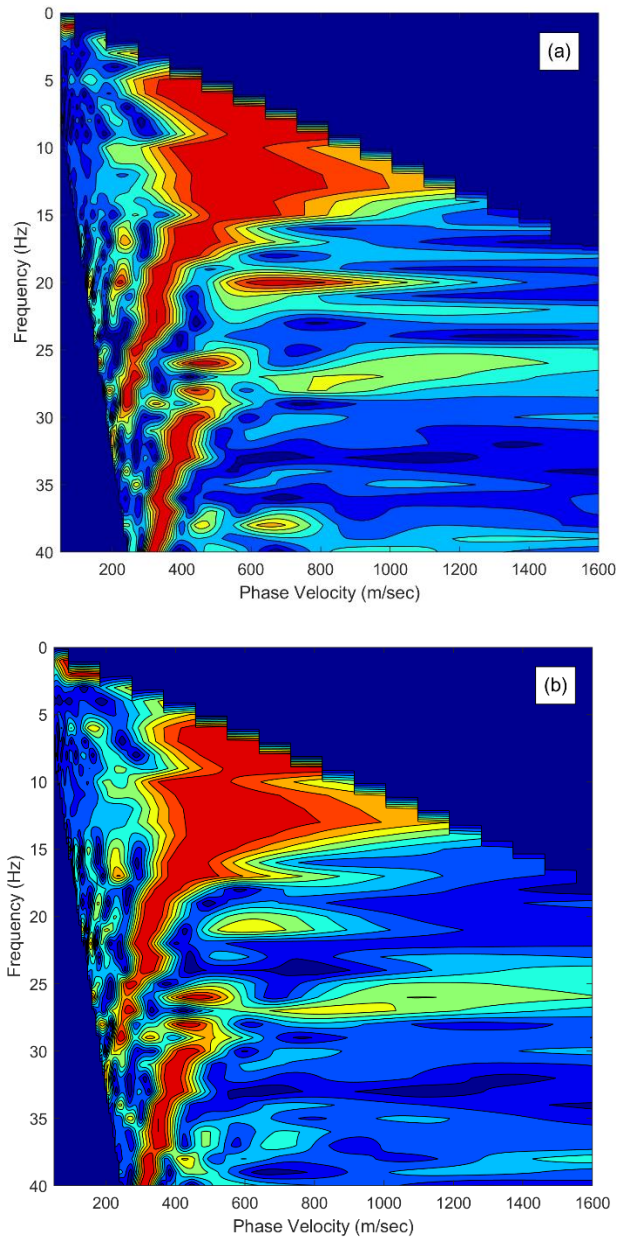

Figure 5-33: Phase Velocity-Frequency Spectra for 5 Stacked 7 kg Sphere at 60 m Signals (a) and Single 7 kg Sphere at 60 m Signal

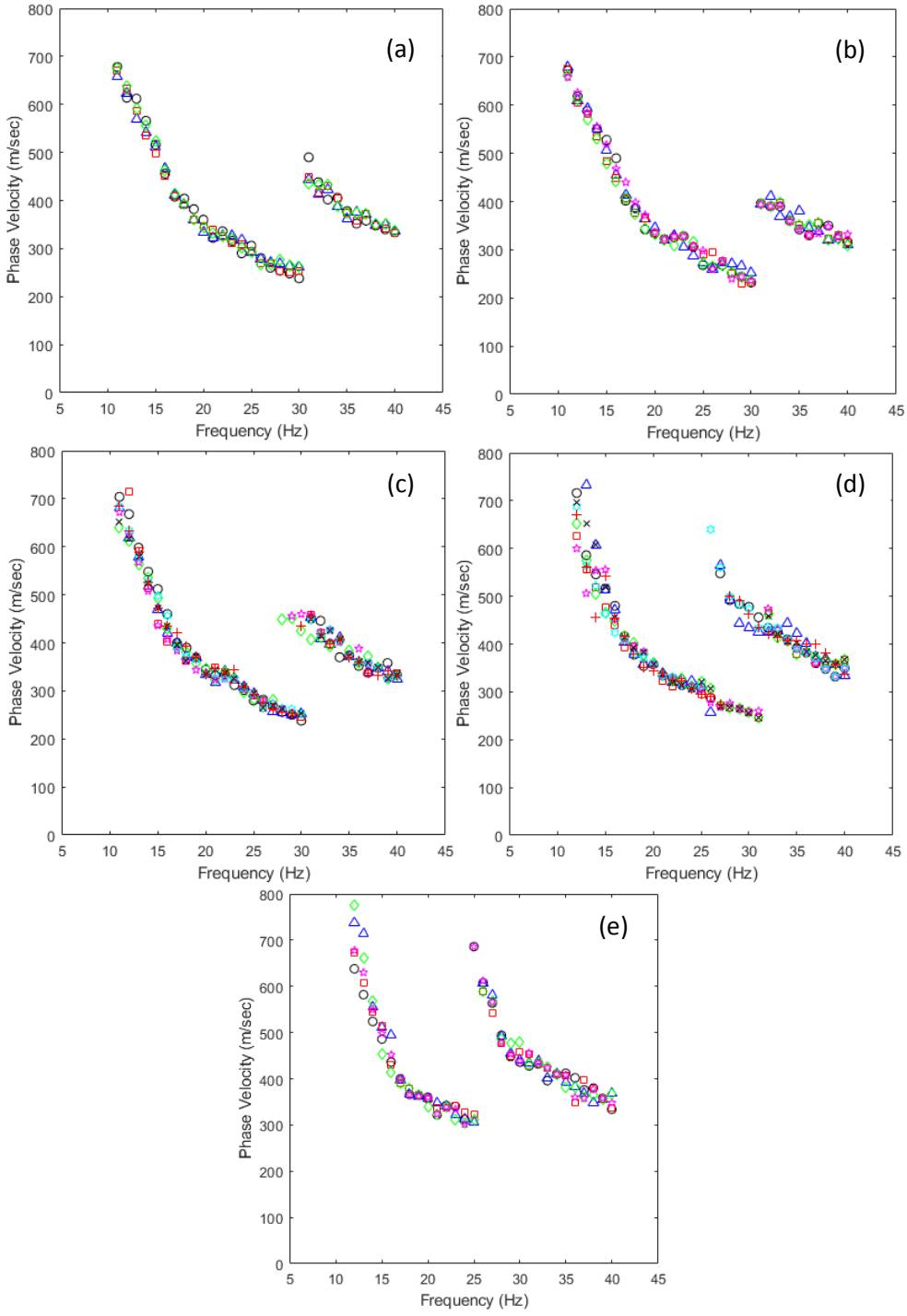

Figure 5-34: Dispersion curves for single weight drops using (a) 7 kg plate 60 m (4 trials); (b) 7 kg sphere 60 m (5 trials); (c) 7 kg plate 30 m (8 trials); (d) 4.7 kg plate 30 m (5 trials); and (e) 4.7 kg plate 15 m (8 trials)

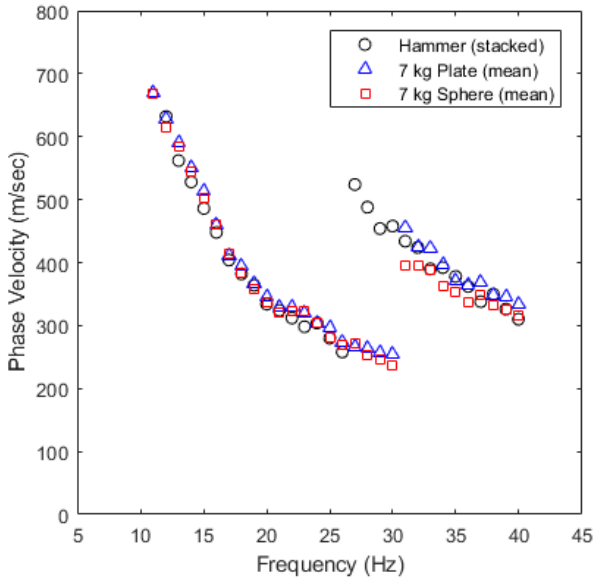

Figure 5-35: Mean dispersion curves for independent 7 kg weights dropped from 60 m and stacked 5.4 kg hammer dispersion curves

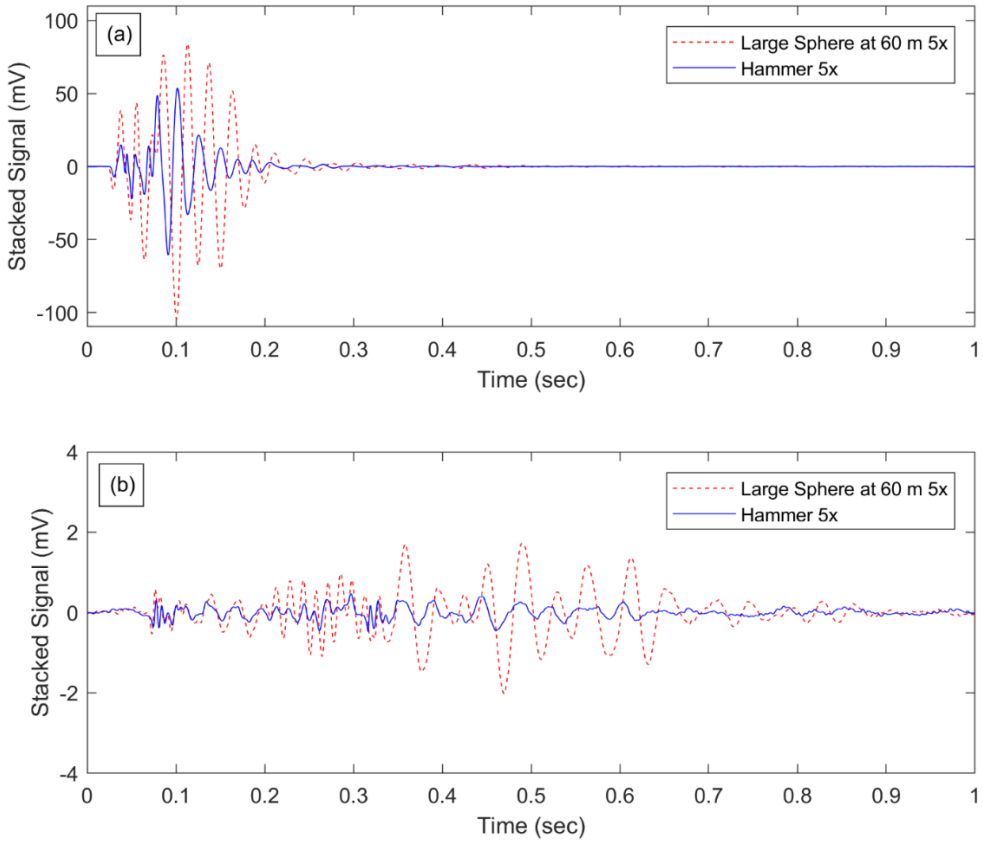

Figure 5-36: Stacked (5x) time domain signals for large sphere dropped from 60 m and hammer (a) at the first geophone; and (b) at the last geophone (90 m from first geophone)

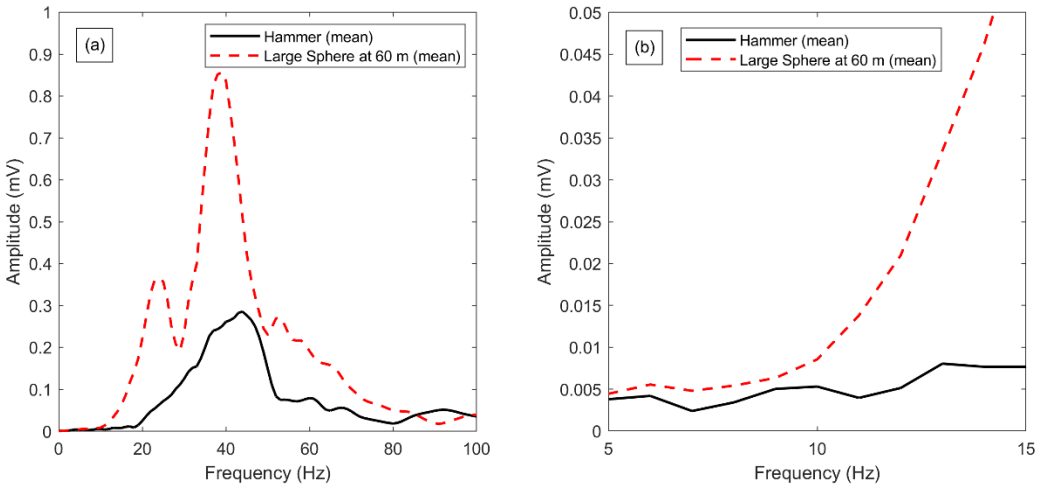

Figure 5-37: (a) Mean frequency domain signal for large sphere dropped from 60 m and hammer; and (b) at low frequencies

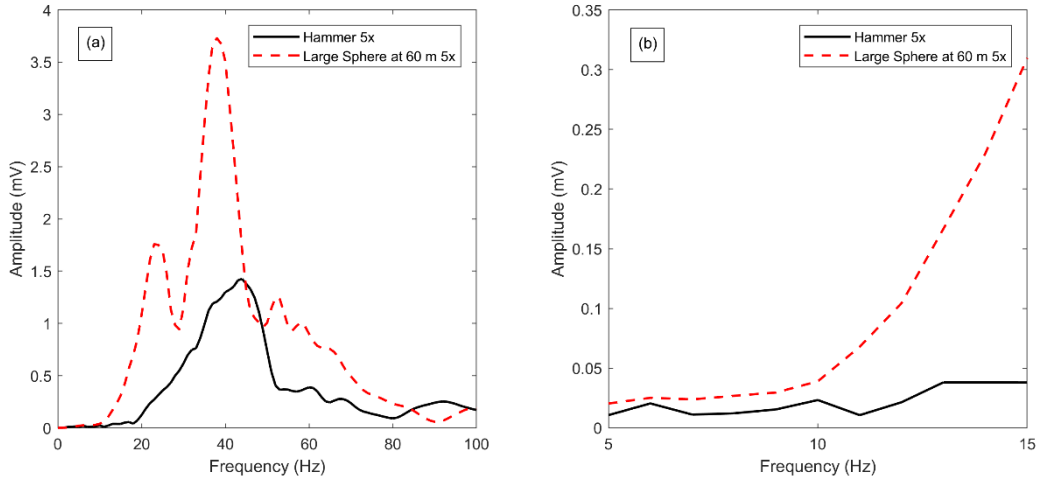

Figure 5-38: (a) Stacked (5x) frequency domain signal for large sphere dropped from 60 m and hammer; and (b) at low frequencies

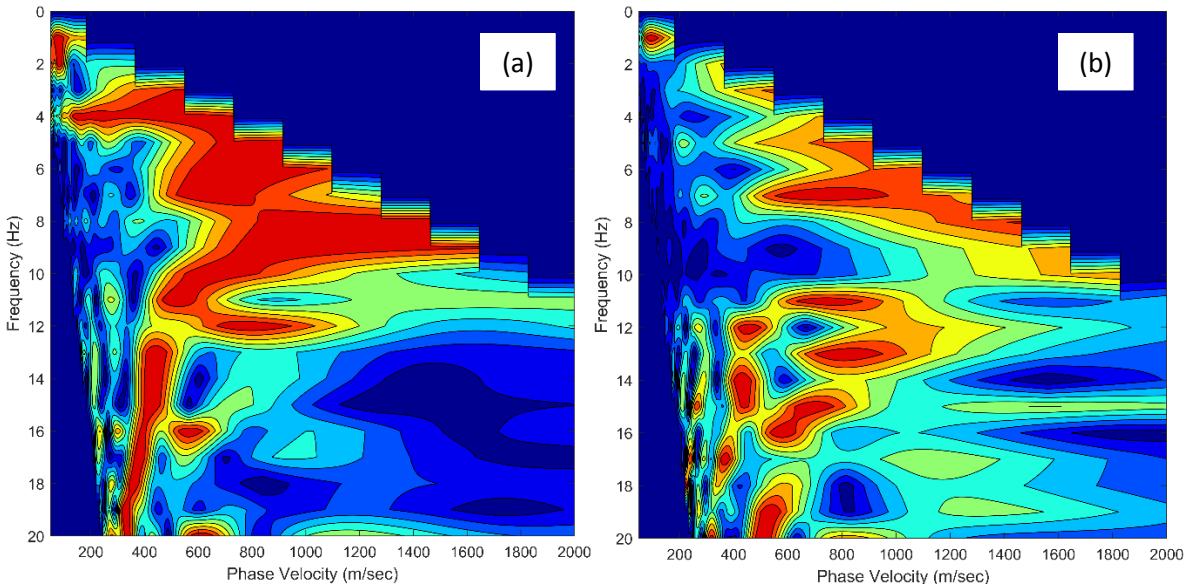

Figure 5-39: Phase velocity-frequency spectra for stacked signals (5x) for (a) 7 kg large sphere dropped from 60 m and (b) hammer

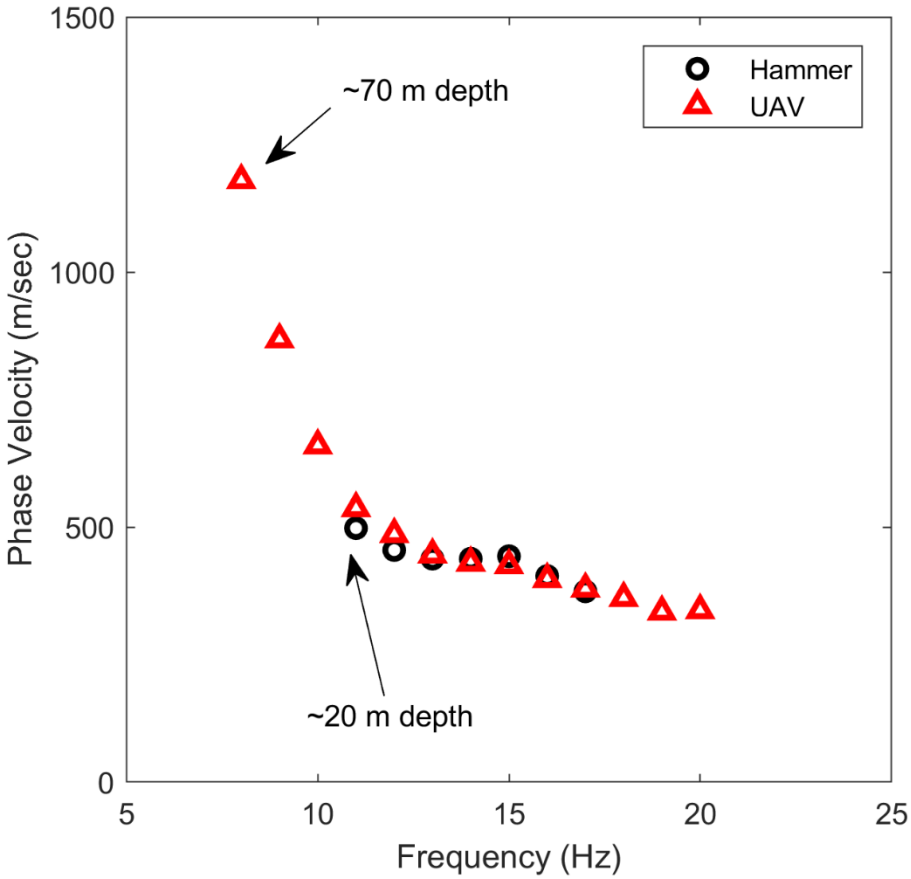

Figure 5-40: Dispersion curves interpreted from spectra in Figure 5-39; estimated depth of investigation is approximated as one half of the longest wavelength

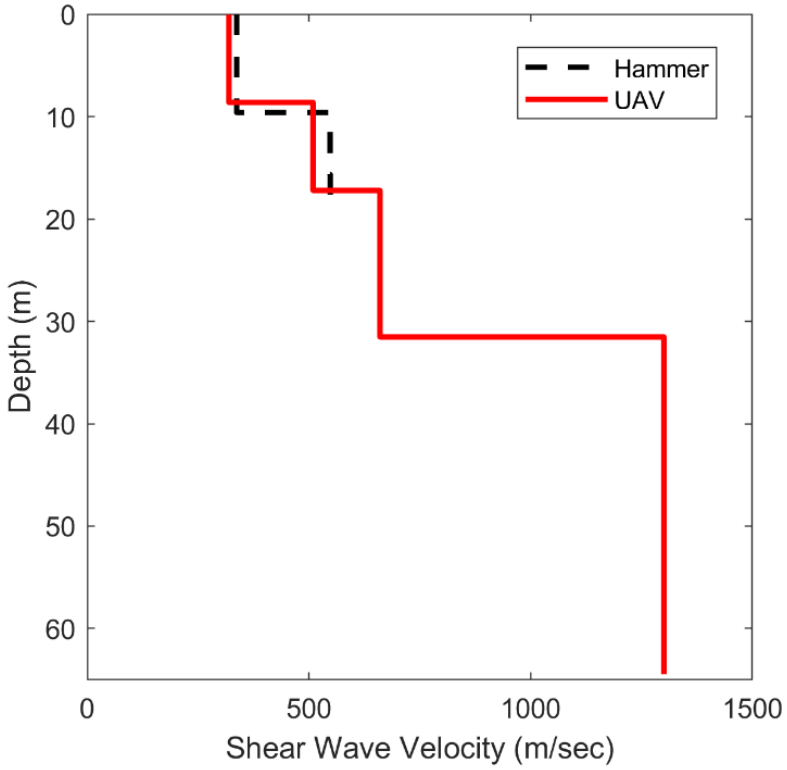

Figure 5-41: V_s profiles for dispersion curves in Figure 5-40

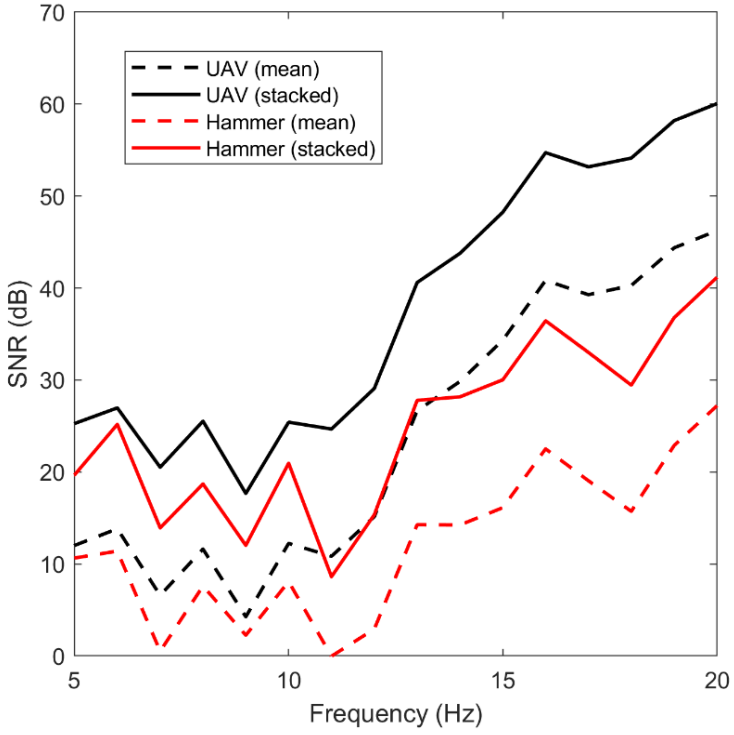

Figure 5-42: Comparison of SNR for stacked and unstacked hammer and UAV signals

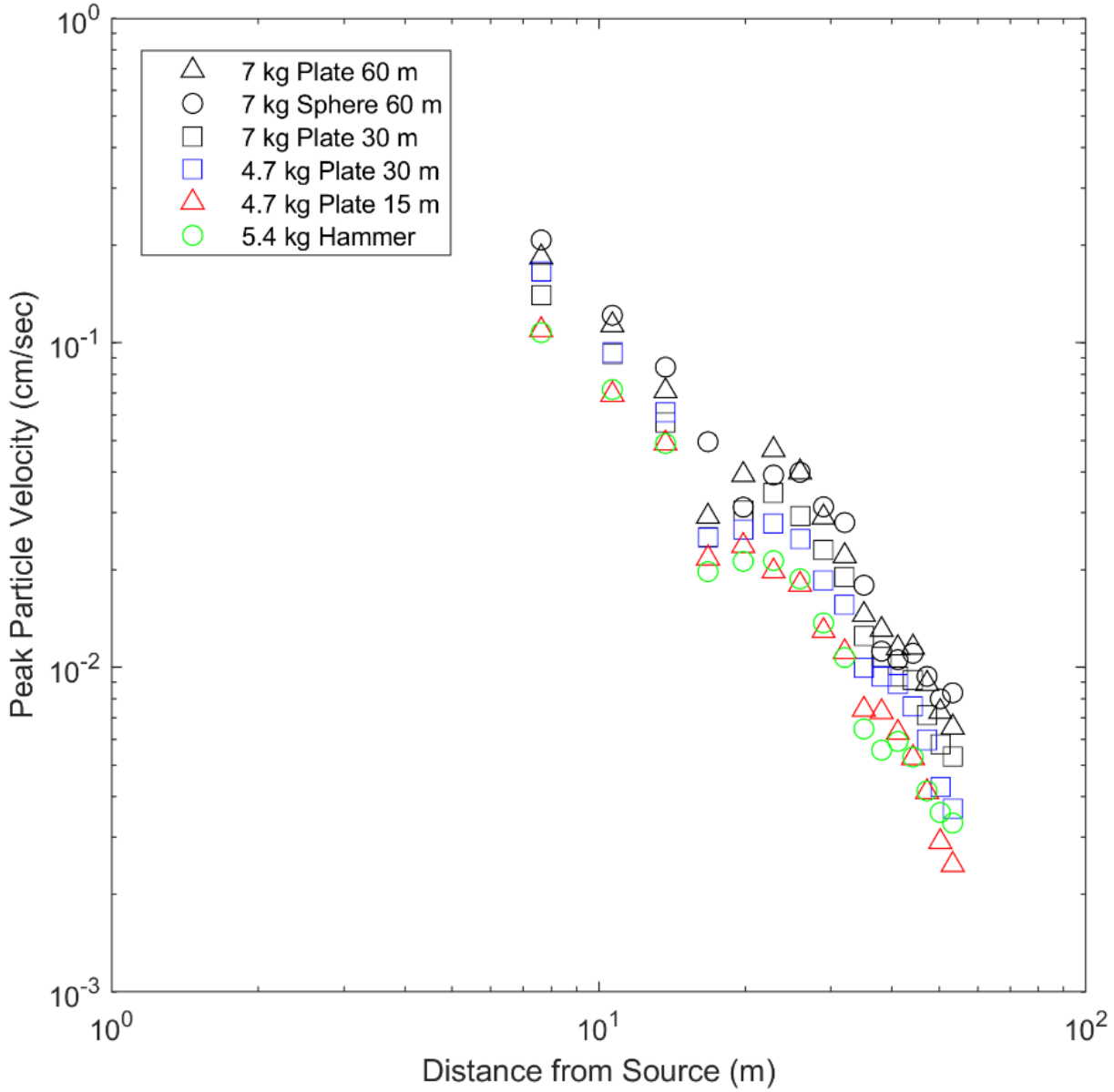

Figure 5-43: Estimated PPV induced by hammer and UAV-dropped weight impact sources

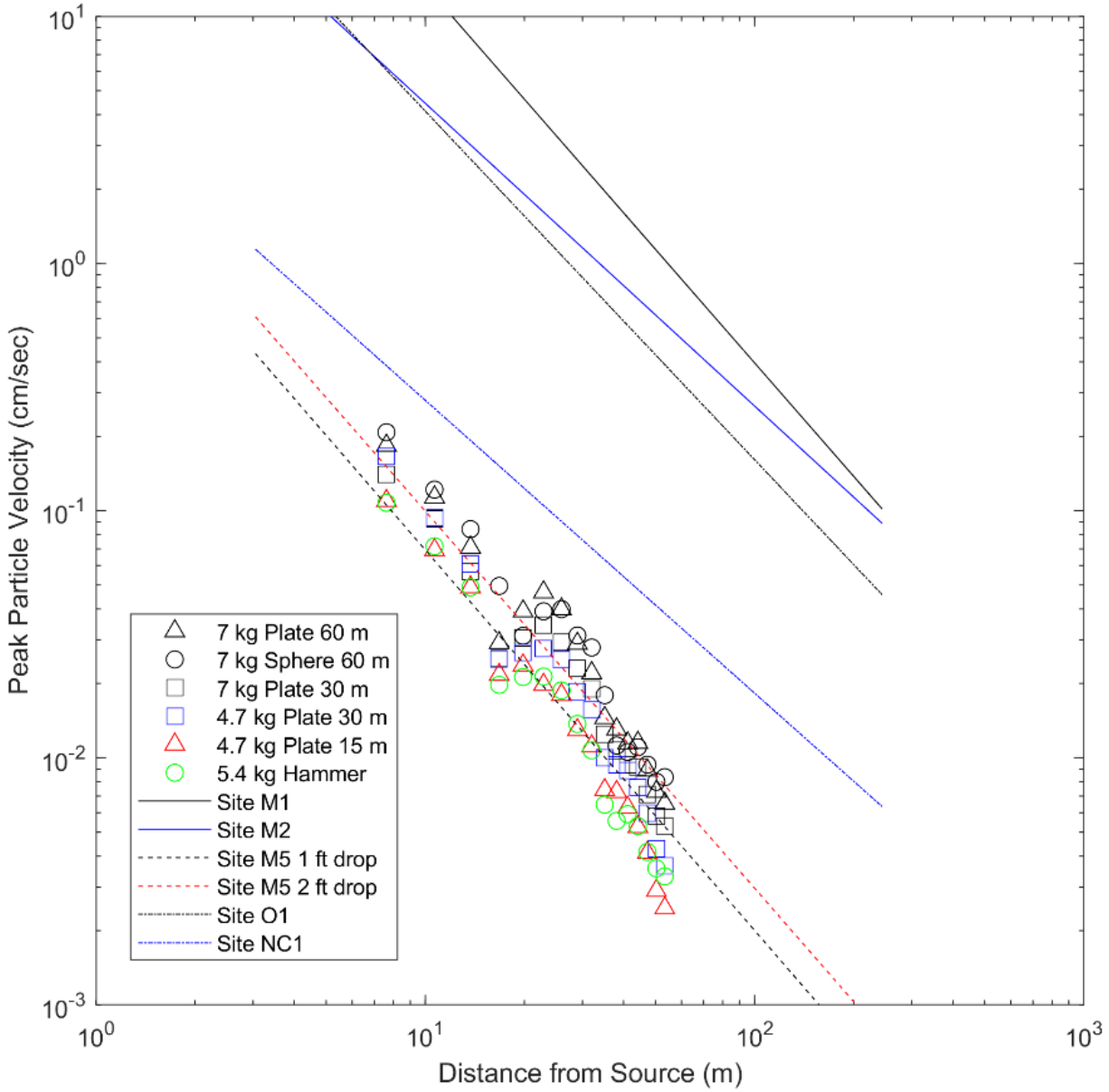

Figure 5-44: Estimated PPV induced by hammer and UAV-dropped weight impact sources compared to pseudo-attenuation curves produced from drop weight results reported by Woods and Jedele (1985)

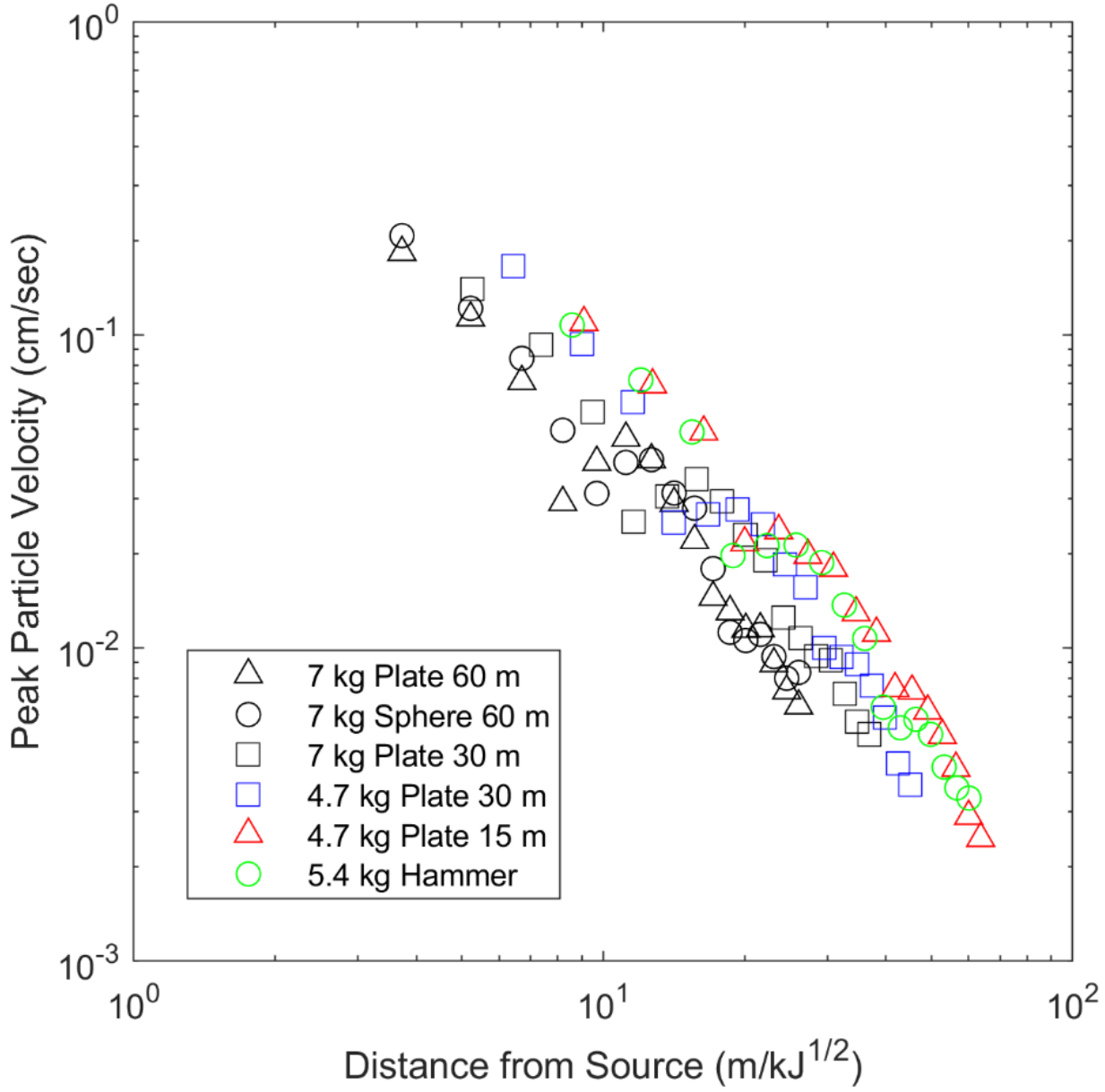

Figure 5-45: Estimated PPV induced by hammer and UAV-dropped weight impact sources as a function of scaled distance

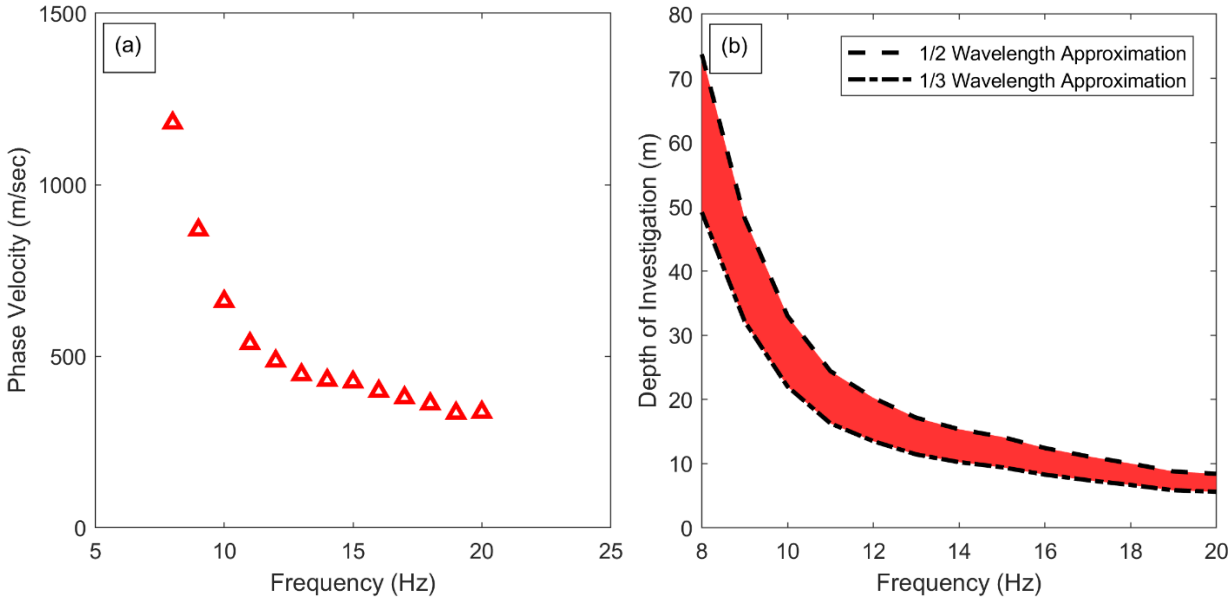

Figure 5-46: (a) Experimental dispersion curve for UAV-deployed source and 90 m geophone array and (b) range of theoretical depth of investigation based on wavelength approximations

5.4 References

Aki, K. (1957). "Space and Time Spectra of Stationary Stochastic Waves with Special Reference to Microtremors." *Bull. Earth Res. Inst. Tokyo Univ.* 25, 415–457.Alshibli, K. A., Okeil, A. M., Alramahi, B., and Zhang, Z., 2009, Statistical assessment of repeatability of CPT measurements: Contemporary topics in In Situ Testing, Analysis, and Reliability of Foundations, GeoFlorida 2009, Orlando, Florida, 87-94.

Andrus, R. D., and Stokoe, K. H., II. (2000). "Liquefaction resistance of soils from shear-wave velocity." *J. Geotech. Geoenviron. Eng.*, 126(11), 1015–1025.

Asten, M. (2006). "On Bias and Noise in Passive Seismic Data from Finite Circular Array Data Processed using SPAC Methods." *Geophysics*, 71(6), 153–162.

Athanasopoulos, G. A., Pelekis, P. C., and Anagnostopoulos, G. A. (2000). "Effect of Soil Stiffness in the Attenuation of Rayleigh-Wave Motions from Field Measurements." Soil Dynamics and Earthquake Engineering, 19: 277-288.

Bettig, B., Bard, P. –Y., Scherbaum, F., Riepl, J., Cotton, F., Cornou, C., and Hatzfeld, D. (2001). "Analysis of Dense Array Noise Measurements Using the Modified Spatial Autocorrelation Method (SPAC): Application to the Grenoble Area." *Boll. di Geofis. Teor. ed Appl.*, 42(3–4), 281–304.

Boiero, D., and Socco, L. V. (2014). "Joint Inversion of Rayleigh-Wave Dispersion and P-Wave Refraction Data for Laterally Varying Layered Models." Geophysics, 79(4): 49-59.

Chen, J. –R., and Kulhawy, F. H. (2014). "Characteristics and intercorrelations of index properties for cohesionless gravelly soils." Geocongress 2014 Technical Papers, 1-13.

Comina, C., Foti, S., Boiero, D., and Socco, L. V. (2011). "Reliability of Vs30 Evaluations from Surface Wave Tests." Journal of Geotechnical and Geoenvironmental Engineering, 137(6): 579-586.

Cox, B. R., Bachhuber, J., Rathje, E., Wood, C. M., Dulberg, R., Kottke, A., Green, R. A., and Olson, S. M. (2011). "Shear wave velocity and geology-based seismic microzonation of Port-au-Prince, Haiti." *Earthquake Spectra*, 27(S1), 67-92.

Cox, B. R., Wood, C. M., and Hazirbaba, K. (2012). "Frozen and unfrozen shear wave velocity seismic site classification of Fairbanks, Alaska." *Journal of Cold Regions Engineering*, 26(3), 118-145.

Cox, B.R., Wood, C.M., Teague, D.P. (2014). "Synthesis of the UTexas1 Surface Wave Dataset Blind-Analysis Study: Inter-Analyst Dispersion and Shear Wave Velocity Uncertainty." ASCE Geo-Congress 2014: Geo-Characterization and Modeling for Sustainability, Atlanta, GA, 23-26 February 2014.

Cox, B. R., and Teague, D. P. (2016). "Layering Ratios: A Systematic Approach to the Inversion of Surface Wave Data in the Absence of A-Priori Information." Geophysical Journal International, Advance Access.

Dowding, C. H. (2000). "Construction Vibrations." *International Society of Explosives.*

Duffy, B., Campbell, J., Finnemore, M., and Gomez, C. (2014). "Defining Fault Avoidance Zones and Associated Geotechnical Properties using MASW: A Case Study on the Springfield Fault, New Zealand." Engineering Geology, 183: 216-229.

Forbriger, T. (2003). "Inversion of Shallow-Seismic Wavefields: I. Wavefield Transformation." *Geophysical Journal International*, 153, 719-734.

Foti, S., Comina, C., Boiero, D., and Socco, L. V. (2009). "Non-Uniqueness in Surface-Wave Inversion and Consequences on Seismic Site Response Analyses." Soil Dynamics and Earthquake Engineering, 29: 982-993.

Garofalo, F., Foti, S., Hollender, F., Bard, P. Y., Cornou, C., Cox, B. R., Ohrnberger, M., Sicilia, D., Asten, M., Di Giulio, G., Forbriger, T., Guillier, B., Hayashi, K., Martin, A., Matsushima, S., Mercerat, D., Poggi, V., and Yamanaka, H. (2016). "InterPACIFIC Project: Comparison of Non-Invasive Methods for Seismic Site Characterization. Part I: Intra-Comparison of Surface Wave Methods." *Soil Dynamics and Earthquake Engineering*, 82, 222-240.

Greenwood, W., Zekkos, D., and Sahadewa, A. (2015). "Spatial Variation of Shear Wave Velocity of Waste Materials from Surface Wave Methods." *Journal of Environmental and Engineering Geophysics*, 20(4), 287-301.

Greenwood, W. W., Zhou, H., Zekkos, D., and Lynch, J. (2018). "Experiments using a UAV-Deployed Impulsive Source for Multichannel Analysis of Surface Waves Testing." *Geotechnical Earthquake Engineering and Soil Dynamics V*, ASCE, Austin, TX.

Griffiths, S. C., Cox, B. R., Rathje, E. M., and Teague, D. P. (2016a). "Surface-Wave Dispersion Approach for Evaluating Statistical Models That Account for Shear-Wave Velocity Uncertainty." *Journal of Geotechnical and Geoenvironmental Engineering*, 142(11).

Griffiths, S. C., Cox, B. R., Rathje, E. M., and Teague, D. P. (2016b). "Mapping Dispersion Misfit and Uncertainty in Vs Profiles to Variability in Site Response Estimates." *Journal of Geotechnical and Geoenviromental Engineering*, 142(11).

Hayashi, K., and Suzuki, H. (2004). "CMP Cross-Correlation Analysis of Multi-Channel Surface-Wave Data." *Exploration Geophysics*, 35: 7-13.

Joh, S. –H., Stokoe, K. H., II, Lee, I. –W., Kang, T. –H., Rosenblad, B., and Bay, J. A. (2006). "Joint Inversion for Apparent Phase Velocities of Rayleigh and Love Waves." GeoCongress 2006, ASCE.

Kramer, S. L. (1994). "Geotechnical earthquake engineering." Prentice Hall, Upper Saddle River, NJ.

Lai, C. G., Rix, G. J., Foti, S., and Roma, V. (2002). "Simultaneous Measurement and Inversion of Surface Wave Dispersion and Attenuation Curves." Soil Dynamics and Earthquake Engineering, 22: 923-930.

Leong, E. C., and Aung, A. M. W. (2013). "Global Inversion of Surface Wave Dispersion Curves Based on Improved Weighted Average Velocity Method." Journal of Geotechnical and Geoenvironmental Engineering, 139(12): 2156-2169.

Lin, Y. –C., Stokoe, K. H., II, and Rosenblad, B. L. (2008). "Variability in Vs Profiles and Consistency between Seismic Profiling Methods: A Case Study in Imperial Valley, California." International Conference on Site Characterization (ISC-3), Taipei, Taiwan, 75-81.

Luke, B., and Calderón-Macías, C. (2007). "Inversion of Seismic Surface Wave Data to Resolve Complex Profiles." Journal of Geotechnical and Geoenvironmental Engineering, 133: 155-165.

Maranò, S., Reller, C., Loeliger, H. –A., and Fäh, D. (2012). "Seismic Wave Estimation and Wavefield Decomposition: Application to Ambient Vibrations." *Geophysical Journal International*, 191, 175-188.

Maraschini, M., and Foti, S. (2010). "A Monte Carlo Multimodal Inversion of Surface Waves." Geophysical Journal International, 182: 1557-1566.

Maraschini, M., Ernst, F., Foti, S., and Socco, L. V. (2010). "A New Misfit Function for Multimodal Inversion of Surface Waves." Geophysics, 75(4): 31-43.

McMechan, G. A., and Yedlin, M. J. (1981). "Analysis of Dispersive Wave by Wave Field

Transformation." *Geophysics*, 46, 868–874.
Misbah, A. S., and Strobbia, C. L. (2014). "Joint Estimation of Modal Attenuation and Velocity from Multichannel Surface Wave Data." Geophysics, 79(3): 25-38.
Nasseri-Moghaddam, A., Cascante, G., and Hutchinson, J. (2005). "A New Quantitative Procedure to Determine the Location and Embedment Depth of a Void Using Surface Waves." *J. of Env. and Eng. Geophysics*, 10, 51-64.
Nolet, P., and Panza, G. F. (1976). "Array Analysis of Seismic Surface Waves: Limits and Possibilities." *Pure Appl. Geophys.*, 114, 776–790.
Okada, H. (2003). "The microtremor survey method." *Geophysical Monograph Series* No. 12: Society of Exploration Geophysicists, Tulsa, OK.
Park, C.B., Miller, R.D., and Xia, J. (1998). "Imaging dispersion curves of surface waves on multi-channel record" in Expanded Abstracts: *68th Annual International Meeting, Society of Exploration Geophysicists*, 1377–1380.
Park, C.B., Miller, R.D., and Xia, J. (1999). Multichannel analysis of surface waves." *Geophysics*, 64(3), 800–808.
Park, C.B., Miller, R.D., Ryden, N., Xia, J., and Ivanov, J. (2005). "Combined use of active and passive surface waves." *Journal of Environmental and Engineering Geophysics*, 10(3), 323–334.
Phoon, K. –K., and Kulhawy, F. H., (1999). "Characterization of geotechnical variability." *Canadian Geotechnical Journal*, 36(4), 612-624.
Piatti, C., Socco, L. V., Boiero, D., and Foti, S. (2012). "Constrained 1D Joint Inversion of Seismic Surface Waves and P-Refraction Travel-Times." *Geophysical Prospecting*, 61, 77–93.
Richart, F. E., Jr., Hall, J. R., and Woods, R. D. (1970). "Vibrations of Soils and Foundations." *Prentice-Hall*, Englewood Cliffs, NJ.
Rix, G., J., Lai, C. G., and Spang, A. W. Jr. (2000). "In Situ Measurement of Damping Ratio Using Surface Waves." *Journal of Geotechnical and Geoenvironmental Engineering*, 126, 472-480.
Sahadewa, A., Zekkos, D., and Woods, R.D. (2012). "Observations from the implementation of a combined active and passive surface wave based methodology." in *Proceedings of the State of the Art and Practice in Geotechnical Engineering* (Geocongress 2012), 2786–2795.
Sheehan, A. J., Olson, R. E., Park, K., and Stokoe, K. H., II. (2010). "Estimation of settlement of footings under working loads using equivalent-linear elasticity." GeoFlorida 2010: Advances in analysis, modeling & design (CD-ROM), ASCE, Reston, VA, 1708–1717.
Socco, L. V., Foti, S., and Boiero, D. (2010). "Surface-Wave Analysis for Building Near-Surface Velocity Models – Established Approaches and New Perspectives." Geophysics, 75(5): 83-102.
Stokoe, K. H., II, Wright, S. G., Bay, J. A., and Roesset, J. M. (1994). "Characterization of Geotechnical Sites by SASW Method." In *Geophysical Characterization of Sites*, Ed. R. Woods, 15-26. International Science, New York.
Stokoe, K. H., II, and Santamarina, J. C. (2000). "Seismic-wave based testing in geotechnical engineering." *International Conference on Geotechnical and Geological Engineering*, 1, 1490–1536.
Stokoe, K. H., II, Joh, S. –H., Wooods, R. D. (2004a). "Some Contributions of In Situ Geophysical Measurements to Solving Geotechnical Engineering Problems." International Conference on Site Characterization (ISC-2), Porto, Portugal, 15-50.

Stokoe, K. H., II, Rosenblad, B. R., Wong, I. G., Bay, J. A., Thomas, P. A., and Silva, W. J. (2004b). "Deep Vs Profiling Along the Top of Yucca Mountain Using a Vibroseis Source and Surface Waves." 13th World Conference on Earthquake Engineering, Vancouver, B.C.

Supranata, Y. E., Kalinski, M. E., and Ye, Q. (2007). "Improving the Uniqueness of Surface Wave Inversion Using Multiple-Mode Dispersion Data." Journal of Geotechnical and Geoenvironmental Engineering, 7(5): 333-343.

Vipulanandan, C., Ahossin Guezo, Y. J., and Bilgin, Ö., (2007). "Geotechnical properties of marine and deltaic soft clays." Advances in Measurement and Modeling of Soil Behavior, GeoDenver, Denver CO, 1-13.

Wathelet, M., Jongmans, D., and Ohrnberger, M. (2004). "Surface-Wave Inversion using a Direct Search Algorithm and its Application to Ambient Vibration Measurements." Near Surface Geophysics, 2: 211-221.

Wong, I. G., Stokoe, K. H., II, Cox, B. R., Lin, Y. –C., and Menq, F. –Y. (2011). "Shear wave velocity profiling of strong motion sites that recorded the 2001 Nisqually, Washington, earthquake." *Earthquake Spectra*, 27(1), 183-212.

Woods, R. D., and Jedele, L. P. (1985). "Energy-Attenuation Relationships from Construction Vibrations." *Vibration Problems in Geotechnical Engineering*, Special Technical Publication, ASCE, 187-202.

Xia, J., Miller, R. D., Park, C. B., and Ivanov, J. (2000). "Construction of 2-D Vertical Shear-Wave Velocity Field by the Multichannel Analysis of Surface Wave Technique." Proc. of the Symposium on the Application of Geophysics to Engineering and Environmental Problems (SAGEEP), Arlington, VA, pp. 1197-1206.

Xia, J., Miller, R. D., Park, C. B., and Tian, G. (2003). "Inversion of High Frequency Surface Waves with Fundamental and Higher Modes." Journal of Applied Geophysics, 52: 45-57.

Yoon, S., and Rix, G. J. (2009). "Near-Field Effects on Array-Based Surface Wave Methods with Active Sources." Journal of Geotechnical and Geoenvironmental Engineering, 135(3): 399-406.

Zekkos, D., Sahadewa, A., Woods, R. D., and Stokoe, K. H. (2014b). "Development of model for shear wave velocity of municipal solid waste." *Journal of Geotechnical and Geoenvironmental Engineering*, **140**(3), 04013030.

Zywicki, D. J. (1999). "Advanced Signal Processing Methods Applied to Engineering Analysis of Seismic Surface Waves." *Georgia Institute of Technology*.

CHAPTER 6

Conclusions and Recommendations for Future Research

6.1 Summary of Conclusions

This research explored the applications of UAVs for surface and subsurface characterization of geosystems and developed frameworks for expanding UAV-based efforts in post-earthquake reconnaissance, and site characterization. The three main thrusts of the research were to use SfM photogrammetry to derive surface geometries at geotechnical sites, develop image processing techniques to characterize rock features exposed at the surface, and employ UAV-enabled seismic surface wave methods to assess subsurface material properties. This section summarizes the main conclusions that have been drawn in the three main research thrusts.

6.1.1 UAV-Based 3D Imaging of Geotechnical Sites

Camera-equipped UAVs were used to document complex 3D geometries at geotechnical sites using SfM photogrammetry. The technological capabilities of these surveying techniques have improved significantly during the duration of this research and will continue to improve. The point clouds generated by SfM were subsequently used to manually analyze the structure of rock masses in 3D to assign strength parameters (GSI) and delineate failure planes (strike, dip). The UAVs collected images for generating cm-resolution models of 75-150 m high landslides in less than 30 minutes of total site time. SfM models were found to be useful for analyzing rock masses

to assign GSI values and identify failure planes in landslides that are used in stability analyses. It was found that making visual observations in 2D images (used as input for SfM) was useful while conducting measurements in the 3D model. This lends credence to the idea that source imagery should be coupled with 3D modeling results when developing automated rock mass characterization methods. Mapping needs to account for the smallest feature required to be visible in the imagery and therefore flight parameters should be set based on the target resolution. In this research, UAV-based SfM was used to measure the spacing and orientation of discontinuities for geomechanical characterization of rock masses, delineate landslide geometries, and document other geotechnical sites. The UAV was also useful for decision making in the field. The UAV was used to track the path taken by a debris flow and identify landslides that contributed to the debris, supporting field interpretations of observed performance.

A network of GCPs is required at each site when performing SfM surveys. GCPs and checkpoints should be placed to cover the target areas. GCPs and check points should also be placed to capture 3D geometry. Using additional points is necessary when recording laser points on natural upslope features because some may be less well-defined in the model. In addition to planning the distribution of GCPs at a site, the required flight time must be estimated. For manual flights, pilot experience, environmental conditions, and UAV technology will affect flight time. Currently, automated flights are not optimized for surveying areas with relatively significant elevation change, complex 3D geometry, or close-range visual inspection. Advances in flight planning and obstacle avoidance are needed to support the collection of images of detailed features such as rock discontinuities.

A variety of conditions affect the flight performance of UAVs. Weather is a principal component including precipitation, temperature, and wind. In cases of precipitation and

temperature, UAV operations are unlikely to be conducted unless a platform specifically designed to be resilient to freezing temperatures, extremely high temperatures, or precipitation is being used. Wind is the weather condition most likely to need significant consideration as wind speed and direction vary during flight. Stability is most affected by wind gusts and can present significant risk if the UAV is flying close to a target for visual (or other sensing types) inspection (*e.g.* rock structure, bridge components). Weather conditions may affect the collected data in addition to UAV performance. For example, the position of the sun can render image collection from some orientations useless. Sunlight can also cause uneven lighting on the target surface. Geometric results of SfM may not be affected due to the illumination-invariant feature detection, unless shadows are dark enough that features cannot be detected. The lighting variation will affect the colors observed on the surface and influence results from interpretations of the SfM outputs and processing of the input images.

6.1.2 Processing of UAV-Derived 2D and 3D Imagery Outputs for Rock Mass Characterization

An explicit image processing method for fracture detection in rock masses was developed. The algorithm was designed to address some of complexities that make vision-based discontinuity assessments difficult including surface texture and color variation. The fracture detection algorithm was tested on three image sets from different sources: images of a weathered, vesicular basalt roadside outcrop, a marble quarry, and a mixed set of images of different rock types and resolutions. When parameters are applied globally to a large image, changing brightness across the image reduces detection rates. To address this, the fracture detection algorithm was then integrated with SLIC to cluster pixels prior to performing fracture detection to help isolate the influence of lighting, texture, and color variation.

The developed fracture detection method has the ability to be fully automated, but has limitations such as detecting fractures in rocks with highly-textured surfaces or surface staining caused by weathering. A semi-automated approach which introduces additional control parameters for the user to adjust can perform well on a wider range of rock masses. For use with highly textured rocks (*e.g.* vesicles), or rocks with color variation, but with high fracture contrast, the modified Otsu's threshold greatly improves performance by reducing the number of false positives. For textured (noisy) rocks, a Gaussian filter is recommended when blurring of fracture edges is not a concern. In general, the algorithm should not be expected to detect fractures with widths < 3 pixels, which is an important consideration in the data acquisition stage. However, fractures as thin as 2 pixels could potentially be detected, but their persistence may not be fully captured. The semi-automatic fracture detection was tested on example profiles. The results showed agreement when compared to manual measurements, but the technique often underestimated fracturing, by about 10-20% when the modified Otsu's threshold was applied, due to the inability to identify very thin fractures. In other cases, the algorithm fracture count was within about 15% of manual fracture counting. Fracture detection results were used to inform geomechanical analyses, such as the calculation of RQD. A heat map of detected fractures on a profile performed well at identifying regions of broken-up and intact rock automatically. However, soil and overlying debris were identified as intact and broken-up rock respectively. These issues could potentially be resolved through pre-processing identification of material types to separate soil with techniques that consider color or texture and use 3D geometry to find potential overlying debris.

An updated version of SLIC was also developed which incorporates depth (3D) information into the clustering algorithm for use with RGBD images generated from SfM results.

RGBD images contain information from other camera perspectives. The relative weighting of image depth for clustering (N_d) is difficult to define automatically. For the purposes of this application, the clustering weight was equivalent to the GSD of the image scaled by a factor, K = 5-20. The updated SLIC algorithm and the selection of K will require additional validation before being extended to other applications. When clustering was performed on RGBD images, the intra-cluster variance decreased and resulted in clusters more closely following the 3D structure of the rock. A framework to integrate fracture detection on segmented images was also implemented. The detected fractures coinciding with RGBD pixels were transformed to 3D and synthesized with the point cloud. With discontinuities labeled in the 3D point cloud, their orientation (strike/dip) could be measured. Other information (RQD, GSI, V_s, material classification, etc.) tied to an image can also be mapped to 3D and tied to the point cloud. The individual components of the framework are designed to be open-ended for integration with other 2D/3D image processing techniques which could be underlying components of UAV-based analysis.

6.1.3 UAV-Enabled Subsurface Characterization using Multichannel Channel Analysis of Surface Waves

A third thrust of this research was subsurface characterization using UAVs. A UAV was used to lift and drop a 7 kg payload to generate seismic surface waves as a replacement for a hammer or more costly seismic source. Both spherical and plate-shaped weights were dropped from heights of 15 - 60 m. The UAV-dropped weights were found to outperform a hammer for energy input below 10 Hz, which is critical for surface wave testing at greater depths. A 7 kg plate was found to perform similarly, in general, to 7 kg spheres, but the spheres were found to more reliable, and practical, due to the improved consistency of impact to the ground (*i.e.* spheres cannot

land along an edge). The plate also appeared to rock more during flight and when in free fall. The spheres additionally outperformed the plate for the frequencies of interest for surface wave dispersion. Two 7 kg spheres of different sizes were compared. The two 7 kg spherical weights caused significant shearing of the ground surface and did not bounce (*i.e.* recoil) following impact. As the forcing area is smaller for the small sphere, the weight penetrated the ground further than the large sphere.

A practical limitation to physically-large weights was also observed. The large sphere had a greater lateral surface area and made the UAV flight with the large payload more sensitive to windy conditions. The inaccuracy of drop weight impact locations was found to be insignificant for variations of less than 3% of the total array length. The signal generated by the UAV-deployed weight was used to perform a dispersion analysis without the need for signal stacking. At the test site, the dispersion analysis went to 8 Hz due to limitations in array geometry at the test site. The UAV-generated signal contained sufficient content at 5 Hz, which was the minimum sensing frequency of the geophones used, to propagate waves up to an estimated 120 m. It is possible that energy input from the drop weight can extend to even lower frequencies and higher amplitudes. However, additional testing at other site types with different subsurface and background noise conditions is warranted to further explore UAV-based impulse deployment. By using a 90 m array length, it was demonstrated that the UAV-dropped weight could be used to investigate to greater depths in the subsurface (due to the low frequencies). At the test site used in this study, the UAV increased the depth of investigation for a 90 m geophone array from 18 m to 64 m. This increase in investigation depth demonstrates that the UAV-based surface wave testing has great value outside of post-disaster reconnaissance but could also be used for seismic profiling at a wide range of sites.

6.2 Recommendations for Future Research

Chapter 1 showed an envisioned paradigm shift where UAVs revolutionized post-disaster reconnaissance by not only altering conventional reconnaissance methods in all three phases, but introduced an automation concept where previous stages could be returned to, and updated with new information. This would allow for both the breadth and depth of reconnaissance studies to improve and capture more, higher-quality perishable data. In order to achieve the paradigm shift documented in Chapter 1, more novel research is needed in a wide variety of areas. In the context of UAV-enabled seismic surface wave testing, the development of a UAV-deployed impact source is an important component for developing an autonomous framework for subsurface imaging and estimating shear wave velocity. But some components require additional research effort include wireless and mobile sensors, payload instrumentation and retrieval, and automated interpretation of results to inform operational decision making on-board the UAV. One example of on-board decision making would be to predict the maximum allowable array length with minimal information at a site. This can be predicted by combining any *a priori* information about site conditions (*i.e.* attenuation), results of previous drop weight testing at other sites, and a measure of background noise at the site. In addition to expanding on the conclusions in the previous section, the following are research areas where impactful contributions can be made:

Subsurface sensing: The primary focus of UAV-based sensing has been on surface model development via remote sensing. UAVs are establishing themselves as a critical remote sensing tool that are highly adaptable to a range of sensors used at different spatial and temporal resolutions. The work that has been done on UAV-based sensing of below-surface features is limited. In this case, the surface could be a structural component, the ground, or ice. Examples of geophysical methods which have already been established on other aerial platforms being

implemented with or considered for use with small UAVs such as magnetic surveys, GPR, and SWM were noted. For geo-infrastructure applications, subsurface sensing is necessary and one of the major limitations is cost of mobilizing equipment and accessing remote or dispersed sites.

Swarms and UAV cooperation: As UAVs become integrated in spaces occupied by other aircraft, and inevitably other UAVs, methodologies for managing the interaction, intended or otherwise, between UAVs is critical. Research into groups of cooperating UAVs, or swarms, has expanded greatly in recent years. While this topic is not covered in this review, it is gaining significant traction outside of civil engineering. UAV swarms may perform the same basic operation simultaneously, such as aerial surveying, or perform complementary operations, such as sensor placement and interrogation.

Interfacing with humans: Some cases of human-UAV interaction in the fields of construction management and post-disaster reconnaissance have been identified. These studies have generally concluded that human-UAV interaction is an important direction for research. The interactions of interest can, similar to multi-UAV interactions, be intentional or unintentional. The interactions also do not have to occur in physical space, they can be virtual.

Decision-Making Frameworks: One component of developing fully-autonomous UAS is understanding how to integrate human cognition for decision making. An early step in that direction would be to have humans decide the next UAV operations in real time, such as in a post-disaster scenario to select sites of interest and *in situ* testing locations. This pseudo-training data could help construct the foundational autonomous frameworks.

Next Generation Imaging: 3D modeling using SfM has been shown to be a robust approach for geometric documentation of geotechnical sites. The 3D imaging captures highly-detailed geometry with many potential uses. As the generation of 3D models becomes established, methods

for integrating them with other workflows, such as 3D stability analyses, are necessary. Additionally, geospatial data collected by multi-sensor UAVs could benefit greatly from fusion with image-derived geometry and material properties.

APPENDICES

A Matlab Functions for Multichannel Analysis of Surface Waves

```
function [V,t] = GeoRead(files,fileno,Fs)
% Project:          Multichannel Analysis of Surface Waves
% Function:         GeoRead.m
% Author:           William W. Greenwood
% Affiliation:      University of Michigan
% Last Revised:     10 April 2018
% Purpose:          Read sensor time history from file
%%%%%%%%%%%%%%%%%%%%%%%%%%%%%%%%%%%%%%%%%%%%%%%%%%%%%%%%%%%%%%%%%%%%%%%%%%%%%%%
% INPUT:
% files:            Cell array containing file name strings
% fileno:           File number to be read (index of files)
% Fs:               Sampling frequency of data in files{fileno}
%%%%%%%%%%%%%%%%%%%%%%%%%%%%%%%%%%%%%%%%%%%%%%%%%%%%%%%%%%%%%%%%%%%%%%%%%%%%%%%
% OUTPUT:
% V:                Matrix of sensor data. One column per channel.
% t:                Time vector for sensor data
%%%%%%%%%%%%%%%%%%%%%%%%%%%%%%%%%%%%%%%%%%%%%%%%%%%%%%%%%%%%%%%%%%%%%%%%%%%%%%%
% Sample File Format:
%  x1        x2       x3       x4        x5        x6       ...
% 0.0134   0.0015   0.0002   0.0001   -0.0001   -0.0002     ...
%  ...       ...      ...      ...       ...       ...
%%%%%%%%%%%%%%%%%%%%%%%%%%%%%%%%%%%%%%%%%%%%%%%%%%%%%%%%%%%%%%%%%%%%%%%%%%%%%%%

data=tdfread(files{fileno});
N=size(data,2); % number of channels
V=zeros(length(data.x1),N);

% Reverse channel numbers to ascending (i.e. Geo 1 = Ch 1).
for k=1:N
    str='x';
    temp=num2str(N+1-k);
    for j=1:length(temp)
        str(end+1)=temp(j);
    end
    V(:,k)=data(1).(str);
end
T=1/Fs; % Period
t=T*(0:length(V)-1); % Time vector
end
```

```
function [handle,spec] = DispFig(A,PhV,f,V,t,c,Fmax)
% Project:          Multichannel Analysis of Surface Waves
% Function:         DispFig.m
% Author:           William W. Greenwood
% Affiliation:      University of Michigan
% Last Revised:     10 April 2018
% Purpose:          Plot output of dispersion analysis
%%%%%%%%%%%%%%%%%%%%%%%%%%%%%%%%%%%%%%%%%%%%%%%%%%%%%%%%%%%%%%%%%%%%%%%%%%%%%%%
% INPUT:
% A                 Phase velocity-frequency spectrum
% PhV:              Automatic dispersion curve points
% f:                Vector of Frequencies
% V:                Matrix of sensor time histories
% t:                Time vector for sensor data
% c:                Vector of trial phase velocities (min c : 1 : max c)
% Fmax:             Maximum frequency for dispersion analysis
%%%%%%%%%%%%%%%%%%%%%%%%%%%%%%%%%%%%%%%%%%%%%%%%%%%%%%%%%%%%%%%%%%%%%%%%%%%%%%%
% OUTPUT:
% handle:           Figure handle of output figure
% spec:             Figure handle of separate spectral plot
%%%%%%%%%%%%%%%%%%%%%%%%%%%%%%%%%%%%%%%%%%%%%%%%%%%%%%%%%%%%%%%%%%%%%%%%%%%%%%%

handle=figure;
hold on
subplot(3,2,[2 4])
contourf(c,f(1:length(PhV)),A)
colormap(jet)
set(gca,'ydir','reverse')
xlabel('Phase Velocity (m/sec)')
ylabel('Frequency (Hz)')
title('Dispersion')
axesHandles = findobj(get(handle,'Children'), 'flat','Type','axes');
axis(axesHandles,'square')

subplot(3,2,6)
hold on
plot(f(11:Fmax),PhV(11:Fmax),'bo','MarkerSize',2)
xlabel('Frequency (Hz)')
ylabel('Phase Velocity (m/sec)')
title('Selected Dispersion Points')
axis([0 size(A,1) 0 1.1*max(PhV)])
box on

for k=[1 round(size(V,2)/2) size(V,2)]
    if k == 1
        p=1;
    elseif k == round(size(V,2)/2)
        p=3;
    else
        p=5;
    end
    subplot(3,2,p)
    plot(t,V(:,k))
    xlabel('Time (sec)')
    ylabel('Signal (mV)')
    str=sprintf('Geophone %i',k);
```

```
    title(str)
end

spec=figure;
contourf(c,f(1:length(PhV)),A)
colormap(jet)
set(gca,'ydir','reverse')
xlabel('Phase Velocity (m/sec)')
ylabel('Frequency (Hz)')
axesHandles = findobj(get(handle,'Children'), 'flat','Type','axes');

end
```

```
function [A,f] = Dispersion(V,x,Fmax,Fs,c)
% Project:          Multichannel Analysis of Surface Waves
% Function:         Dispersion.m
% Author:           William W. Greenwood
% Affiliation:      University of Michigan
% Last Revised:     10 April 2018
% Purpose:          Perform Park et al. (1998) dispersion technique
%%%%%%%%%%%%%%%%%%%%%%%%%%%%%%%%%%%%%%%%%%%%%%%%%%%%%%%%%%%%%%%%%%%%%%%%%%%%%%%
% INPUT:
% V:                Matrix of sensor time histories
% x:                Vector of sensor distances from source
% Fmax:             Maximum frequency for dispersion analysis
% Fs:               Sampling frequency of data in V
% c:                Vector of trial phase velocities (min c : 1 : max c)
%%%%%%%%%%%%%%%%%%%%%%%%%%%%%%%%%%%%%%%%%%%%%%%%%%%%%%%%%%%%%%%%%%%%%%%%%%%%%%%
% OUTPUT:
% A:                Phase velcoity-frequency spectral amplitude
% f:                Vector of Frequencies
%%%%%%%%%%%%%%%%%%%%%%%%%%%%%%%%%%%%%%%%%%%%%%%%%%%%%%%%%%%%%%%%%%%%%%%%%%%%%%%

n=Fs; % n-point fft

% Frequency vector f or w:
    f_delta = (Fs/n); % Frequency increment
    f=0:f_delta:f_delta*(n-1); % Frequency vector
     w=f*2*pi; % Frequency vector in radians
S=fft(V,n)/Fs; % Fast Fourier Transform to frequency domain.

P=angle(S); % Frequency-dependence of phase velocity is stored in phase.

% Transform to c-f domain.
A=zeros(Fmax+1,length(c));
for k=1:size(A,1)
    for h=1:length(c)
        for i=1:size(V,2)
                A(k,h)=A(k,h)+P(k,i)*exp(-1i*w(k)*(x(i))/c(h));
        end
    end
    A(k,:)=abs(A(k,:));
    A(k,:)=A(k,:)/max(A(k,:)); % Normalize
end

end
```

```
function [A] = Limitation(A,x,c,f)
% Project:          Multichannel Analysis of Surface Waves
% Function:         Limitation.m
% Author:           William W. Greenwood
% Affiliation:      University of Michigan
% Last Revised:     10 April 2018
% Purpose:          Apply spatial constraints to c-f spectrum
%%%%%%%%%%%%%%%%%%%%%%%%%%%%%%%%%%%%%%%%%%%%%%%%%%%%%%%%%%%%%%%%%%%%%%%%%%%%%%%
% INPUT:
% A:                Phase velocity-frequency spectrum
% x:                Vector of sensor distances from source
% c:                Vector of trial phase velocities (min c : 1 : max c)
% f:                Vector of Frequencies
%%%%%%%%%%%%%%%%%%%%%%%%%%%%%%%%%%%%%%%%%%%%%%%%%%%%%%%%%%%%%%%%%%%%%%%%%%%%%%%
% OUTPUT:
% A:                Phase velocity-frequency spectral amplitude with limits
%%%%%%%%%%%%%%%%%%%%%%%%%%%%%%%%%%%%%%%%%%%%%%%%%%%%%%%%%%%%%%%%%%%%%%%%%%%%%%%

SL=x(end)-x(1); % Array spread length
% Determine geophone spacings
Spacing=zeros(length(x)-1,1);
for k=1:length(Spacing)
    Spacing(k)=x(k+1)-x(k);
end

for k=1:size(A,1)
    for j=1:size(A,2)
        if c(j)/f(k)> 2*SL || c(j)/f(k) < 2*max(Spacing)
            A(k,j)=0;
        end
    end
end
end
```

```
function [depth,cv,mu_vec,sig_vec] = lognorm_vs(depths,vs)
% Project:          Multichannel Analysis of Surface Waves
% Function:         lognorm_vs.m
% Author:           William W. Greenwood
% Affiliation:      University of Michigan
% Last Revised:     10 April 2018
% Purpose:          Fit lognormal distribution to set of Vs profiles
%%%%%%%%%%%%%%%%%%%%%%%%%%%%%%%%%%%%%%%%%%%%%%%%%%%%%%%%%%%%%%%%%%%%%%%%%%%%%%%
% INPUT:
% depths:           Vs profile depth vectors
% vs:               Vs vectors
%%%%%%%%%%%%%%%%%%%%%%%%%%%%%%%%%%%%%%%%%%%%%%%%%%%%%%%%%%%%%%%%%%%%%%%%%%%%%%%
% OUTPUT:
% depth:            Discretized depth vector
% cv:               Coefficient of Variation profile (E[Vs]/SD[Vs])
% mu_vec:           Median Vs profile
% sig_vec:          Stdev Vs profile
%%%%%%%%%%%%%%%%%%%%%%%%%%%%%%%%%%%%%%%%%%%%%%%%%%%%%%%%%%%%%%%%%%%%%%%%%%%%%%%

p=size(vs,2); % num profiles
vsp=cell(p,1);
dp=cell(p,1);
breaks=cell(p,1);

% Discretize Vs profiles
for k=1:p % for each profile...
    max_depth = max(depths(:,p));
    dvec = (0:0.1:max_depth);
    temp=depths(:,k);
    layers=[];
    vels=[];
    for d=unique(temp)'
        ind=find(temp==d);
        if length(ind)>1
            layers(end+1)=d;
            vels(end+1)=vs(ind(1),k);
        end
    end
    ind=find(temp==layers(end));
    vels(end+1)=vs(ind(2),k); % need final Vs change
    dvec=round(dvec,1);
    layers=round(layers,1);
    breaks{k}=layers;
    for d=1:length(layers)
        ind=find(dvec==layers(d));
        dvec=[dvec(1:ind) dvec(ind:end)];
    end

    dvec=dvec';


    vvec=zeros(length(dvec),1);
    for d=1:length(layers)
        ind1=find(dvec<layers(d));
        ind2=find(vvec==0);
        ind=intersect(ind1,ind2);
```

```
        vvec(ind)=vels(d);
        ind=find(dvec==layers(d));
        vvec(ind(1))=vels(d);
    end
    % Fill after final layer break
    ind=find(vvec==0);
    vvec(ind)=vels(end);
    vsp{k}=vvec;
    dp{k}=dvec;

end

dpstat=dp;
vsstat=vsp;

for k=1:p
    layers=breaks{k};
    for d=1:length(layers)
        ind=find(dpstat{k}==layers(d));
        dpstat{k}(ind(1))=[];
        vsstat{k}(ind(1))=[];
    end
end

temp=zeros(length(dpstat{1}),p);
for k=1:p
    temp(:,k)=vsstat{k};
end

% Lognormal distribution
mu_vec=zeros(length(dpstat{1}),1);
sig_vec=mu_vec;

for d=1:length(dpstat{1})
    pd=fitdist(temp(d,:)','LogNormal');
    mu_vec(d)=pd.mu;
    sig_vec(d)=pd.sigma;
end

temp=zeros(length(dpstat{1}),p);
for k=1:p
    temp(:,k)=vsstat{k};
end

temp=log(temp);

depth=dpstat{1};

expect=exp(mu_vec+((sig_vec.^2)/2)); % m/sec
std=expect.*sqrt(exp(sig_vec.^2)-1); % m/sec
expect_plus=expect+std;
expect_minus=expect-std;
cv=std./expect;

end
```

```
function [vsi,avs,bvs] = Empirical_Fit(depth,vs)
% Project:          Multichannel Analysis of Surface Waves
% Function:         Empirical_Fit.m
% Author:           William W. Greenwood
% Affiliation:      University of Michigan
% Last Revised:     10 April 2018
% Purpose:          Fit empirical model (hyperbolic) to Vs profile
%%%%%%%%%%%%%%%%%%%%%%%%%%%%%%%%%%%%%%%%%%%%%%%%%%%%%%%%%%%%%%%%%%%%%%%%%%%%%%%
% INPUT:
% depth:            Vs profile depth vector
% vs:               Vs vector
%%%%%%%%%%%%%%%%%%%%%%%%%%%%%%%%%%%%%%%%%%%%%%%%%%%%%%%%%%%%%%%%%%%%%%%%%%%%%%%
% OUTPUT:
% vsi:              Initial Vs parameter
% avs:              Initial slope parameter
% bvs:              Maximum velocity parameter
%%%%%%%%%%%%%%%%%%%%%%%%%%%%%%%%%%%%%%%%%%%%%%%%%%%%%%%%%%%%%%%%%%%%%%%%%%%%%%%

fo=fitoptions('Method','NonlinearLeastSquares');
myfittype=fittype('vsi+depth/(avs+bvs*depth)','independent',{'depth'},...
    'dependent',{'vs'},'coefficients',{'vsi','avs','bvs'},'options',fo);

myfit=fit(depth,vs,myfittype,'Lower',[0 0 0],'Upper',[inf inf inf],...
    'StartPoint',[500 .1 .005]);

vsi=myfit.vsi;
avs=myfit.avs;
bvs=myfit.bvs;

end
```

```
function [PhV] = Dispersion_Curve(A,c)
% Project:          Multichannel Analysis of Surface Waves
% Function:         Dispersion_Curve.m
% Author:           William W. Greenwood
% Affiliation:      University of Michigan
% Last Revised:     10 April 2018
% Purpose:          Automatically select initial dispersion curve
%%%%%%%%%%%%%%%%%%%%%%%%%%%%%%%%%%%%%%%%%%%%%%%%%%%%%%%%%%%%%%%%%%%%%%%%%%%%%%%
% INPUT:
% A                 Phase velocity-frequency spectrum
% c:                Vector of trial phase velocities (min c : 1 : max c)
%%%%%%%%%%%%%%%%%%%%%%%%%%%%%%%%%%%%%%%%%%%%%%%%%%%%%%%%%%%%%%%%%%%%%%%%%%%%%%%
% OUTPUT:
% PhV:              Automatic dispersion curve points
%%%%%%%%%%%%%%%%%%%%%%%%%%%%%%%%%%%%%%%%%%%%%%%%%%%%%%%%%%%%%%%%%%%%%%%%%%%%%%%


% Find maximum value in dispersion
index=zeros(size(A,1),1);
PhV=index; % Phase Velocities
for k=1:length(index)
     index(k)=max(A(k,:));
     for i=1:length(c)
         if A(k,i)==index(k)
             PhV(k)=c(i);
         end
     end
end
end
```

```
function [a0] = Alpha_0(V,x,sensor_a,sensor_b,Fs,fmin,fmax)
% Project:          Multichannel Analysis of Surface Waves
% Function:         Alpha_0.m
% Author:           William W. Greenwood
% Affiliation:      University of Michigan
% Last Revised:     10 April 2018
% Purpose:          Estimate frequency-independent attenuation coefficient
%%%%%%%%%%%%%%%%%%%%%%%%%%%%%%%%%%%%%%%%%%%%%%%%%%%%%%%%%%%%%%%%%%%%%%%%%%%%%%%
% INPUT:
% V:                Sensor time histories
% x:                Distance from source for each sensor
% sensor_a:         First sensor for attenuation estimation (column of V)
% sensor_b:         Second sensor for attenuation estimation (column of V)
% Fs:               Sampling Frequency of time histories in V
% fmin:             Minimum frequency for curve fitting
% fmax:             Maximum Frequency for curve fitting
%%%%%%%%%%%%%%%%%%%%%%%%%%%%%%%%%%%%%%%%%%%%%%%%%%%%%%%%%%%%%%%%%%%%%%%%%%%%%%%
% OUTPUT:
% a0:               Frequency-independent coeff of attenuation (sec/m)
%%%%%%%%%%%%%%%%%%%%%%%%%%%%%%%%%%%%%%%%%%%%%%%%%%%%%%%%%%%%%%%%%%%%%%%%%%%%%%%
A=V(:,sensor_a);
B=V(:,sensor_b);
f_att=f(fmin+1:fmax+1);
d=zeros(size(V));% Displacement time history
for k=1:size(d,2)
    d(:,k)=(1/Fs)*cumtrapz(V(:,k)/810); % t(2) is the time increment
end

fft_d=fft(d,Fs)/Fs;
fft_d=abs(fft_d(fmin+1:fmax+1,:));

noverlap=0;
win=size(V,1)/2;
[Pxx,~]=pwelch(A,rectwin(win),noverlap,Fs,Fs);
[Pyy,~]=pwelch(B,rectwin(win),noverlap,Fs,Fs);
[Pyx,~]=cpsd(B,A,rectwin(win),noverlap,Fs,Fs);
Coh=Pyx./((Pxx.^(1/2)).*(Pyy.^(1/2)));
Cxy=abs(Coh).^2;
tag=[];
    for k=fmin:fmax
        if Cxy(k+1) < 0.99
            tag(end+1)=k;
        end
    end
f_temp=f_att;
f_temp(tag-fmin+1)=[];
ratio=fft_d(:,sensor_a)./fft_d(:,sensor_b);
ratio(tag-fmin+1)=[];
coeff1=1/((x(norm_sensor)/x(trial_sensor))^0.5);
fo=fitoptions('exp1','Lower',[coeff1 -inf],'Upper',[coeff1 +inf]);
e=fit(f_temp',ratio,'exp1',fo);

co=coeffvalues(e);
a0=(co(2)/(x(sensor_b)-x(sensor_a)))/(0.3084); % convert to m

end
```

```
function [a,f_att] = Attenuation_Curve(V,x,Fs,fmin,fmax)
% Project:          Multichannel Analysis of Surface Waves
% Function:         Attenuation_Curve.m
% Author:           William W. Greenwood
% Affiliation:      University of Michigan
% Last Revised:     10 April 2018
% Purpose:          Estimate frequency-independent attenuation coefficient
%%%%%%%%%%%%%%%%%%%%%%%%%%%%%%%%%%%%%%%%%%%%%%%%%%%%%%%%%%%%%%%%%%%%%%%%%%%%
% INPUT:
% V:                Sensor time histories
% x:                Distance from source for each sensor
% Fs:               Sampling Frequency of time histories in V
% fmin:             Minimum frequency for curve fitting
% fmax:             Maximum Frequency for curve fitting
%%%%%%%%%%%%%%%%%%%%%%%%%%%%%%%%%%%%%%%%%%%%%%%%%%%%%%%%%%%%%%%%%%%%%%%%%%%%
% OUTPUT:
% a:               Frequency-dependent coefficient of attenuation (1/m)
% f_att:           Vector of corresponding frequencies
%%%%%%%%%%%%%%%%%%%%%%%%%%%%%%%%%%%%%%%%%%%%%%%%%%%%%%%%%%%%%%%%%%%%%%%%%%%%
f_att=f(fmin+1:fmax+1);
d=zeros(size(V));% Displacement time history
for k=1:size(d,2)
    d(:,k)=(1/Fs)*cumtrapz(V(:,k)/810);
end

fft_d=fft(d,Fs)/Fs;
fft_d=abs(fft_d(fmin+1:fmax+1,:));
cod=cell(size(f_att));
alpha_0=zeros(size(f_att));
alpha_lower=zeros(size(f_att));
alpha_upper=zeros(size(f_att));

for k=1:length(f_att)
    y=fft_d(k,:);
    myfittype=fittype('A1*sqrt(r1/x)*exp(-a0*freq*(x-r1))','independent'...
        ,{'x'},'dependent',{'y'},'coefficients',{'a0'},'problem',{'A1',...
        'r1','freq'});
    Amp1=fft_d(k,1);
    rad1=x(1);
    trial_freq=f_att(k);
    myfit=fit(x',y',myfittype,'Lower',-inf,'Upper',inf,...
        'StartPoint',.0005,'problem',{Amp1,rad1,trial_freq},'TolFun',...
        1e-20,'TolX',1e-20);
    cod{k}=myfit;
    alpha_0(k)=cod{k}.a0;
    temp=confint(cod{k});
    alpha_lower(k)=temp(1);
    alpha_upper(k)=temp(2);
    myfit_lower=myfit;
    myfit_upper=myfit;
    myfit_lower.a0=alpha_lower(k);
    myfit_upper.a0=alpha_upper(k);
end

a=f_att.*alpha_0/.3048;
end
```

B Test Images for Fracture Detection

B.1 Marble Image Set

Figure B-1: Image M1 (Vertical scale 35 cm)

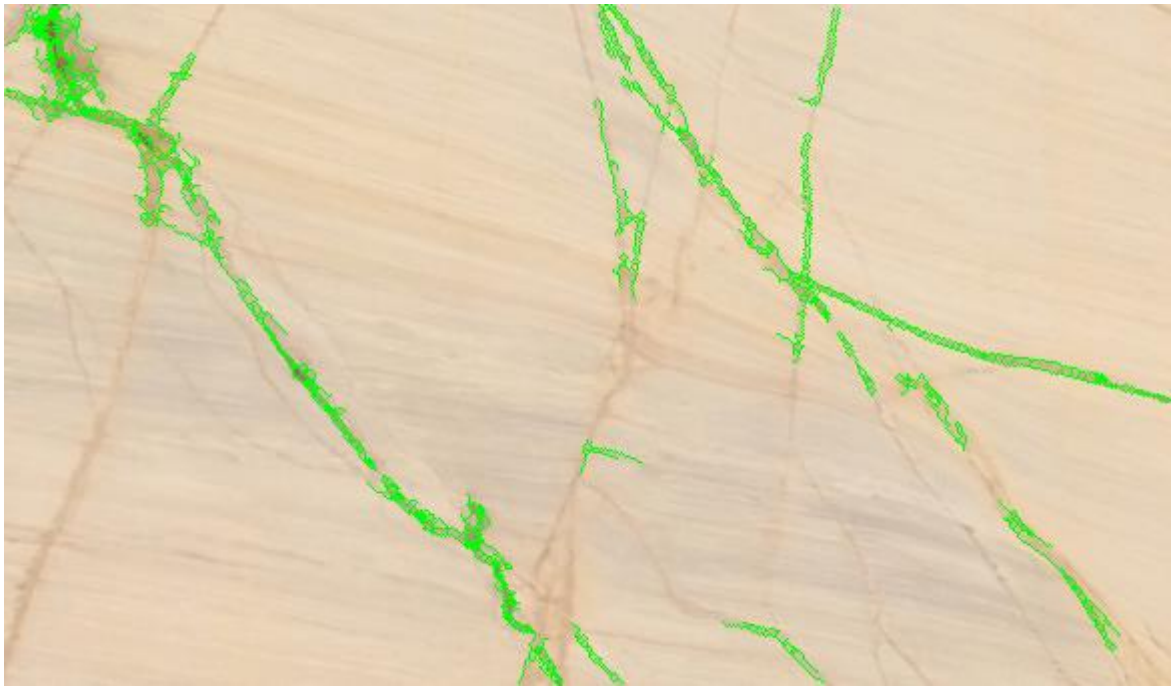

Figure B-2: Image M1 kb=0.4

Figure B-3: Image M2 (Vertical scale: 35 cm)

Figure B-4: Image M2 kb=0.4

Figure B-5: Image M3 (Vertical Scale: 30 cm)

Figure B-6: Image M3 kb=0.4

Figure B-7: Image M4 (Vertical scale: 30 cm)

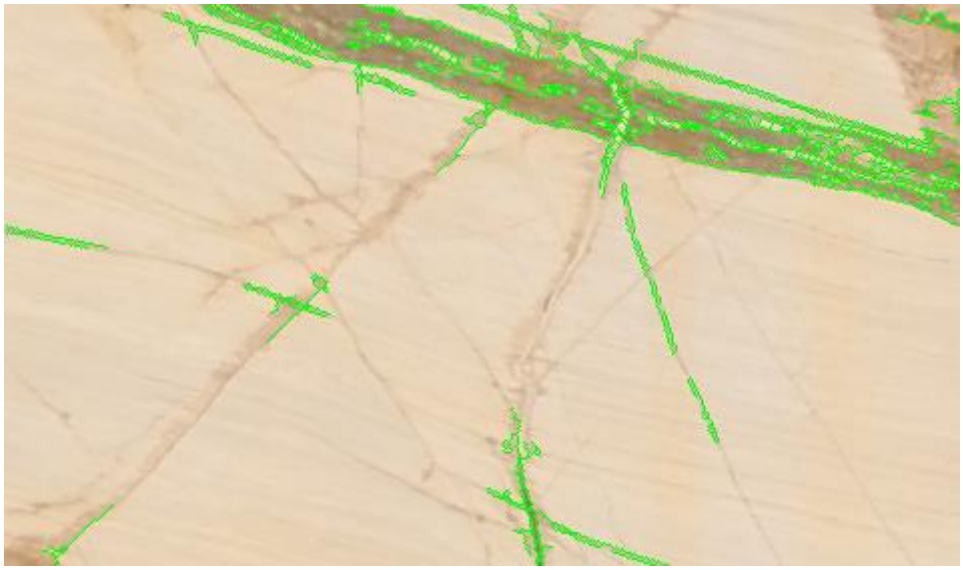

Figure B-8: Image M4 kb=0.4

Figure B-9: Image M5 (Vertical scale: 35 cm)

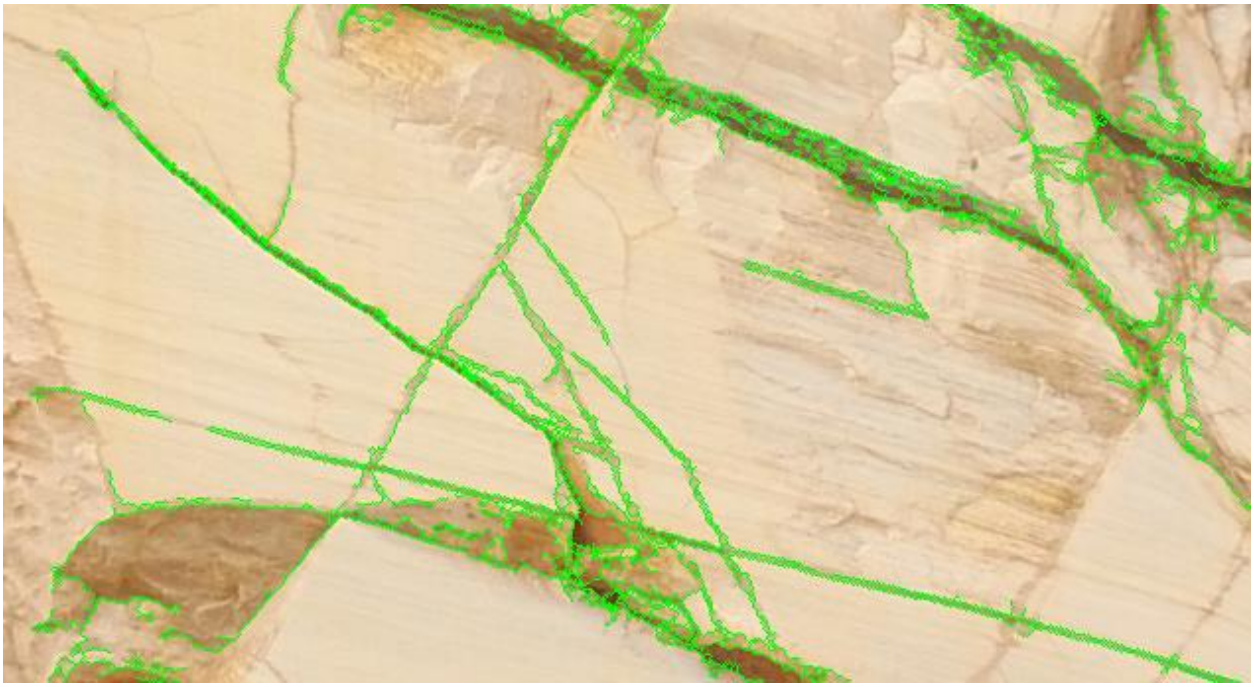

Figure B-10: Image M5 kb=0.4

Figure B-11: Image M6 (Vertical scale: 30 cm)

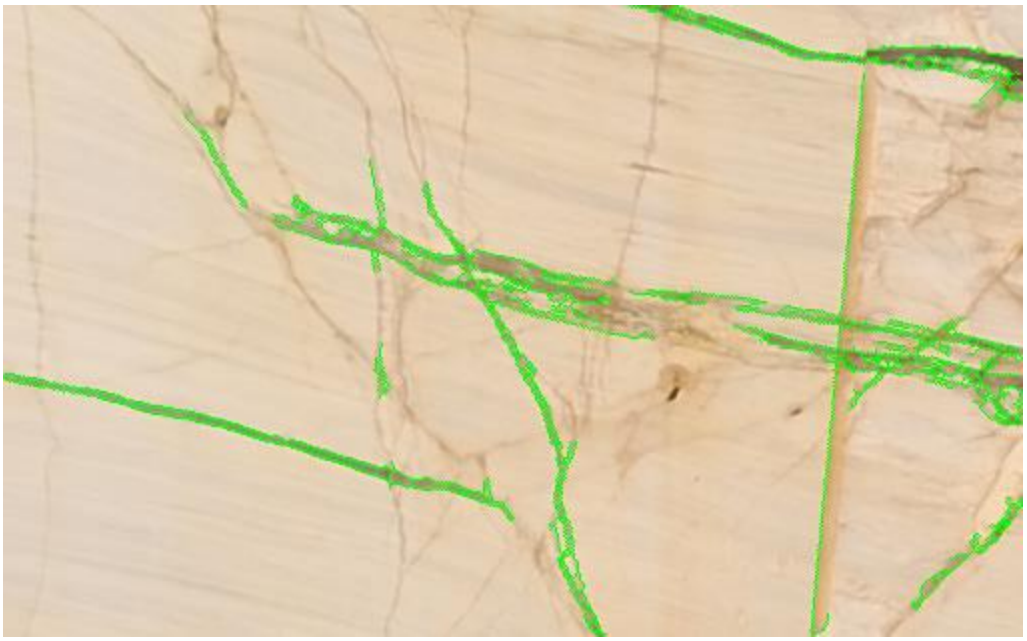

Figure B-12: Image M6 kb=0.4

Figure B-13: Image M7 (Vertical scale: 30 cm)

Figure B-14: Image M7 kb=0.4

Figure B-15: Image M8 (Vertical scale: 35 cm)

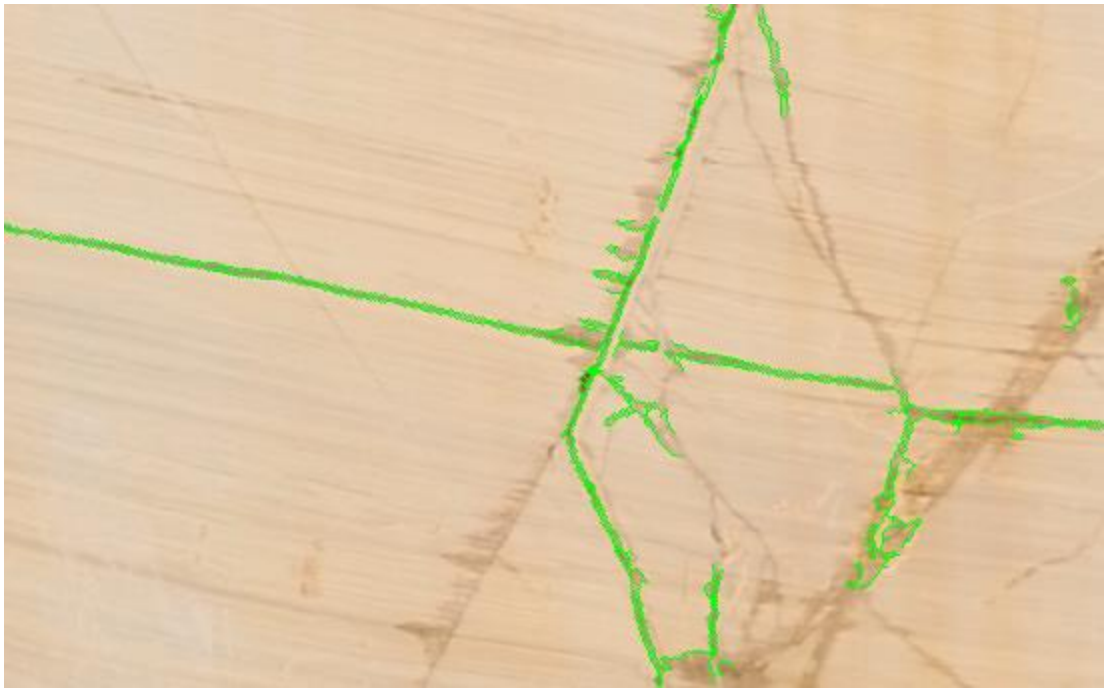

Figure B-16: Image M8 kb=0.4

Figure B-17: Image M9 (Vertical scale: 30 cm)

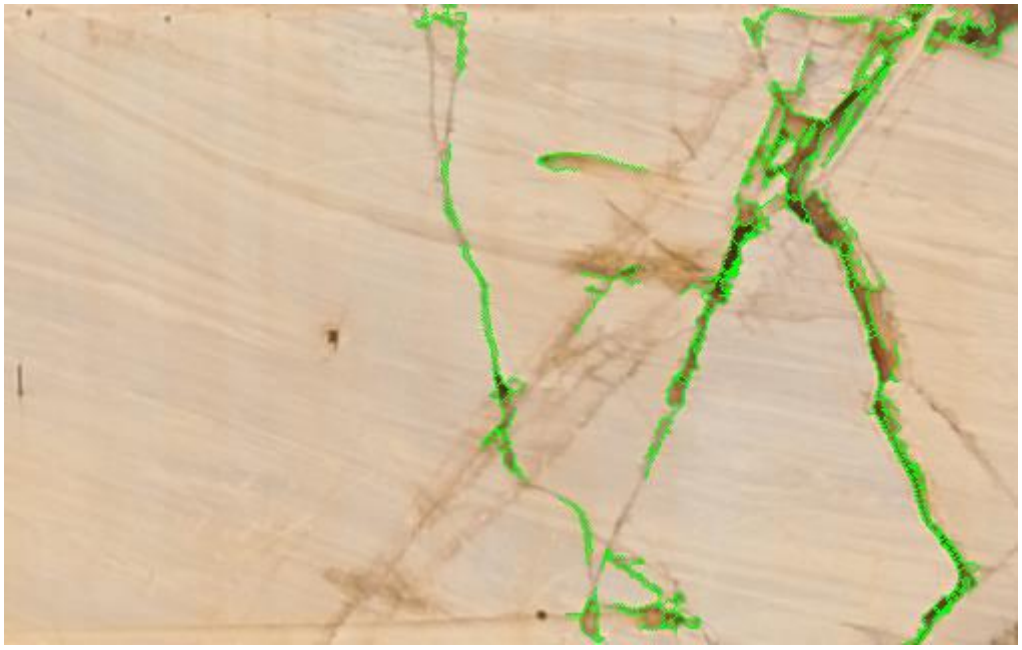

Figure B-18: Image M9 kb=0.4

Figure B-19: Image M10 (Vertical scale: 30 cm)

Figure B-20: Image M10 kb=0.4

Figure B-21: Image M11 (Vertical scale: 35 cm)

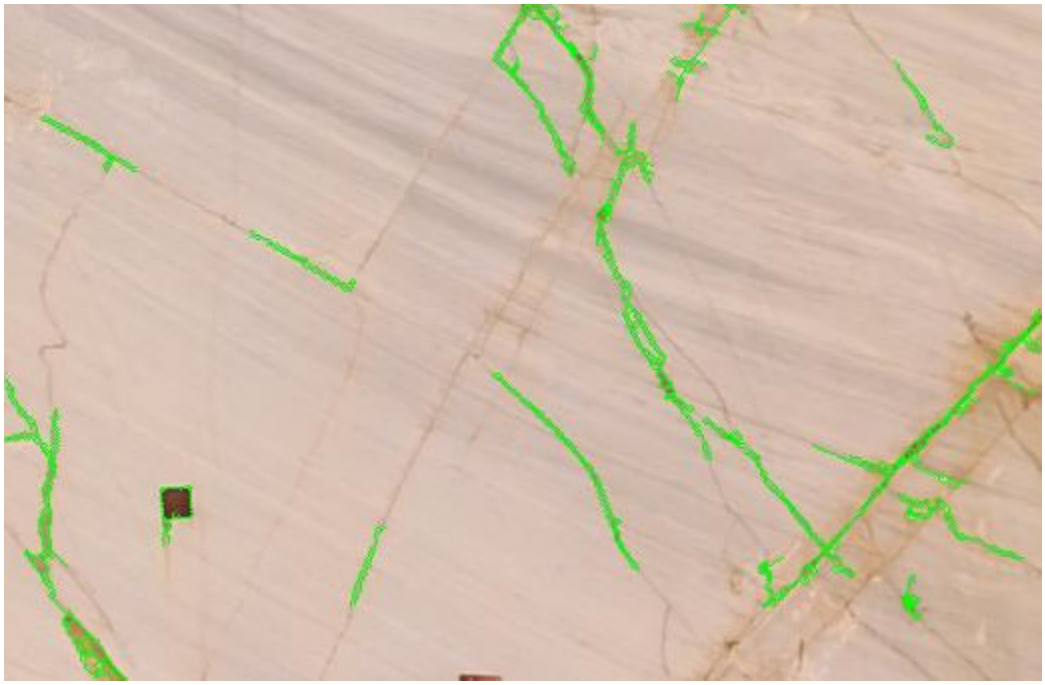

Figure B-22: Image M11 kb=0.4

Figure B-23: Image M12 (Vertical scale: 30 cm)

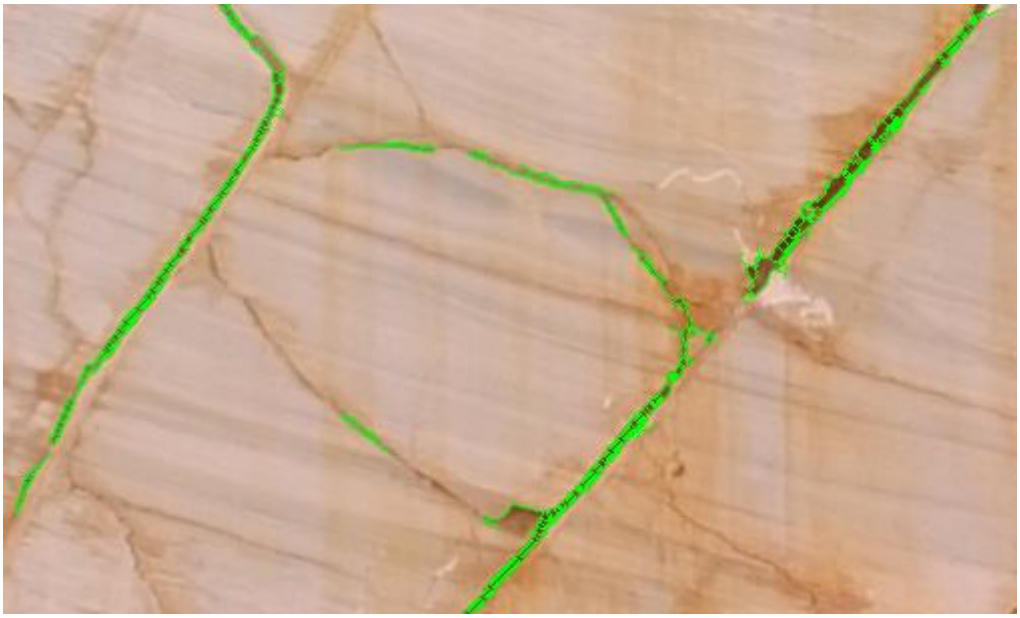

Figure B-24: Image M12 kb=0.4

Figure B-25: Image M13 (Vertical scale: 30 cm)

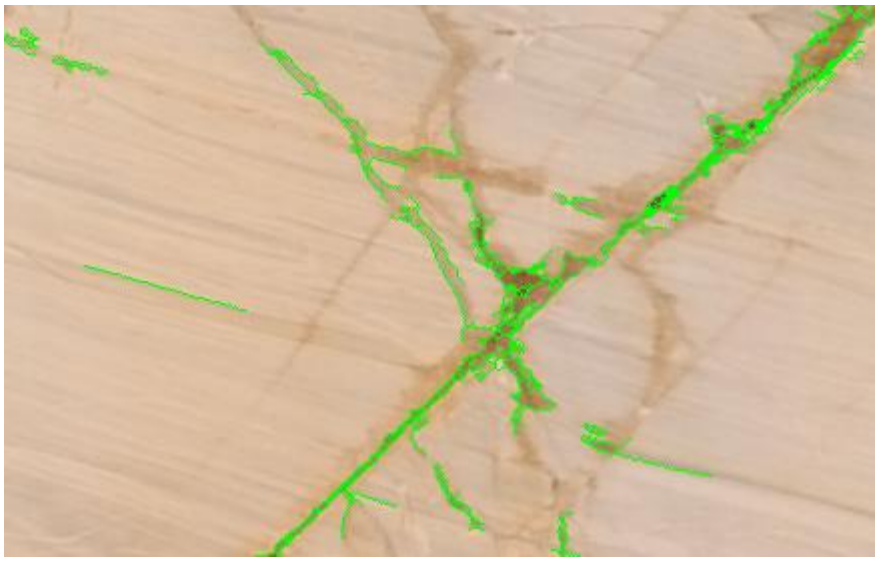

Figure B-26: Image M13 kb=0.4

Figure B-27: Image M14 (Vertical scale: 30 cm)

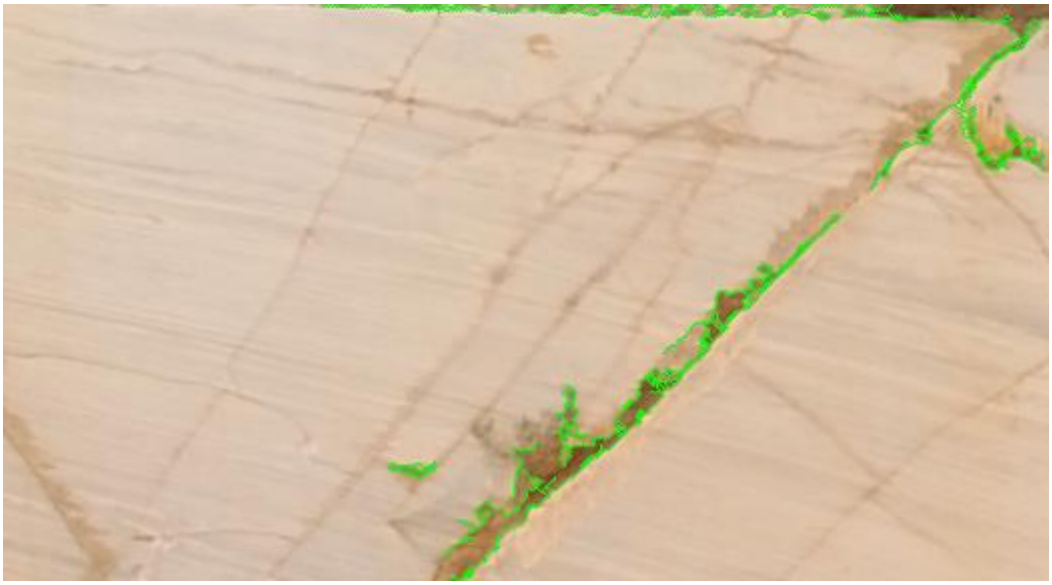

Figure B-28: Image M14 kb=0.4

Figure B-29: Image M15 (Vertical scale: 35 cm)

Figure B-30: Image M15 kb=0.4

Figure B-31: Image M16 (Vertical scale: 35 cm)

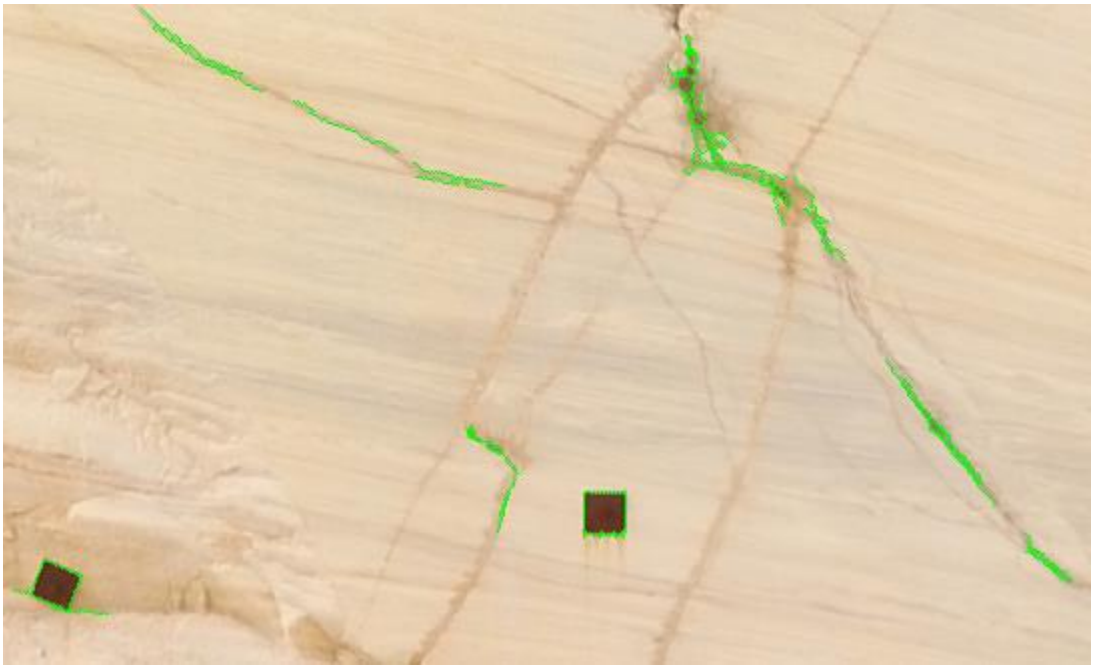

Figure B-32: Image M16 kb=0.4

Figure B-33: Image M17 (Vertical scale: 25 cm)

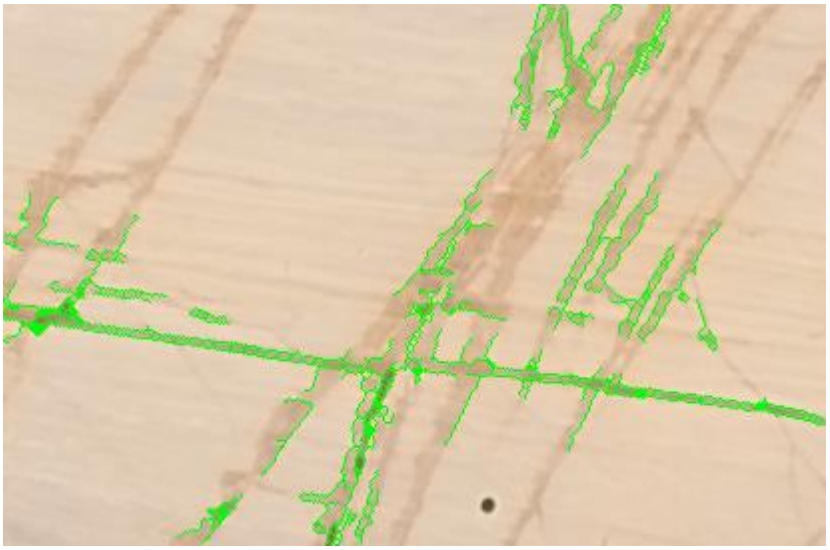

Figure B-34: Image M17 kb=0.4

Figure B-35: Image M18 (Vertical scale: 25 cm)

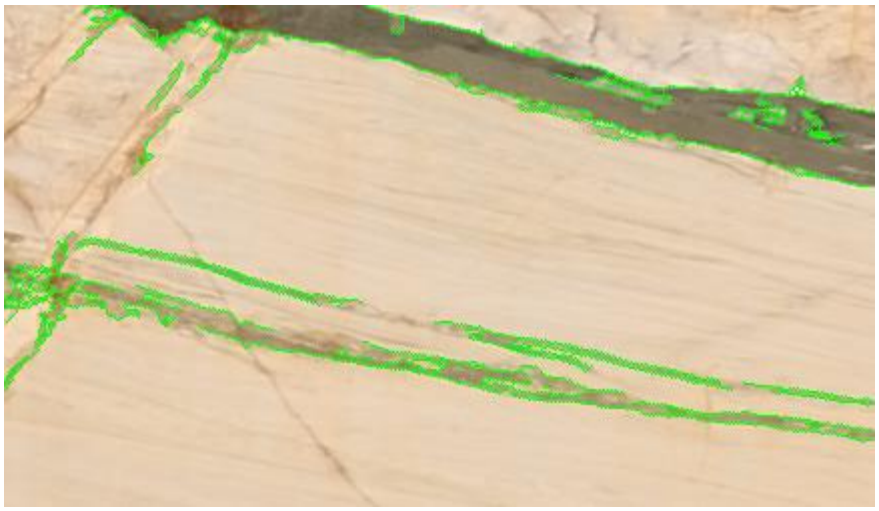

Figure B-36: Image M18 kb=0.4

B.2 Basalt Image Set

Figure B-37: Image BA1 (Vertical scale: 27 cm)

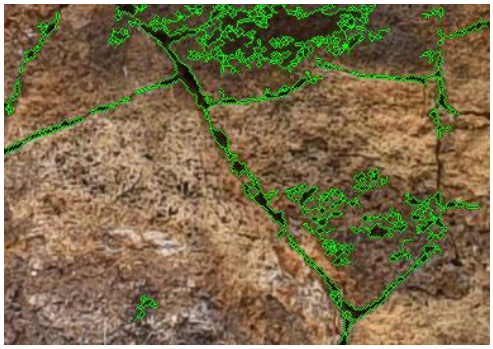

Figure B-38: Image BA1 k_b=0.3 O_s=0.5

Figure B-39: Image BA2 (Vertical scale: 20 cm)

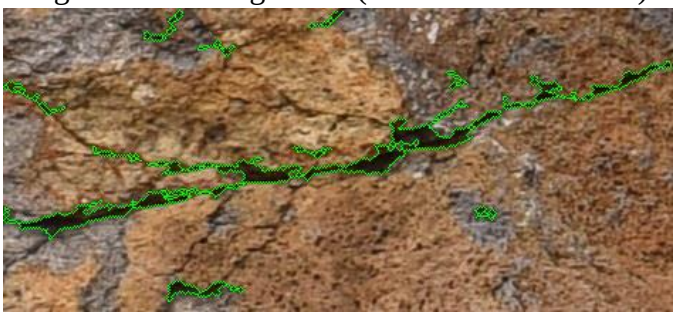

Figure B-40: Image BA2 k_b=0.3 O_s=0.5

Figure B-41: Image BA3 (Vertical scale: 15 cm)

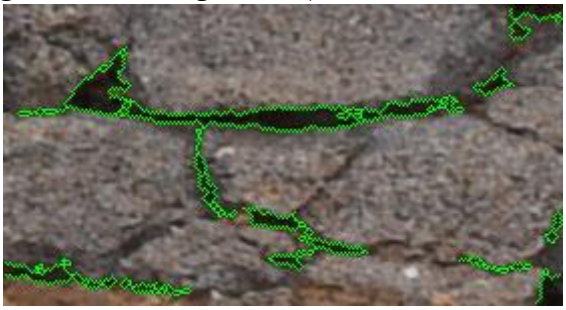

Figure B-42: Image BA3 k_b=0.3 O_s=0.5

Figure B-43: Image BA4 (Vertical scale: 20 cm)

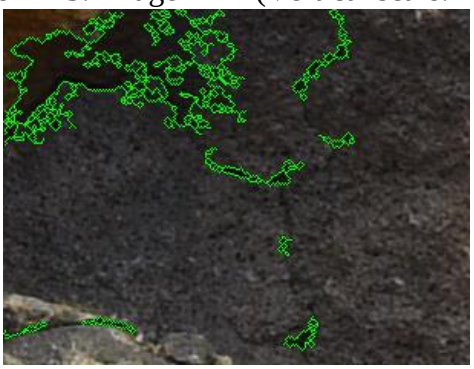

Figure B-44: Image BA4 k_b=0.3 O_s=0.5

Figure B-45: Image BA5 (Vertical scale: 20 cm)

Figure B-46: Image BA5 k_b=0.3 O_s=0.5

Figure B-47: Image BA6 (Vertical scale: 16 cm)

Figure B-48: Image BA6 k_b=0.3 O_s=0.5

Figure B-49: Image BA7 (Vertical scale: 25 cm)

Figure B-50: Image BA7 k_b=0.3 O_s=0.5

Figure B-51: Image BA8 (Vertical scale: 25 cm)

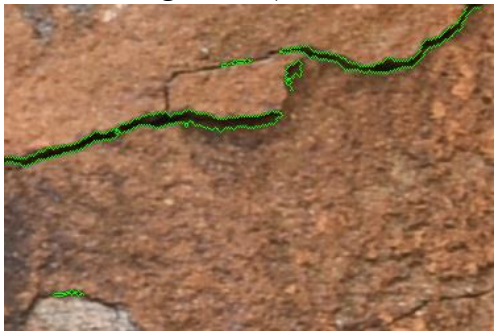

Figure B-52: Image BA8 k_b=0.3 O_s=0.5

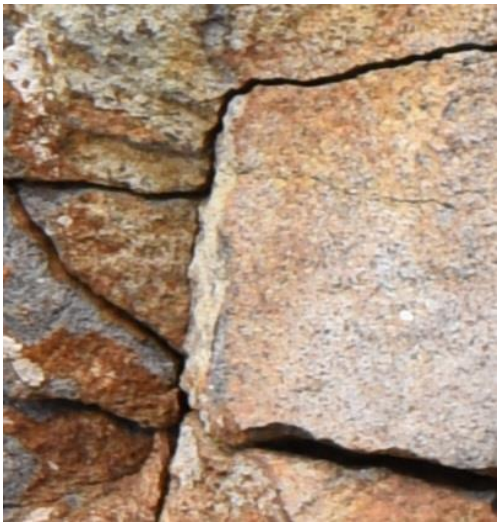

Figure B-53: Image BA9 (Vertical scale: 42 cm)

Figure B-54: Image BA9 k_b=0.3 O_s=0.5

Figure B-55: Image BA10 (Vertical scale: 20 cm)

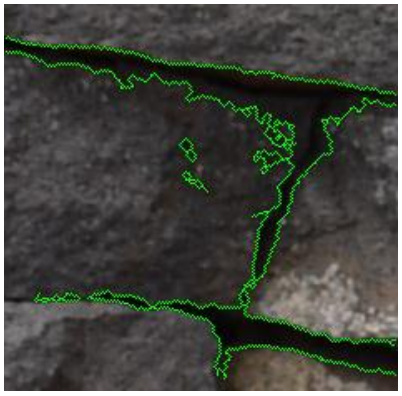

Figure B-56: Image BA10 k_b=0.3 O_s=0.5

Figure B-57: Image BA11 (Vertical scale: 20 cm)

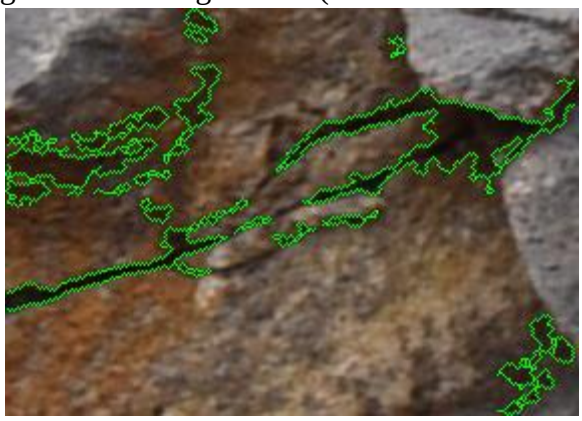

Figure B-58: Image BA11 k_b=0.3 O_s=0.5

Figure B-59: Image BA12 (Vertical scale: 30 cm)

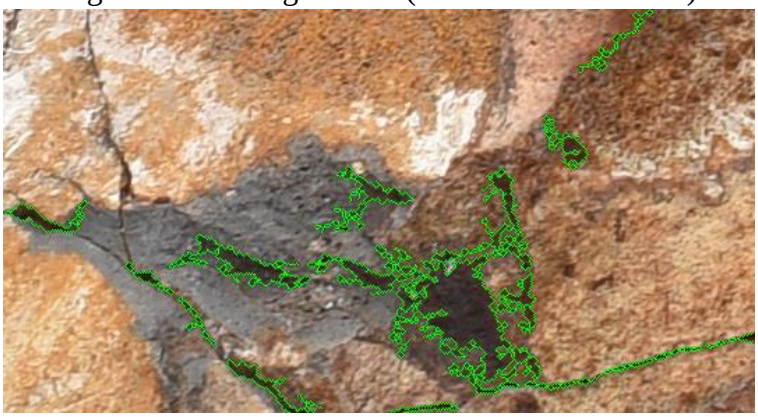

Figure B-60: Image BA12 k_b=0.3 O_s=0.5

Figure B-61: Image BA13 (Vertical scale: 27 cm)

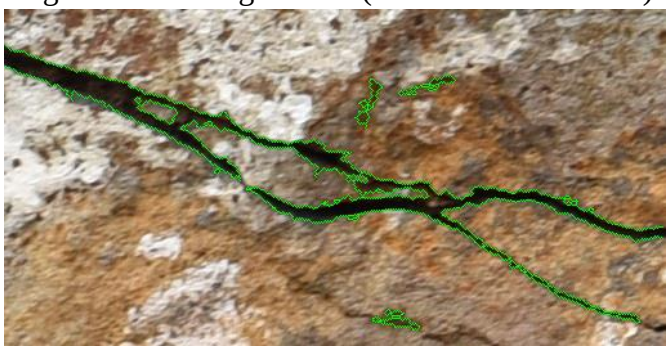

Figure B-62: Image BA13 k_b=0.3 O_s=0.5

Figure B-63: Image BA14 (Vertical scale: 34 cm)

Figure B-64: Image BA14 k_b=0.3 O_s=0.5

Figure B-65: Image BA15 (Vertical scale: 24 cm)

Figure B-66: Image BA15 k_b=0.3 O_s=0.5

Figure B-67: Image BA16 (Vertical scale: 35 cm)

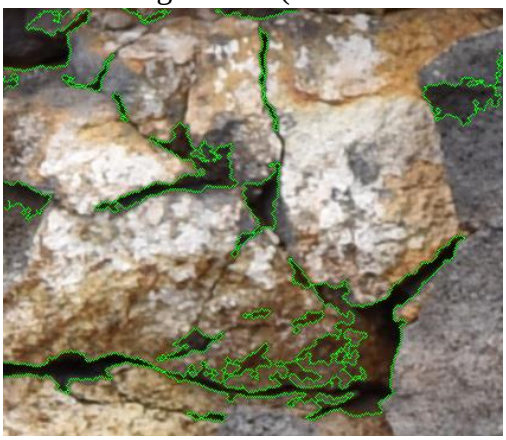

Figure B-68: Image BA16 k_b=0.3 O_s=0.5

Figure B-69: Image BA17 (Vertical scale: 30 cm)

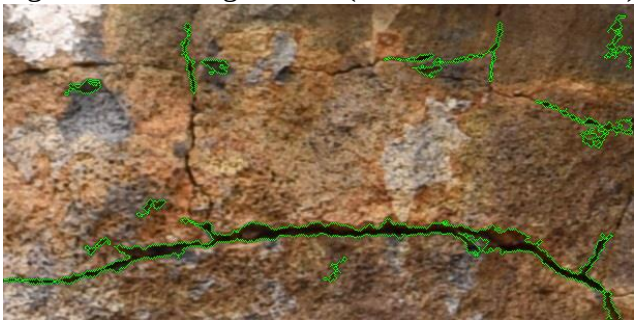

Figure B-70: Image BA17 k_b=0.3 O_s=0.5

Figure B-71: Image BA18 (Vertical scale: 30 cm)

Figure B-72: Image BA18 k_b=0.3 O_s=0.5

Figure B-73: Image BA19 (Vertical scale: 37 cm)

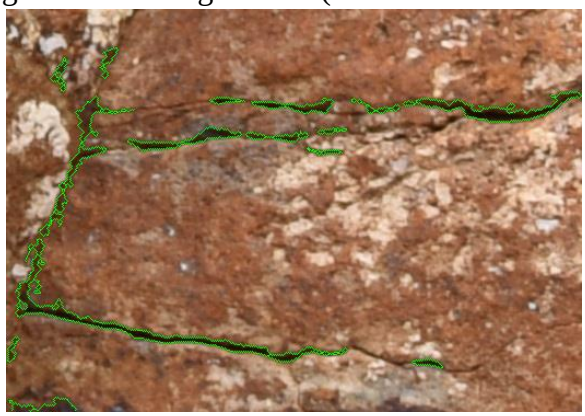

Figure B-74: Image BA19 k_b=0.3 O_s=0.5

Figure B-75: Image BA20 (Vertical scale: 17 cm)

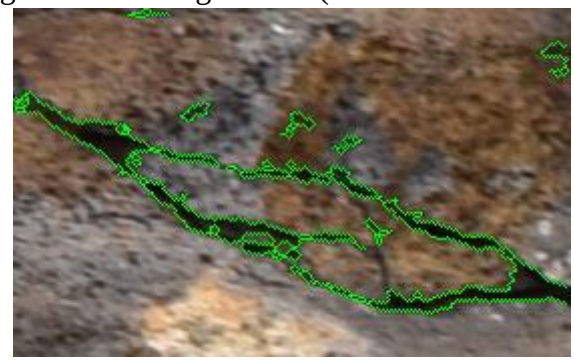

Figure B-76: Image BA20 k_b=0.3 O_s=0.5

Figure B-77: Image BA21 (Vertical scale: 25 cm)

Figure B-78: Image BA21 k_b=0.3 O_s=0.5

Figure B-79: Image BA22 (Vertical scale: 45 cm)

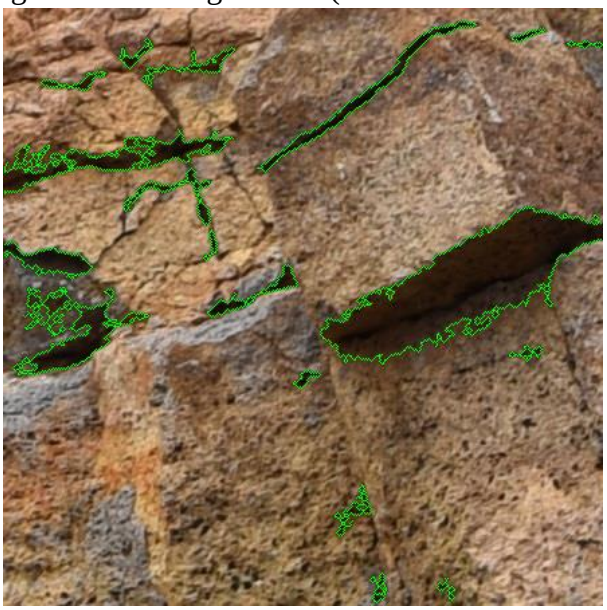

Figure B-80: Image BA22 k_b=0.3 O_s=0.5

Figure B-81: Image BA23 (Vertical scale: 25 cm)

Figure B-82: Image BA23 k_b=0.3 O_s=0.5

Figure B-83: Image BA24 (Vertical scale: 25 cm)

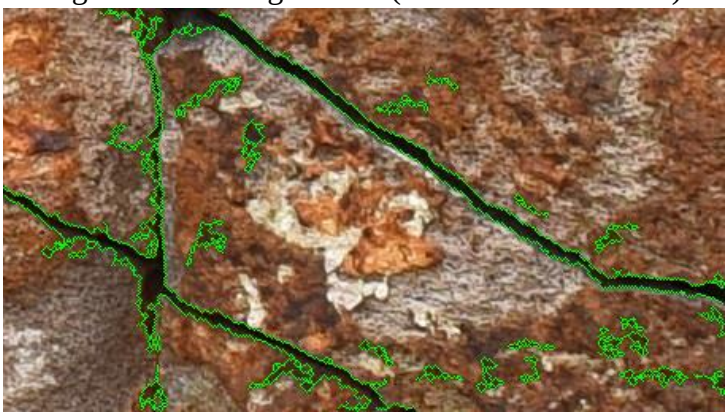

Figure B-84: Image BA24 k_b=0.3 O_s=0.5

Figure B-85: Image BA25 (Vertical scale: 20 cm)

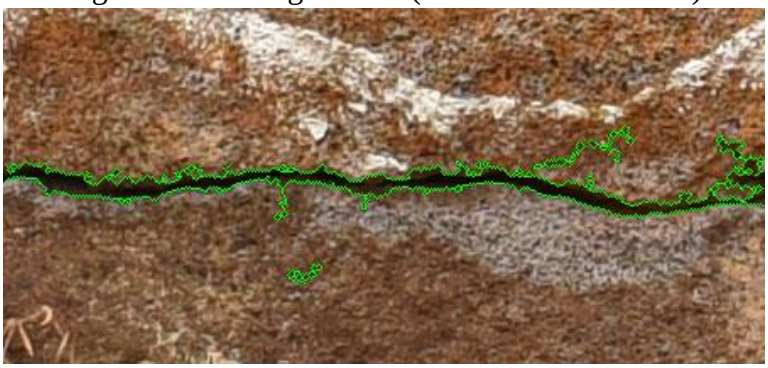

Figure B-86: Image BA25 k_b=0.3 O_s=0.5

Figure B-87: Image BA26 (Vertical scale: 27 cm)

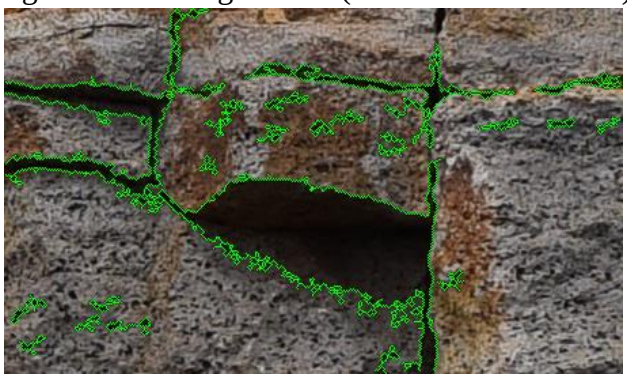

Figure B-88: Image BA26 k_b=0.3 O_s=0.5

Figure B-89: Image BA27 (Vertical scale: 30 cm)

Figure B-90: Image BA27 k_b=0.3 O_s=0.5

Figure B-91: Image BA28 (Vertical scale: 30 cm)

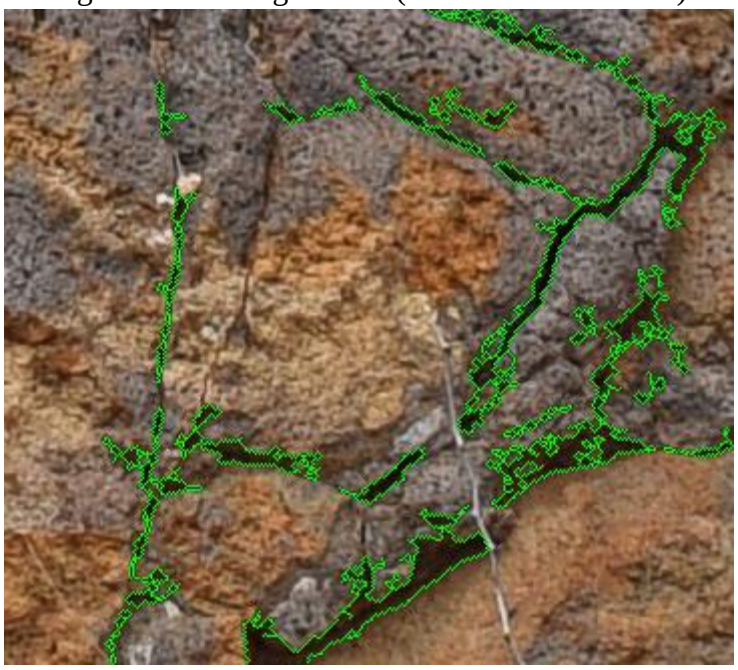

Figure B-92: Image BA28 k_b=0.3 O_s=0.5

B.3 Third Image Set

Figure B-93: Image H2 (Vertical scale: 10 cm)

Figure B-94: Image H2 k_b=0.4

Figure B-95: Image H3 (Vertical scale: 20 cm)

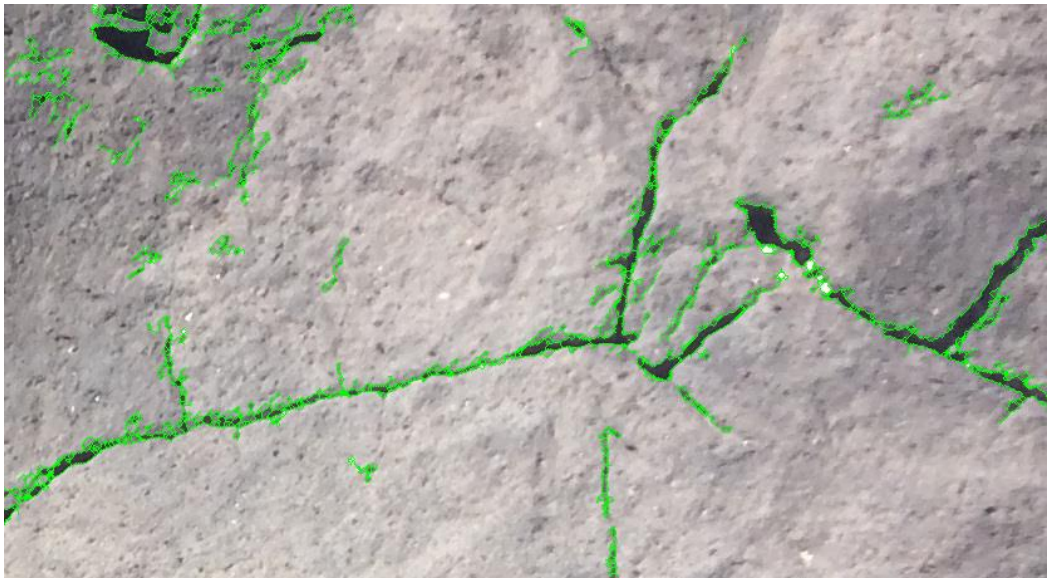

Figure B-96: Image H3 k_b=0.4

Figure B-97: Image H4 (Vertical scale: 15 cm)

Figure B-98: Image H4 k_b=0.4

Figure B-99: Image IDL (Vertical scale: 5 cm)

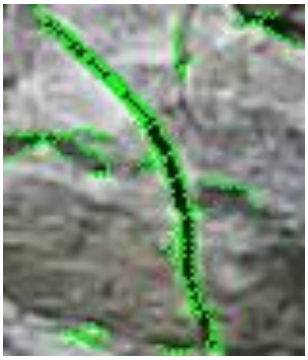

Figure B-100: Image IDL k_b=0.4

Figure B-101: Image K1 (Vertical scale: 50 cm)

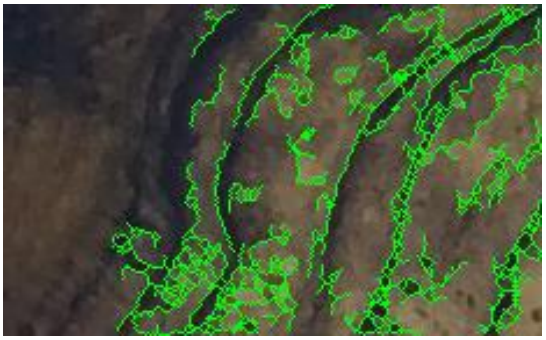

Figure B-102: Image K1 k_b=0.4

Figure B-103: Image K2 (Vertical scale: 30 cm)

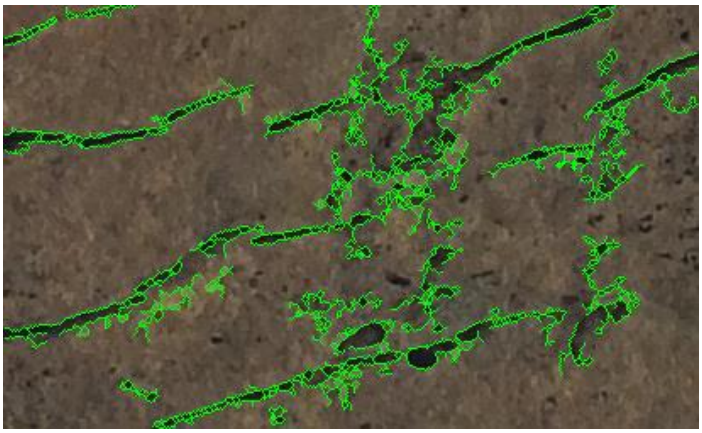

Figure B-104: Image K2 k_b=0.4

Figure B-105: Image L1 (Vertical scale: 20 cm)

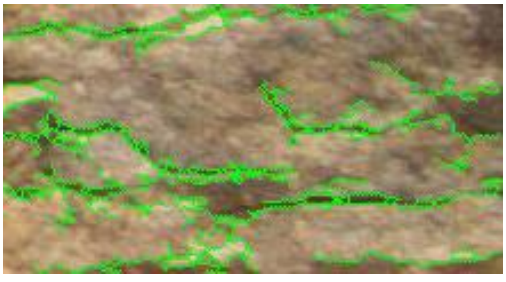

Figure B-106: Image L1 k_b=0.4

Figure B-107: Image L2 (Vertical scale: 20 cm)

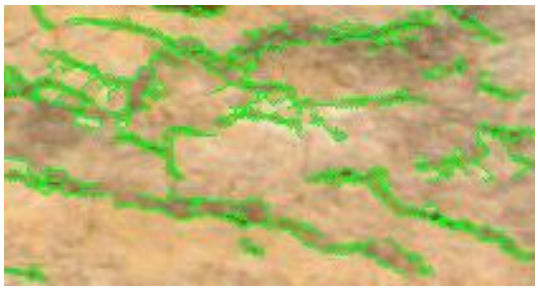

Figure B-108: Image L2 k_b=0.4

Figure B-109: Image NP1 (Vertical scale: 30 cm)

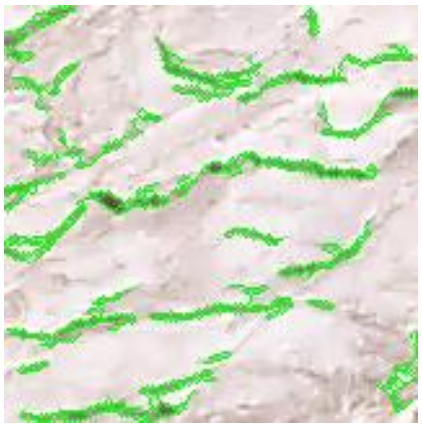

Figure B-110: Image NP1 k_b=0.4

Figure B-111: Image NP4 (Vertical scale: 20 cm)

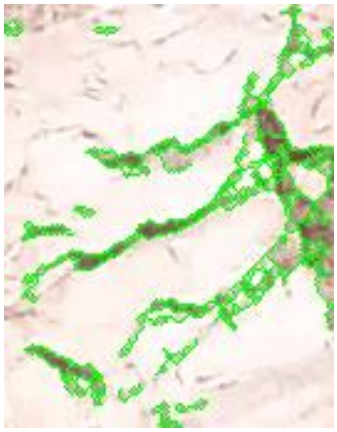

Figure B-112: Image NP4 k_b=0.4

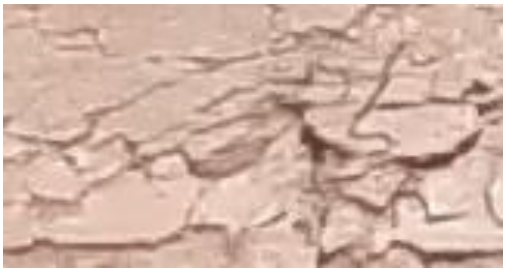

Figure B-113: Image NP5 (Vertical scale: 50 cm)

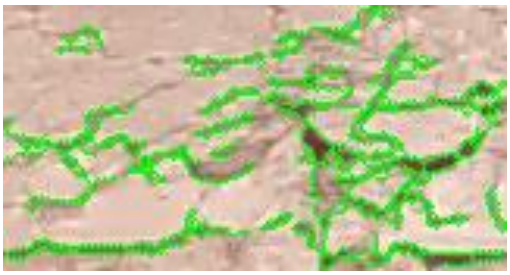

Figure B-114: Image NP5 k_b=0.4

Figure B-115: Image NZ1 (Vertical scale: 20 cm)

Figure B-116: Image NZ1 k_b=0.4

Figure B-117: Image NZ2 (Vertical scale: 18 cm)

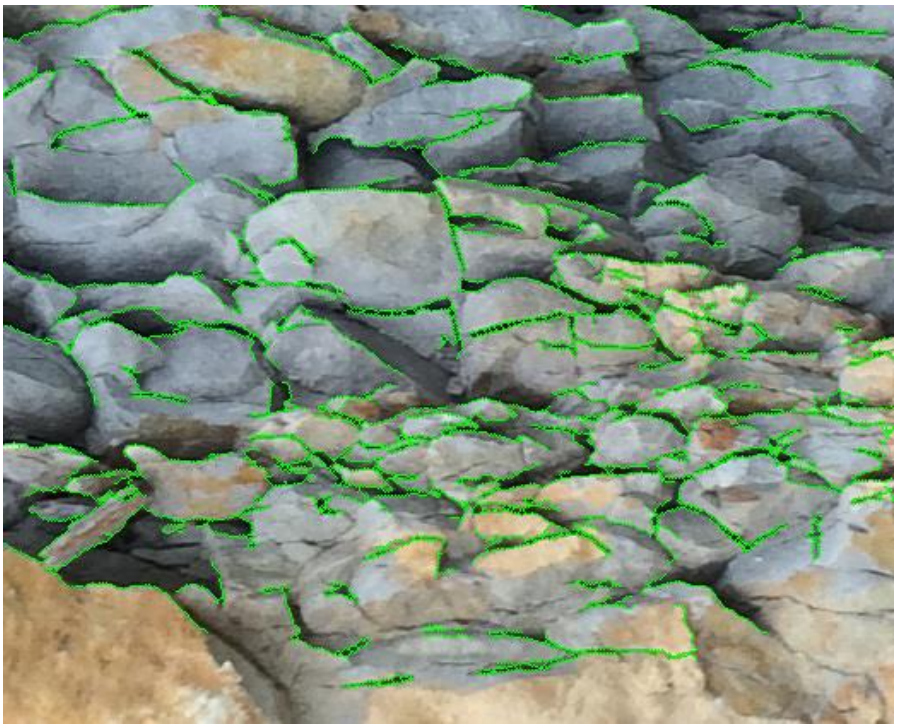

Figure B-118: Image NZ2 k_b=0.4

Figure B-119: Image NZ3 (Vertical scale: 12 cm)

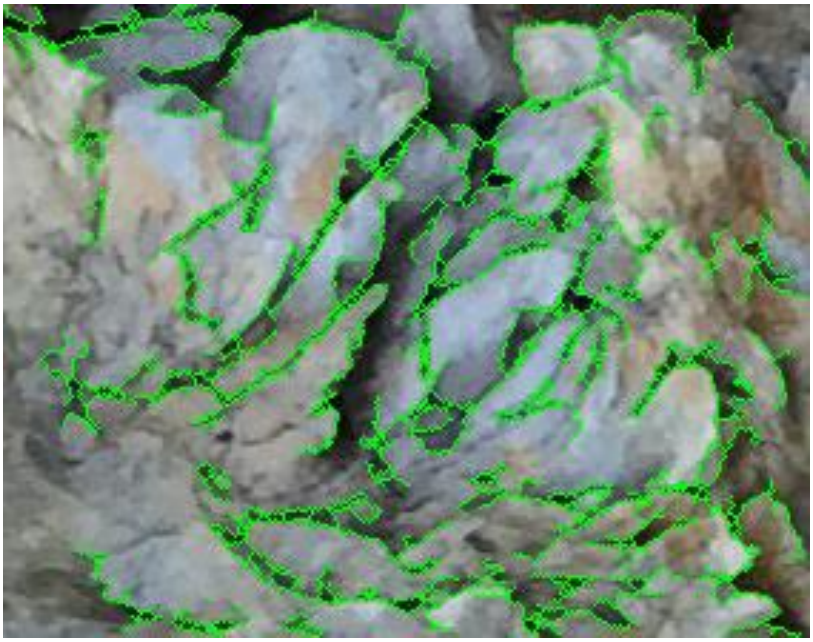

Figure B-120: Image NZ3 k_b=0.4

Figure B-121: Image NZ4 (Vertical scale: 8 cm)

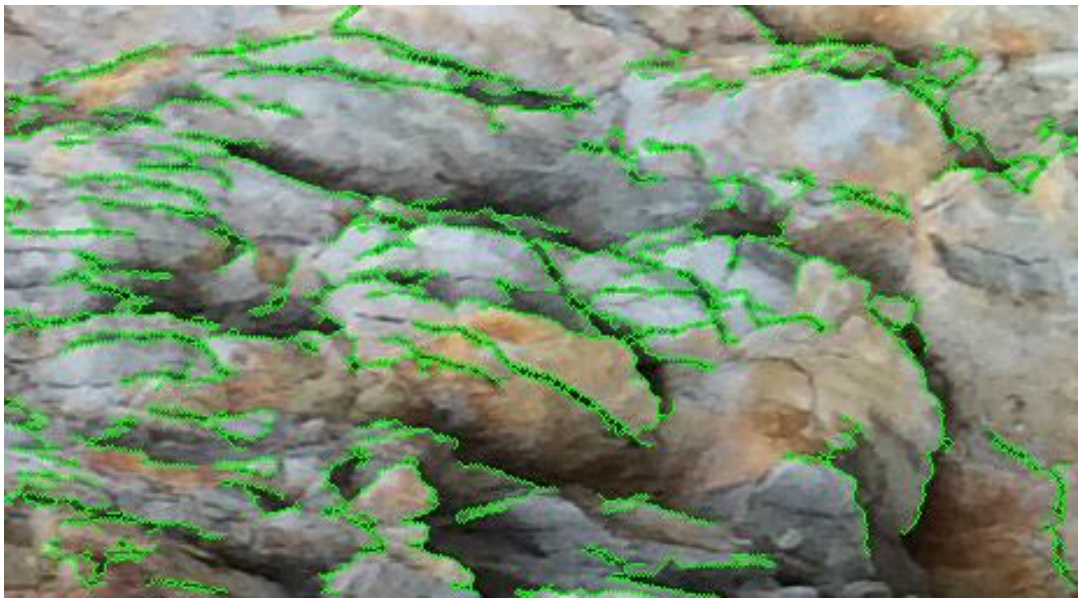

Figure B-122: Image NZ4 k_b=0.4

Figure B-123: Image NZ5 (Vertical scale: 15 cm)

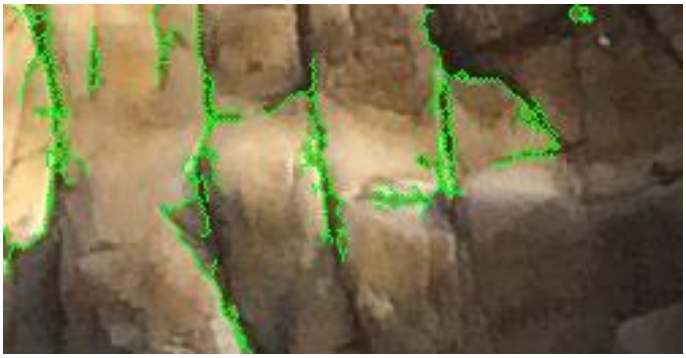

Figure B-124: Image NZ5 k_b=0.4

Figure B-125: Image NZ10 (Vertical scale: 18 cm)

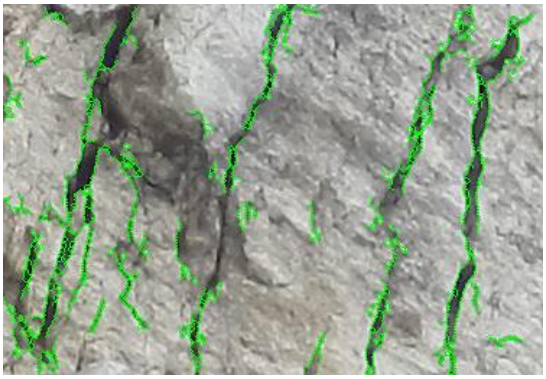

Figure B-126: Image NZ10 k_b=0.4

Figure B-127: Image NZ11 (Vertical scale: 25 cm)

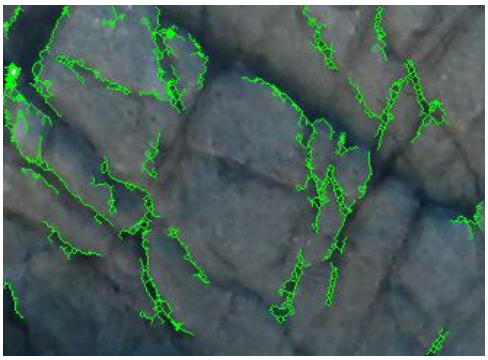

Figure B-128: Image NZ11 k_b=0.4

Figure B-129: Image NZ12 (Vertical scale: 25 cm)

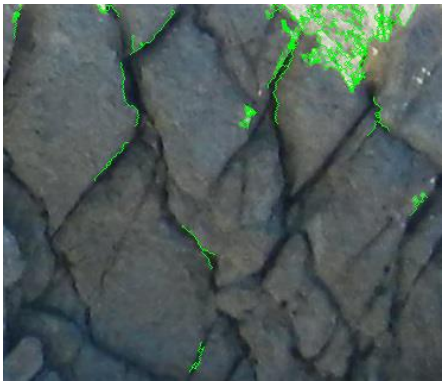

Figure B-130: Image NZ12 k_b=0.4

Figure B-131: Image NZ13 (Vertical scale: 15 cm)

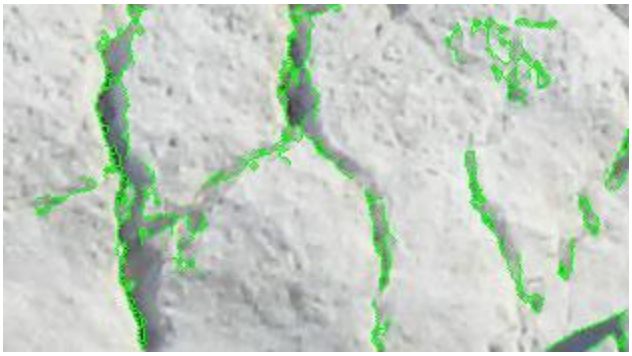

Figure B-132: Image NZ13 k_b=0.4

Figure B-133: Image NZ17 (Vertical scale: 30 cm)

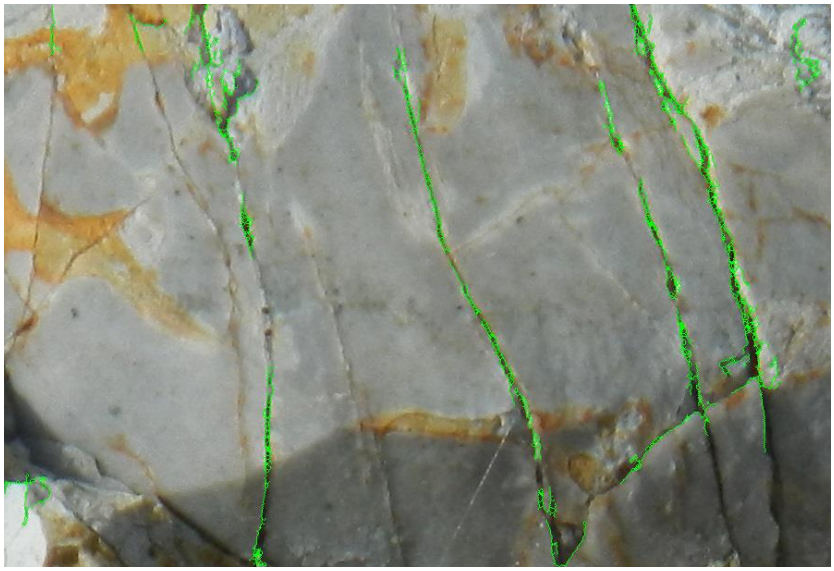

Figure B-134: Image NZ17 k_b=0.4

Figure B-135: Image NZ18 (Vertical scale: 25 cm)

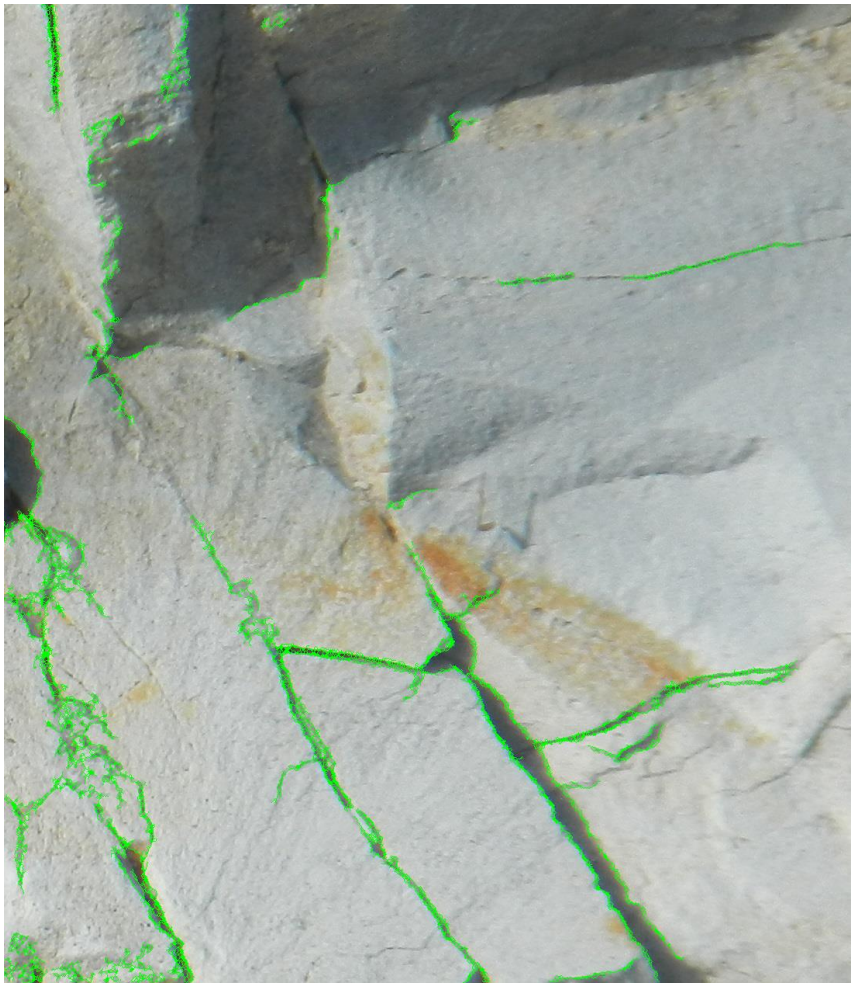

Figure B-136: Image NZ18 k_b=0.4

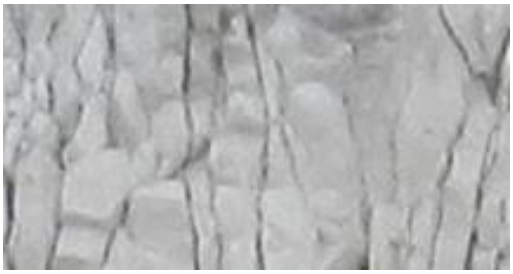

Figure B-137: Image NZ21 (Vertical scale: 35 cm)

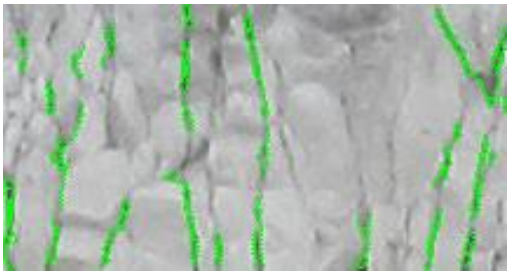

Figure B-138: Image NZ21 k_b=0.4

Figure B-139: Image S1 (Vertical scale: 80 cm)

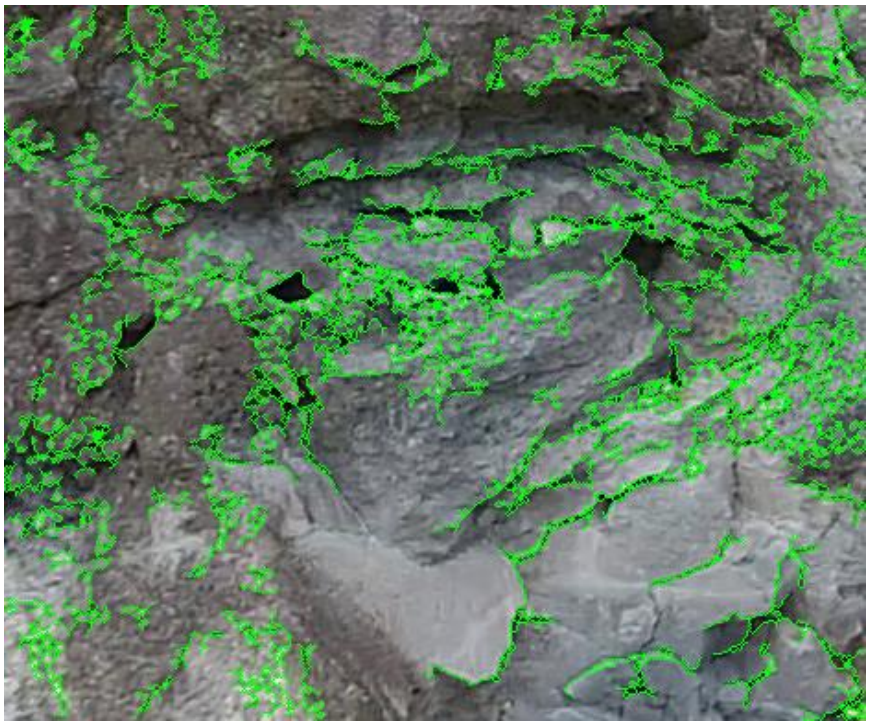

Figure B-140: Image S1 k_b=0.4

Figure B-141: Image S2 (Vertical scale: 40 cm)

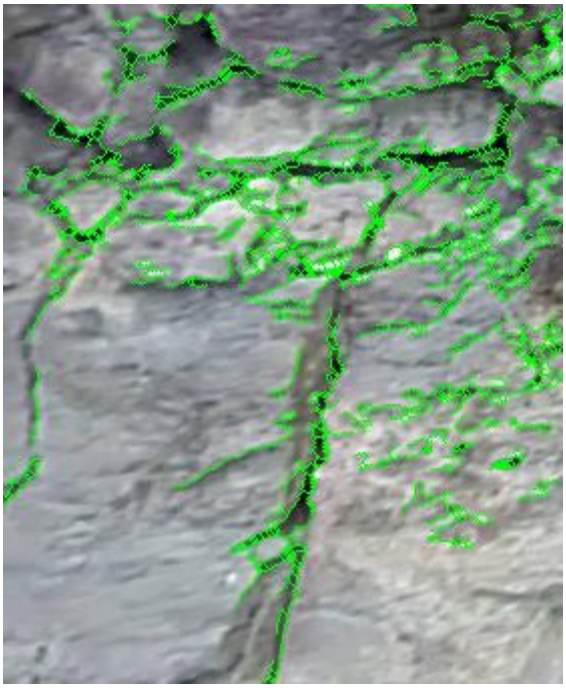

Figure B-142: Image S2 k_b=0.4

Figure B-143: Image S3 (Vertical scale: 25 cm)

Figure B-144: Image S3 k_b=0.4

Figure B-145: Image S4 (Vertical scale: 30 cm)

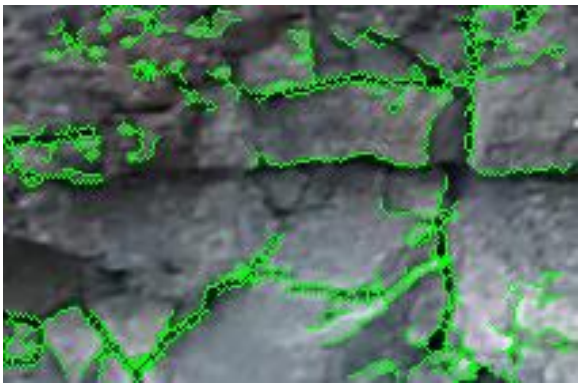

Figure B-146: Image S4 k_b=0.4

Figure B-147: Image S5 (Vertical scale: 25 cm)

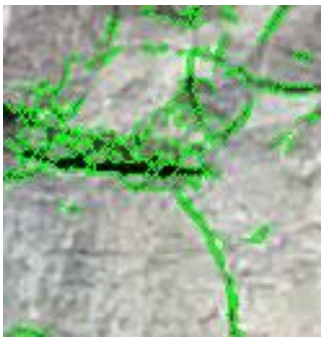

Figure B-148: Image S5 k_b=0.4